Combining Tectonic Geomorphology and Paleoseismology for Understanding of Earthquake Recurrence

by

J. Barrett Salisbury

A Dissertation Presented in Partial Fulfillment
of the Requirements for the Degree
Doctor of Philosophy

Approved November 2016 by the
Graduate Supervisory Committee:

Ramón Arrowsmith, Chair
Manoochehr Shirzaei
Duane DeVecchio
Kelin Whipple
Arjun Heimsath

ARIZONA STATE UNIVERSITY

December 2016

ABSTRACT

There is a need to understand spatio-temporal variation of slip in active fault zones, both for the advancement of physics-based earthquake simulation and for improved probabilistic seismic hazard assessments. One challenge in the study of seismic hazards is producing a viable earthquake rupture forecast—a model that specifies the expected frequency and magnitude of events for a fault system. Time-independent earthquake forecasts can produce a mismatch among observed earthquake recurrence intervals, slip-per-event estimates, and implied slip rates. In this thesis, I developed an approach to refine several key geologic inputs to rupture forecasts by focusing on the San Andreas Fault in the Carrizo Plain, California. I use topographic forms, sub-surface excavations, and high-precision geochronology to understand the generation and preservation of slip markers at several spatial and temporal scales—from offset in a single earthquake to offset accumulated over thousands of years. This work results in a comparison of slip rate estimates in the Carrizo Plain for the last ~15 kyr that reduces ambiguity and enriches rupture forecast parameters. I analyzed a catalog of slip measurements and surveyed earth scientists with varying amounts of experience to validate high-resolution topography as a supplement to field-based active fault studies. The investigation revealed that (for both field and remote studies) epistemic uncertainties associated with measuring offset landforms can present greater limitations than the aleatoric limitations of the measurement process itself. I pursued the age and origin of small-scale fault-offset fluvial features at Van Matre Ranch, where topographic depressions were previously interpreted as single-event tectonic offsets. I provide new estimates of slip in the most recent earthquake, refine the centennial-scale fault slip rate,

and formulate a new understanding of the formation of small-scale fault-offset fluvial channels from small catchments (<7,000 m^2). At Phelan Creeks, I confirm the constancy of strain release for the ~15,000 years in the Carrizo Plain by reconstructing a multistage offset landform evolutionary history. I update and explicate a simplified model to interpret the geomorphic response of stream channels to strike-slip faulting. Lastly, I re-excavate and re-interpret paleoseismic catalogs along an intra-continental strike-slip fault (Altyn Tagh, China) to assess consistency of earthquake recurrence.

DEDICATION

For NDS

ACKNOWLEDGMENTS

A large portion of this project was conducted in the field over intensely hot, long days and I heartily thank everyone that helped in the field over the course of this dissertation: Sinan Akciz, Ramón Arrowsmith, Nathan Brown, Caitlyn Fischman, Lisa Grant Ludwig, Daniel Halford, Emily Kleber, Matthew Marin, Gayatri Marliyani, Eui-jo Marquez, Nik Midttun, Juliet Olsen, Tom Rockwell, Michael Say, Tsurue Sato, Jessica Sutton, & Alana Williams. Thank you to the many participants in our public and classroom surveys, and thank you to Dominique Garello, David Haddad, Tom Rockwell, and Olaf Zielke for administering the surveys to their students. Thank you to Javier Colunga for help with database management and technical issues I've encountered over the years. Thank you to our many colleagues at the State Key Laboratory of Earthquake Dynamics, Institute of Geology, China Earthquake Administration in Beijing.

Discussions with many colleagues including Sinan Akciz, Lisa Grant-Ludwig, Tom Rockwell, and Kate Scharer have helped to focus our thinking on the problems identified in this dissertation. Also, many thanks to my friends and mentors in the Active Tectonics, Quantitative Structural Geology and Geomorphology/Surface Processes Research Groups at ASU.

A special thank you to L. Bidart and A. J. Phelan for access to the Van Matre Ranch and Phelan Creeks properties. We could not have completed this work without their interest and assistance.

This research was supported by the Southern California Earthquake Center. SCEC is funded by NSF Cooperative Agreement EAR-1033462 & USGS Cooperative Agreement G12AC20038. UCERF3 was supported by the California Earthquake

Authority, US Geological Survey, and the Southern California Earthquake Center. This work was also supported by the US Geological Survey National Earthquake Hazards Reduction program (G11AP20029 and G11AP20020). Any use of trade, firm, or product names is for descriptive purposes only and does not imply endorsement by the U.S. Government. B4 lidar data are from the B4 Lidar Project (NCALM, USGS, OSU, & EAR Geophysics at NSF) and are available at OpenTopography (*http://www.opentopography.org)*. Work on very high resolution topography using structure from motion was supported in part by a Strategic University Partnership between Arizona State University and the Jet Propulsion Laboratory.

I would like to thank my previous advisors that helped set the foundation for a productive scientific career: Dr. Dave Harbor and Dr. Tom Rockwell. Thank you to my committee for providing constructive commentary and for providing stimulating discussion during the last several years. Thank you to my family for supporting me from the very beginning, letting me talk about research as much as I wanted, and happily accepting rocks as gifts for many years. Lastly and most importantly, a sincere thank you to my current advisor, Dr. Ramón Arrowsmith, for his constant encouragement and support. I am very lucky to have been a part of this research group at ASU.

TABLE OF CONTENTS

CHAPTER Page

CHAPTER Page

LIST OF TABLES

LIST OF FIGURES

CHAPTER 1

INTRODUCTION

OVERVIEW

There is a fundamental need to understand the spatio-temporal variation of slip in active fault zones, both for the advancement of physics-based earthquake simulation and for improved probabilistic seismic hazard assessments. Worldwide, populations in earthquake-vulnerable urban environments are rapidly increasing (Billham, 2004). In California alone, 38 million people live near earthquake-producing faults (Field et al., 2014). Quantification of seismic hazard is the key to earthquake-resistant construction and community preparedness—both of which are required to mitigate potentially devastating impacts of large earthquakes (Allen, 2007).

One of the main challenges in the study of seismic hazards is producing a viable earthquake rupture forecast—a model that specifies the frequency and magnitude of events expected for a fault system. There have been major recent advances towards this end (e.g., UCERF3; Field et al., 2014; Figure 1.1) but time-independent earthquake forecasts (i.e., long-term forecasts) often produce a mismatch with observed earthquake recurrence intervals, slip-per-event estimates, and implied slip rates. This is because the timespans between successive earthquakes and co-seismic slip at a point (even on a single, isolated fault strand) can be highly irregular. Therefore, to improve our earthquake hazard forecasts, a better understanding of earthquake rupture histories over a range of timescales is needed.

Information regarding past rupture histories are of three main types: 1) instrumental (e.g., GPS and InSAR, seismic networks; modern to hundreds of years),

historic (i.e., written accounts; modern to a few thousand years, but with significant quality degradation further into the past), and geologic (e.g., slip rate studies, paleoseismic catalogs; modern to tens of thousands of years) (Jordan, 2011). In modern rupture forecasts, geologic constraints represent up to 75% of all input data. Specifically, these data include fault models (the physical geometry of faults in a system), deformation models (the rates at which faults in a system slip over many earthquakes, as interpreted from dated, fault-offset landforms), and earthquake rate models (the long-term rate of earthquakes derived from paleoseismic studies) and thus their magnitudes (measured in the field for historic and prehistoric ruptures) (Field et al., 2014).

In this thesis, I explore ways to refine deformation and earthquake rate models—key geologic inputs into earthquake rupture forecasts. I focus on high-resolution surficial topographic forms and sub-surface fault zone geomorphology to reveal the tectonically-influenced evolution of features at a range of spatial scales. We pursue a rapidly-advancing technique known as structure from motion (SfM), which allows for cost-effective generation of sub-decimeter scale topography from unconstrained low-altitude or ground-based photographs. We use a helium balloon-mounted digital camera to document subtle topographic features for enhanced interpretation prior to excavation. Additionally, we use ground-based photographs to preserve 3-D representations of fluvial channel and alluvial fan geometries as well as to document sedimentary relationships in our excavations.

I also employ a ground-breaking geochronologic technique known as post-infrared infrared-stimulated luminescence (pIR-IRSL)—an advanced form of optically stimulated luminescence (OSL) dating. We calculate the burial ages of potassium-

feldspar grains with a high degree of certainty and we use these dates in combination with the more traditional radiocarbon (^{14}C) estimates of stratigraphic age. We show that the fading-corrected pIR-IRSL ages are as consistent and potentially more precise than the ^{14}C ages in the Carrizo Plain. These are exciting results and add considerable strength to the interpretations presented in this dissertation. Additionally, these techniques promise continued advancement in the study of active tectonics.

I begin with a review of the process of measuring small-scale geomorphic features (mostly stream channels) that have been interpreted as single- and multiple-event slip markers from fast-slipping faults in North America. I then shift focus to the Carrizo Plain reach of the San Andreas Fault (SAF), south-central California (where some of the earliest conceptual models of earthquake recurrence were formulated) to investigate a set of topographic depressions interpreted as single-event tectonic offsets. Next, I focus on the evolution of a pair of offset stream channels (offset ~125 and ~238 m) in the Carrizo Plain to reconstruct stages in their evolutionary history to estimate slip rates at a range of temporal scales. Lastly, I move to a far less-studied, major (~1,300 km-long) intra-continental strike-slip fault, the Altyn Tagh, China, to re-excavate and re-interpret an earthquake catalog to assess the consistency of earthquake recurrence. We compare earthquake histories on opposite sides of a major geometric complexity (in an otherwise straight fault segment) to understand controls on fault rupture lengths.

THE CARRIZO PLAIN REACH OF THE SAN ANDREAS FAULT

My work shows that even in an area where basic fault parameters are already known, there is much to be gained from high-resolution geomorphic studies such as these. The significance of tectonic landforms throughout the Carrizo Plain has long been recognized (Lawson et al., 1908; Arnold and Johnson, 1910; Wood and Buwalda, 1931; Hill and Dibblee, 1953; Wallace, 1968; Sieh, 1978) and several types of fault studies have been conducted there.

The Carrizo Plain section of the SAF, located between Parkfield and the Big Bend, has a relatively simple geometry, the highest slip rate in California (3.4 – 3.6 cm/yr, Sieh and Jahns, 1984; 3.6 cm/yr, Meade and Hager, 2005; 3.6 cm/yr, Schmalzle et al, 2006; 3.1 cm/yr, Noriega et al., 2006), and ruptured historically in the M*w* 7.8 Fort Tejon earthquake of 1857 (Figure 1.2). Early models of earthquake recurrence for this stretch of the SAF are simple, suggesting that repeat, large events at longer time intervals dominate the earthquake record (Sieh and Jahns, 1984; Grant and Sieh, 1994; Liu et al., 2004; Liu-Zeng et al., 2006; Zielke, et al., 2010) (Figure 1.3). For example, excavations of stream offsets and beheaded channels by Liu-Zeng et al. (2006) near Wallace Creek revealed that as many as four of the last six events ruptured with >5 m of slip, implying a somewhat regular but not strictly uniform rupture behavior. Similarly, Zielke et al. (2010, 2012) use high-resolution topographic data to suggest that average slip in 1857 was ~5 m, and that some other older large earthquakes likely have similar magnitudes of slip (Figure 1.4).

However, it is possible that discrete evidence of the smallest events (e.g., <1 m, from smaller earthquakes or the tail ends of ruptures) will be lost at the surface and only

preserved in the paleoseismic record (e.g., Akciz, et al., 2010; Zielke et al., 2010, 2012, 2015). In a paleoseismic and paleoflood correlation study, Grant Ludwig et al. (2010) suggested variable slip (0.5 to 5.9 m) for the last five ruptures at nearby Bidart Fan. Investigators can adequately measure the surface expression of small-scale offset landforms (Chapter 2, Salisbury et al., 2015; Zielke et al., 2015) but it is important to note, however, that the surficial geomorphic record will be dominated by the largest of event offsets.

Continued investigations in the Carrizo Plain with improved geochronologic techniques have refined the paleoseismic earthquake catalog and argued that the average recurrence of earthquakes along the SAF is likely as frequent as 99 ± 46 years (includes current open interval; Akciz et al., 2010) instead of the >200-year recurrence proposed by Sieh and Jahns (1984) (Figure 1.3). The Uniform California Earthquake Rupture Forecast, Version 3 (UCERF3) calculates a maximum likelihood recurrence for the Carrizo Plain segment of the SAF (at Bidart fan) at 115 yrs (86 – 154 yrs 16 – 84% bounds; Field, et al., 2014). If one assumes a perfect correspondence between successive paleoseismic events and discrete offsets identified at the surface or in the shallow subsurface, then coupling the conservative recurrence rate proposed by Akciz et al. (2010) with cumulative offsets from Liu-Zeng et al. (2006) or Zielke et al. (2010) implies slip rates as high as ~60 mm/yr and ~50 mm/yr, respectively, both of which greatly exceed ~33 mm/yr rate estimated from millennial-scale offset landforms (Sieh and Jahns, 1984) and geodesy (Meade and Hager, 2005; Schmalzle, et al., 2006).

This mismatch between inferred slip rates, recurrence intervals, and slip per event suggests that recurrence timing and moment distribution are significantly more variable

than originally thought (Weldon et al., 2004; Scharer et al., 2014; Dawson, 2013; Madden et al., 2013; Rockwell et al., 2014; Field et al., 2014). In the Carrizo Plain, therefore, it is inaccurate to assume a perfect correspondence between the earthquakes preserved in sub-surface sediments and with the earthquakes preserved in the geomorphic record (as suggested by Akciz, et al., 2010 and Zielke, et al, 2010). Reconciliation of these discrepancies between measurable fault parameters is crucial to proper hazard characterization so I explore the possibility that slip in individual earthquakes may be smaller overall or significantly more variable than previously estimated.

I provide new estimates of slip in the most recent event at the Van Matre Ranch Site, refine the centennial-scale slip rate (Figure 1.5), and formulate a new understanding of the formation of small-scale fault-offset fluvial channels from small catchments (<7,000 m^2). I also show that there is minimal millennial-scale slip rate variability in the Carrizo Plain (Figure 1.5) and update and explicate a conceptual tectono-stratigraphic model to interpret the geomorphic response of stream channels to continued strike-slip faulting.

CHAPTER OUTLINE

My dissertation is divided into six chapters. I have arranged the chapters such that the discussion begins with the youngest, smallest offset geomorphic features and progresses to older features that preserve larger amounts of cumulative slip. In Chapter 2, I take a close look at how scientists conduct surficial studies of active faults and some of the common ways in which they estimate slip in individual earthquakes. There have recently been major scientific advancements in the generation of high-resolution (sub meter-scale) topographic datasets (e.g., SfM) for studying slip distributions of historic

and prehistoric earthquakes. Such information is essential for estimation of paleo-earthquake extents and magnitudes and for evaluation of conceptual models of earthquake recurrence (e.g., Shimazaki and Nakata, 1980; Sieh and Jahns, 1984; Schwartz and Coppersmith, 1984; Field et al., 2014). The increasing availability of high-resolution topographic data has allowed for the generation of many datasets for input into earthquake recurrence models, but it is important that the limitations of measurements from such datasets are properly understood. I examine the influence of operator decisions on remote offset measurements and provide a framework for remotely analyzing strike-slip offset. I also highlight some of the most commonly-faced problems encountered when measuring small-scale tectonic offsets (remotely and in the field) and provide suggestions about how to avoid them. The results of this analysis provided much of the inspiration for Chapter 3.

Chapter 2 was published in the Geological Society of America journal *Geosphere* in 2015. My co-authors include David E. Haddad (ASU, currently with Conoco Phillips, Houston, TX), Tom Rockwell (San Diego State University), Ramón Arrowsmith (Arizona State University), Chris Madugo (Oregon State University, currently with Pacific Gas & Electric, San Francisco, CA), Olaf Zielke (King Abdulah University of Science and Technology, Saudi Arabia), and Kate Scharer (United States Geological Survey, Pasadena, CA).

In Chapter 3, I take a hands-on approach to explore the epistemic uncertainties associated with measuring small-scale tectonic offsets that were discussed in Chapter 2. This study highlights that seemingly simple geomorphic features (represented in high-resolution topographic data or viewed in the field) may require 3-D subsurface

excavations and high-precision geochronology to fully understand the pre-earthquake morphology and post-earthquake geomorphic modification. I show that several key geomorphic features previously interpreted as single-earthquake, tectonic slip markers have been interpreted incorrectly or incompletely. I provide a new estimate of slip in the most recent earthquake for this site in the Carrizo Plain and provide a new centennial-scale slip rate (Figure 1.5). I also develop a new understanding for the behavior of small-catchment (<7,000 m^2) drainage basins in a semi-arid landscape that can be used in future studies to help interpretation at other locations along the San Andreas Fault. I plan to submit Chapter 3 to the Geological Society of America *Bulletin* for publication.

In Chapter 4, I focus on larger offset stream channels at Phelan Creeks (offset ~125 m and 238 m) and excavate many trenches to piece together the evolutionary history of the channels for ~7,000 years of faulting. This work was initiated in the 1990s by John Sims at the United States Geological Survey. Except for a few meeting abstracts, the existing work is largely unpublished. I combine our new geochronologic results with existing data and perform a complete overhaul of interpretations at that site. By reconstructing and dating different stages of offset history, I provide several much-needed constraints for slip rates in the Carrizo Plain throughout the Holocene (Figure 1.5). These excavations inform our models of the geomorphic response of large-scale stream channels to continued strike-slip faulting. This dissertation results in a comparison of short- and long-term slip rates along the south-central San Andreas Fault that can be used to reduce ambiguity and enrich rupture forecast parameters for the region. I plan to submit Chapter 4 to the American Geophysical Union *Journal of Geophysical Research: Earth Surface* for publication.

In Chapter 5, I take a traditional paleoseismic approach to evaluating the frequency of earthquake recurrence on the west-central Altyn Tagh Fault, Xinjiang China. A team explored this area in 2007 with the same intention but a lack of datable materials precluded developing a well-constrained earthquake catalog for this reach (the Cherchen He reach) of fault (Muretta, 2009). I take the opportunity to re-excavate, refresh, and re-interpret the faulted stratigraphy to compare the consistency of interpretations between research teams and to re-sample materials for an improved earthquake chronology. I independently produce a consistent interpretation from a similar sequence of faulted sediments, re-sample correlative stratigraphic units for radiocarbon constraints, and strengthen age estimates for the last four events on the west-central Altyn Tagh Fault.

In Chapter 6, I provide concluding remarks and thoughts for future research.

REFERENCES

Akciz, S.O., Grant Ludwig, L., Arrowsmith, J R., and Zielke, O., 2010, Century-long average time intervals between earthquake ruptures of the San Andreas fault in the Carrizo Plain, California: Geology, v. 38, no. 9, p.787 – 790, doi: 10.1130/G30995.1.

Allen, R. M., 2007, Earthquake hazard mitigation: new directions and opportunities: in Schubert, Gerald (Ed.), Treatise on Geophysics, Earthquake Seismology, vol. 4, Elsevier.

Arnold, R., and Johnson, H. R., 1910, Preliminary report on the McKittrick-Sunset oil region, Kern and San Luis Obispo counties, California: U. S. Geological Survey Bulletin 406.

Billham, R., 2004, Urban earthquake fatalities: a safer world, or worse to come?: Seismological Research Letters, v. 75, p. 706 – 712.

Dawson, T.E., 2013. Appendix A: Updates to the California reference fault parameter database: UCERF3 fault models 3.1 and 3.2: US Geological Survey Open-File Report.

Field, E. H., Arrowsmith, J R., Biasi, G. P., Bird, P., Dawson, T. E., Felzer, K. R., Jackson, D. D., Johnson, K. M., Jordan, T. H., Madden, C., Michael, A. J., Milner, K. R., Page, M. T., Parsons, T., Powers, P. M., Shaw, B. E., Thatcher, W. R., Weldon, R. J., and Zeng, Y., 2014, Uniform California Earthquake Rupture Forecast, Version 3 (UCERF3)—The time-independent model: Bulletin of the Seismological Society of America, v. 104, no.3, p. 1122 – 1180, doi: 10.1785/0120130164.

Grant, L. B., and Sieh, K., 1994, Paleoseismic evidence of clustered earthquakes on the San Andreas fault in the Carrizo Plain, California: Journal of Geophysical Research, v. 99, no. B4, p. 6819 – 6841.

Grant Ludwig, L., Akciz, S. O., Noriega, G. R., Zielke, O., and Arrowsmith, J R., 2010, Climate-modulated channel incision and rupture history of the San Andreas fault in the Carrizo Plain: Science, v. 327, p.1117 – 1119, doi: 10.1126/science.1182837.

Grant Ludwig, L., Akciz, S. O., Arrowsmith, J R., and Salisbury, J. B., *in press*, Re-measurement of the San Andreas Fault slip rate at Wallace Creek, Carrizo Plain, CA.

Hill, M. L., and Dibblee, T. W., 1953, San Andreas, Garlock, and Big Pine faults, California study of the character, history, and tectonic significance of their displacements: Bulletin of the Geological Society of America, v. 64, p. 443 – 458.

Jordan, T. H., Chen, Y., Gasparini, P., Madariaga, R., Main, I., Marzocchi, W., Papadopoulos, G., Sobolev, G., Yamoaka, K., and Zschau, J., 2011, Operational earthquake forecasting: state of knowledge and guidelines for utilization: Annals of Geophysics, v. 54, no. 4, p. 316 – 391.

Lawson, A. C., and others, 1908, Report of the earthquake investigation commission upon the California earthquake of April 18, 1906: Carnegie Institution of Washington, D. C.

Liu, J., Klinger, Y., Sieh, K., and Rubin, C., 2004, Six similar sequential ruptures of the San Andreas fault, Carrizo Plain, California: Geology, v. 32, no. 8, pp. 649 – 652, doi: 10.1130/G20478.1.

Liu-Zeng, J., Klinger, Y., Sieh, K., Rubin, C., and Seitz, G., 2006, Serial ruptures of the San Andreas fault, Carrizo Plain, California, revealed by three-dimensional excavations: Journal of Geophysical Research, v. 111, B02306, doi: 10.1029/2004JB003601.

Madden, C., Haddad, D. E., Salisbury, J. B., Zielke, O., Arrowsmith, J R., Weldon II, R. J., and Colunga, J., 2013, Compilation of Slip-in-the-Last-Event Data and Analysis of Last Event, Repeated Slip, and Average Displacement for Recent and Prehistoric Ruptures, Appendix R *in* Field, E. H., Arrowsmith, J R., Biasi, G. P., Bird, P., Dawson, T. E., Felzer, K. R., Jackson, D. D., Johnson, K. M., Jordan, T. H., Madden, C., Michael, A. J., Milner, K. R., Page, M. T., Parsons, T., Powers, P. M., Shaw, B. E., Thatcher, W. R., Weldon II, R. J., and Zeng, Y., 2013, Uniform California earthquake rupture forecast, version 3 (UCERF3), The time-independent model: U.S. Geological Survey Open-File Report 20131165, 97 p., California Geological Survey Special Report 228, and Southern California Earthquake Center Publication 1792, http://pubs.usgs.gov/of/2013/1165.

Meade, B. J., and Hager, B. H., 2005, Block models of crustal motion in southern California constrained by GPS measurements: Journal of Geophysical Research, v. 110, B03403, doi: 10.1029/2004JB003209.

Muretta, M., 2009, Holocene earthquake geology of the central Altyn Tagh fault, Xinjiang, China: Implications for recurrence interval, strain release, and fault behavior: M.S. Thesis, *unpublished*, Arizona State University.

Noriega, G.R., Arrowsmith, J R., Grant, L. B., Young, J. J., 2006, Stream Channel Offset and Late Holocene Slip Rate of the San Andreas Fault at the Van Matre Ranch Site, Carrizo Plain, California: Bulletin of the Seismological Society of America, v. 96, no. 1, p.33 – 47, doi: 10.1785/0120050094.

Rockwell, T.K., Dawson, T. E., Young Ben-Horin, J., Seitz, G., 2014, A 21 event, 4,000-year history of surface ruptures in the Anza Seismic Gap, San Jacinto Fault, and implications for long-term earthquake production on a major plate boundary fault: Pure and Applied Geophysics, v. 172, no. 5, p. 1143 – 1165, doi: 10.1007/s00024-014-0955-z.

Salisbury, J. B., Haddad, D. E., Rockwell, T. K., Arrowsmith J R., Madugo, C., Zielke, O., and Scharer, K., 2015, Validation of meter-scale surface faulting offset measurements from high-resolution topographic data: Geosphere, v. 11, no. 6, doi: 10.1130/GES01197.1.

Scharer, K., Salisbury, J. B., Arrowsmith, J R., and Rockwell, T. K., 2014, Southern San Andreas Fault Evaluation Field Activity: Approaches to Measuring Small Geomorphic Offsets—Challenges and Recommendations for Active Fault Studies: Seismological Research Letters, v. 85, no. 1, doi: 10.1785/022013010B.

Schmalzle, G., Dixon, T., Malservisi, R., and Govers, R., 2006, Strain accumulation across the Carrizo segment of the San Andreas Fault, California: Impact of laterally varying crustal properties: Journal of Geophysical Research: Solid Earth, vol. 111, no. B5, https://doi.org/10.1029/2005JB003843.

Schwartz, D. P., and Coppersmith, K. J., 1984, Fault behavior and characteristic earthquakes: examples from the Wasatch and San Andreas fault zones: Journal of Geophysical Research, v. 89, no. B7, p. 5681 – 5698.

Shimazaki, K., and Nakata, T., 1980, Time-predictable recurrence model for large earthquakes: Geophysical Research Letters, v. 7, no. 4, p. 279 – 282.

Sieh, K. E., 1978, Slip along the San Andreas fault associated with the great 1857 earthquake: Bulletin of the Seismological Society of America, v. 68, no. 5, p. 1421 – 1448.

Sieh, K. E., and Jahns, R. H., 1984, Holocene activity of the San Andreas fault at Wallace Creek, California: Geological Society of America Bulletin, v. 95, p. 883 – 896.

Wallace, R. E., 1968, Notes on stream channels offset by the San Andreas fault, southern coast ranges, California, *in* Dickson, W. R., and Grantz, A., eds., Proceedings of Conference on Geologic Problems of the San Andreas Fault system*,* Stanford University Publication, Geological Sciences, v. 11*,* p. 6 – 21.

Weldon, R., Scharer, K., Fumal, T., Biasi, G., 2004, Wrightwood and the earthquake cycle: What a long recurrence record tells us about how faults work: GSA Today, v. 14, no. 9, p. 4 – 10, doi: 10.1130/1052-5173(2004)014<4:WATECW>2.0CO;2.

Wood, H. O., and Buwalda, J. P.,1931, Horizontal displacement along the San Andreas fault in the Carrizo Plain, California: Geological Society of America Bulletin, v. 42, p. 298 – 299.

Zielke, O., Arrowsmith J R., Grant Ludwig, L., Akciz, S. O., 2010, Slip in the 1857 and Earlier Large Earthquakes Along the Carrizo Plain, San Andreas Fault: Science, v. 327, p.1119 – 1122, doi: 10.1126/science.1182781.

Zielke, O., Arrowsmith, J R., Grant Ludwig, L., Akciz, S. O., 2012, High-resolution topography-derived offsets along the 1857 Fort Tejon earthquake rupture trace, San Andreas Fault: Bulletin of the Seismological Society of America, v. 102, no. 3, p. 1135 – 1154, doi: 10.1785/0120110230.

Zielke, O., Klinger, Y., and Arrowsmith, J R., 2014, Fault slip and earthquake recurrence along strike-slip faults – Contributions of high-resolution geomorphic data: Tectonophysics, v. 638, p. 43 – 62, doi: 10.1016/j.tecto.2014.11.004.

FIGURE CAPTIONS

Figure 1.1 – 3-D perspective view of California showing all 2,606 modeled fault sections (shown as black rectangles) colored by the long-term the frequency with which $M \geq 6.7$ earthquakes occur (i.e., the participation rates). Results represent a weighted average of all model outputs from over 700 distinct logic-tree branches. From Field et al., 2014.

Figure 1.2 – Summary of slip rate estimates from existing studies in the Carrizo Plain. The red portion of the San Andreas Fault in the California inset map represents the extent of the 1857 surface rupture. Place abbreviations: SD—San Diego, SB—Santa Barbara, SF—San Francisco.

Figure 1.3 – Summary of recurrence interval estimates from paleoseismic studies in the Carrizo Plain.

Figure 1.4 – Summary of slip-per-event estimates in the Carrizo Plain.

Figure 1.5 – Age vs. Offset plot for the Carrizo Plain for the last 15,000 years. Box dimensions represent age and offset uncertainties. Black boxes represent age vs. offset plots provided by this dissertation. The red line represents the slip rate calculated by Sieh and Jahns (1984) for the last 3,700 years from the small (130 m) offset at Wallace Creek. Magenta lines represent uncertainties. The dashed black line is the slip rate (36 mm/yr, ~475 m offset) calculated at the 13,250 yr timescale in the same study. The dashed black line also represents the geodetic rate of 36 mm/yr (Schmalzle et al., 2006).

FIGURES

Figure 1.1

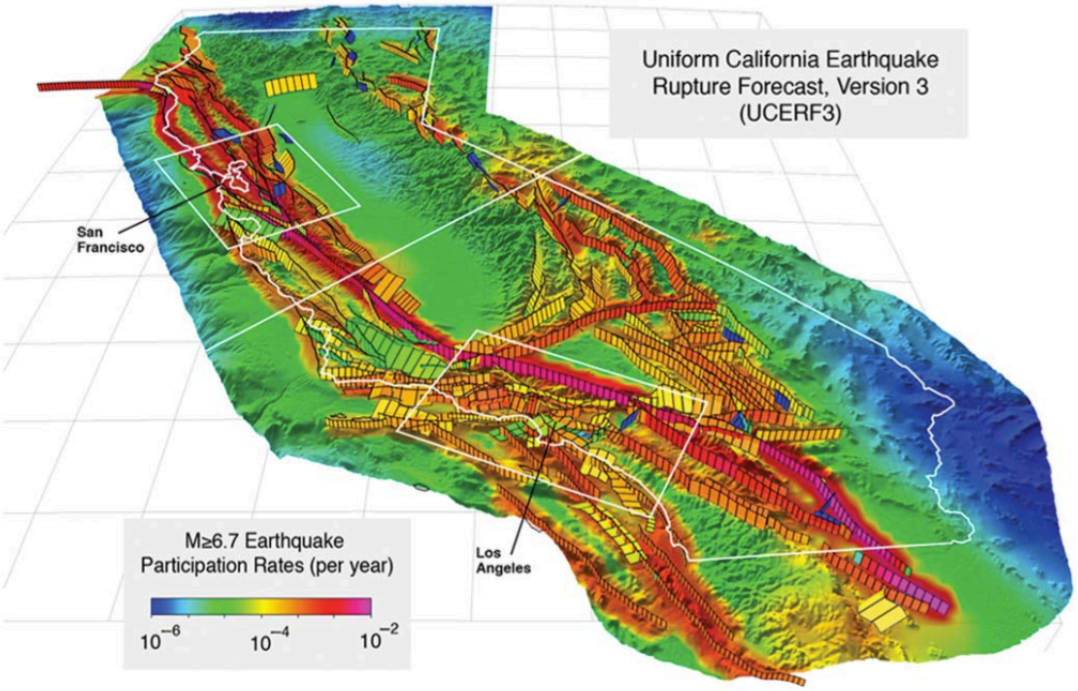

Figure 1.2

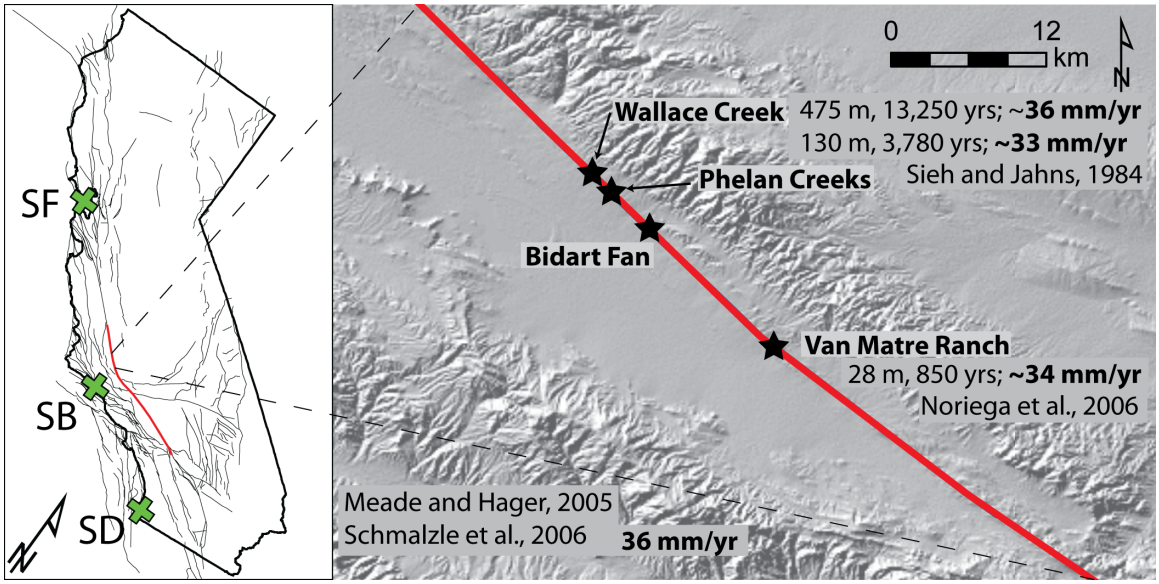
SF
SB
SD
0
12
km
N
Wallace Creek
475 m, 13,250 yrs; ~36 mm/yr
130 m, 3,780 yrs; ~33 mm/yr
Sieh and Jahns, 1984
Phelan Creeks
Bidart Fan
Van Matre Ranch
28 m, 850 yrs; ~34 mm/yr
Noriega et al., 2006
Meade and Hager, 2005
Schmalzle et al., 2006
36 mm/yr

Figure 1.3

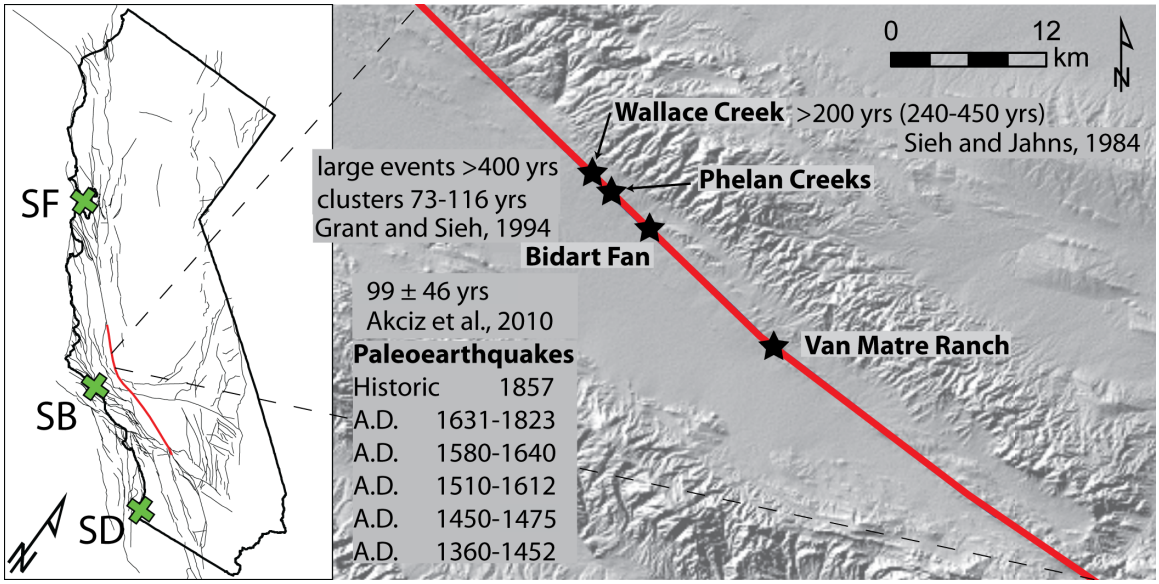
SF
SB
SD
0
12
km
N
Wallace Creek
>200 yrs (240-450 yrs)
Sieh and Jahns, 1984
Phelan Creeks
large events >400 yrs
clusters 73-116 yrs
Grant and Sieh, 1994
Bidart Fan
99 ± 46 yrs
Akciz et al., 2010
Van Matre Ranch
Paleoearthquakes
Historic 1857
A.D. 1631-1823
A.D. 1580-1640
A.D. 1510-1612
A.D. 1450-1475
A.D. 1360-1452

Figure 1.4

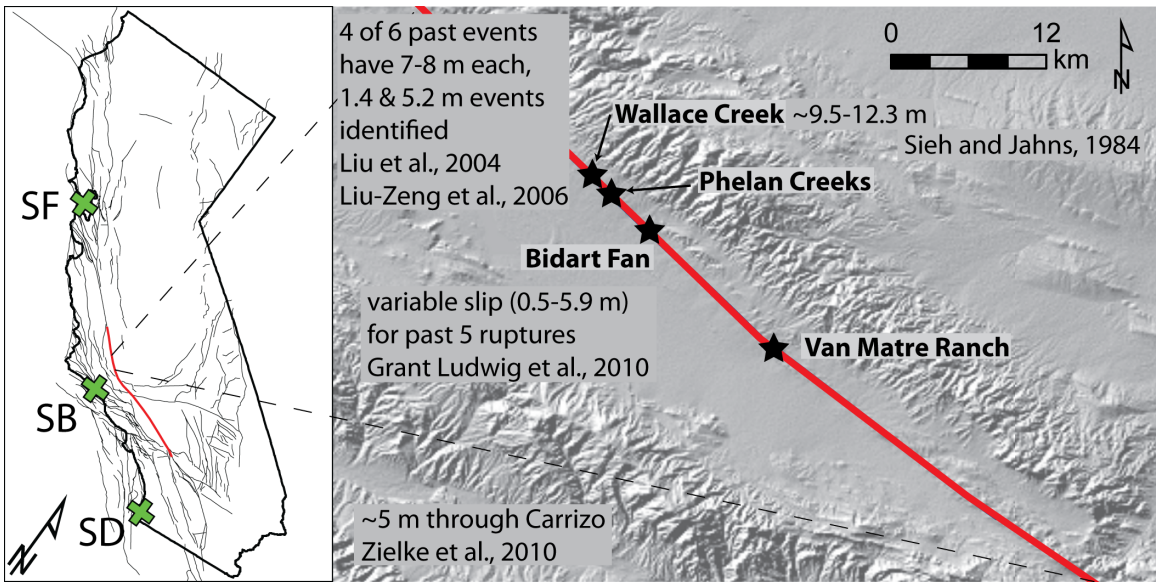
SF
SB
SD
4 of 6 past events
have 7-8 m each,
1.4 & 5.2 m events
identified
Liu et al., 2004
Liu-Zeng et al., 2006
0
12
km
N
Wallace Creek ~9.5-12.3 m
Sieh and Jahns, 1984
Phelan Creeks
Bidart Fan
variable slip (0.5-5.9 m)
for past 5 ruptures
Grant Ludwig et al., 2010
Van Matre Ranch
~5 m through Carrizo
Zielke et al., 2010

Figure 1.5

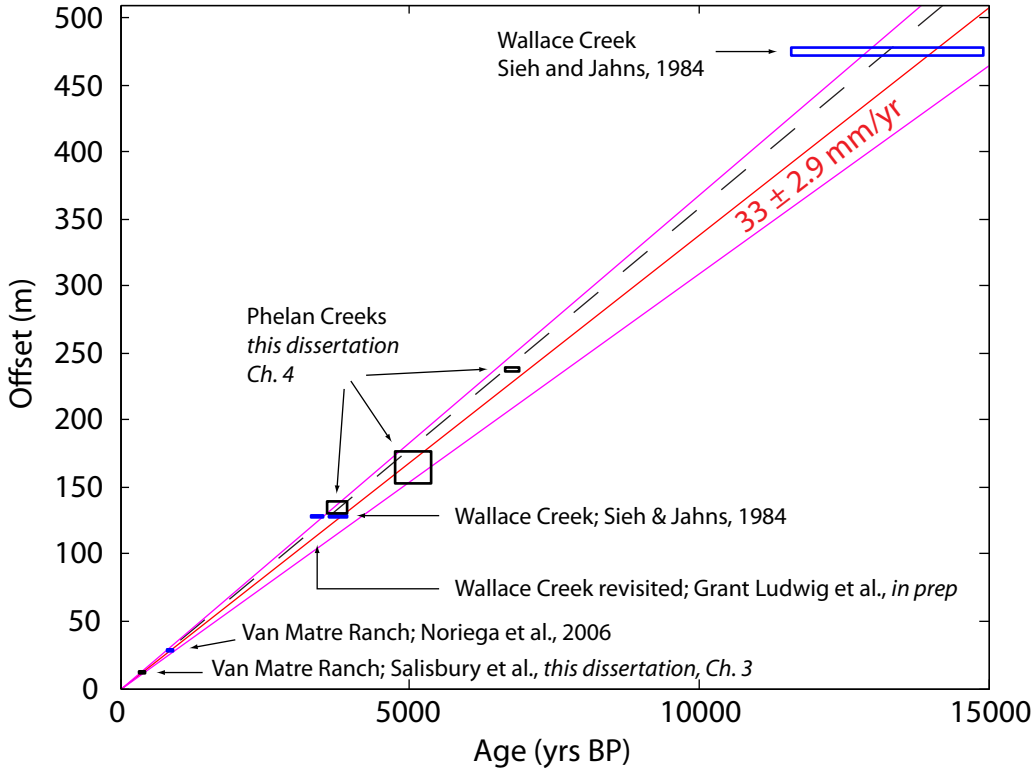
Wallace Creek
Sieh and Jahns, 1984
33 ± 2.9 mm/yr
Phelan Creeks
this dissertation
Ch. 4
Wallace Creek; Sieh & Jahns, 1984
Wallace Creek revisited; Grant Ludwig et al., in prep
Van Matre Ranch; Noriega et al., 2006
Van Matre Ranch; Salisbury et al., this dissertation, Ch. 3
Offset (m)
Age (yrs BP)
0
50
100
150
200
250
300
350
400
450
500
0
5000
10000
15000

CHAPTER 2

VALIDATION OF METER-SCALE SURFACE FAULTING OFFSET MEASUREMENTS FROM HIGH-RESOLUTION TOPOGRAPHIC DATA

ABSTRACT

Studies of active fault zones have flourished with the availability of high-resolution topographic data, particularly where airborne Light Detection and Ranging (lidar) and structure from motion (SfM) datasets provide a means to remotely analyze sub-meter scale fault geomorphology. To determine surface offset at a point along a strike-slip earthquake rupture, geomorphic features (e.g., stream channels) are measured days to centuries after the event. Analysis of these and cumulatively offset features produces offset distributions for successive earthquakes that are used to understand earthquake rupture behavior. As researchers expand studies to more varied terrain types, climates, and vegetation regimes, there is an increasing need to standardize and uniformly validate measurements of tectonically displaced geomorphic features. A recently-compiled catalog of nearly 5,000 earthquake offsets across a range of measurement and reporting styles provides insight into quality-rating and uncertainty trends from which we formulate best-practice and reporting recommendations for remote studies. Additionally, a series of public and beginner-level studies validate the remote methodology for a number of tools and emphasize considerations to enhance measurement accuracy and precision for beginners and professionals alike. Our investigation revealed that (1) standardizing remote measurement methods and reporting quality rating schemes is essential for the utility and repeatability of fault-offset measurements, (2) measurement discrepancies often involve misinterpretation of the offset geomorphic feature and are a

function of the investigator's experience, (3) comparison of measurements made by a single investigator in different climatic regions reveals systematic differences in measurement uncertainties attributable to variation in feature preservation, (4) measuring more components of a displaced geomorphic landform produces more consistently repeatable estimates of offset, and (5) inadequate understanding of pre-event morphology and post-event modifications represents a greater epistemic limitation than the aleatoric limitations of the measurement process itself.

INTRODUCTION

The geomorphic expression of active fault zones contains valuable information about earthquake surface ruptures, including offset amounts and their distribution along and across a fault. Where a dominant sense of slip persists, horizontally and vertically offset geomorphic features can be used to constrain cumulative offset after initiation and quasi-stabilization of the landforms (e.g., Wallace, 1968, 1990; Burbank and Anderson, 2001; Cowgill et al., 2007; McCalpin, 2009) (Figure 2.1). In addition to developing long-term slip histories, offset features can be coupled with paleoseismic and geochronologic constraints to reconstruct surface offset distributions of successive earthquake events. Such information is essential for estimation of paleo-earthquake extents and magnitudes and for evaluation of conceptual models for earthquake recurrence (e.g., Shimazaki and Nakata, 1980; Sieh and Jahns, 1984; Schwartz and Coppersmith, 1984; Field et al., 2014).

Several recent studies have highlighted the scientific potential of high-resolution topographic datasets for reconstruction of strike-slip surface offsets, formulation and evaluation of earthquake recurrence models, and earthquake forecasts (e.g., Hudnut et al., 2002; Haugerud et al., 2003; WGCEP, 1988; Grant-Ludwig et al., 2010; Zielke et al. 2010, 2012; Salisbury et al., 2012). Direct reconstruction of slip in earthquakes using these data will come from full 3D differencing of datasets that are recorded before and after great earthquakes (where they exist; e.g., Borsa and Minster, 2012; Nissen et al., 2012; Oskin et al., 2012; Nissen et al., 2014). Where full displacement fields are unattainable (i.e., for past earthquakes), surface slip accumulation patterns come from

reconstruction of preserved offset landforms measured in the field or with high-resolution topography derived either from lidar scans or structure from motion photogrammetry.

The increasing availability of high-resolution topographic data and resources for offset reconstructions is a provocative prospect, but models of slip accumulation are only as reliable as the individual slip measurements upon which they are based. In practice, making reliable measurements in the field or with remotely assessed high-resolution topographic data is not a trivial task, in part because the initial conditions (i.e., shape) of the channel/marker are not known and also because the geomorphic modification of an offset feature is often not well understood or constrained. Additionally, one's ability to reliably assess offset landforms is controlled by user experience and is just one of many factors (e.g., climatic calibrations, geomorphic evolution) whose influences we must continue to research as we pursue these types of studies.

In this paper, we examine the influence of operator decisions on remote offset measurements to provide a framework for remotely analyzing strike-slip offset. Though there are many similarities, it should be noted that dip-slip faults produce a fundamentally different type of offset landforms with somewhat different sources of uncertainty. We provide best-practice recommendations for making remote measurements of tectonically offset geomorphic features, provide information regarding the best way to report measurement data for fault behavior analysis, and provide insight into common challenges faced when making remote measurements. This work represents a critical step towards enhancing consistency of analyses based on high-resolution digital topography and establishes community protocols for future work.

We used a database of meter-scale slip measurements compiled from numerous paleoseismic and tectono-geomorphic studies of active faults in California (the Uniform California Earthquake Rupture Forecast 3-UCERF3; Madden et al., 2013; Field et al., 2014) to summarize the existing field- and remotely-based measurements of offset geomorphic features, compare the existing field-based measurements with new remote offset measurements, and investigate the benefits of standardizing offset measurement methods and reporting schemes. Finally, with a series of public surveys, we explored the influence of investigator experience, offset quality, and measurement tools on the repeatability of remotely measured fault-offset geomorphic features and factors that can affect measurement accuracy.

BACKGROUND

The early studies of offset geomorphic features were conducted in the field with the support of aerial photographs (e.g., Wallace, 1968; Sieh, 1978; Lienkaemper and Sturm, 1989). In many instances, however, comprehensive field examinations are impractical or impossible because of temporal, financial, and land access limitations. In such conditions, remotely sensed datasets alone can provide additional coverage and are useful for the identification of new faults and displaced geomorphic features. The aerial imagery and high-resolution (i.e., less than 1 meter per pixel) topographic datasets increasingly supplement and sometimes replace conventional field studies. Measuring offsets is not trivial and it is important that they are conducted with care (as they have a direct influence on the resulting slip accumulation patterns). It is therefore relevant to estimate the reliability and repeatability that is associated with those remote-sensing measurement approaches.

We restrict this discussion to high-resolution topography and evaluate tools that are currently used for purely remote measurements to evaluate their effectiveness and repeatability given variable degrees of user skill levels. For a complete description of those tools and underlying methods, please see: "Measuring Earthquake-Generated Surface Offsets from High-Resolution Digital Topography" in the electronic supplement to this article. A recent review by Zielke, et al., 2015 also summarizes aspects of this activity. In this paper, we explore in depth the validation of offset measurements. Here we briefly introduce the UCERF3 dataset as a basis for our study, the major assumptions inherent to studies of offset features, and the generally accepted methods for making offset measurements.

The Uniform California Earthquake Rupture Forecast 3

The Working Group on California Earthquake Probabilities recently updated databases describing active faults and paleoseismicity within California in a major effort known as the Uniform California Earthquake Rupture Forecast 3 (UCERF3; *www.wgcep.org; Field et al., 2013; 2104*). The UCERF3 offset database focuses on California's fast slipping strike- and dip-slip faults, combining historic, prehistoric, paleoseismic, and geomorphic data for single and multi-event offsets. The database [UCERF3, Appendix R by Madden et al. 2013] represents the best available compilation of fault offset data from a variety of investigators, faults, environments, base maps, and quality rating schemes (Figure 2.2), providing an excellent opportunity to examine a large number of results from paleoseismic and tectono-geomorphic studies. This diversity of the data, however, was also challenging because it meant we had to regularize the different data sets to make them comparable.

Madden et al. (2013) standardized the quality rating schemes used to rank offsets in existing studies by assigning each UCERF3 database entry a rank from 1 to 3, where 1 is high (best) quality, and 3 is low (worst) quality. Offset measurements lacking a quality rating (predominantly from historic ruptures) were assigned a quality of "1" for the UCERF3 compilation. For potentially hazardous fast-slipping faults that did not have existing work, Madden et al. (2013) generated new measurements of meter-scale offsets from analyses of high resolution topography datasets using a standard measurement protocol. In this study, we treat this subset of new measurements as its own dataset as we explore methodologies and build upon the reporting standards proposed by Madden et al. (2013). We use the UCERF3 offset database as part of our examination of repeatability of surface offset measurements from high-resolution topography. Scharer et al. (2014) conducted an examination of field-based offset measurements with similar intentions. Zielke et al. (2015) provided a review of data types and methodologies of some recent studies with considerations for earthquake recurrence models.

Offset Channel Measurements

Inherent to the reconstruction of lateral slip in past earthquakes using offset landforms are four major assumptions: 1) offset along faults occurs co- and post-seismically (with no significant inter-seismic contribution by creep); 2) deformation is focused along the fault with little to no off-fault deformation; 3) the frequency of erosional and depositional events that sculpt landforms is such that sufficient markers are generated between successive earthquakes. If geomorphic markers are altered less frequently than earthquake recurrence, even the smallest discernable offsets may represent multiple earthquake ruptures; and 4) offset in successive earthquakes is large

enough to be uniquely recognized in an offset landform. This may not always hold in the reconciliation of inferred offset sequences from landforms and rupture sequences from paleoseismology (e.g., Zielke et al., 2010; Akciz et al., 2010; Ludwig et al., 2010; Zielke et al., 2015).

The preservation of offset markers is dependent upon a variety of conditions—the fidelity of landforms to record tectonic offset depends not only on the original shape and orientation with respect to the fault, but also on the climatically controlled post-offset erosional and depositional modifications to the feature. Following tectonic displacement, pre-earthquake patterns of aggradation (or degradation) can be altered (Haddad et al., 2012) and in some instances, streams with high transport capacity may bury or erode tectonic offsets completely. Most importantly, the relationship between the size of a geomorphic feature and the magnitude of tectonic offset will ultimately dictate whether an earthquake will leave a distinct mark in surficial geomorphology (Cowgill et al., 2007). Given that surface-rupturing strike-slip earthquakes typically produce surface offsets of $10^0 – 10^1$ m (Wells and Coppersmith, 1994), ephemeral channels of $10^0 – 10^2$ m width provide the best opportunity to measure past offsets and are thus the most common for developing slip reconstructions (*San Andreas fault (SAF)*: Wallace, 1968; Sieh, 1978; Lienkaemper, 2001; Zielke et al., 2010, 2012; *Garlock fault (GF)*: McGill and Sieh, 1991; *San Jacinto fault (SJF)*: Salisbury et al., 2012; *Elsinore fault (EF)*: Rockwell and Pinault, 1986; Rockwell, 1990; *Talas Fergana fault*: Trifonov et al., 1992; *Altyn Tagh fault*: Washburn et al., 2001; *Fuyun fault*: Awata et al., 2010; Klinger et al, 2011; *North Anatolian fault*: Kondo et al., 2005, 2010; *Bocono fault*: Audemard, 2008; *Denali 2002*

earthquake: Haeussler et al., 2004; see also reviews by McCalpin, 2009; Yeats et al., 1997; Burbank and Anderson, 2001).

An offset measurement typically contains multiple parts: the quantitative measurement of tectonic offset, the quantitative, aleatoric uncertainty of that measurement, and an assessment of epistemic quality associated with the measurement. Measuring the tectonically offset features requires delineation of several geomorphic components including the fault trace orientation and width, offset landform elements (e.g., the channel margins or thalweg), and the projection lines of landform elements into the surface fault trace (e.g., the piercing line). The along-fault distance between landform element projections is the offset measurement (Sieh, 1978; Lienkaemper and Sturm, 1989; Lindvall et al., 1989; Lienkaemper et al., 2001) (Figure 2.1). Quantitative (aleatoric) uncertainty of the measurement typically comes from assessment of minimum and maximum credible offset reconstructions (e.g. Lienkaemper et al., 2001). The acceptable offset range (AOR) is dependent on the scale of geomorphic features versus magnitudes of offset, the clarity of landform features, and the precision of particular measurement tools.

The quality rating is an assessment made by the geologist and depends on the simplicity of landform projections and fault trace delineations. This rating has been conducted several ways, but typically "high" quality measurements are made from obvious fault-normal piercing lines that are offset by narrow, well defined fault zones; "low" quality measurements are made from less-obvious, ambiguous, poorly preserved, or highly oblique piercing lines that are offset by a broad, poorly defined fault trace (Sieh, 1978; Lienkaemper et al., 2001; Madden et al., 2013). We represent these two

important quality controls with a bivariate rubric that compares obliquity between the offset feature elements and the fault zone with fault zone width (as an indicator of structural complexity) (Figure 2.3).

One of the primary controls on measurement accuracy stems from the difficulty of remotely interpreting the evolutionary history of a landform (both before and after tectonic perturbations). These types of epistemic uncertainties directly control the soundness of quantitative, aleatoric uncertainties and are often difficult to unravel without field excavations (Scharer et al., 2014). However, a rating scheme of some sort helps to systematize what is discernable in the topography and it can be useful for subsequent data compilation and "stacking"—effectively emphasizing highly reliable measurements and deemphasize questionable ones (McGill and Sieh, 1991; Zielke, et al., 2010; Klinger, et al., 2011; Zielke, et al., 2015; e.g., McGill and Sieh, 1991; McCalpin, 2009; Salisbury et al., 2012; Madden, et al., 2013).

There are significant advantages to using imagery and high-resolution topography to measure surface offsets. Aerial views of offset features preclude some of the foreshortening associated with human perspectives on the ground and in some instances (in dense vegetation, for example) can provide a more representative view of the offset geomorphic feature (e.g., Lienkaemper et al., 2001; Salisbury et al., 2012). Further, the ability to change lighting direction (hillshade rendering) helps to illuminate features in complex terrain (Oskin, et al., 2007). Klinger et al. (2011) use the aerial perspective to assess the quality of an aggregate of channels after a single restorative back-slipping step. Similar to Lienkaemper and Sturm (1989), Zielke and Arrowsmith (2012) utilized recently-acquired high-resolution topography to define channel shape for automatic

detection of piercing lines with minimal subjective user input with a program called LaDiCaoz (Lateral Displacement Calculator by Olaf Zielke).

Reporting of Offset Measurements

Historically, individual offset measurements have been reported using a range of approaches. Most often, offset is presented as a single measurement (typically the offset reconstruction preferred by the scientist) and uncertainties on that measurement (e.g., Lienkaemper, 2001; Sieh, 1978). Most of the literature does not discuss which probability distribution should be used to describe the measurement. Exceptions include McGill and Sieh (1991), who assumed a Gaussian probability distribution was appropriate and used the preferred measure and uncertainties as the mean and 2-sigma uncertainties, respectively (Figure 2.4). Subsequent studies have experimented with alternative probability distribution shapes. In instances where offset reconstructions are less clear and preferred offset estimates span several meters, a rectangular or trapezoidal ("boxcar") distribution is useful (Brooks et al., 2013; Figure 2.4). Alternatively, triangular PDFs provide a simple representation of measurement data, particularly when measurement uncertainties are asymmetric (Madden et al., 2012; Figure 2.4).

Several recent studies use LaDiCaoz, a Matlab script to determine the offset (Chen et al., 2015; Salisbury et al., 2012; Zielke and Arrowsmith, 2012). This program determines the offset by improving the goodness of fit between two cross-feature profiles upstream and downstream of the fault; from this, the user determines preferred offset and a range of offsets. When these are assumed to be Gaussian probability density functions (PDFs), the best estimate of offset magnitude is the mode, and plus/minus estimates (aleatoric uncertainties) represent ±2-sigma uncertainties (black curves, Figure 2.4).

Representing offset magnitudes as distributions offers an intuitive method of combining individual PDFs along strike for Cumulative Offset Probability Distributions (COPDs) for a fault reach (over length of $10^2 – 10^3$ m). COPDs may reveal groups of similarly offset geomorphic features that represent slip in individual ground-rupturing events—a technique pioneered by McGill and Sieh (1991), among others. For this step, the individual PDFs can be scaled by their qualitative ranking to create weighted COPDs, thereby emphasizing offsets with low epistemic uncertainties and deemphasizing those with high epistemic uncertainties. Each style of measurement representation has distinct advantages and disadvantages in terms of true representation of the epistemic and aleatoric uncertainties and the generation of the COPD. Zielke, et al., (2015) provide additional review on COPDs including their construction and interpretation.

METHODS

We report what factors ultimately control the overall accuracy of a measurement and what level of precision is achievable by users of different skill levels with tools of varying complexity based on analysis of the UCERF3 offset feature database and our own controlled experiments.

Analysis of the Uniform California Earthquake Rupture Forecast 3 Compilation

We utilized the UCERF3 database to summarize traits of existing measurements of geomorphic features offset up to 20 m. We noted the number of component measurements (i.e., individual horizontal and vertical offset measurements) in addition to the number of unique geographic measurement sites. In many instances, multiple measurements were made at the same location (horizontal and vertical offsets recorded by the channel thalweg and one or two of the channel margins) or multiple measurements

were made using different methods (lidar, aerial photographs, field measurements) for the same feature. For an investigation of method reliability, we assessed the consistency of replicate measurements made at a point with different tools. We mined the database to compare existing field-based measurements with lidar-derived offset measurements where both exist for particular landforms and we analyzed new lidar-derived measurements made specifically for the UCERF3 effort.

Offset Measurement Validation Experiment.

We explored validation of offset measurements by inviting the participation of students, colleagues, geoscience community members, and the general public to measure ten pre-defined geomorphic offsets using high-resolution topography as a base. See Table 1 for site coordinates. Our experiment consisted of two major components: an online public survey element (conducted Fall 2012 – Fall 2013; n = 55 participants) and a classroom-based hardcopy element (conducted Fall 2012 – Spring 2014; n = 102 participants). The setup for both was the same: we chose ten different offset features from major active faults in western North America and asked people to measure them. The materials used in this study are provided in the electronic supplement. We focused primarily on major strike-slip faults where geomorphic features that developed roughly normal to fault strike are horizontally offset by single or repeated surface-rupturing earthquakes. Most fault-offset features we chose are of fluvial origin (e.g., channel walls, margins, or thalwegs) and are composed of elements that can be projected to the fault plane and used as piercing lines to estimate fault slip. Features vary in estimated age from several to hundreds of years old and are of poor to excellent quality. Participants were told that offsets were along northwest-striking right-lateral faults, but in general there was

no annotation of the figure to indicate the fault or offset itself. Site locations are shown as yellow stars in Figure 2.2. Survey responses (including mapped fault traces and piercing lines) were anonymously submitted to an online database or the document was filled out by hand and mailed to us.

In addition to the measurement results from the surveys, we collected information about experience levels of participants with three questions. The first question asked about general experience level:

1) I have no prior experience whatsoever.

2) I am familiar with the basic geologic principles and/or high-resolution topographic data.

3) I have measured offset geomorphic features in the field or with high-resolution topography/imagery.

4) I have extensive experience measuring offset features in the field or with high-resolution topography/imagery.

The second question gathered information about data types that one may have previously used to measure offset features (field methods, aerial photography, high-resolution digital elevation models, etc.) and how measurements were made (tape measure/ruler, total station, Google Earth, GIS, etc.). The third question asked whether one had taken or taught Field Geology, Geomorphology, Earthquake Geology, Quaternary Geology, Tectonic Geomorphology, or GIS.

We selected three primary methods by which to complete the survey in order to reflect the range of work styles and experience of current researchers. The different tools included a paper image and scale, the Google Earth ruler tool, and a Matlab GUI for

calculating back-slip required to properly restore tectonic deformation (LaDiCaoz; Zielke and Arrowsmith, 2012). In one sub-experiment we used a simpler variant of LaDiCaoz for classroom studies, allowing the fault restoration to be determined by progressively back-slipping images of topography without a corresponding explicit goodness-of-fit determination.

The paper-based survey was designed to be suitable for classroom dissemination, but some individual participants also used it. The survey was used in undergraduate geology classes at San Diego State University (SDSU), Arizona State University (ASU), and the University of Potsdam, Germany. Each image consisted of a combination of three lidar-derived products: an opaque "hillshade," a semi-transparent digital elevation model (DEM), and a contour map. We used both EarthScope (Prentice et al., 2009) and B4 lidar (Bevis at al., 2005) data, the latter of which were manually filtered to remove vegetation using a multiscale curvature classification algorithm (Evans and Hudak, 2004). Map scales and contour intervals ranged from 1:175 to 1:800 and 10 – 100 cm, respectively. Participants were asked to delineate the fault and geomorphic features (e.g., channel thalweg, channel margins, bar crest, etc.) used to estimate tectonic offset. Each page had a scale bar on the bottom right corner that was torn off and used for measuring. Participants were asked to report the measurements and uncertainties and to rate the quality of the offset using the provided rubric.

The Google Earth-based measurement survey was popular because of convenience. We saved georeferenced map images from the paper survey as *.kmz files and provided them for download from the survey webpage. It was therefore possible to zoom to each site, view topographic imagery and contextual image data, delineate

features, and measure offsets with little GIS experience. Survey instructions included step-by-step text as well as short YouTube video tutorials on the use of the Google Earth application for this purpose. For each site/image, the participants:

1) zoomed to the site,
2) defined the fault and offset features as paths for at least one offset (but they were encouraged to use multiple offset landscape elements),
3) measured the offset features using the ruler tool,
4) saved the result from the measurement with a title corresponding to the analyzed feature (e.g., "channel thalweg measurement"). Additionally, we asked for any other comments to be included with the measurement path description.

The resulting measurements and line work were saved as a location file in Google Earth (*.kmz) and anonymously uploaded to our database upon completion of the experience survey.

The LaDiCaoz graphical user interface allows for direct interaction with DEMs to measure and record horizontal offsets (Zielke and Arrowsmith, 2012). We provided raw, small-scale DEM files for each of the ten sites and assumed that participants had experience using LaDiCaoz to measure offset features. We circled targets on the topographic images to ensure that participants measured the same offsets because the small-scale maps contained several offset features. LaDiCaoz allows users to save preferred offset measurements, the measurement uncertainties, and the quality ratings. These results were anonymously uploaded to our server upon completion of the experience survey.

While the available measurement methods spanned a range of complexity, most

submitted responses were generated in Google Earth. We sifted results manually and compiled offsets, measurement uncertainties, and quality ratings, grouping measurements by geomorphic features as some sites contained multiple offset stream channels. In the case of our Google Earth results, we collected traces that participants used to delineate fault zones and offset landforms for graphical comparison.

RESULTS

The UCERF3 database and our experimental survey provide a rich suite of data on which to build our understanding of offset measurements. We are also able to explore the controls of measurement accuracy for different groups of investigators. We start our presentation of results with exploration of the UCERF3 database and measures of offset magnitude, uncertainty, and quality, as measured from different physiographic settings by different investigators using lidar and field-based approaches. Transitioning from the UCERF3 examination, the final presented results come from our measurement experiment survey that included both the online public and the classroom hardcopy elements of this study**.**

Analysis of the UCERF3 Offset Database

There are 4,918 component measurements (individual horizontal and vertical slip measurements) made at 1,522 geographic locations along UCERF3-defined fault strands (Figures 2.2 and 2.5; Madden et al., 2013). Of the total component measurements, 2,759 are from historic earthquake ruptures (22 UCERF3 segments) and 2,159 are of prehistoric offsets (40 UCERF3 segments). Most measurements in the UCERF3 database are of the highest quality rating (1) (Figure 2.2), principally because many existing measurements had no initial quality rating and were assigned a high quality rank in the UCERF3

compilation (Madden et al., 2013). Most of them are also from 20th century California earthquakes so the presumption of high quality preservation is reasonable.

Measurement methods differ significantly for historic and prehistoric offsets groups. Historic surface rupture measurements are dominated by field measurements, whereas most prehistoric earthquake slip measurements are a combination of field- and lidar-based measurements, or one of the two (Figure 2.5a, 2.5c). Measurements for more than half of the studied faults (16 of 25 strands) are exclusively from paleoseismic excavations with relatively few offset measurements (Figure 2.2a). Slip measurements in these cases are made from sub-surface channel or structural reconstructions with a wide range of uncertainties (Figure 2.5d).

In most cases, only one measurement is made for each location, but for some faults there are significantly more measurements than measurement sites (Figure 2.5b, 2.5d). This is particularly apparent along the prehistoric San Jacinto Fault (SJF) and Garlock fault (GF) ruptures, where there exist both field and lidar measurements for the same set of features. For historic ruptures such as along the Emerson fault (1992 Landers earthquake), there are many sites with both horizontal and vertical measurements made for the same geomorphic feature.

We note a crude logarithmic relation between offset magnitude and associated measurement uncertainty (Figure 2.6). For the smallest field-based measurements (millimeter- and centimeter-scale historic earthquake ruptures), there are often no measurement uncertainties assigned. Where it can be determined, field-based historic earthquake measurements tend to have lower uncertainties for a given offset than prehistoric earthquake measurements, the majority of which involve more degraded

geomorphic features analyzed using aerial photographs or high-resolution topography. Many different investigators made these measurements using a variety of methods in a range of site conditions.

In contrast, the new remote measurements compiled and generated for the UCERF3 database all used similar methods and reporting schemes, albeit by different investigators along different faults (Elsinore, Garlock, Owens Valley, creeping, Cholame, Carrizo, Big Bend, Mojave, and Coachella portions of the SAF and the Clark strand of the SJF). Note that the SJF and GF have accompanying field studies, and the recent 2004 Parkfield earthquake rupture measurements are not included. We categorize these new measurements according to the same subjective, semi-quantitative quality ranking scheme described in the methods section where 1 is for the highest quality and 3 is for the lowest quality; we use these quality ratings to compare other measurement attributes (Figures 2.3 and 2.7). We define the difference between maximum and minimum estimated offsets for a feature as the acceptable offset range (AOR). For experienced investigators, AORs correlate with offset magnitude. The SAF is special in several ways: it has significantly more measurements, the largest average offset magnitudes per fault segment (>10 m) with correspondingly large AORs, and is the only fault system with increasing AORs and worsening quality ratings.

Several individual sites include field- and lidar-based measurements for the same set of offset landforms. Zielke et al. (2010) compared new lidar measurements with Sieh's (1978) field-based measurements along the SAF. Salisbury et al. (2012) presented a comparison of field and two different lidar-derived measurements for numerous targets (Figure 2.8a). Madden et al. (2013) compared lidar measurements from the Garlock Fault

with McGill and Sieh's (1991) field measurements (Figure 2.8b). In general, repeated observations are well correlated within the error of individual measurements. Salisbury et al. (2012) showed that in some cases, field measurements were systematically lower than those from lidar surveys and attributed this to the synoptic perspective available from a remote view of the bare earth (e.g., Lienkaemper, 2001).

Offset Measurement Validation Experiment

Our measurement survey results are divided into two categories: the online public survey element (conducted Fall 2012 – Fall 2013), and the classroom-based hardcopy element (conducted Fall 2012 – Spring 2014).

For our online public survey, we received 55 anonymous responses (consisting of experience level, mapped fault traces, and piercing lines) from individuals of all experience levels. Of the 55 online responses, 28 participants used Google Earth and we emphasize them in the following discussion. Even though we provided a simple quality-based rating scheme (Figure 2.3), few of the participants reported measurement uncertainties or estimates of measurement quality. In some cases, the only quality descriptions were general, rather than guided by the scheme.

For comparison, we split responses into two groups: experienced users (levels 3 & 4) and inexperienced users (levels 1 & 2). The difference in experience level is manifest in the polygon that spans the faults mapped by each group; inexperienced users generally had a wider area that encompassed parts of the terrain for which there was no geomorphic evidence of a fault (e.g., scarps, hillside benches, offset topography) (Figure 2.9). Reported offset measurements are predominantly in agreement with one another with experienced users determining a slightly lower mean offset than inexperienced users in 7

of the 10 cases. Offsets 1, 3, and 6 have the best correlation between groups. In several instances, inexperienced users have more variable responses, either due to fault mis-location or fault azimuth variability (offsets 5, 8, 9, and 10). Offsets 2 and 4 represent significantly poorer interpretations by inexperienced users due to fault mis-location and fault-strike uncertainty, respectively. The standard deviation of the site measurements increases with larger feature size and total displacement (Figure 2.9b).

We have ~100 paper-based surveys from beginner-level participants in upper-level undergraduate geology classrooms at SDSU, ASU, and the University of Potsdam. Many of these surveys were only partially completed, however, and the number of individual measurements for each of the ten features is highly variable (where n ranges from 33 to 101). In addition to the overall group of paper-based surveys, we isolate two sub-groups. In the first sub-group (group A, n = 9), geomorphology students completed the paper-based survey on two occasions: once prior to a lecture on neotectonics and strike-slip faulting and a second time one week later after receiving specialized instruction on how to recognize and measure offsets. In the second sub-group (group B, n = 14), students used the aforementioned, slimmed-down version of LaDiCaoz at the University of Potsdam in Germany, supervised by Zielke.

Subgroup A did not show a marked change in mean offset measurements before and after the introductory lecture. Of ten measured channels, averaged offset estimates of half increased and the other half decreased. However, the average of reported uncertainties for eight of the ten offset features significantly increased after the lecture, which we interpret as the students' increased attention to subtleties of the geomorphology. In general, average quality estimates remained the same pre- and post-

lecture. Subgroup B underestimated offset magnitudes in comparison to the measurements completed on paper by other groups, all of whom consistently underestimated offset magnitudes compared to the authors.

Together, the ~100 beginner surveys represent a statistically significant population of measurement estimates. Extreme measurement outliers have been excluded, as we assume these discrepancies to be less associated with measurement variability and more associated with improper interpretation of offset features themselves (epistemic uncertainty). Figure 2.10 summarizes paper-based classroom survey responses. Average offset estimates and average AORs (for survey participants and authors) are depicted at arbitrary y-axis positions. Note that the geomorphic features are not necessarily depicted at the same scale at which they were measured (see Paper-based survey in the electronic supplement to this article). These results show that while there is considerable spread among the beginning users, the measurement modes consistently fall within the AOR defined by the authors.

DISCUSSION

There are a number of factors, both external and internal, that dictate an individual's ability to "get the right answer" (Bond et al., 2007, 2011). In most scenarios, actual amounts of offset at a particular location are unknown and we consider our most agreed-upon measurement to be the correct answer. That said, a correct measurement must ultimately begin with a proper interpretation of the geomorphic feature in question. Here we discuss the factors that control measurement repeatability for all experience levels.

Epistemic vs. Aleatoric Uncertainty

Epistemic uncertainty relates to the overall interpretation of the geomorphic feature (its evolutionary history both before and after tectonic perturbations). Epistemic uncertainty, therefore, is intrinsic to all measurements and governs the validity of aleatoric uncertainty—a statistical uncertainty associated with the measurement process (black curves, Figure 2.4). The tall, narrow black curve in Figure 2.4 represents low aleatoric uncertainty and the short, wide black curve represents high aleatoric uncertainty.

The results suggest that when a person examines and interprets the topography, and from this develops a model of the offset (i.e. what features to correlate across the fault), the difference in experience level among practitioners [a proxy for epistemic uncertainty, as experienced practitioners can better interpret tectonic versus geomorphic contributions to an offset] contributes a larger share of variability to the final measured offset than does discrete measurement error (aleatoric uncertainty). Particularly for the inexperienced user, it is likely that in some cases epistemic uncertainty will swamp aleatoric uncertainty. This is consistent with other studies (e.g., Gold et al., 2012; Scharer et al., 2014) that established that major discrepancies in offset estimates are usually attributable to improper feature interpretation rather than poor measurement practices. In particular, Gold et al. (2012) present single-operator assessments of measurement error and uncertainties using high-resolution terrestrial-based lidar point clouds. They showed that while high-resolution datasets are fundamental to remotely measuring offset features, fine topographic data cannot necessarily reduce below a certain level the epistemic uncertainty associated with reconstructing the geomorphic features.

Operator Biases

Our interest in validation of geological measurement methods is not new. Bond et al. (2007, 2011) conducted a similar study focusing on interpretations of reflection seismic data by interpreters with various levels of expertise. To quantify the subjectivity of seismic interpretation, Bond et al. define "conceptual uncertainty" as the acceptable range of concepts that geoscientists apply to a single dataset. Bond et al. (2007) argue that conceptual (epistemic) uncertainty must be incorporated into resulting geologic models because they represent fundamental unknowns that outweigh individual measurement uncertainties (aleatoric). Bond et al. (2007) concluded that a range of factors influence how an individual's prior knowledge will affect interpretations, but that particular biases are as pervasive for those with 15+ years of experience just as they are for those with very little experience. In particular, two types of biases are nearly unavoidable: anchoring and confirming biases.

An anchoring bias is failure to depart from initial ideas, whereas confirmation bias involves actively seeking facts to support one's own hypotheses (while actively disregarding conflicting observations). In fact, investigators with more experience are likely to *ask* for confirmation biases, or some sort of a starting point (e.g., "where in the world is this?"—that is, what fault am I looking at and what is the geomorphic setting). Weldon et al. (1996) (Chapter in McCalpin, p. 295) have similarly cautioned "*... bias could be derived from the unconscious choice of a best match of uncertain features that is consistent with previous choices. This statement is not meant to suggest any impropriety in the data collection, but to acknowledge that it is extremely difficult to avoid bias where measurements of 'matches' involves interpretation of the exact location of the feature*

being measured. From experience we know that after one finds several convincing offsets, one's eye is keyed to looking for matches in that range, so that one will often overlook or misinterpret offsets that are unexpected...". In the case of offset channels and our experiments, novices had less of a trained eye to locate and interpret features but also had fewer obvious existing biases. Conversely, experts can more readily identify and interpret features but they also have more pre-existing expectations that lead to operator biases. Zielke et al. (2015) recently suggested implementing a "blind measurement" approach, where the actual offset value is provided to the interpreter only after the measurement is completed; they propose simple adaptation for field studies as well as use of a modified version of LaDiCaoz;

New user performance suffers due to inexperience. We noted behavioral peculiarities common to beginning users. Several comments provided by classroom participants suggest that professionals take for granted the ability to intuitively work with aerial perspective DEMs and high-resolution topography (e.g., ~10 cm contour intervals). The Google Earth interface allows for some terrain familiarization and is typically preferred over the static, paper-based surveys because the zooming allows one to get a better overall view of the fault and feature orientation whereas the paper-based surveys were all large-scale topographic maps, making feature delineation difficult. Also, beginners lack self-confidence in assigning uncertainties (in that they frequently omit aleatoric measurement uncertainties) and nearly always use symmetrical, Gaussian-style distributions around preferred offset values. Furthermore, aleatoric measurement uncertainties typically remain the same magnitude regardless of total amount of offset. For instance, it is common for a plus/minus uncertainty value of 1.5 m uncertainty (3 m

AOR) to accompany a 5 m offset as well as a 25 m offset even though the preservation and expression of such a large feature might be substantially inferior. After receiving detailed instruction about making measurements and assigning uncertainties, most beginners included larger AORs around preferred measurements of all magnitudes.

Identifying the Appropriate Fault Strike

Location and orientation of a fault strand along which a feature is measured can substantially impact the interpretation of offset geomorphic features and subsequent measurement values. Additionally, we see much higher measurement uncertainties when fault strike is ambiguous for a reach. Ease of fault delineation is controlled by expression and preservation of the local fault trace and in many instances, portions of prehistoric ruptures are no longer visible. One pitfall of only making remote measurements in the office is a tendency to focus on individual offsets and to search for them in intuitive locations (along an idealized linear fault trace). In contrast, field geologists are additionally able to rely upon subtle geomorphological evidence of active faults traces to locate sequences of offset features. Where meter-scale faulting is not evident, a common practice is to resort to the regional-scale fault fabric and orientation for along-strike measurements. We think that this is a suitable substitute when micro-geomorphology is no longer preserved or is below the resolution of available lidar datasets.

Rockwell and Klinger (2013) show that for the 1940 Imperial fault rupture (4 – 6 m of offset), making measurements with either a regional fault azimuth or with varying local azimuths (at the scale of 10's of meters) will yield roughly the same reach-averaged estimate of offset. A range of measurements is typically acceptable (offset and

symmetric/asymmetric offset uncertainty) for a given reach, and using a consistent approach to defining the fault strike can minimize the overall spread of offsets.

Fault zone Width and Complexity

The width of faulting and the distance over which features are projected into and across fault zones significantly impacts accuracy of a measurement and associated uncertainty. Narrow (localized) fault zones offsetting clearly defined features require little or no projection and aleatoric measurement uncertainty is low. In contrast, a broad fault zone (up to several meters wide) may lead to large aleatoric measurement uncertainty (regardless of preservation quality or linearity of geomorphic features). Similarly, we note an increase in measurement variation and user uncertainty as features deviate from the ideal fault-normal orientation. In cases where features require lengthy projections, measuring more feature components (e.g., thalweg, margins) results in an offset estimate closer to the collective mean (across various users) and a more robust estimate of measurement uncertainty.

Complications arise as fault zone width and complexity increase. Wide zones of coseismic deformation are often recognized as several discrete fault strands and it can be difficult to determine synchronicity of activity on adjacent strands. As this depends on the spatial scale of individual fault strands, geologic substrate, and subsequent feature preservation, these issues must be dealt with on an individual basis. Where ruptures are relatively young, the degree of scarp degradation can indicate relative ages of activity. For older ruptures this may not be possible. Typically, offsets along neighboring (parallel) fault strands are summed if geomorphic features appear roughly the same age and this summed value is used as an estimate of slip at a point along strike. Reported

uncertainties should acknowledge the largest possible range of offset in these cases; choice of a pdf should be guided by the assurance that the user has in the allocation of slip across a fault zone.

Natural Lateral Variability of Slip in Surface Ruptures

There are now several studies demonstrating significant lateral variability in offsets along historical surface ruptures. Using long fence lines and orchards of planted trees, Rockwell et al. (2002) showed 20 – 30% variability in offsets over short distances (10^1 – 10^2 meters) along the 1999 İzmit and 1999 Düzce ruptures. Similar variations were observed along the 2010 El Mayor-Cucapah rupture in Mexico, using "Cosi corr" (optical correlation) technology (Leprince et al., 2011), with kilometer-scale and 15 km-scale systematic variability. In a reassessment of the 1940 Imperial fault rupture, Rockwell and Klinger (2013) used hundreds of closely spaced crop rows and orchard tree alignments to measure lateral displacement and also note about 30% lateral variability over dimensions of tens to hundreds of meters. All of these observations are consistent with earlier mapping along historical surface ruptures, but in previous cases, it was commonly assumed that the variability was due to the inability to measure the full field of deformation. In contrast, the measurements using long crop rows that extended tens to hundreds of meters from the rupture trace show that these lateral variations in displacement are real and significant.

New studies of lateral variability of surface rupture slip have a direct impact on results of our study from several perspectives. First, if an observer locks into an offset magnitude because of high quality measurements along a stretch of rupture (anchoring bias), there may be a tendency to repeat this offset value, even though the actual

displacement has increased or decreased. Second, the magnitude of offset can be biased by the choice of local fault strike versus regional fault strike if measurements are not made consistently (Rockwell and Klinger, 2013). Both of these factors can have a significant influence on the perception of overall, average, and maximum displacement for an event—factors that are most important for earthquake hazard analysis.

Geomorphic Modification

As offset features age, surface processes modify fault traces and piercing lines and it becomes less likely that features will preserve true tectonic offset. In settings where fluvial modification is significant, there is a high probability that features will be obliterated, reoccupied, or buried outright. In areas where fluvial modification is low, however, a feature may persist for many successive earthquakes and perhaps even for multiple earthquake cycles. The subsequent modification of an offset feature plays a large role in not only whether the feature is a useful indicator of (actual) tectonic offset, but also whether the feature is recognizable.

A simple proxy for the geomorphic diffusion, or smoothing, of offsets can be mean annual precipitation (MAP; e.g., Hanks, 2000). While climate has varied over the last millennium in California, spatial variation in decadal MAP may provide a useful relative gauge of the vigor of geomorphic smoothing in the UCERF3 database. Figure 2.11 shows a plot of measurement uncertainty (as a percentage of total offset magnitude) for a suite of offsets as a function of MAP along a corresponding fault reach. The "SJF" points refer to the Clark strand, divided into two segments—to the northwest and southeast of Burnt Valley. The "SAF" points refer to the Cholame, Carrizo, Big Bend,

and Mojave segments. The data suggest a weak trend of increased uncertainty where precipitation is higher (see below).

Klinger et al. (2011) suggested an exponential decrease of cumulative offset probability distribution (COPD) peaks with increasing offset magnitude (i.e., age) along the Fuyun fault. This phenomenon of decreasing COPD signal strength with increasing offset was attributed to not only the increasing number of successive earthquake events to which the offset has been exposed, but also to the amount of fluvial modification and in-situ geomorphic diffusion to which the offset has been subjected (see also discussion in Zielke et al., 2015). A modest increase in single-investigator uncertainty with increasing MAP could suggest that geomorphic conditions associated with wetter sites are less likely to sharply preserve offset features. The "resilience" of a geomorphic feature is therefore a complete combination of internal and external factors at a particular location.

In this study, we asked participants to measure features embodying a range of preservation states (some that would normally be avoided because of large epistemic uncertainties). This may help explain variability in user-submitted responses for the more challenging sites. The tendency to avoid older, diffuse features predisposes studies to include only those features more recently offset, ultimately exacerbating the natural trend noted by Klinger et al. (2011) and limiting the age of earthquakes to which we can apply these methods.

Offset Quality

Of major importance to hazard models is the quality rating of a measurement. What level of quality is associated with a determination and what level of emphasis should a particular measurement receive? In the course of this study, we have seen two

approaches to the quality rating. The first, more simple approach was a qualitative, "gut feeling" rating (set to some arbitrary numerical scale) that seeks to encompass several variables, such as the understanding of pre-offset morphology, preservation of the feature, as well as fault trace and feature complexities (see the electronic supplement to this article). This intuitive approach is highly subjective, however, and is dependent upon experience both in the field and with high-resolution topography. For this method to be most effective, a clear set of criteria must be defined prior to measuring offsets (e.g., Sieh, 1978), and some lower limit of acceptability must be established, below which offsets measurements would go unused.

The second approach, a semi-quantitative rating rubric (Figure 2.3), is more systematic (and less subjective than the "gut reaction" rating), but it is insufficient for adequate offset feature classification because obliquity of the features and the fault zone width are not necessarily the only controls on reconstruction quality. Even when we choose criteria by which to rate offset quality there will be some subjectivity involved with the process. In some cases, offsets received high or otherwise acceptable quality ratings according to our rubric but user gut reactions were negative (if the tectonic nature of the offset was ambiguous, for instance). Interestingly, new measurements made for this study are predominately medium (2) quality measurements, with highest (1) quality ratings being the least common (Figure 2.7a).

Styles of interpretation vary and depend on prior field experience. Investigators tend to 'subconsciously' define quality thresholds for geomorphic features in question: if features fail to meet these often not consciously defined criteria then features will be ignored and measurements will not be made. We argue that, particularly for lidar studies,

it is important to make measurements of all potential features and then some features can be discarded or given low weight at a later date if necessary. Ignoring particular features can preclude one from discovering small-magnitude offsets, or along strike variability that indicates multiple offsets. We suggest initially making as many credible measurements as possible, using a set of criteria to assign a quality rating, and then disregarding or shifting emphasis away from particularly low-rated offsets later depending on the purpose of the study.

One interesting complication associated with quality ratings is how practitioners choose to treat lidar-based vs. field-based measurements. Presumably we would approach both types of datasets in the same way (via numerical rating or rubric of some sort), but should field measurements inherently be more highly regarded for hazard calculations or vice versa? In areas where fault zone width and rupture complexity are high, the synoptic view afforded by lidar or other remote sensing data is extremely useful for capturing full fault deformation. Conversely, where dense vegetation obstructs the ground surface such that high-quality bare-earth DEM's are unobtainable, field investigation is particularly advantageous. Where possible, a summary set of best measurements characterized both remotely and in the field is preferred.

CONCLUSION

The majority of UCERF3 offset measurements are from historic surface rupture studies and are dominated by field measurements (Madden et al., 2013). Driven by the desire to better understand faulting in the upper crust and to better inform earthquake hazard forecasts, there is an increasing trend towards lidar- and other remotely-based studies that utilize high-resolution topography to analyze historic and prehistoric ruptures.

This work examines key challenges faced when remotely measuring fault-offset geomorphic features. The ability of investigators to perform tasks (making measurements, assigning uncertainties and quality ratings) is highly dependent not only on the geomorphic quality (i.e., preservation) of offset features and digital representation of the features themselves, but also on the investigator's previous experience with neotectonic principles, measurement tools, and fault-specific characteristics (that may introduce biases). Furthermore, fluvial channels in tectonically active regions are prone to change, and degradation begins immediately after feature formation. The longer-lived and larger the geomorphic feature and associated offset, the greater the uncertainty becomes, making offset estimates far into the past more difficult to interpret. Consequently, the applicability of older offsets to fault rupture evaluation and estimating slip accumulation patterns also diminishes. The following conclusions can be made based upon our study:

1. Offset features (particularly those from prehistoric earthquakes) require significant interpretive work for a complete understanding of effects of local climate, geologic substrate, micro-tectonic setting and other factors on the validity of slip

measurements. This understanding is preferably verified in the field when possible, but practical limitations may prevent field studies in some places.

2. Direct comparison of field- and lidar-based measurements for the same geomorphic features (made by experienced investigators) shows that high-resolution topography techniques are a suitable means to investigate fault-offset geomorphic features. Standardizing remote measurement methods and reporting schemes that fully describe the uncertainties is crucial to the utility and repeatability of such studies.

3. Accurate and repeatable performance correlates well with experience. For all participants in our survey, major measurement discrepancies are typically due to different interpretations of the overall geologic features and history (epistemic uncertainty). However, we found that this more often occurs in the least-experienced populations—beginners have more issues with epistemic uncertainties (i.e., understanding topography, consideration of pre-offset channel orientation and form, geomorphic evolution of offset features post offset) than experienced individuals. The bulk of our results, however, suggest that the measurement methods among both groups are sound.

4. Single-investigator comparison of measurements made in different climatic regions reveals systematic differences in measurement uncertainties. Climate, in this case, can be used as a crude proxy for geomorphic modification of offset features in general and warrants further investigation to increase the utility of studies that target older offsets and uninvestigated surface ruptures in different climate regimes.

5. For both remote and field studies, making measurements of all potentially offset geomorphic features is crucial. As we continue to investigate along-strike slip variability, it is important that we avoid biases by preselecting features to measure.

Furthermore, measuring more components of an individual geomorphic feature (e.g., channel thalweg, margins) produces more consistently repeatable estimates of fault offset for a particular feature. For rating the quality of offset measurements, we suggest not only that a clear set of objective criteria be defined prior to measuring offsets, but also that all potentially offset geomorphic markers are addressed – even features that are later deemed to be not offset might tell us something about geomorphic processes at a point.

6. For experienced users, particular styles of offset representation (i.e., Gaussian normal, boxcar, etc) become increasingly important because they provide valuable information regarding epistemic and aleatoric uncertainties associated with particular estimates of displacement. An inadequate understanding of pre-event morphology and post-event modifications (epistemic) represents a greater limitation than feature condition and subsequent representation in the field or computer lab, so in general we find that the uncertainties or the pdf should be generous rather than restrictive.

While field validation is useful for familiarization of fault zone characteristics, in many cases it can be impractical because of temporal, financial, and land access limitations. For these reasons, the use of lidar- and other remote sensing-based studies of active fault zones is becoming pervasive and is something that practitioners must explore with a range of available tools. In this study, we have suggested preferred measurement and reporting protocols—a crucial first step towards enhancing consistency of high resolution topography-based analyses of active faults and establishing community protocols for future work.

ACKNOWLEDGEMENTS

Discussions with many colleagues have helped to focus our thinking on the problems identified in this paper. Thank you to the many participants in our surveys and to Tim Dawson, Suzanne Hecker, and two anonymous reviewers for constructive comments. This work was supported by the US Geological Survey National Earthquake Hazards Reduction program (G11AP20029 and G11AP20020). UCERF3 was supported by the California Earthquake Authority, US Geological Survey, and the Southern California Earthquake Center. The topographic data presented here were gathered by the National Center for Airborne Laser Mapping and processed and delivered by OpenTopography. Any use of trade, firm, or product names is for descriptive purposes only and does not imply endorsement by the U.S. Government.

We received an exempt status from the Institutional Review Board* for our research involving the use of educational tests with human subjects: Federal law 45 CFR 46.101(b) exempt category 7.2.

*Arizona State University's Office of Research Integrity and Assurance

REFERENCES

The Working Group on California Earthquake Probabilities (WGCEP), 1988, Probabilities of large earthquakes occurring in California along the San Andreas fault: USGS Open File Report 88 – 398.

Akciz, S. O., Grant-Ludwig, L., Arrowsmith, J R., and Zielke, O., 2010, Century-long average time intervals between ruptures on the San Andreas Fault in the Carrizo Plain: Geology, v. 38, no. 9, p. 787 – 790, doi: 10.1130/G30995.1.

Audemard, F. A., Ollarves, R., Bechthold, M., Diaz, G., Beck, C., Carrillo, E., Pantosti, D., and Diederix, H., 2008, Trench investigation on the main strand of the Bocono fault in its central section, at Mesa del Caballo, Merida Andes, Venezuela: Tectonophysics, v. 459, p. 38 – 53.

Awata, Y., Fu, B., and Zhang, Z., 2010, Geometry and slip distribution of the 1931 Fuyun Surface Rupture, northwest China. Forecasting large earthquakes from active faults in time and space: Abstracts of the HOKUDAN International Symposium on Active Faulting, Hokudan Earthquake Memorial Park, Awaji City, Japan.

Bevis, M., Hudnut, K., Sanchez, R., Toth, C., Grejner-Brzezinska, D., Kendrick, E., Caccamise, D., Raleigh, D., Zhou, H., Shan, S., Shindle, W., Yong, A., Harvey, J., Borsa, A., Ayoub, F., Shrestha, R., Carter, B., Sartori, M., Phillips, D., and Coloma, F., 2005, The B4 Project: Scanning the San Andreas and San Jacinto Fault Zones: Eos Transactions American Geophysical Union, v. 86, no. 52, Fall meeting supplement, H34B-01.

Bond, C. E., Gibbs, A. D., Shipton, Z. K., and Jones, S., 2007, What do you think this is? "Conceptual uncertainty" in geoscience interpretation: GSA Today, v. 17, no. 11, p. 4 – 10, doi: 10.1130/GSAT01711A.1.

Bond, C. E., Philo, C., and Shipton, Z. K., 2011, When There isn't a Right Answer: Interpretation and reasoning, key skills for twenty-first century geoscience: International Journal of Science Education, v. 33, no. 5, p. 629 – 652.

Borsa, A., and Minster, J. B., 2012, Rapid Determination of Near-Fault Earthquake Deformation Using Differential lidar: Bulletin of the Seismological Society of America, v. 102, p. 1335 – 1347.

Brooks, B.A., Hudnut, K.W., Akciz, S.O., Delano, J., Glennie, C.L., Prentice, C., and DeLong, S., 2013, On Offset Stream Measurements and Recent Coseismic Surface Rupture in the Carrizo Section of the San Andreas Fault: AGU Fall Meeting, Abstract T21D-01.

Burbank, D. W. and Anderson, R. S., 2001, Tectonic Geomorphology, 1st ed., Blackwell Science Inc., Malden, MA.

Chen, T., Akciz, S. O., Hudnut, K. W., Zhang, D. Z., and Stock, J. M., 2015, Fault-Slip Distribution of the 1999 M_W 7.1 Hector Mine Earthquake, California, Estimated from Postearthquake Airborne LiDAR Data: Bulletin of the Seismological Society of America, v. 105, no. 2a, doi: 10.1785/0120130108.

Cowgill, E., 2007, Impact of riser reconstruction on estimation of secular variation in rates of strike-slip faulting: Revisiting the Cherchen River site along the Altyn Tagh fault, NW China: Earth and Planetary Science Letters, v. 254, p. 239 – 255.

Evans, J. S., and Hudak, A. T., 2007, A multiscale curvature algorithm for classifying discrete return lidar in forested environments: IEEE Transactions on Geoscience and Remote Sensing, v. 45, no. 4, p. 1029 – 1038, doi: 10.1109/TGRS.2006.890412.

Field, E. H., Biasi, G. P., Bird, P., Dawson, T. E., Felzer, K. R., Jackson, D. D., Johnson, K. M., Jordan, T. H., Madden, C., Michael, A. J., Milner, K. R., Page, M. T., Parsons, T., Powers, P. M., Shaw, B. E., Thatcher, W. R., Weldon, R. J., and Zeng, Y., 2014, Uniform California Earthquake Rupture Forecast, Version 3 (UCERF3)—The time-independent model: Bulletin of the Seismological Society of America, v. 104, p. 1122 – 1180, doi: 10.1785/0120130164.

Gold, P. O., Cowgill, E., Kreylos, O., and Gold, R. D., 2012, A terrestrial lidar-based workflow for determining three-dimensional slip vectors and associated uncertainties: Geosphere, v. 8, no. 2, p. 431 – 442, doi: 10.1130/GES00714.1.

Grant-Ludwig, L., Akciz, S. O., Noriega, G. R., Zielke, O., and Arrowsmith, J R., 2010, Climate-modulated channel incision and rupture history of the San Andreas Fault in the Carrizo Plain: Science, v. 327, no. 5969, p. 1117 – 1119.

Haddad, D. E., Akciz, S. O., Arrowsmith, J R., Rhodes, D. D., Oldow, J. S., Zielke, O., Toke, N. A., Haddad, A. G., Mauer, J., and Shilpakar, P., 2012, Applications of airborne and terrestrial laser scanning to paleoseismology: Geosphere, v. 8, p. 771 – 785, doi: 10.1130/GES00701.1.

Haeussler, P. J., Schwartz, D. P., Dawson, T. E., Stenner, H. D., Lienkaemper, J. J., Sherrod, B., Cinti, F. R., Montone, P., Craw, P. A., Crone, A. J., and Personius, S. F., 2004, Surface rupture and slip distribution of the Denali and Totschunda faults in the 3 November 2002 M7.9 earthquake, Alaska: Bulletin of the Seismological Society of America, v. 94, no. 6B, p. S23 – S52.

Hanks, T. C., 2000, The age of scarp-like landforms from diffusion equation analysis: Quaternary Geochronology: Methods and Applications, editors Noller, J. S., Sowers, J. M., Lettis W. R., AGU Reference Shelf, Washington, DC, vol. 4, p. 313 – 338.

Haugerud, R. A., Harding, D. J., Johnson, S. Y., Harless, J. L., Weaver, C. S., and Sherrod, B. L., 2003, High-Resolution lidar Topography of the Puget Lowland, Washington – A Bonanza for Earth Science, GSA Today, v. 13, no. 6, p. 4 – 10, doi: 10.1130/1052-5173(2003)13<0004:HLTOTP>2.0.CO;2.

Hudnut, K.W., Borsa, A., Glennie, C., and Minster, J. B., 2002, High-resolution topography along surface rupture of the 16 October 1999 Hector Mine, California, earthquake (M_w 7.1) from airborne laser swath mapping: Bulletin of the Seismological Society of America, v. 92, p. 1570 – 1576, doi: 10.1785/0120000934.

Klinger, Y., Etchebes, M., Tapponnier, P., and Narteau, C., 2011, Characteristic slip for five great earthquakes along the Fuyun fault in China: Nature Geoscience, v. 4, p. 389 – 392, doi: 10.1038/NGEO1158.

Kondo, H., Awata, Y., Emre, Ö., Doğan, A., Özalp, S., Tokay, F., Yildirim, C., Yoshioka, T., and Okumura, K., 2005, Slip distribution, fault geometry, and fault segmentation of the 1944 Bolu-Gerede earthquake rupture, North Anatolian fault, Turkey: Bulletin of the Seismological Society of America, v. 95, p. 1234 – 1249.

Kondo, H., Özaksoy, V., and Yildirim, C., 2010, Slip history of the 1944 Bolu-Gerede earthquake rupture along the North Anatolian fault system – Implications for recurrence behavior of multi-segment earthquakes: Journal of Geophysical Research, v. 115, no. B4, doi: 10.1029/2009JB006413.

Leprince, S., Hudnut, K.W., Akciz, S. O., Hinojosa Corona, A., and Fletcher, J.M., 2011, Surface rupture and slip variation induced by the 2010 El Mayor – Cucapah earthquake, Baja California, quantified using COSI-Corr analysis on pre- and post-earthquake lidar acquisitions: Southern California Earthquake Center Annual Meeting abstract.

Lienkaemper, J. J., 2001, 1857 Slip on the San Andreas Fault Southeast of Cholame, California: Bulletin of the Seismological Society of America, v. 91, no. 6, p. 1659 – 1672.

Lienkaemper, J. J., and Sturm, T. A., 1989, Reconstruction of a channel offset in 1857(?) by the San Andreas fault near Cholame, California: Bulletin of the Seismological Society of America, v. 79, no. 3, p. 901 – 909.

Lindvall, S. C., Rockwell, T. K., and Hudnut, K. W., 1989, Evidence for Prehistoric Earthquakes on the Superstition Hills Fault from Offset Geomorphic Features: Bulletin of the Seismological Society of America, v. 79, no 2, p. 342 – 361.

Madden, C., Haddad, D. E., Salisbury, J. B., Zielke, O., Arrowsmith, J R., Weldon II, R. J., and Colunga, J., 2013, Compilation of Slip-in-the-Last-Event Data and Analysis of Last Event, Repeated Slip, and Average Displacement for Recent and Prehistoric Ruptures, Appendix R *in* Field, E. H., Biasi, G. P., Bird, P., Dawson, T. E., Felzer, K. R., Jackson, D. D., Johnson, K. M., Jordan, T. H., Madden, C., Michael, A. J., Milner, K. R., Page, M. T., Parsons, T., Powers, P. M., Shaw, B. E., Thatcher, W. R., Weldon II, R. J., and Zeng, Y., 2013, Uniform California earthquake rupture forecast, version 3 (UCERF3), The time-independent model: U.S. Geological Survey Open-File Report 20131165, 97 p., California Geological Survey Special Report 228, and Southern California Earthquake Center Publication 1792, http://pubs.usgs.gov/of/2013/1165.

McCalpin, J., 1996, Paleoseismology, 1st ed., Academic Press, San Diego, CA.

McGill, S. F., and Sieh, K. E., 1991, Surficial offsets on the central and eastern Garlock fault associated with prehistoric earthquakes: Journal of Geophysical Research, v. 96, no. B13, p. 21597 – 21621.

Nissen, E., Krishnan, A. K., Arrowsmith, J R., and Saripalli, S., 2012, Three-dimensional surface displacements and rotations from differencing pre- and post-earthquake lidar point clouds: Geophysical Research Letters, v. 39, no. L16301, doi: 10.1029/2012GL052460.

Nissen, E., Maruyama, T., Arrowsmith, J R., Elliot, J. R., Krishnan, A. K., Oskin, M. E., and Saripalli, S., 2014, Coseismic fault zone deformation revealed with differential LiDAR: examples from Japanese Mw 7 intraplate earthquakes: Earth and Planetary Science Letters, v. 405, p. 244 – 256, doi: 10.1016/j.epsl.2014.08.031.

Oreskes, N., Schrader-Frechette, K., and Belitz, K., 1994, Verification, validation, and confirmation of numerical models in the Earth sciences: Science, v. 263, no. 5147, p. 641 – 646.

Oskin, M., Le, K., and Strane, M. D., 2007, Quantifying fault-zone activity in arid environments with high-resolution topography: Geophysical Research Letters, v. 34, no. L23S05, p. 1 – 5, doi: 10.1029/2007GL031295.

Oskin, M., Arrowsmith, J R., Hinojosa Corona, A. H., Elliott, A. J., Fletcher, J. M., Fielding, E., Gold, P. O., Garcia, J. J. G., Hudnut, K. W., Liu-Zeng, J., and Teran, O. J., 2012, Complex surface rupture of the El Mayor-Cucapah earthquake imaged with airborne lidar: Science, v. 335, p. 702 – 705.

Ouchi, S., 2004, Flume experiments on the horizontal stream offset by strike-slip faults: Earth Surface Processes and Landforms, v. 29, p. 161 – 173, doi: 10.1002/esp.1017.

Prentice, C. S., Crosby, C. J., Whitehill, C. S., Arrowsmith, J R., Furlong, K. P., and Phillips D. A., 2009, GeoEarthScope LiDAR illuminates northern California's active faults: EOS Transactions of the American Geophysical Union, v. 90, no. 7.

Rockwell, T. K., and Pinault, C. T., 1986, Holocene slip events on the southern Elsinore fault, Coyote Mountains, southern California, *in* Ehlig, P., ed., Neotectonics and Faulting in Southern California, Geological Society of America Guidebook and Volume, Cordilleran Section, Boulder, Colorado, p. 193 – 196.

Rockwell, T. K., 1990, Holocene activity of the Elsinore fault in the Coyote Mountains, Southern California, *in* Friends of the Pleistocene Winter Fieldtrip: Western Salton Trough Soils and Neotectonics Guidebook, San Diego State University, San Diego, California, p. 30 – 42.

Rockwell, T. K., Lindvall, S., Dawson, T., Langridge, R., Lettis, W., and Klinger, Y., 2002, Lateral offsets on surveyed cultural features resulting from the 1999 İzmit and Düzce Earthquakes, Turkey: Bulletin of the Seismological Society of America, v. 92, no 1, p. 79 – 94.

Rockwell, T. K., and Klinger, Y., 2013, Surface Rupture and Slip Distribution of the 1940 Imperial Valley Earthquake, Imperial Fault, Southern California: Implications for Rupture Segmentation and Dynamics: Bulletin of the Seismological Society of America, v. 103, no. 2A, p. 629 – 640, doi: 10.1785/0120120192.

Salisbury, J. B., Rockwell, T. K., Middleton, T., and Hudnut, K., 2012, Lidar and field observations of slip distribution for the most recent surface ruptures along the central San Jacinto fault: Bulletin of the Seismological Society of America, v. 102, no. 2, p. 598 – 619, doi: 10.1785/0120110068.

Scharer, K., Salisbury, J. B., Arrowsmith, J R., and Rockwell, T. K., 2014, Southern San Andreas Fault Evaluation field activity: Approaches to measuring small geomorphic offsets – challenges and recommendations for active fault studies: Seismological Research Letters, v. 85, no. 1, doi: 10.1785/0220130108.

Scholz, C. H., 2002, The mechanics of earthquakes and faulting, 2nd ed., Cambridge University Press, Cambridge, U.K.

Schwartz, D. P., and Coppersmith, K. J., 1984, Fault behavior and characteristic earthquakes: examples from the Wasatch and San Andreas fault zones: Journal of Geophysical Research, v. 89, no. B7, p. 5681 – 5698.

Shimazaki, K., and Nakata, T., 1980, Time-predictable recurrence model for large earthquakes: Geophysical Research Letters, v. 7, no. 4, p. 279 – 282.

Sieh, K. E., 1978, Slip along the San Andreas fault associated with the great 1857 earthquake: Bulletin of the Seismological Society of America, v. 68, no. 5, p. 1421 – 1448.

Sieh, K. E., and Jahns, R. H., 1984, Holocene activity of the San Andreas fault at Wallace Creek, California: Geological Society of America Bulletin, v. 95, p. 883 – 896.

Trifonov, V. G., Makarov, V. I., and Skobelev, S. F., 1992, The Talas-Fergana active right-lateral fault: Annales Tectonicae, v. 6, p. 224 – 237.

Wallace, R. E., 1968, Notes on stream channels offset by the San Andreas fault, southern coast ranges, California, *in* Dickson, W. R., and Grantz, A., eds., Proceedings of Conference on Geologic Problems of the San Andreas Fault system, Stanford University Publication, Geological Sciences, v. 11, p. 6 – 21.

Wallace, R. E., ed., 1990, The San Andreas fault system, California: United States Geological Survey Professional Paper 1515.

Washburn, Z., Arrowsmith, J R., Forman, S. L., Cowgill, E., Wang, X. F., Zhang, Y. Q., and Chen, Z. L., 2001, Late Holocene earthquake history of the central Altyn Tagh fault, China: Geology, v. 29, p. 1051 – 1054.

Wells, D. L., and Coppersmith, K. J., 1994, New empirical relationships among magnitude, rupture length, rupture width, rupture area and surface displacement: Bulletin of the Seismological Society of America, v. 84, no. 4, p. 974 – 1002.

Yeats, R. S., Sieh, K. E., and Allen, C. R., 1997, The Geology of Earthquakes, Oxford University Press, Oxford, New York, 568.

Zielke, O., Arrowsmith, J R., Grant-Ludwig, L., and Akciz, S. O., 2010, Slip in the 1857 and earlier large earthquakes along the Carrizo Plain, San Andreas Fault: Science, v. 327, p. 1119 – 1122.

Zielke, O., and Arrowsmith, J R., 2012, LaDiCaoz and LiDARimager -MATLAB GUIs for lidar data handling and lateral displacement measurement: Geosphere - Special issue on high resolution topography, v. 8, no.1, p. 206 – 221, doi:10.1130/GES00686.1.

Zielke, O., Arrowsmith, J R., Grant-Ludwig, and L., Akciz, S. O., 2012, High resolution topography-derived offsets along the 1857 Fort Tejon earthquake rupture trace, San Andreas Fault: Bulletin of the Seismological Society of America, v. 102, no. 3, p. 1135 – 1154, doi: 10.1785/0120110230.

Zielke, O., Klinger, Y., Arrowsmith, J R., 2015, Fault Slip and Earthquake Recurrence Along Strike-Slip Faults – Contributions of High-Resolution Geomorphic Data: Tectonophysics, v. 638, p. 43 – 62, doi: 10.1016/j.tecto.2014.11.004.

FIGURE CAPTIONS

Figure 2.1 – ~3 m offset from the Clark strand of the San Jacinto Fault near Anza, CA. People mark the location of the channel thalweg wich is bound by the channel margins (green). Landform elements are projected to the fault trace (red) and the offset is the distance (horizontally or vertically) along the fault trace between the projected elements. Inset diagram illustrates sources of measurement uncertainty. Here, we only show measurement projections for the thalweg but all paired features (i.e. channel margins, ridge crests) can be measured. This is offset #5 from our repeatability survey (see Figures 2.9 and 2.10).

Figure 2.2 – (a) Measurement tally per fault strand, *NFTS—North Frontal Thrust System (b) location map for offset measurements—those made on ruptures occurring prior to 1910 are 'prehistoric measurements', 'Public Survey Locations' also shown on inset maps in Figures 2.9 and 2.10, (c) measurement method, and (d) quality rating tally for entire UCERF3 database (where 1 = high quality and 3 = low quality). City name abbreviations: SF—San Francisco, SB—Santa Barbara, SD—San Diego. Fault name abbreviations: SAF—San Andreas, GL—Garlock, OV—Owens Valley, SJF—San Jacinto, EL—Elsinore.

Figure 2.3 – Simplified example bivariate rubric for feature quality: the orientation of a channel with respect to the fault trace vs. fault zone localization. Each rubric square contains possible quality rankings.

Figure 2.4 – Curves are Probability Density Functions (PDFs) of varying accuracy and precision. The different positions of the red (dotted line) and black curves (stacked dashed and solid lines) are a consequence of epistemic uncertainty; the aleatoric uncertainty is the width of the PDF. For example, a preexisting jog in a channel could make the preferred measure greater than the actual offset.

Figure 2.5 – Summary of UCERF3 database by event age—historic vs. prehistoric (Madden et al., 2013). (a & c) Measurement methods tally and (b & d) number of offset measurements (blue) vs. unique geographic sites (red). *NFTS—North Frontal Thrust System.

Figure 2.6 – Offset measurement aleaetory uncertainty versus offset. Calico-Hidalgo (n=30), Camp Rock (138), Compton (12), Elsinore (57), Eureka Peak (24), Emerson (610), San Andreas (544), San Jacinto (918), Garlock (537), Homestead Valley (377), Johnson Valley (292), Lavic Lake (240), Owens Valley (145), Panamint Valley (12), Pisgah-Bullion (119), and Puente Hills fault (12).

Figure 2.7 – (a) Quality rating tally for new measurements, adapted from the original source to the UCERF3 quality-rating scheme. (b) Comparison of average surface slip magnitudes versus AOR (i.e., magnitude of aleatoric uncertainty) for each quality rank of measurements.

Figure 2.8 – Field vs. lidar measurements (a) made along the SJF by a single investigator (Salisbury et al., 2012) and (b) along the GF, where lidar measurements are from Haddad (Madden et al., 2013) and field measurements are from McGill and Sieh (1991). Lines show 1:1 correlation expected if measurements agreed. Figure from Madden et al. (2013).

Figure 2.9 – (a) Envelope of fault mapping categorized by experience level. Each box contains a hillshade with semi-transparent DEM overlay and contour lines (contour interval and center elevation defined in upper right corner). (b) Group measurement averages and standard deviations of measurements for each feature shown by experience level. Offset magnitudes (agreed upon by authors) shown in italics.

Figure 2.10 – Histogram summary of offset measurements generated with paper-based classroom survey. Average displacement estimates and average measurement uncertainties for the authors are depicted as vertical black lines and gray bars, respectively.

Figure 2.11 – Analysis of uncertainties for measurement made along portions of the San Jacinto (SJF) and San Andreas fault (SAF) systems with differing mean annual precipitation (MAP) values. The data suggest a weak trend of increased uncertainty where precipitation is higher. Climate data provided by: PRISM Climate Group, Oregon State University, http://prism.oregonstate.edu, created 4 Feb 2004.

FIGURES

Figure 2.1

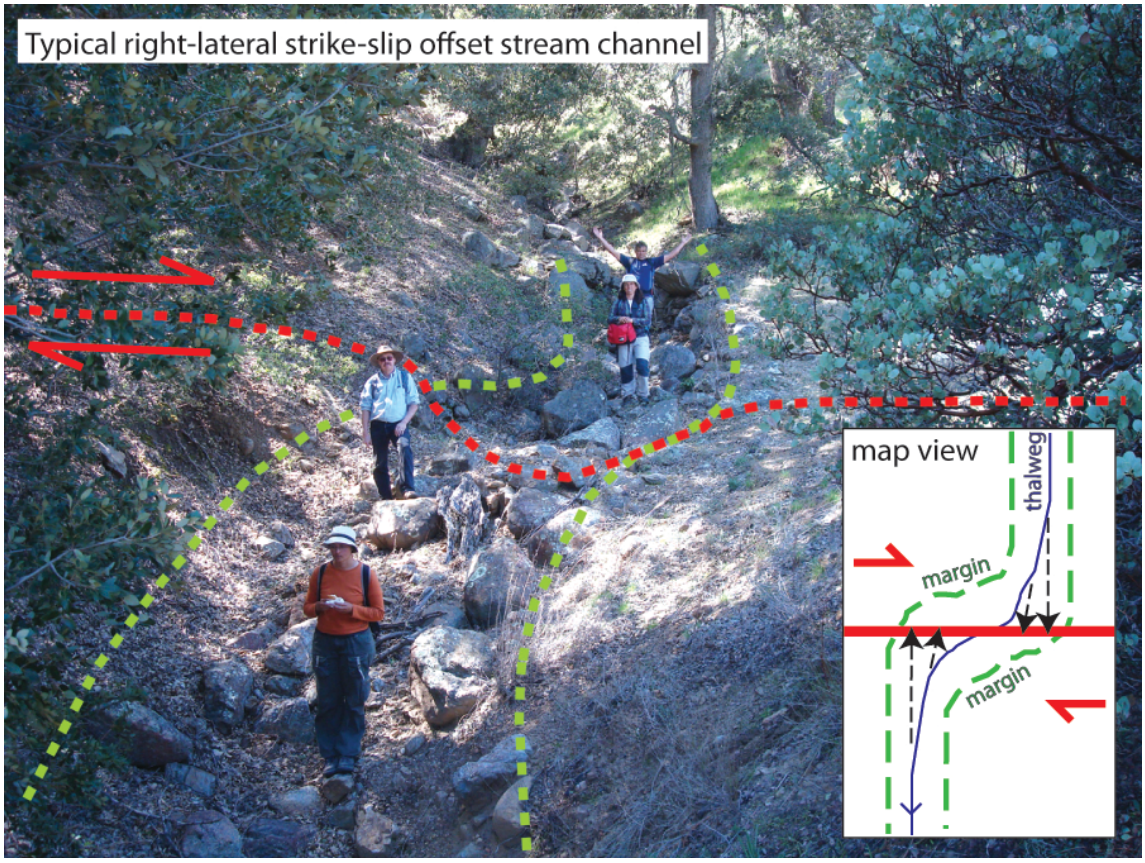

Figure 2.2

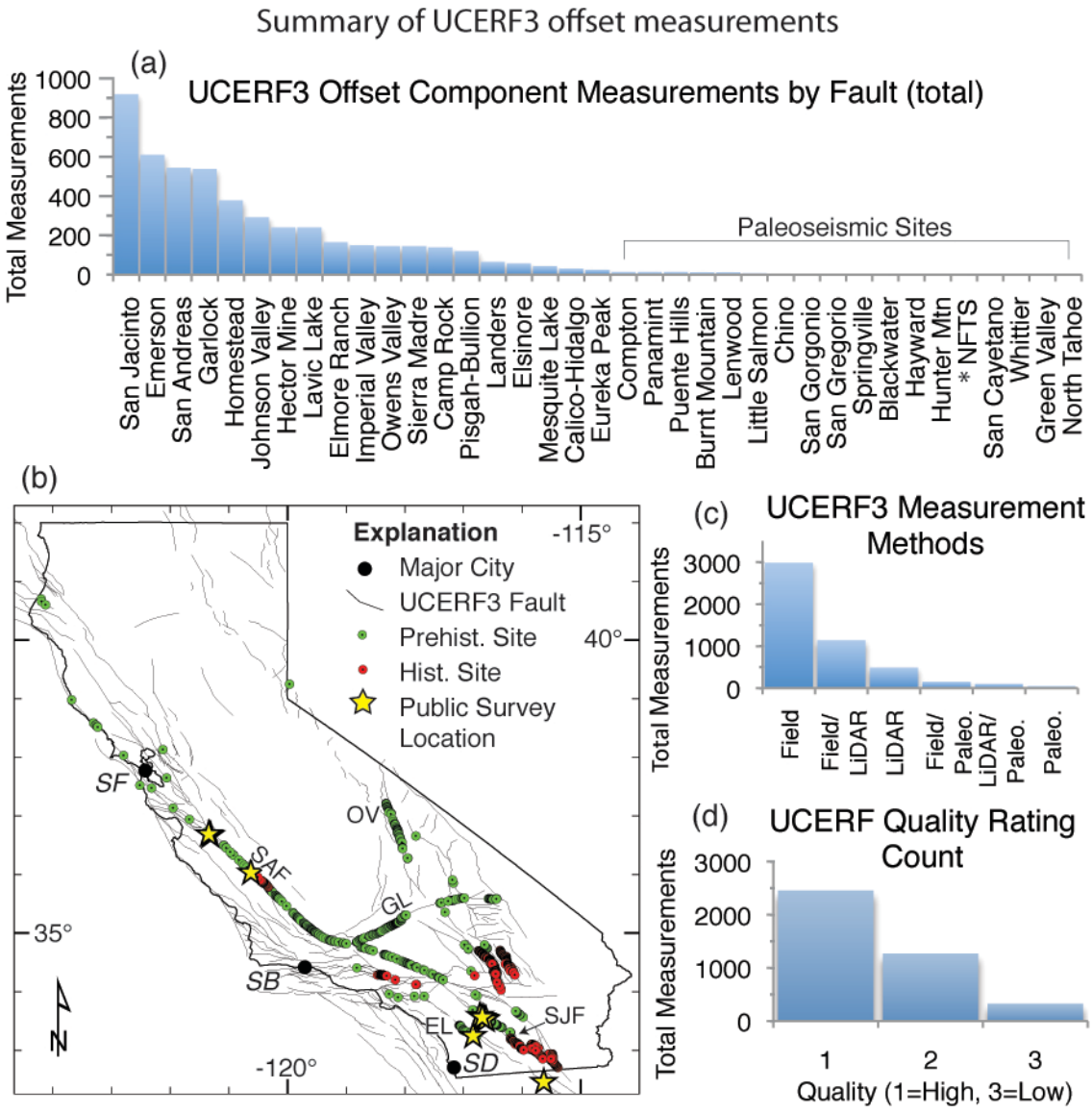
Summary of UCERF3 offset measurements
(a)
UCERF3 Offset Component Measurements by Fault (total)
Total Measurements
1000
800
600
400
200
0
Paleoseismic Sites
San Jacinto
Emerson
San Andreas
Garlock
Homestead
Johnson Valley
Hector Mine
Lavic Lake
Elmore Ranch
Imperial Valley
Owens Valley
Sierra Madre
Camp Rock
Pisgah-Bullion
Landers
Elsinore
Mesquite Lake
Calico-Hidalgo
Eureka Peak
Compton
Panamint
Puente Hills
Burnt Mountain
Lenwood
Little Salmon
Chino
San Gorgonio
San Gregorio
Springville
Blackwater
Hayward
Hunter Mtn
* NFTS
San Cayetano
Whittier
Green Valley
North Tahoe
(b)
Explanation
Major City
UCERF3 Fault
Prehist. Site
Hist. Site
Public Survey Location
-115°
40°
35°
-120°
SF
SAF
OV
GL
SB
EL
SJF
SD
(c)
UCERF3 Measurement Methods
Total Measurements
3000
2000
1000
0
Field
Field/ LiDAR
LiDAR
Field/ Paleo.
LiDAR/ Paleo.
Paleo.
(d)
UCERF Quality Rating Count
Total Measurements
3000
2000
1000
0
1
2
3
Quality (1=High, 3=Low)

Figure 2.3

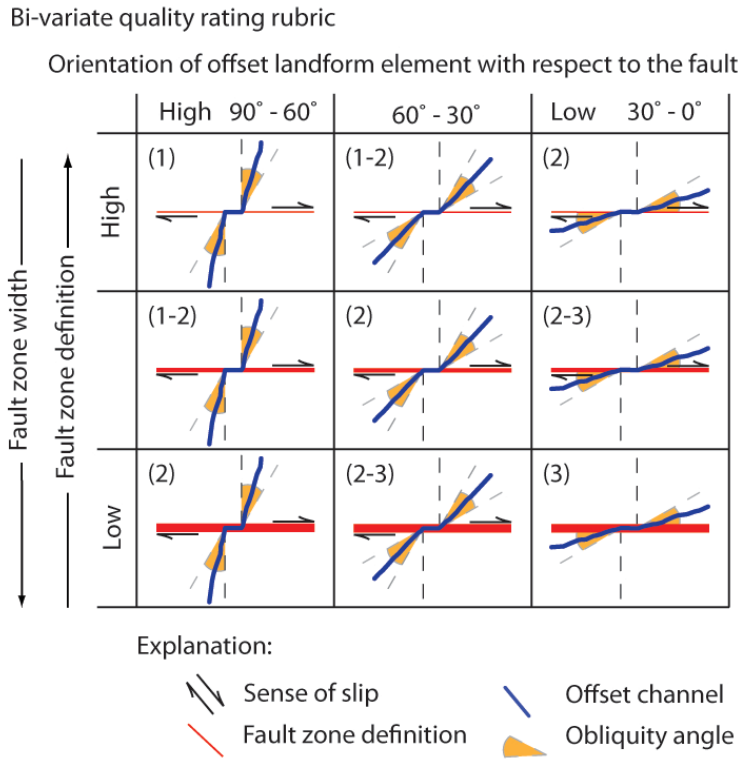
Bi-variate quality rating rubric
Orientation of offset landform element with respect to the fault
High 90° - 60°
60° - 30°
Low 30° - 0°
Fault zone width
Fault zone definition
High
Low
(1)
(1-2)
(2)
(1-2)
(2)
(2-3)
(2)
(2-3)
(3)
Explanation:
Sense of slip
Fault zone definition
Offset channel
Obliquity angle

Figure 2.4

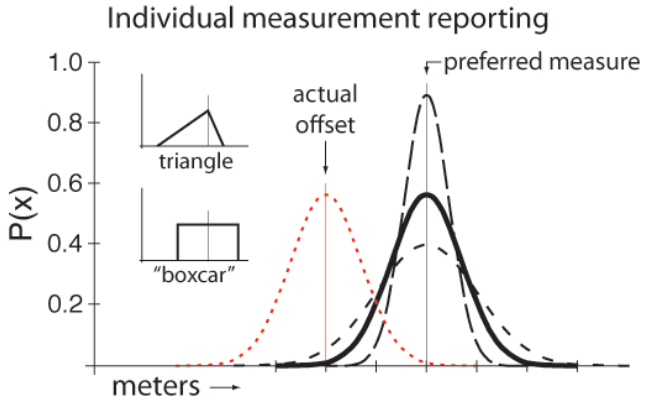
Individual measurement reporting
preferred measure
actual
offset
triangle
"boxcar"
P(x)
1.0
0.8
0.6
0.4
0.2
meters

Figure 2.5

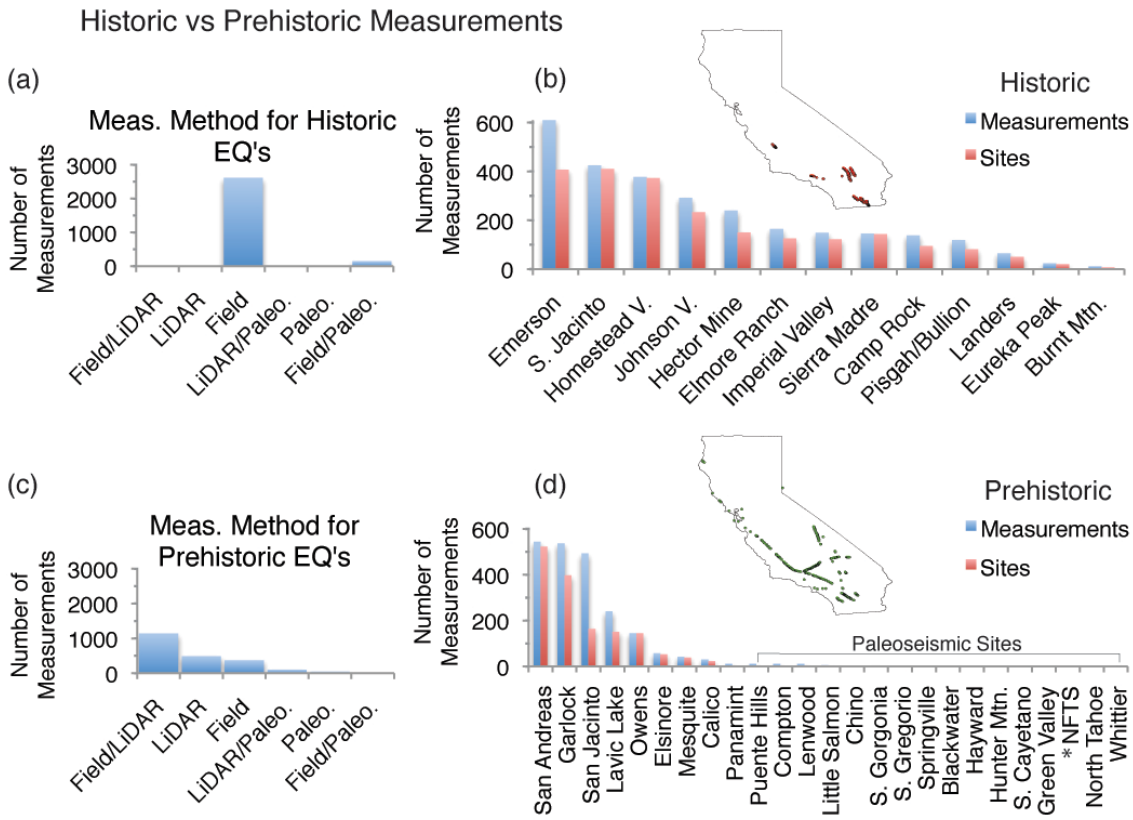
Historic vs Prehistoric Measurements
(a)
Meas. Method for Historic EQ's
Number of Measurements
3000
2000
1000
0
Field/LiDAR
LiDAR
Field
LiDAR/Paleo.
Paleo.
Field/Paleo.
(b)
Historic
Measurements
Sites
Number of Measurements
600
400
200
0
Emerson
S. Jacinto
Homestead V.
Johnson V.
Hector Mine
Elmore Ranch
Imperial Valley
Sierra Madre
Camp Rock
Pisgah/Bullion
Landers
Eureka Peak
Burnt Mtn.
(c)
Meas. Method for Prehistoric EQ's
Number of Measurements
3000
2000
1000
0
Field/LiDAR
LiDAR
Field
LiDAR/Paleo.
Paleo.
Field/Paleo.
(d)
Prehistoric
Measurements
Sites
Number of Measurements
600
400
200
0
Paleoseismic Sites
San Andreas
Garlock
San Jacinto
Lavic Lake
Owens
Elsinore
Mesquite
Calico
Panamint
Puente Hills
Compton
Lenwood
Little Salmon
Chino
S. Gorgonia
S. Gregorio
Springville
Blackwater
Hayward
Hunter Mtn.
S. Cayetano
Green Valley
* NFTS
North Tahoe
Whittier

Figure 2.6

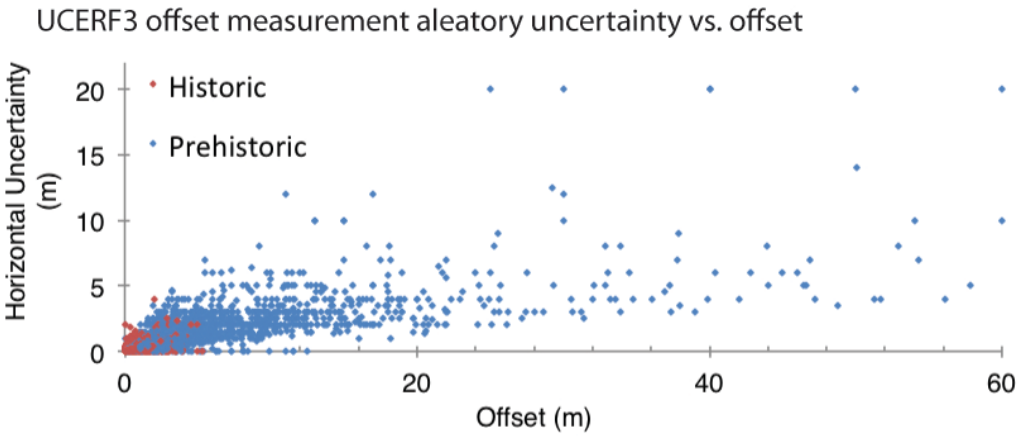
UCERF3 offset measurement aleatory uncertainty vs. offset
Historic
Prehistoric
Horizontal Uncertainty (m)
0
5
10
15
20
0
20
40
60
Offset (m)

Figure 2.7

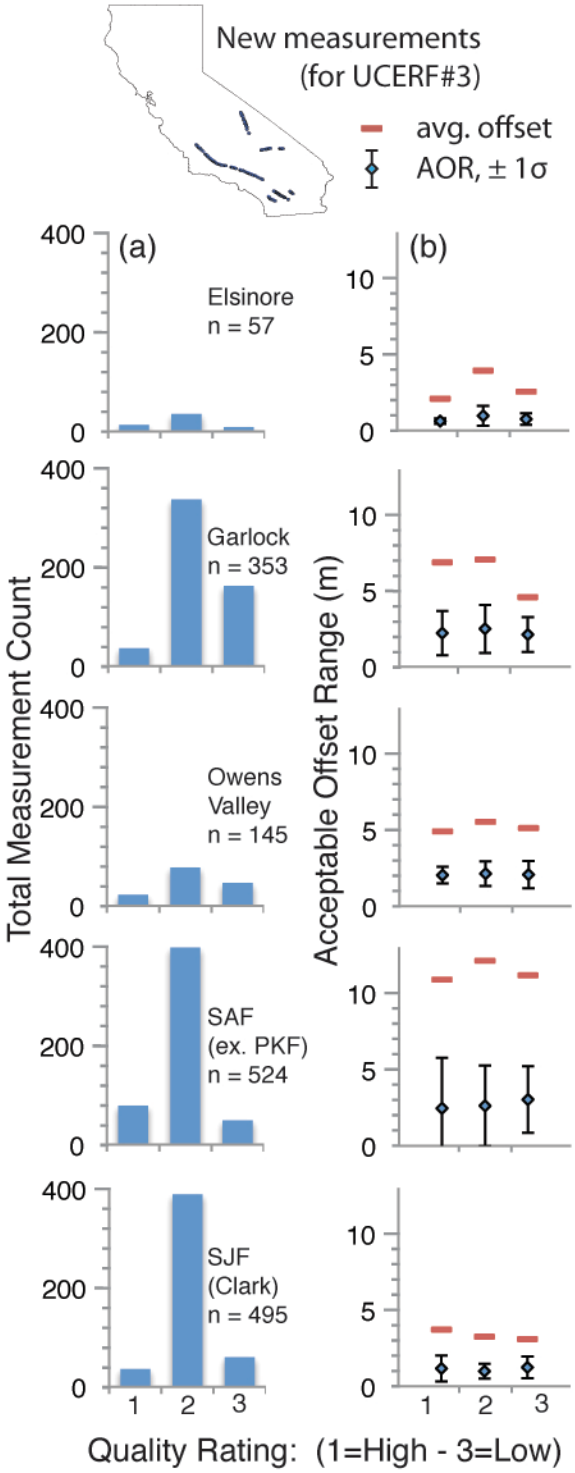
New measurements
(for UCERF#3)
avg. offset
AOR, ± 1σ
(a)
(b)
Elsinore
n = 57
Garlock
n = 353
Owens
Valley
n = 145
SAF
(ex. PKF)
n = 524
SJF
(Clark)
n = 495
Total Measurement Count
Acceptable Offset Range (m)
Quality Rating: (1=High - 3=Low)

Figure 2.8

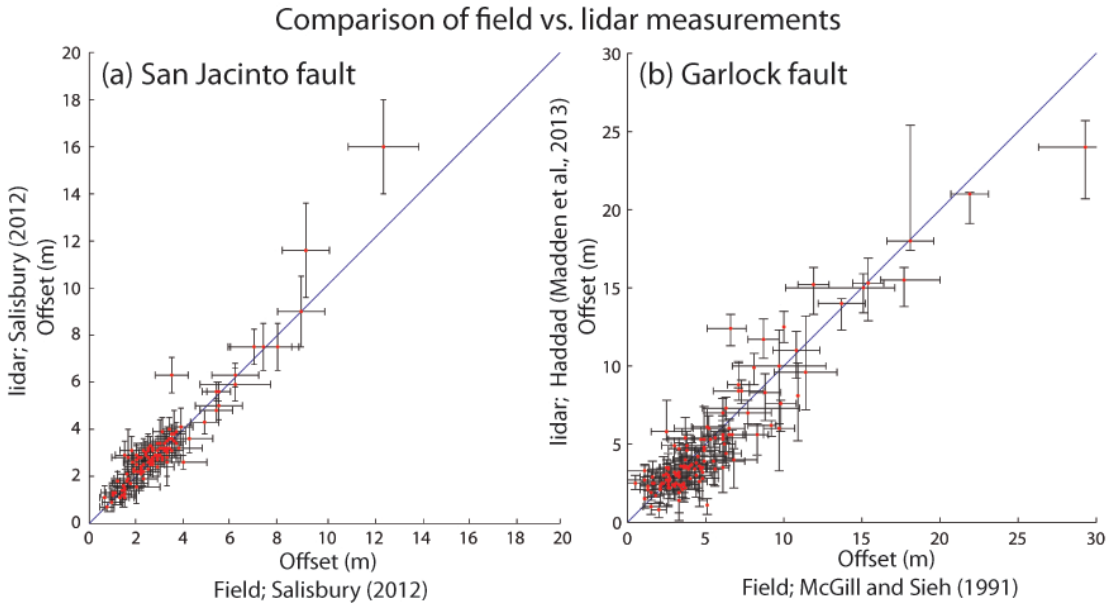
Comparison of field vs. lidar measurements
(a) San Jacinto fault
lidar; Salisbury (2012) Offset (m)
Offset (m)
Field; Salisbury (2012)
(b) Garlock fault
lidar; Haddad (Madden et al., 2013) Offset (m)
Offset (m)
Field; McGill and Sieh (1991)

Figure 2.9

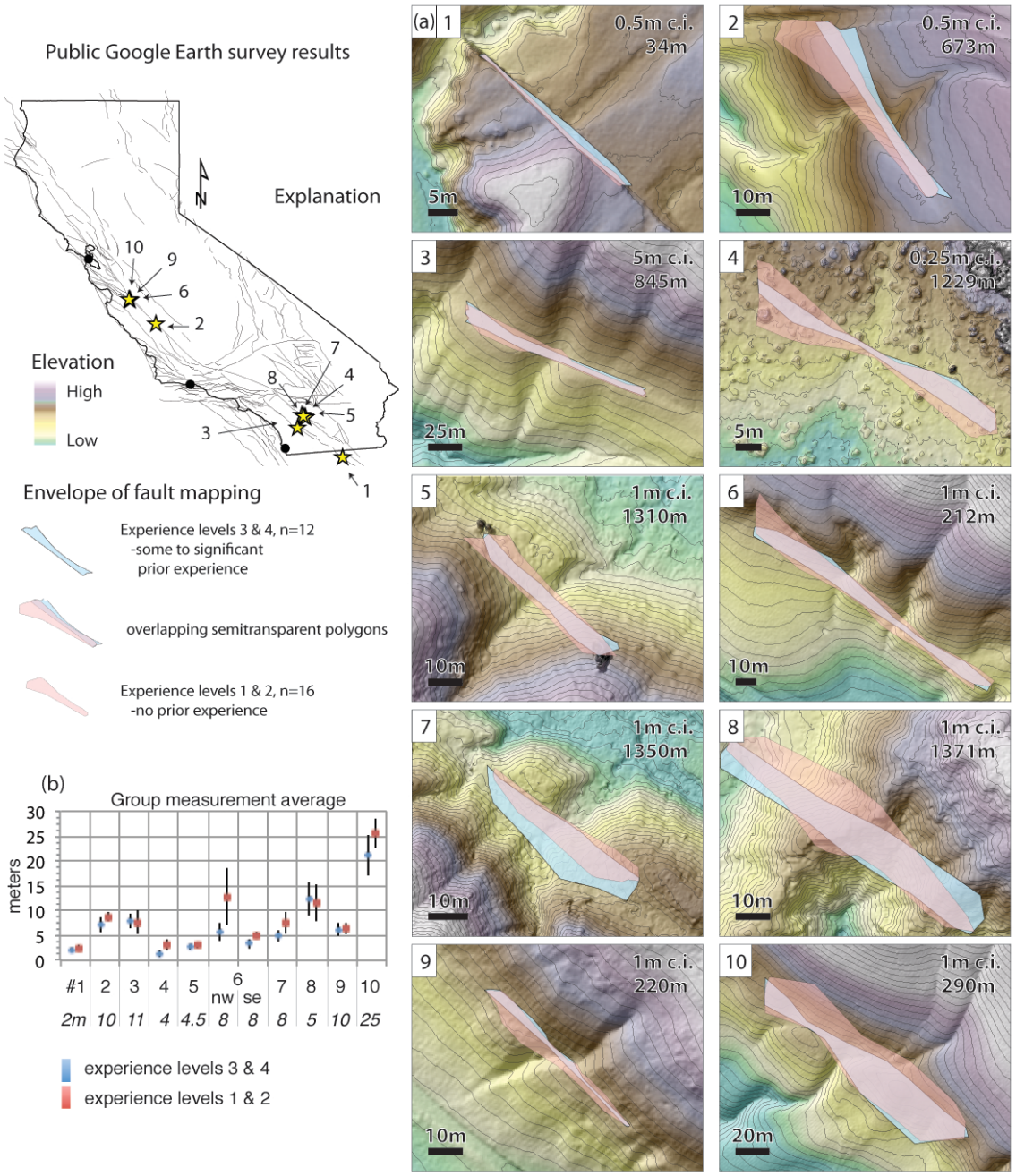
Public Google Earth survey results
Explanation
Elevation
High
Low
Envelope of fault mapping
Experience levels 3 & 4, n=12
-some to significant
prior experience
overlapping semitransparent polygons
Experience levels 1 & 2, n=16
-no prior experience
(b)
Group measurement average
meters
#1 2 3 4 5 6 nw 6 se 7 8 9 10
2m 10 11 4 4.5 8 8 8 5 10 25
experience levels 3 & 4
experience levels 1 & 2
(a)
0.5m c.i.
34m
0.5m c.i.
673m
5m c.i.
845m
0.25m c.i.
1229m
1m c.i.
1310m
1m c.i.
212m
1m c.i.
1350m
1m c.i.
1371m
1m c.i.
220m
1m c.i.
290m

Figure 2.10

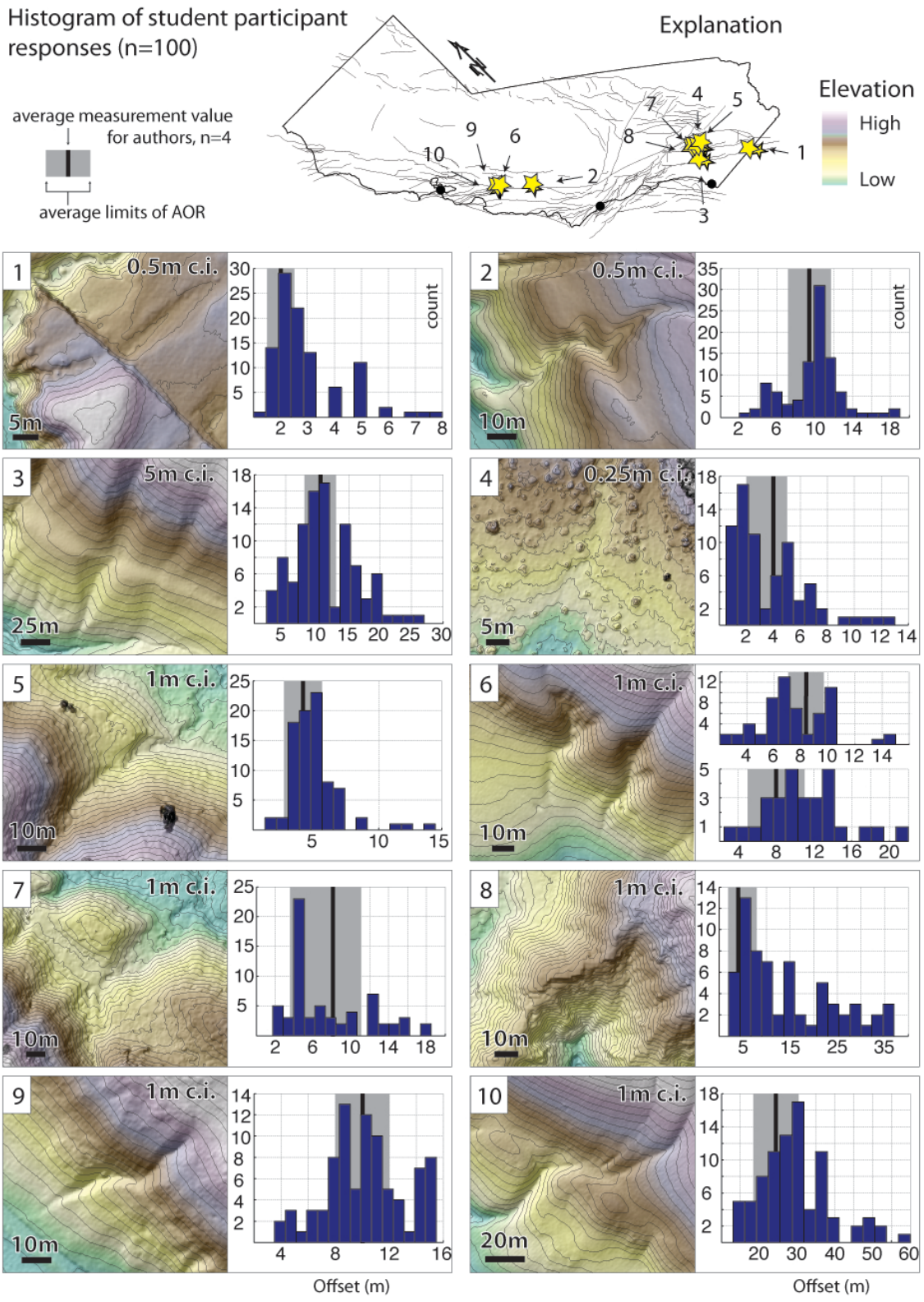
Histogram of student participant responses (n=100)
average measurement value for authors, n=4
average limits of AOR
Explanation
Elevation
High
Low
1
2
3
4
5
6
7
8
9
10
0.5m c.i.
5m
10m
5m c.i.
25m
0.25m c.i.
1m c.i.
20m
count
Offset (m)

Figure 2.11

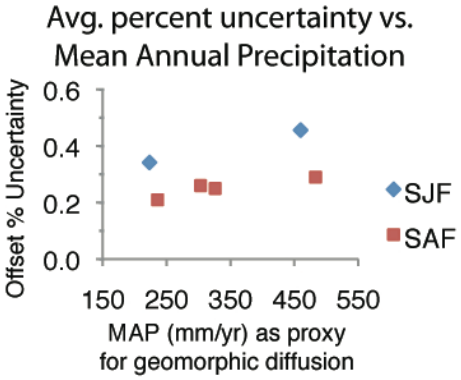
Avg. percent uncertainty vs.
Mean Annual Precipitation
Offset % Uncertainty
0.6
0.4
0.2
0.0
150
250
350
450
550
MAP (mm/yr) as proxy
for geomorphic diffusion
SJF
SAF

CHAPTER 3

THE AGE AND ORIGIN OF SMALL OFFSETS AT VAN MATRE RANCH ALONG THE SAN ANDREAS FAULT IN THE CARRIZO PLAIN, CALIFORNIA

ABSTRACT

Small displacement fault-offset features are rarely dated, making it challenging to attribute slip to individual earthquakes. We investigated the origins of subtle topographic depressions previously interpreted as beheaded channels representing small offsets at Van Matre Ranch (VMR) along the San Andreas Fault (SAF) in the Carrizo Plain. We excavated four fault-parallel trenches (T1 – T4) across subtle depressions and sampled for single-grain post-infrared infrared-stimulated luminescence (pIR-IRSL) age estimates of channel fill. Only one channel (T2) is young enough (0.38 ± 0.06 ka) to be associated with a nearby feeder drainage (sourced ~12 m to the SE) and provides a short-term slip rate of 31.6 +5.9/-4.3 mm/yr, consistent with estimates from decadal geodesy and other slip rate studies in the area. The age of the T2 channel fill falls within the uncertainty ranges of the penultimate earthquake through fourth event back as dated at Bidart fan ~12 km to the northwest. Hand excavated exposures at T1 (35 m to the NW of T2) indicate that the T2 channel sediments have experienced at least two earthquake events. At T1, hand-dug trenches show that the "beheaded gully" is a fosse between two small offset alluvial fans. Reconstruction of the young alluvial fan apex shows that slip in the M_w 7.8 Fort Tejon earthquake of 1857 was ~4 m. Therefore, slip in the penultimate earthquake (PE) is ≤~8 m at the VMR site. However, we cannot discount that T2 channel sediments have experienced as many as four earthquakes, thus making slip in the PE <8 m. Interestingly, buried channel ages are much older at the other trenches (4.26 – 8.12 ka). A

constant slip rate of 33 mm/yr suggests distant sources and significantly larger drainage basins beyond the SE end of our study area. Our results indicate: a) there may be appreciable high-frequency variation in paleoearthquake slip along strike and in successive earthquakes at a point; b) beheaded topographic depressions on the downstream side of the fault have the potential to, but do not necessarily, capture drainage basins on the opposite (i.e. upstream) side of the fault with continued slip; and c) small catchments do not produce channel landforms or deposits as frequently as has been previously suggested.

INTRODUCTION

Small-scale fault-offset fluvial landforms are commonly cited in slip-per-event studies as indicators of slip magnitude for earthquakes. Although it has long been assumed that even small-scale drainages generate fluvial markers more frequently than earthquakes that offset them (e.g., Wallace, 1968; Sieh, 1978; Sieh and Jahns, 1984; McGill and Sieh, 1991; Klinger et al., 2011; Zielke et al., 2010, 2012; Madden et al., 2013), these offsets (<10's of m) are rarely dated, making attribution of slip to dated earthquakes tenuous. Improved understanding of the relative frequency of geomorphic marker (e.g., rill, gully, or levee) formation versus marker displacement is key for understanding fault offset accumulation patterns used to inform models of earthquake recurrence (e.g., Field et al., 2014).

In this project, we excavated and dated four subtle topographic depressions previously interpreted as beheaded gullies at Van Matre Ranch along the San Andreas Fault (SAF) to understand the creation and preservation of topographic channel forms and resulting cut/fill sequences in the southeastern Carrizo Plain, California (Figure 3.1 – 3.2). We test the hypothesis that depressions seemingly offset from nearby feeders are not only associated with the nearby feeders, but also contain channel sediments that are progressively and predictably older with greater offset. We refine the short-term slip rate, evaluate slip in the most recent event, combine these results with recent earthquake timing (from an existing nearby paleoseismic site) to speculate about slip in older events, and synthesize a better understanding of the geomorphic controls of subtle, small-scale fault-zone topography the southeastern Carrizo Plain.

BACKGROUND

The Carrizo Plain section of the SAF, located between Parkfield and the Big Bend, has a relatively simple geometry, the highest slip rate in California (3.4 – 3.6 cm/yr, Sieh and Jahns, 1984; 3.6 cm/yr, Schmalzle et al., 2006; Meade and Hager, 2005; 3.1 cm/yr, Noriega et al., 2006), and ruptured historically in the M*w* 7.8 Fort Tejon earthquake of 1857 (Figure 3.1). Early models of earthquake recurrence for this stretch of the SAF were simple, suggesting that repeat, large events at longer time intervals dominated the earthquake record (Sieh and Jahns, 1984; Schwartz and Coppersmith, 1984; Grant and Sieh, 1994; Liu et al., 2004; Liu-Zeng et al., 2006; Zielke, et al., 2010). For example, excavations of stream offsets and beheaded channels by Liu-Zeng et al. (2006) near Wallace Creek revealed that as many as four of the last six events ruptured with >5 m of slip, implying not strictly uniform rupture behavior. Similarly, Zielke et al. (2010, 2012) use high-resolution topographic data to suggest that average slip in 1857 was ~5 m, and that some other older large earthquakes likely have similar magnitudes of slip.

However, it is possible that discrete evidence of the smallest events (e.g., <1 m, from smaller earthquakes or the tail ends of ruptures) will be lost at the surface (and lost in cumulative offset probability stacks; e.g., Zielke, et al., 2015) and only preserved in the paleoseismic record (e.g., Akciz, et al., 2010; Zielke et al., 2010, 2012, 2015). In a paleoseismic and paleoflood correlation study, Grant Ludwig et al. (2010) suggested variable slip (0.5 to 5.9 m) for the last five ruptures at nearby Bidart Fan (Figure 1). We can adequately measure the surface expression of small-scale offset landforms (Salisbury

et al., 2015; Zielke et al., 2015) but it is important to note that the surficial geomorphic record will be dominated by the largest of event offsets.

Continued investigations in the Carrizo Plain with improved geochronologic techniques have refined the paleoseismic earthquake catalog and argued that the average recurrence of earthquakes along the SAF is likely as frequent as 99 ± 46 years (includes current open interval; Akciz et al., 2010) instead of the >200-year recurrence proposed by Sieh and Jahns (1984). The Uniform California Earthquake Rupture Forecast, Version 3 (UCERF3) calculates a maximum likelihood recurrence for the Carrizo Plain segment of the SAF (at Bidart fan) at 115 yrs (86 – 154 yrs 16 – 84% bounds; Field, et al., 2014). If we assume a perfect correspondence between successive paleoseismic events and discrete offsets identified at the surface or in the shallow subsurface, then coupling the conservative recurrence rate proposed by Akciz et al. (2010) with cumulative offsets from Liu-Zeng et al. (2006) or Zielke et al. (2010) implies slip rates as high as ~60 and ~50 mm/yr, respectively, both of which greatly exceed ~33 mm/yr rate measured from millennial-scale offset landforms (Sieh and Jahns, 1984) and geodesy (Meade and Hager, 2005; Schmalzle, et al., 2006).

This mismatch between inferred slip rates, recurrence intervals, and slip per event suggests that recurrence timing and moment distribution are significantly more variable than originally thought (Weldon et al., 2004; Scharer et al., 2014; Dawson, 2013; Madden et al., 2013; Rockwell et al., 2014; Field et al., 2014). In the Carrizo Plain, therefore, it is incorrect to assume a perfect correspondence between the earthquakes preserved in sub-surface sediments and with the earthquakes preserved in the geomorphic record (as suggested by Akciz, et al., 2010 and Zielke, et al, 2010). Reconciliation of these

discrepancies between measurable fault parameters is crucial for proper hazard characterization so we must explore the possibility that slip in individual earthquakes may be smaller overall or significantly more variable than previously estimated. We combine investigation of the geomorphic evolution of small-scale fault-offset features and single-grain post-infrared infrared-stimulated luminescence (pIR-IRSL) dating of K-feldspar grains to test the linkage of geomorphic offsets to dated paleoearthquakes.

We focused on the VMR reach of the Carrizo Plain where the SAF is well-expressed and preserves several closely-spaced topographic depressions, previously interpreted as beheaded gullies (Figures 3.1 – 3.3) (Sieh, 1978). At VMR, several catchments (~1,500 – 3,000 m^2) NE of the SAF drain to the SW and are truncated by the well-expressed SAF. There, groups of displaced offset features, noted by Wallace (1968) and investigated by Sieh (1978), have been attributed to displacement in successive earthquakes (Figures 3.1 – 3.3). These earthquakes are radiocarbon-dated at the nearby Bidart Fan, ~12 km to the northwest. Prior to the 1857 Fort Tejon (M_w 7.8) earthquake, the most recent ground-rupturing events, expressed as two-sigma ranges, occurred 1631 – 1823, 1580 – 1640, 1510 – 1612, 1450 – 1475, 1360 – 1452 AD (Akciz et al. 2010). The last four events (including the historic 1857 rupture) from Bidart Fan are shown in Figure 3.4.

At VMR, Sieh (1978) identified and measured several topographic depressions to estimate slip magnitudes for the 1857 Fort Tejon earthquake (Figure 3.3). Some of these features were re-measured by Zielke et al. (2010, 2012) with the B4 lidar data (Bevis et al., 2005). The topographic depressions, interpreted to represent fluvial channels, are offset ~8 to ~12 m (Figure 3.3). Noriega et al. (2006) investigated a 28-m offset channel

nearby and dated the initial incision at A.D. 1160, inferring a 29.3 – 35.6 mm/yr slip rate for the site (Figure 3.1B). Considering the foundation of work conducted there, VMR is an excellent natural laboratory to directly test whether we can use chronometric approaches to date short-lived ephemeral fluvial features.

METHODS

We targeted four subtle topographic depressions previously interpreted as beheaded channels offset ~10 m from feeder channels. Prior to excavation, we used low-altitude balloon aerial photographs to construct a 3 cm digital elevation models (DEM) of the VMR site in Agisoft PhotoScan Pro (see review by Johnson, et al., 2014) (Figures 3.2 & 3.3). We used the high-resolution topography to document the surficial geomorphology in even greater detail than the B4 lidar data (Bevis et al., 2005; see discussion by Arrowsmith and Zielke, 2009) and refined proposed fault-parallel trench locations for backhoe excavation. We targeted four feeder channels and had a backhoe cut four fault-parallel trenches on the southwest side of the SAF across downstream elements of beheaded depressions (T1–T4, Figure 3.3). Trenches were extra wide (~2 m) to avoid the need for shoring. Where necessary, we hand dug trenches (T5 – T10) to completely reveal channel bottoms, precisely locate fault traces and evaluate fault zone width, reveal 3-D sedimentary geometries, and pursue piercing lines (defined by channel thalwegs/margins) into the fault trace (Figure 3.3). We photographed trench exposures and generated high-resolution orthophotographs in Agisoft Photoscan Pro (see Bemis, et al., 2015). We logged trench stratigraphy at 1:20 scale on printed orthophotographs. We used a total station to document the trench locations, record channel geometries, and establish a local network of ground control points used in our structure from motion

models. We collected 19 samples for post-infrared infrared-stimulated luminescence (pIR-IRSL) analysis of single-grain potassium-feldspar crystals at the Department of Earth, Planetary, and Space Sciences department at the University of California, Los Angeles. We analyzed 15 of these samples, the results of which can be seen in Table 3.1.

Post-IR IRSL dating methods

Sample preparation, instrumentation, and environmental dose-rate determination

In southern California, quartz crystals generally have notoriously low OSL sensitivity (Lawson et al., 2012). For all samples, we instead isolated K-feldspar grains under dim amber lighting conditions. We wet-sieved samples to isolate the 175 – 200 μm size fraction and treated with 3% HCl to dissolve carbonates and iron oxides. We separated grains by density within lithium metatungstate (measured density 2.565 g/cm^3) to isolate the most potassium-rich portion of feldspar grains (Rhodes, 2015). We washed grains in HF for 10 minutes to remove the grain surface (to increase brightness) and lastly dry-sieved to remove grains etched below a diameter of 175 μm. We mounted samples on aluminum single-grain discs for analysis in a TL-DA-20 Risø automated reader equipped with a single-grain IR laser and detected emissions with a Schott BG3-BG39 filter combination.

We used a portable NaI gamma spectrometer to determine the *in situ* gamma dose-rate contribution for all samples except J1055, which was within 22 cm of J1054; we applied the J1054 gamma dose-rate measurement to both samples (Table 3.1). For the beta dose-rate, we employed inductively-coupled plasma mass spectrometry (ICP-MS) to estimate the U and Th contents, and inductively-coupled optical emission spectrometry

(ICP-OES) to determine the K content. We converted compositional values to annual dose-rates using the conversion factors of Adamiec and Aitken (1998). We derived the alpha dose-rate contribution from an assumed internal potassium content of 12.5 ± 0.12 wt. % (Huntley and Baril, 1997) and measured the water content by oven-drying a portion of sediment from each sample tube.

Equivalent dose determination

We measured the luminescence responses of samples with a post-infrared infrared-stimulated luminescence (p-IR IRSL) protocol. Until recently, luminescence dating of sedimentary K-feldspars suffered from the problem of signal fading (Huntley and Lamothe, 2001). To circumvent this limitation, workers noticed that, while the initial IR stimulation fades at room temperature, a subsequent IR stimulation at elevated temperature (i.e., p-IR IRSL) is less affected by fading (Buylaert et al., 2009). Our protocol (Table 3.2) employs a second stimulation at 225 °C (lower than the conventional 290 °C) to balance signal stability with solar sensitivity (Brown et al., 2015).

Most samples yield single-grain equivalent dose (D_e) distributions that are internally consistent. The variability of luminescence between grains is characterized by the overdispersion parameter. Overdispersion is caused mainly by differences in natural beta dose rates to individual grains but is unaccounted for by defined sources of error (e.g., Figure 3.5A). Well-bleached sediments typically have overdispersion values within the range of ~10 – 30 % (Arnold and Roberts, 2009), and of our well-bleached samples (all except J1054, J1061, and J1063), overdispersion ranged from 12 – 29 % (with an

average value of 20 ± 5 %). For these samples, we used the Central Age Model (CAM) to determine D_e values (e.g., Galbraith et al., 1999).

Of the three poorly-bleached samples, J1054 and J1061 exhibit dose distribution groupings (e.g., Brown et al., 2015). We selected the youngest group from within each sample, and in both cases, overdispersion values are consistent with a well-bleached population (e.g., Figure 3.5B). For sample J1063, the dose distribution is continuous. We used the Minimum Age Model (MIM, assuming four parameters; Galbraith et al., 1999) for this sample, imposing an overdispersion of 15%. Figure 3.5 illustrates the two end-members of D_e distributions, plotted as a function of precision, increasing radially from the left, and D_e value, increasing counter-clockwise (i.e., the 'Radial Plot' of Galbraith et al., 1999). The poorly-bleached J1063 exhibits a range of single-grain D_e values, the lowest edge of which likely represents the true (or minimum) burial dose (Figure 3.5B). By contrast, J1065 is well-bleached, with nearly all grains consistent within ± 2σ (the salmon-colored region; Figure 3.5A). The D_e values display notable internal consistency when sampled in stratigraphic sequence. For example, J1054 – J1058 were all taken from the same panel of T1 and each of the three sedimentary packages sampled young moving stratigraphically upward (Table 3.1).

Fading correction

We tested eight of the samples for signal fading at room temperature (Huntley and Lamothe, 2001). We gave samples a known beta dose, preheated them, and then left them in the dark for ~20 minutes to two months. After different pause times, we measured the luminescence response to determine how much the signal faded. While the responses

varied, we observed a mean *g*-value of 1.33 ± 0.02 % loss per decade (time constant of 1173 s) for the samples. We corrected all samples for fading loss using the 'Luminescence' package within the **R** programming environment (Kreutzer et al., 2012).

RESULTS

We use the pIR-IRSL age estimates of channel fills to estimate how long the fluvially-transported sediments have been buried. Figure 3.3 shows locations of the exposed channel fills (blue trench outlines) with respect to the subtle topographic depressions. Three of the four subtle depressions (T2, T3, and T4) have channel fill deposits that are aligned directly beneath the modern topographic depression (previously interpreted as beheaded channels). One trench (T1) contains two distinct channel fills that are not associated with any modern topographic depression (Figure 3.3).

Based on the existing short-term slip rate study conducted at this site (Noriega et al., 2006) fading-corrected pIR-IRSL age estimates of channel fill indicate that only one channel fill (T2) was buried recently enough to be associated with flow from a nearby feeder drainage. The package of sandy silts from within a coarse pebble channel deposit at T2 are buried ~57 cm below the surface and are capped by unconsolidated sediments that showed very little evidence of soil formation and support the contention that they were deposited recently (sample J1063, Figure 3.5B and 3.6). These sediments, offset 12 m from the nearby feeder, have a minimum age estimate of 0.38 ± 0.06 ka (J1063) and provide a short term slip rate of 31.6 +5.9/-4.3 mm/yr. This slip rate is consistent with decadal geodesy and other slip rate studies in the area (Sieh and Jahns, 1984; Meade and Hager, 2005; Noriega et al., 2006, Schmalze, et al., 2006) (Figure 3.7), but is impossible to be sure of the channel configuration at the time T2 sediments were deposited. Also,

only a small portion of the measured grains are young. The poorly-bleached T2 sample (J1063) exhibits a range of single-grain D_e values, the lowest edge of which (minimum age model) likely represents the true (or minimum) burial dose (Figure 3.5B).

At T1, although we found two buried channel complexes, neither of the two are associated with the subtle topographic depression interpreted as a channel (Figure 3.3 and 3.8). Hand-dug trenches show that the young "beheaded gully" contains no signs of fluvial sediments. Beneath the topographic depression we find only lightly indurated fan material. Instead, our excavations reveal two small, very young (unconsolidated) alluvial fan deposits (Figure 3.9). Between these two alluvial fans is the fosse, or depression that was previously interpreted as a once-active channel. We precisely locate the fault trace in trenches T9 and T5, confirm fan stratigraphy in T7, and excavate the paleo-feeder channel location in T6 to confirm the young source of the offset alluvial fan and reconstruct the tectonic offset of the young alluvial fan apex (Figure 3.9). Measured with high confidence, slip in 1857 (the most recent event, A) was 3.8 m ± 50 cm at this site (Figure 3.9).

Interestingly, at trenches T4, T3, and T1, buried channel ages are much older (Figure 3.10, 3.11, and 3.8, respectively). From the southeast to northwest, buried channel ages are: T4—4.28 ka, T3—5.62 ka, T1 southeast—7.32 ka, and T1 northwest—7.04 ka (Table 3.1, ages summarized on Figure 3.3). Coupling these results with an assumed long-term slip rate of ~33 mm/yr suggests distant sources – significantly larger drainage basins (~7,000 – 6,000 m^2) beyond the SE end of our study area (Figure 3.1, Table 3.3 and 3.4). Although it is not possible to pinpoint the exact sources because of pIR-IRSL uncertainties and ambiguous paleo-channel configurations, we speculate about

how far the buried channels have traveled. Table 3.4 shows the distances channel deposits have traveled (and potential correlative drainage basins) based on their depositional ages and a constant slip rate throughout the Holocene.

At T4, we have two distinct sets of sediments at different stratigraphic positions (~70 cm of stratigraphic separation) beneath the modern topographic depression, albeit on laterally opposite trench walls ~2 m apart (Figure 3.10). In the southwest exposure, there is a 1 m-deep coarse sand and pebble channel fill from which we have two pIR-IRSL age estimates: 4.26 ± 0.36 ka (J1069) and 4.30 ± 0.44 ka (J1070). There is no corresponding channel deposit directly across the trench, but there is an equivalent channel shape cut into the older, indurated fan material (Figure 3.10, shown with dashed red outline). At the top of the northeast exposure, there is a ~2 m-wide, 20 cm-thick surficial package of laminated channel silts (Figure 3.10). There is no equivalent channel deposit on the opposite side of the trench. This latter deposit was not sampled for pIR-IRSL age control.

DISCUSSION

Channel processes and offset markers in the Carrizo Plain

A significant result of this study is the discovery that the channel sediments buried <2 m beneath the subtle topographic depressions (interpreted as beheaded, locally-sourced gullies) are significantly older in origin than expected. The major incisional and depositional episodes (i.e., the cutting and subsequent backfilling of paleo-channels) occurred at the outlets to the significantly larger drainage basins to the southeast (Figure 3.1, Table 3.4). Furthermore, this incision and deposition occurred several thousands of years ago and each one of the downstream channel segments we see buried in the

subsurface was beheaded from its original feeder. We emphasize that the topographic form at VMR may not necessarily be the same as the subsurface form. At T1, these buried sediments are not associated with a modern topographic expression of a channel (Figure 3.3). At T2, T3, and T4, however, the buried sediments and modern topographic expressions of channels reveal a more complex story of incision and backfilling of channels, abandonment, and fluvial rejuvenation with faulting throughout the Holocene. This complexity is a significant limitation to measuring slip markers in only surficial geomorphology and shows that (aleatoric) measurement uncertainties may be dwarfed or negated by epistemic uncertainties pertaining to the offset feature (e.g., Gold et al., 2012; Scharer et al., 2014; Salisbury et al., 2015; Zielke et al., 2015).

There are several important implications. First, we are only able to reach the conclusion that the buried sediments in our trenches have distant sources after excavating and establishing age control for multiple buried deposits. When possible, field mapping should be combined with analysis of high-resolution topographic data or aerial photographs (e.g., Scharer et al., 2014), but to positively remove most epistemic uncertainties associated with offset reconstructions, subsurface observations are necessary. This is problematic, as excavations and high-precision dating are not only time consuming but also expensive. Therefore, it is crucial that as we continue active fault studies using high-resolution topography and field mapping that we strategically employ sub-surface studies like this one as a linchpin around which to base more abundant, more loosely constrained data (e.g., surface slip measurement catalogs).

Even small-scale topographic depressions in semi-arid, active strike-slip environments have the potential to be long-lived and re-occupied after their initial beheading or abandonment (Salisbury et al., *in prep*, Chapter 4). However, when and how these long-lived topographic stream channels and their subsurface deposits and boundaries are totally or partially rejuvenated in an episode of stream piracy is complex and site-specific. While drainage capture and stream abandonment may happen multiple times during continued faulting, we first consider the simple scenario—the possibility that there is no rejuvenation as a topographic depression is passed in front of new catchments. In these cases, like we observe at T1, buried channel deposits can potentially outlast their surficial expressions. In the Carrizo Plain, geomorphic diffusion is controlled primarily by vigorous bioturbation (e.g., burrowing by kangaroo rats) in addition to other geomorphic processes (e.g., rainsplash, soil creep). The diffusive transport rates are ~10x higher in the Carrizo Plain than in the Basin and Range, for example (Arrowsmith et al., 1998). Topographic signatures of channels this size (<~4 m wide, <~2 m deep) have disappeared after about 6 ky, as the channel deposits in T1 that are ~8.12 – 6.33 ka (J1054, J1055, J1056, and J1058) and ~7.45 – 6.62 ka (J1061 and J1062) no longer have any surface expression (Figure 3.3, 3.8, Table 1).

In more complex cases where downstream (beheaded) channel segments capture existing upstream feeders, there is a chance for renewed fluvial modification in the downstream channel segments. Whether or not and to what extent incision (and subsequent deposition) occurs is dependent upon many site-specific conditions including the relative sizes and slopes of channel elements and the sizes of storms driving geomorphic change. This study shows that each offset marker—as straightforward as it

may seem at the surface—can potentially warrant its own set of subsurface 3D excavations to fully understand the recent history of tectonic offset versus geomorphic response. These unavoidable epistemic uncertainties must be explored to confidently use such geomorphic markers as earthquake slip indicators.

We see preserved sedimentological evidence for two different styles of renewed fluvial modification in long-lasting, beheaded channel segments: one at T2, where capture triggered significant incision, and one at T4, where capture produced very little incision. The first scenario, at T2, occurred as the surface expression (southwest of the SAF) of an existing beheaded channel (sourced from far southeast, D7 – D9) captured basin D2 and triggered significant re-incision into the subsurface sediments sourced from D7 – D9 (Figure 3.1, 3.6). Trench T2 contains buried channel sediments with a complex age distribution indicating significant re-incision resulting from drainage capture (sample J1063, Figure 3.5b, Table 1). We use the Minimum Age Model for an age estimate of 0.38 ± 0.06 ka. While only a portion of the grains reflect this minimum age, we know that the youngest grains were sub-aerially exposed and most-thoroughly bleached during an active transport event prior to burial in a partial bleaching event. If sediment transport occurs without sufficient sun exposure (e.g., during a heavy storm event, in an opaque slurry of sediments) then existing optically stimulated luminescence signals are not properly reset, resulting in an age overestimation. We interpret the distribution of grain ages to indicate that ~380 years ago, an existing topographic depression with a buried channel deposit was incised and backfilled, causing a partial bleaching of sediments at the surface. We take the youngest age estimates, therefore, to represent the small portion

of grains that were completely reset in the last exposure, or the minimum age for the deposit.

In the second scenario, at T4, the surface expression of an existing beheaded channel (sourced from D7 – D9) captured a drainage basin farther northwest after beheading but did not trigger significant incision. In this case, the original, subsurface sediments sourced from D7 – D9 are largely intact. Trench T4 contains two distinct sedimentary packages that indicate the topographic depression under investigation is from a distant source and that there has been a recent, local drainage capture but without significant incision (Figure 3.10). In addition to the deep sediments buried beneath the modern topographic depression in the southwest wall of our trench (~4.28 ka; J1069 and J1070), the northeast exposure contains fine-grained silty channel sediments at the surface (Figure 3.10). We do not sample these surficial sediments because the uncertainties associated with the long-term geologic dose-rate (and thereby the luminescence age) become large within about ~ 30 cm of the modern surface (due to the overwhelming influence of cosmic ray bombardment and the incomplete geometry of gamma rays from surrounding sediments). However, the fact that these delicate sediments are preserved at the surface in an area of such vigorous bioturbation indicates that they are very young, likely sourced from the most proximal drainage. We use these two packages of channel sediments to argue that the original topographic depression was sourced from the larger basins to the southeast, and captured the D4 drainage basin without triggering significant incision because D4 is such a small catchment at only ~1,500 m^2.

Channels incise when they have sufficient specific stream power per unit bed area—a function of discharge (i.e., drainage area) and local stream gradient (e.g., Whipple & Tucker, 1999). We hypothesize that in the semiarid Carrizo Plain, drainage area is more important than channel gradient to generating the power required to incise new channel forms. Figure 3.1B shows catchment-averaged gradients (as a general proxy for local stream gradient) and Table 3.3 lists drainage areas. Although drainage D2, at ~3,000 m^2, apparently does have the power to erode and refresh sediments at ~60 cm depth, it appears that in general there may be a critical threshold in this setting with typical channel slopes for drainage area at ~7,000 m^2 required to cut significant channels that persist in the landscape. If the bulk of our channel deposits are indeed sourced from the larger basins to the southeast of our trench area, then the implication is that small-catchment systems (<7,000 m^2) in the Carrizo Plain produce fewer channel deposits than has been assumed and tend to produce un-channeled fans instead. We have discovered that the beheaded channel depressions have very little to do with the smaller, steeper catchments nearby making it more important to date small-scale offset markers by accessing their related surface deposits when possible.

Recent Slip along the San Andreas Fault

We have a high quality, single event 3D excavated slip measurement of 3.8 m ± 50 cm for the 1857 event at VMR (Figure 3.9). The 12 m offset channel at T2 (Sample J1603) dated at 380 ± 60 years BP, therefore, represents slip in at least two earthquakes. We compare the depositional age range of the T2 channel sediments (sample J1603: 1596 – 1716 AD; Table 1) to the paloeoseismic record at nearby Bidart Fan, ~12 km to the northwest (Figure 3.4). The ages of events B – D, prior to event A (1857), expressed as

two-sigma uncertainty ranges are: 1631 – 1864 AD, 1580 – 1640 AD, and 1510 – 1612 AD, respectively (Figure 3.4). This confirms that the T2 channel has experienced at least two earthquakes but could have experienced as many as 4. Therefore, penultimate slip could have been as much as 8 m, but we cannot discount that there may have been 8 m total slip in events B – D. There is some ambiguity regarding the exact channel configuration at the time young T2 sediments were deposited.

For this ~150 m reach of the SAF, existing surface slip measurements are 7.8 – 8.2 m (four measurements, Sieh, 1978) and 11.8 m (single measurement, Zielke, 2012). While the former measurements are interpreted as single-event offsets, the 11.8 m measurement is attributed to slip in two events (because Zielke identified several ~5 m offsets nearby in the B4 lidar data). Additionally, Zielke et al. (2010) initially noted several low-quality/uncertain offsets in the same reach, but subsequently omitted them from the 2012 paper because they were too weak to be defendable with high-resolution topography alone.

Only a few subsurface estimates of 1857 slip exist in the Carrizo Plain: 7.9 m at Wallace Creek (18 km NW, Liu-Zeng et al, 2006), and 6.7 m at Phelan Creeks (16 km NW, Grant & Sieh., 1994). Our most recent event slip measurement is significantly lower than other sub-surface estimates, lower than that of Sieh (1978) based on surface slip measurements, and at the low end of the range proposed for the 1857 earthquake by Zielke et al. (2010), also based on surface slip measurements.

This discrepancy in slip for the 1857 earthquake can be explained several ways. First, it is possible that some portion of total deformation is accommodated on other unseen fault strands or as off-fault deformation nearby and our measurement does not

reflect the total slip in 1857. We evaluated the surrounding area using B4 lidar imagery and aerial photographs and though there are some subtle lineaments ~1 km to the southeast of our study area that do not appear to be recently active. Additionally, the channel elements that we used as extended piercing lines (in trenches T1 and T10) do not appear to warp across the narrow fault zone that we exposed in trenches T9, T5, and T8.

Second is the possibility that we are observing true slip variability for the 1857 rupture. Other sub-surface slip measurements are 15+ km to the northwest and slip distributions commonly exhibit long-wavelength (10's of km) spikes or troughs where surficial materials and depth to bedrock vary, where fault geometries change or complexity increases, or when nearing the ends of ruptures. This low-frequency spatial variation easily explains the difference between our ~4 m offset and the 7.9 m and 6.7 m offsets seen at the northern end of the Carrizo Plain. Furthermore, paleoseismic evidence corroborates this type of variation in slip. The fourth earthquake at Bidart Fan (12 km to the northwest; Event D), indicated by the development of a sag pond ~10 m wide and several 10's of cm deep, lead Akciz et al. (2010) to confidently hypothesize that the fourth event was comparable to the 1857 event in terms of magnitude and lateral slip (that we have shown here to be 3.8 ± 0.5 m) (Figure 3.9). However, the fourth event offset at Wallace Creek (~18 km to the northwest) was potentially as small as 1.4 m according to Liu-Zeng et al. (2006). Alternatively, high-frequency variation in along-strike slip has been well-documented elsewhere (e.g., Rockwell et al., 2002), where investigators observed up to 35% variability in slip measurements over only 100 m. However, this does not explain the discrepancy between our 4 m measurement (at T1, this study, Figure 3.9) and the ~7.9 m (Wallace Creek; Liu-Zheng et al., 2006) and ~6.1

m (Phelan Creeks; Grant and Sieh, 1994) estimates of slip from offset features in other parts of the Carrizo Plain. It is likely that the geomorphic offsets at VMR measure landforms that are not actually offset from the sources that were originally inferred, or if the reconstruction is correct, that the total offset is not from only a single earthquake.

CONCLUSION

The results of this study compel a reconsideration our interpretation of several topographic depressions previously interpreted as single-earthquake offsets in the southeastern Carrizo Plain, highlighting known limitations of measuring slip markers in surficial geomorphology alone. We have shown that long-lived topographic depressions have the potential to be, but are not necessarily, reoccupied with continued slip and that small catchments (<7,000 m^2) in the Carrizo Plain do not produce channel deposits as frequently as has been assumed. A high-confidence subsurface estimate of slip at Van Matre Ranch for the 1857 earthquake (3.8 m ± 50 cm) suggests that slip along strike in large events is variable and that slip at a point in successive earthquakes is also variable. Slip in the penultimate event could be as much as 8 m, but we cannot discount that 8 m of slip may have been accommodated in three events prior to the 1857 earthquake. This study highlights the need for similar studies involving sub-surface excavations and high-precision geochronology as we build a database of surface slip measurements for fault offset accumulation and earthquake hazard evaluation.

TABLES

pIR-IRSL Lab Results

Lab code	Field code	Trench	Depth (m)	K (%)	Th (ppm)	U (ppm)	Measured gamma dose-rate (Gy/ka)	Total dose-rate (Gy/ka)	Equivalent dose (Gy)	Uncorrected age (ka)	Fading-corrected post-IR IRSL
J1054	CP15-01	T1_NE	2	2.4	7	2.69	1.23 ± 0	4.19 ± 0.3	29 ± 1.6	6.91 ± 0.58	7.72 ± 0.63
J1055	CP15-02	T1_NE	2.1	2.9	5.1	2.12	same as J1054	4.5 ± 0.3	32.7 ± 1.9	7.27 ± 0.66	8.12 ± 0.77
J1056	CP15-03	T1_NE	1.73	2.3	6	2.56	1.49 ± 0	4.32 ± 0.2	27.6 ± 1.3	6.39 ± 0.48	7.13 ± 0.54
J1058	CP15-05	T1_NE	1.45	2.9	6.1	2.41	1.48 ± 0.01	4.83 ± 0.3	27.4 ± 1.1	5.67 ± 0.44	6.33 ± 0.48
J1061	CP15-08	T1_NE	2.1	2.5	5.3	2.42	1.34 ± 0	4.37 ± 0.3	29.16 ± 1.46	6.67 ± 0.54	7.45 ± 0.58
J1062	CP15-09	T1_NE	1.75	2.4	6.5	3.28	1.42 ± 0	4.43 ± 0.3	26.23 ± 1.31	5.93 ± 0.46	6.62 ± 0.51
J1063	CP15-10	T2_NE	0.57	2.3	6.8	3.11	1.36 ± 0	4.32 ± 0.2	1.53 ± 0.21	0.35 ± 0.05	0.38 ± 0.06
J1064	CP15-11	T2_SW	0.64	2.4	7.3	3.45	1.45 ± 0	4.58 ± 0.3	7.98 ± 0.47	1.74 ± 0.15	1.93 ± 0.17
J1065	CP15-12	T3_NE	1.8	2.8	5.4	2.11	1.45 ± 0	4.66 ± 0.3	22.09 ± 1.09	4.74 ± 0.39	5.28 ± 0.45
J1066	CP15-13	T3_NE	1.67	2.6	5.9	1.92	1.42 ± 0	4.49 ± 0.3	23.17 ± 1.64	5.16 ± 0.5	5.85 ± 0.55
J1067	CP15-14	T3_NE	1.22	3.1	9.7	2.33	1.59 ± 0	5.18 ± 0.3	23.08 ± 1.03	4.46 ± 0.36	5.18 ± 0.41
J1068	CP15-15	T3_NE	1.06	2.6	6.6	2.2	1.53 ± 0	4.68 ± 0.3	26.36 ± 1.61	5.63 ± 0.49	6.17 ± 0.54
J1069	CP15-16	T4_SW	0.82	2.9	5.8	1.8	1.53 ± 0	4.83 ± 0.3	18.32 ± 0.81	3.79 ± 0.3	4.26 ± 0.34
J1070	CP15-17	T4_SW	0.82	2.7	6.2	2.31	1.49 ± 0	4.7 ± 0.3	17.79 ± 1.33	3.78 ± 0.37	4.3 ± 0.44
J1072	CP15-19	T10_NE	2.1	2.4	7.7	3.06	1.49 ± 0	4.5 ± 0.3	21.8 ± 1.46	4.85 ± 0.43	5.57 ± 0.5

*measured g -value of 1.33 ± 0.02 (t_C = 1173 s)

Table 3.1 – pIR-IRSL results including lab and field codes, trench exposure, sample depth, Potassium, Thorium, and Uranium concentrations, measured gamma dose, dose-rate, equivalent dose measurements, and uncorrected and fading-corrected age estimates.

Step	Treatment	Description
1	Irradiation for t s	Natural dose (i.e., do nothing) for first cycle, laboratory dose for subsequent cycles
2	Heat to 250 C for 60 s	Preheat
3	IR laser stimulation at 50 C for 3 s per grain	IRSL
4	IR laser stimulation at 50 C for 3 s per grain	post-IR IRSL, L_x
5	Irradiation for t s	Test dose (same dose every cycle)
6	Heat to 250 C for 60 s	Preheat
7	IR laser stimulation at 50 C for 3 s per grain	Test dose IRSL
8	IR laser stimulation at 50 C for 3 s per grain	Test dose post-IR IRSL, T_x
9	IR diode stimulation at 290 C for 40 s	Hot bleach to empty all traps

Step	Treatment	Description
1	Irradiation for t s	Natural dose (i.e., do nothing) for first cycle, laboratory dose for subsequent cycles
2	Heat to 250 C for 60 s	Preheat
3	IR laser stimulation at 50 C for 3 s per grain	IRSL
4	IR laser stimulation at 50 C for 3 s per grain	post-IR IRSL, L_x
5	Irradiation for t s	Test dose (same dose every cycle)
6	Heat to 250 C for 60 s	Preheat
7	IR laser stimulation at 50 C for 3 s per grain	Test dose IRSL
8	IR laser stimulation at 50 C for 3 s per grain	Test dose post-IR IRSL, T_x
9	IR diode stimulation at 290 C for 40 s	Hot bleach to empty all traps

Table 3.2 – Post-IR IRSL protocol used for luminescence dating in this study. This single-aliquot regenerative cycle is repeated for the natural dose and all subsequent laboratory doses.

	Area (m^2)
D1	1,858
D1.2	576
D2	2,902
D2.2	1,749
D3	2,933
D4	1,503
D5	6,959
D6	2,877
D7	6,516
D8	12,962
D9	16,961

Table 3.3 – Van Matre Ranch drainage basin areas as labeled in Figure 3.1B.

	Max. Age (ka)	Min. Age (ka)	Max.-Min Dist. (m)	Basin
T1 NW	7.45 ± 0.58	6.62 ± 0.51	246-218	7/8-7
T1 SE	8.12 ± 0.77	6.33 ± 0.48	268-209	8/9-7
T3	6.17 ± 0.54	5.18 ± 0.41	204-171	9-8/9
T4	4.3 ± 0.44	4.26 ± 0.24	142-141	8/9

Table 3.4 – Speculated sources for old channel deposits based on a constant slip rate of 33 mm/yr.

ACKNOWLEDGEMENTS

We heartily thank our field assistants: Caitlyn Fischman, Matthew Marin, Eui-jo Marquez, Nik Midttun, Juliet Olsen, Michael Say, Jessica Sutton, & Alana Williams. Also, a special thank you to L. Bidart for access to the Van Matre Ranch property. Discussions with Kate Scharer have been particularly helpful. Thanks to Kelin Whipple and Duane DeVecchio for comments on an earlier version of this manuscript. This research was supported by the Southern California Earthquake Center (Contribution No. 7152). SCEC is funded by NSF Cooperative Agreement EAR-1033462 & USGS Cooperative Agreement G12AC20038. B4 lidar data are from the B4 Lidar Project (NCALM, USGS, OSU, & EAR Geophysics at NSF) and are available at OpenTopography (*http://www.opentopography.org)*. Salisbury's work on the very high-resolution topography using structure from motion was supported in part by a strategic University Partnership between Arizona State University and NASA's Jet Propulsion Laboratory.

REFERENCES

Adamiec, G., and Aitken, M., 1998, Dose-rate conversion factors: update: Ancient TL, v. 16, p. 37 – 50.

Arnold, L.J., and Roberts, R.G., 2009, Stochastic modelling of multi-grain equivalent dose (D_e) distributions: Implications for OSL dating of sediment mixtures: Quaternary Geochronology, v. 4, p. 204 – 230, doi: 10.1016/j.quageo.2008.12.001.

Arrowsmith, J. R., Rhodes, D. D., and Pollard, D. D.,1998, Morphologic dating of scarps formed by repeated slip events along the San Andreas Fault, Carrizo Plain, California: Journal of Geophysical Research: Solid Earth, v. 103, no. 5.

Arrowsmith, J. R., and Zielke, O., 2009, Tectonic geomorphology of the San Andreas Fault zone from high resolution topography: An example from the Cholame segment: Geomorphology, v. 113, p. 70 – 81, doi: 10.1016/j.geomorph.2009.01.002.

Akciz, S.O., Grant Ludwig, L., Arrowsmith, J R., and Zielke, O., 2010, Century-long average time intervals between earthquake ruptures of the San Andreas fault in the Carrizo Plain, California: Geology, v. 38, no. 9, p.787 – 790, doi: 10.1130/G30995.1.

Bemis, S. P., Micklethwaite, S., Turner, D., James, M. R., Akciz, S. O., Thiele, S. T., and Bangash, H. A., 2014, Ground-based and UAV-based photogrammetry: A multi-scale, high-resolution mapping tool for structural geology and paleoseismology: Journal of Structural Geology, v. 69, p. 163 – 178, doi: 10.1016/j.jsg.2014.10.007.

Bevis, M., Hudnut, K., Sanchez, R., Toth, C., Grejner-Brzezinska, D., Kendrick, E., Caccamise, D., Raleigh, D., Zhou, H., Shan, S., Shindle, W., Yong, A., Harvey, J., Borsa, A., Ayoub, F., Shrestha, R., Carter, B., Sartori, M., Phillips, D., and Colma, F., 2005, The B4 project: Scanning the San Andreas and San Jacinto fault zones: EOS (Transactions American Geophysical Union), v. 86., no. 52, fall meeting supplement, H34B-01.

Brown, N.D., Rhodes, E.J., Antinao, J.L., McDonald, E.V., 2015, Single-grain post-IR IRSL signals of K-feldspars from alluvial fan deposits in Baja California Sur, Mexico: Quaternary International, v. 362, p. 132 – 138, doi: 10.1016/j.quaint.2014.10.024.

Buylaert, J.P., Murray, A.S., Thomsen, K.J., Jain, M., 2009, Testing the potential of an elevated temperature IRSL signal from K-feldspar: Radiation Measurements, v. 44, p. 560 – 565, doi: 10.1016/j.radmeas.2009.02.007.

Dawson, T.E., 2013. Appendix A: Updates to the California reference fault parameter database: UCERF3 fault models 3.1 and 3.2: US Geological Survey Open-File Report.

Field, E. H., Arrowsmith, J R., Biasi, G. P., Bird, P., Dawson, T. E., Felzer, K. R., Jackson, D. D., Johnson, K. M., Jordan, T. H., Madden, C., Michael, A. J., Milner, K. R., Page, M. T., Parsons, T., Powers, P. M., Shaw, B. E., Thatcher, W. R., Weldon, R. J., and Zeng, Y., 2014, Uniform California Earthquake Rupture Forecast, Version 3 (UCERF3)—The time-independent model: Bulletin of the Seismological Society of America, v. 104, no.3, p. 1122 – 1180, doi: 10.1785/0120130164.

Galbraith, R.F., Roberts, R.G., Laslett, G.M., Yoshida, H., and Olley, J.M., 1999, Optical dating of single and multiple grains of quartz from Jinmium Rock Shelter, Northern Australia: Part I, Experimental design and statistical models: Archaeometry, v. 41, no. 2, p. 339 – 364, doi: 10.1111/j.1475-4754.1999.tb00987.x.

Gold, P. O., Cowgill, E., Kreylos, O., and Gold, R. D., 2012, A terrestrial lidar-based workflow for determining three-dimensional slip vectors and associated uncertainties: Geosphere, v. 8, no. 2, p. 431 – 442, doi: 10.1130/GES00714.1.

Grant Ludwig, L., Akciz, S. O., Noriega, G. R., Zielke, O., and Arrowsmith, J R., 2010, Climate-modulated channel incision and rupture history of the San Andreas fault in the Carrizo Plain: Science, v. 327, p.1117 – 1119, doi: 10.1126/science.1182837.

Grant, L. B., and Sieh, K., 1994, Paleoseismic evidence of clustered earthquakes on the San Andreas fault in the Carrizo Plain, California: Journal of Geophysical Research, v. 99, no. B4, p. 6819 – 6841.

Huntley, D.J., and Baril, M.R., 1997, The K content of the K-feldspars being measured in optical dating or in thermoluminescence dating: Ancient TL, v. 15, no. 1, p. 11 – 13.

Huntley, D.J., and Lamothe, M., 2001, Ubiquity of anomalous fading in K-feldspars and the measurement and correction for it in optical dating: Canadian Journal of Earth Science, v. 38, p. 1093 – 1106.

Johnson, K., Nissen, E., Saripalli, S., Arrowsmith, J R., McGarey, P., Scharer, K., Williams, P., and Blisniuk, K., 2014, Rapid mapping of ultrafine fault zone topography with structure from motion: Geosphere, v. 10, no. 5, p 969 – 986, doi: 10.1130/GES01017.1.

Klinger, Y., Etchebes, M., Tapponnier, P., and Narteau, C., 2011, Characteristic slip for five great earthquakes along the Fuyun fault in China: Nature Geoscience, v. 4, p. 389 – 392, doi: 10.1038/NGEO1158.

Kreutzer, S., Schmidt, C., Fuchs, M., Dietze, M., Fischer, M., Fuchs, M., 2012, Introducing an R package for luminescence dating analysis: Ancient TL, v. 30, no. 1, p. 1 – 8.

Lawson, M. J., Roder, B. J., Stang, D. M., Rhodes, E., 2012, OSL and IRSL characteristics of quarts and fledspar from Southern California, USA: Radiation Measurements, v. 27, no. 9, p. 830 – 836, doi: 10.1016/j.radmeas.2012.03.025.

Liu, J., Klinger, Y., Sieh, K., and Rubin, C., 2004, Six similar sequential ruptures of the San Andreas fault, Carrizo Plain, California: Geology, v. 32, no. 8, pp. 649 – 652, doi: 10.1130/G20478.1.

Liu-Zeng, J., Klinger, Y., Sieh, K., Rubin, C., and Seitz, G., 2006, Serial ruptures of the San Andreas fault, Carrizo Plain, California, revealed by three-dimensional excavations: Journal of Geophysical Research, v. 111, B02306, doi: 10.1029/2004JB003601.

Madden, C., Haddad, D. E., Salisbury, J. B., Zielke, O., Arrowsmith, J R., Weldon II, R. J., and Colunga, J., 2013, Compilation of Slip-in-the-Last-Event Data and Analysis of Last Event, Repeated Slip, and Average Displacement for Recent and Prehistoric Ruptures, Appendix R *in* Field, E. H., Arrowsmith, J R., Biasi, G. P., Bird, P., Dawson, T. E., Felzer, K. R., Jackson, D. D., Johnson, K. M., Jordan, T. H., Madden, C., Michael, A. J., Milner, K. R., Page, M. T., Parsons, T., Powers, P. M., Shaw, B. E., Thatcher, W. R., Weldon II, R. J., and Zeng, Y., 2013, Uniform California earthquake rupture forecast, version 3 (UCERF3), The time-independent model: U.S. Geological Survey Open-File Report 20131165, 97 p., California Geological Survey Special Report 228, and Southern California Earthquake Center Publication 1792, http://pubs.usgs.gov/of/2013/1165.

McGill, S. F., and Sieh, K. E., 1991, Surficial offsets on the central and eastern Garlock fault associated with prehistoric earthquakes: Journal of Geophysical Research, v. 96, no. B13, p. 21597 – 21621.

Meade, B. J., and Hager, B. H., 2005, Block models of crustal motion in southern California constrained by GPS measurements: Journal of Geophysical Research, v. 110, B03403, doi: 10.1029/2004JB003209.

Noriega, G.R., Arrowsmith, J R., Grant, L. B., Young, J. J., 2006, Stream Channel Offset and Late Holocene Slip Rate of the San Andreas Fault at the Van Matre Ranch Site, Carrizo Plain, California: Bulletin of the Seismological Society of America, v. 96, no. 1, p.33 – 47, doi: 10.1785/0120050094.

Rhodes, E.J., 2015, Dating sediments using potassium feldspar single-grain IRSL: Initial methodological considerations: Quaternary International, v. 362, p. 14 – 22.

Rockwell, T. K., Lindvall, S., Dawson, T., Langridge, R., Lettis, W., and Klinger, Y., 2002, Lateral offsets on surveyed cultural features resulting from the 1999 Izmit and Dizce Earthquakes, Turkey: Bulleting of the Seismological Society of America, v. 92, no. 1, p 79 – 94.

Rockwell, T.K., Dawson, T. E., Young Ben-Horin, J., Seitz, G., 2014, A 21 event, 4,000-year history of surface ruptures in the Anza Seismic Gap, San Jacinto Fault, and implications for long-term earthquake production on a major plate boundary fault: Pure and Applied Geophysics, v. 172, no. 5, p. 1143 – 1165, doi: 10.1007/s00024-014-0955-z.

Salisbury, J. B., Haddad, D. E., Rockwell, T. K., Arrowsmith J R., Madugo, C., Zielke, O., and Scharer, K., 2015, Validation of meter-scale surface faulting offset measurements from high-resolution topographic data: Geosphere, v. 11, no. 6, doi: 10.1130/GES01197.1.

Scharer, K., Salisbury, J. B., Arrowsmith, J R., and Rockwell, T. K., 2014, Southern San Andreas Fault Evaluation Field Activity: Approaches to Measuring Small Geomorphic Offsets—Challenges and Recommendations for Active Fault Studies: Seismological Research Letters, v. 85, no. 1, doi: 10.1785/022013010B.

Scharer, K., Weldon, R., Streig, A., and Fumal, T., 2014, Paleoearthquakes at Frazier Mountain, California delimit extent and frequency of past San Andreas Fault ruptures along 1857 trace: Geophysical Research Letters, v. 41, no. 13, p. 4527 – 4534, doi: 10.1002/2014GL060318.

Schmalzle, G., Dixon, T., Malservisi, R., and Govers, R., 2006, Strain accumulation across the Carrizo segment of the San Andreas Fault, California: Impact of laterally varying crustal properties: Journal of Geophysical Research: Solid Earth, vol. 111, no. B5, https://doi.org/10.1029/2005JB003843.

Schwartz, D. P., and Coppersmith, K., 1984, Fault behavior and characteristic earthquakes: examples from the Wasatch and the San Andreas Fault zones: Journal of Geophysical Research, v. 89, no. B7, p. 5681 – 5698.

Sieh, K.E., 1978, Slip along the San Andreas fault associated with the great 1857 earthquake: Bulletin of the Seismological Society of America, v. 68, no. 5, p.1421 – 1448.

Sieh, K. E., and Jahns, R. H., 1984, Holocene activity of the San Andreas fault at Wallace Creek, California: Geological Society of America Bulletin, v. 95, p. 883 – 896.

Wallace, R.E., 1968, Notes on stream channels offset by the San Andreas fault, southern Coast Ranges, California: in Proceedings of Conference on Geologic Problems of the San Andreas Fault System, Stanford University Publications in Geological Sciences, eds. Dickinson W. R., and Grantz, A., v. 11, pp.6 – 21.

Weldon, R., Scharer, K., Fumal, T., Biasi, G., 2004, Wrightwood and the earthquake cycle: What a long recurrence record tells us about how faults work: GSA Today, v. 14, no. 9, p. 4 – 10, doi: 10.1130/1052-5173(2004)014<4:WATECW>2.0CO;2.

Whipple, K. X, and Tucker, G. E., 1999, Dynamics of the stream-power river incision model: Implications for height limits of mountain ranges, landscape response timescales, and research needs: Journal of Geophysical Research, v. 104, no. B8, p. 17,661 – 17,674.

Zielke, O., Arrowsmith J R., Grant Ludwig, L., Akciz, S. O., 2010, Slip in the 1857 and Earlier Large Earthquakes Along the Carrizo Plain, San Andreas Fault: Science, v. 327, p.1119 – 1122, doi: 10.1126/science.1182781.

Zielke, O., and Arrowsmith, J R., 2012, LaDiCaoz and LiDARimager – MATLAB GUIs for LiDAR data handling and lateral displacement measurement: Geosphere, v. 8, no. 1, p. 206 – 221, doi: 10.1130/GES00686.1.

Zielke, O., Arrowsmith, J R., Grant Ludwig, L., Akciz, S. O., 2012, High-resolution topography-derived offsets along the 1857 Fort Tejon earthquake rupture trace, San Andreas Fault: Bulletin of the Seismological Society of America, v. 102, no. 3, p. 1135 – 1154, doi: 10.1785/0120110230.

Zielke, O., Klinger, Y., and Arrowsmith, J R., 2014, Fault slip and earthquake recurrence along strike-slip faults – Contributions of high-resolution geomorphic data: Tectonophysics, v. 638, p. 43 – 62, doi: 10.1016/j.tecto.2014.11.004.

FIGURE CAPTIONS

Figure 3.1 – A) Inset map of California showing major faults of the San Andreas system with the ~350 km 1857 rupture in blue. Carrizo Plain is shown by gray rectangle. Main image is B4 lidar hillshade with semi-transparent digital elevation model overlay for Van Matre Ranch. Place abbreviations: PKF—Parkfield Reach; BB—The Big Bend reach. The blue arrow highlights the Noriega et al., 2006 excavated channel. B) B4 lidar hillshade showing locations of main excavations and associated drainage basins as well as neighboring basins to the southeast (colored by catchment-average gradient).

Figure 3.2 – Annotated low-altitude (~200 m) balloon aerial photograph showing study area prior to excavation. The catchments are outlined in Figure 3.1B and are also shown in Figure 3.3.

Figure 3.3 – Hillshade of high-resolution (0.03 m per pixel) digital elevation model made from low altitude balloon aerial photographs in Agisoft PhotoScan Pro. Location of SAF (as pinpointed in trenches T9, T5, and T8) shown as red line. Yellow polygons are trench exposures with surveyed channel deposits shown as blue lines coincident with trench outlines. Red arrows indicate geomorphic features previously interpreted as beheaded gullies. Boxed blue ages correspond to average age of nearby channel deposits (parenthetical number indicates number of samples). Unboxed text with red outlines are existing surface slip measurements from Sieh, 1978 (his numbers 46 – 49) and Zielke et al., 2012 (ZA8400a).

Figure 3.4 – Probability density functions for the last four earthquake ages at nearby Bidart Fan (~12 km to the northwest) from Akciz et al., 2010. Magenta line represents the median pIR-IRSL age for T2 beheaded gully channel deposit, bar width represents two-sigma age uncertainty.

Figure 3.5 – Two end-members of D_e distributions: A) for a well-bleached sample with internally consistent dose distribution, a Central Age Model (CAM) is used; B) for a partially-bleached sample with a continuous dose distribution, a Minimum Age Model (MIM) is used. pIR-IRSL results are plotted as a function of precision (increasing radially from the left) and D_e value (increasing counter-clockwise). See Table 1 for a summary of the pIR-IRSL geochronology in this study.

Figure 3.6 – T2 Logs and Photomosaics. The southwest wall has been reflected so that the reflected view of both walls is to the northeast. We use this same explanation of log symbols in all subsequent trench logs. We sample a silt package from within the the well-defined gravel-rich channel (offset ~12 m from the modern active channel feeder) from on the northeast wall, as the channel equivalent on the southwest wall is diffuse and bioturbated. X:Y scale is 1:1.

Figure 3.7 – Summary of slip-rate studies for the past 7,000 years in the Carrizo Plain. The black boxes represent new results presented in this dissertation. The background rate of 33.9 ± 2.9 mm/yr is from Sieh and Jahns, 1984, and closely matches slip rates inferred from geodetic measurements (33 mm/yr, Meade and Hager, 2005; Schmalzle, et al., 2006).

Figure 3.8 –T1 Logs and Photomosaics. The southwest wall has been reflected so that the reflected view of both walls is to the northeast. We found two distinct buried channel deposits (~ 11.5 m apart), neither of which are associated with a modern topographic depression. X:Y scale is 1:1.

Figure 3.9 – A) Map view of T1 and additional hand excavations on 0.03 m hillshade shown with 10 cm contours. Magenta polygons define small alluvial fans that surround the T1 fosse. Yellow stars are piercing points for lateral offset measurement. B) Oblique 3D view of ground photo-based Agisoft PhotoScan Pro model of the T5-6-7 complex. View is almost directly north showing young alluvial fan stratigraphy (magenta, confirmed in T7) faulted and offset from the excavated paleo-feeder (located in T6). The lateral separation of the fan apex from its across-fault equivalent (piercing points shown as yellow stars) is 3.8 m. C) Fault-perpendicular trench log and photomosaic from T5NW showing young alluvial fan deposited directly on older fan material, faulted in 1857, and capped by colluvium.

Figure 3.10 – T4 trench wall orthophotograph and simplified trench log excerpts showing locations and depths of two distinctly different channel deposits. The SW wall has been reflected so that the effective view of both walls is to the NE. The two sample ages from the buried channel are 4.26 ± 0.34 ka and 4.30 ± 0.44 ka. Dashed red outline indicates a similar channel shape on the opposite trench wall cut into indurated fan material. X:Y scale is 1:1.

Figure 3.11 –T1 Logs and Photomosaics. The southwest wall has been reflected so that the reflected view of both walls is to the northeast. Channel deposits are gravel-rich, wide, and prone to collapse. In some areas, we were not able to excavate the full channel margins. X:Y scale is 1:1.

FIGURES

Figure 3.1

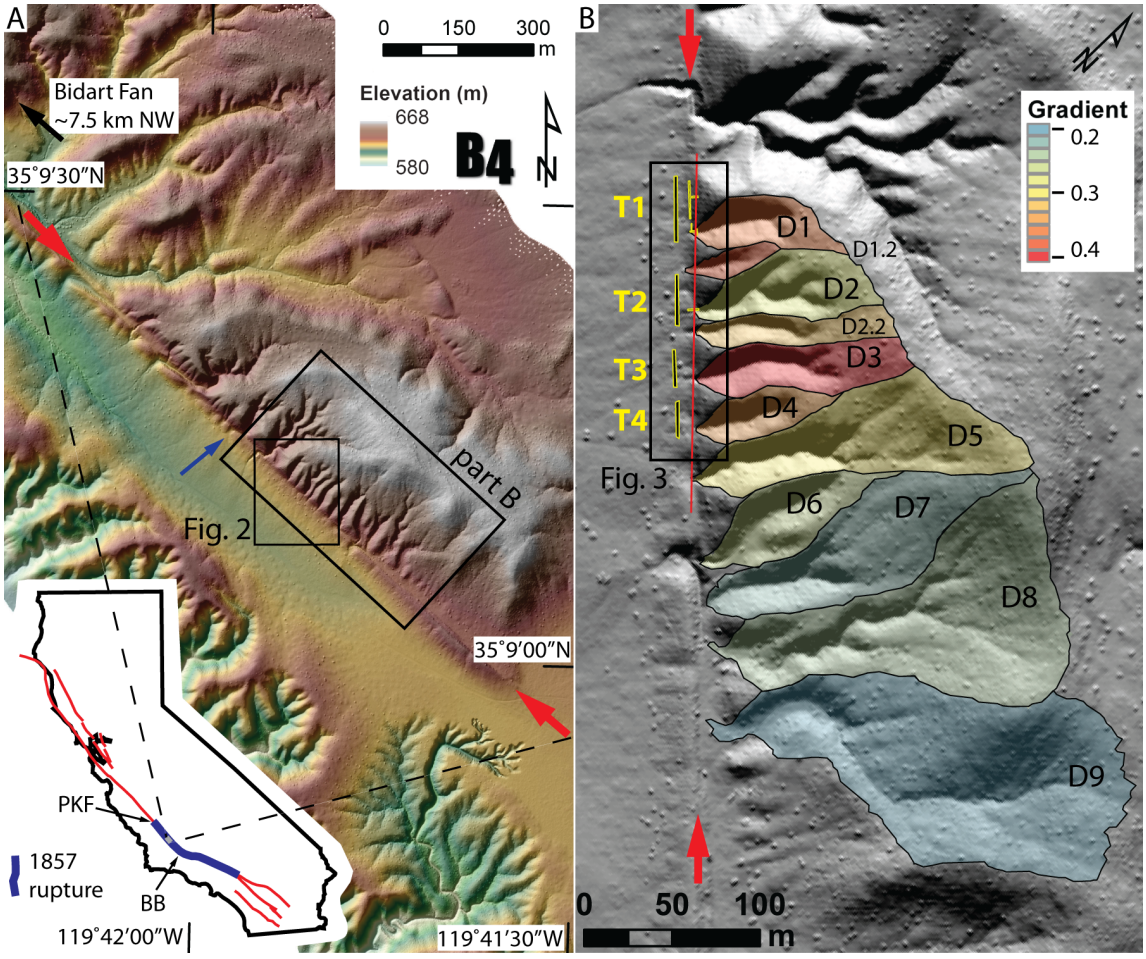

Figure 3.2

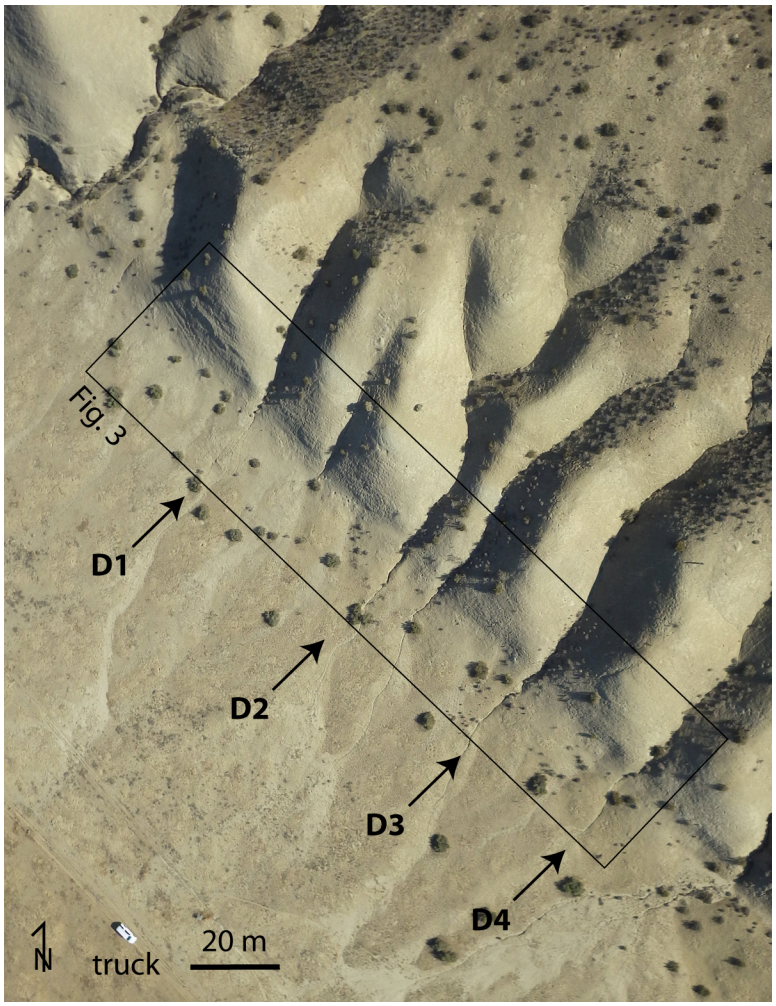

Figure 3.3

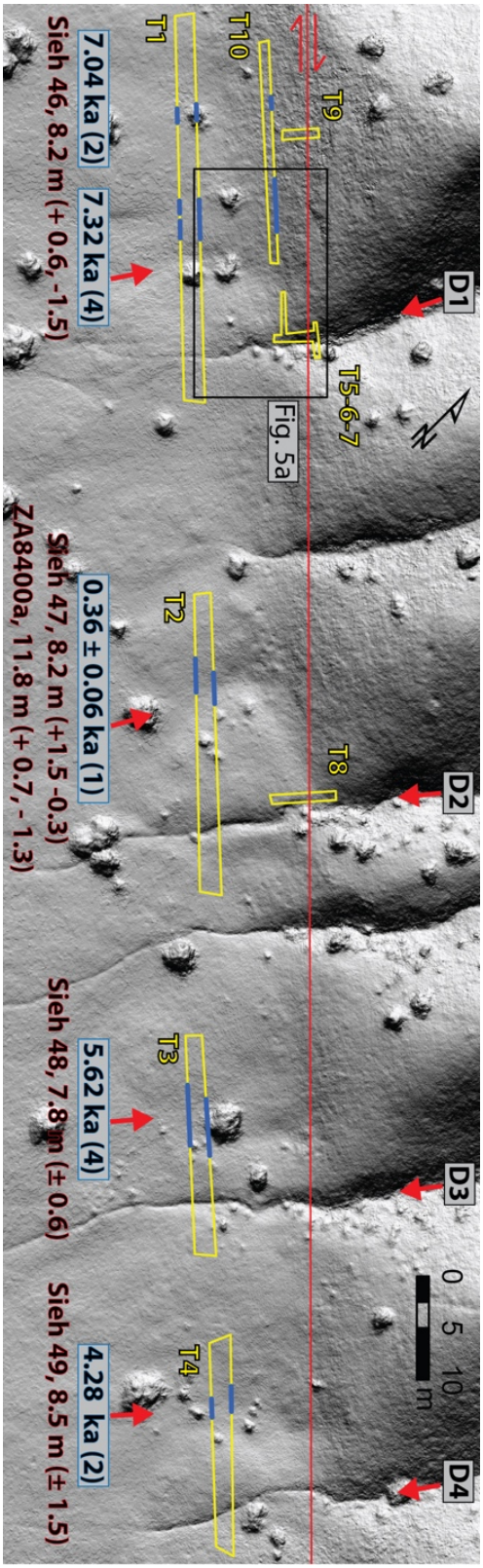
T1
T10
T9
T5-6-7
T8
T2
T3
T4
D1
D2
D3
D4
Fig. 5a
7.04 ka (2)
7.32 ka (4)
Sieh 46, 8.2 m (+ 0.6, -1.5)
0.36 ± 0.06 ka (1)
Sieh 47, 8.2 m (+1.5 -0.3)
ZA8400a, 11.8 m (+ 0.7, - 1.3)
5.62 ka (4)
Sieh 48, 7.8 m (± 0.6)
4.28 ka (2)
Sieh 49, 8.5 m (± 1.5)
0
5
10
m

Figure 3.4

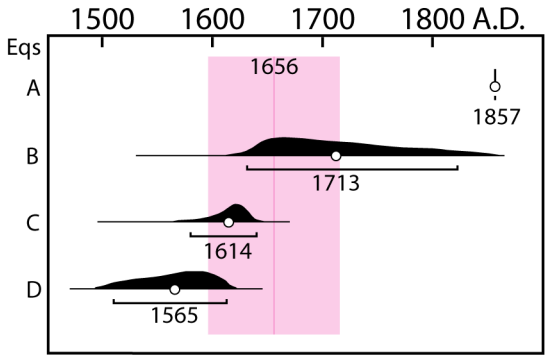

Figure 3.5

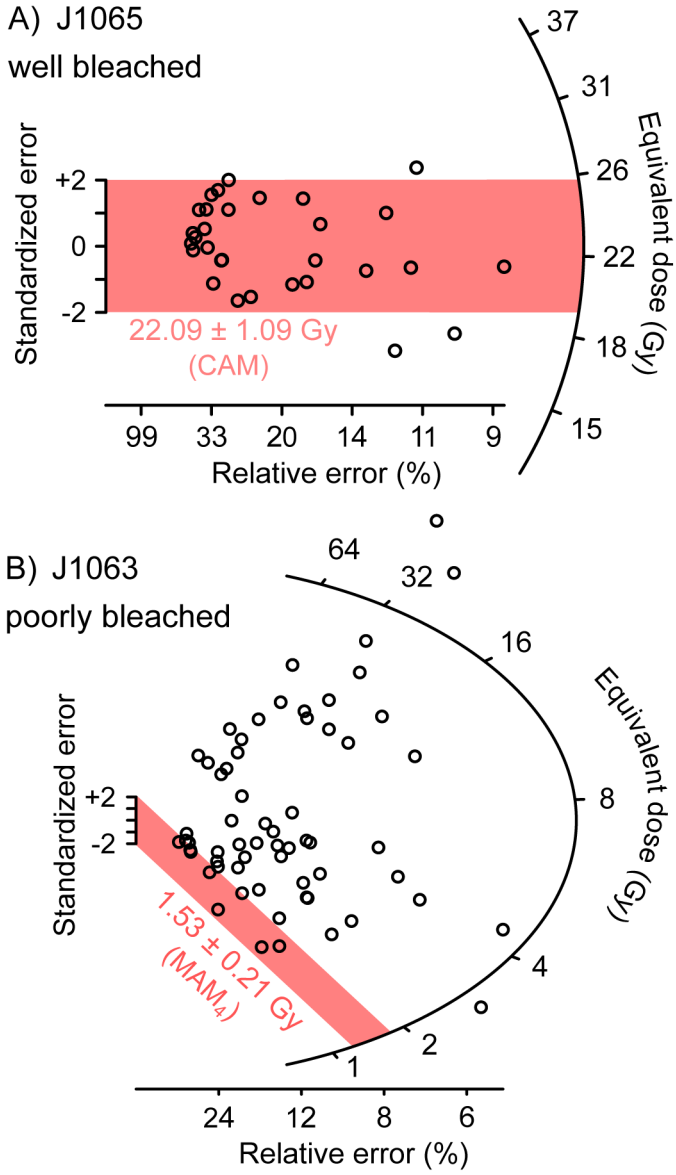
A) J1065
well bleached
Standardized error
+2
0
-2
22.09 ± 1.09 Gy
(CAM)
99
33
20
14
11
9
Relative error (%)
37
31
26
22
18
15
Equivalent dose (Gy)
B) J1063
poorly bleached
Standardized error
+2
-2
1.53 ± 0.21 Gy
(MAM4)
24
12
8
6
Relative error (%)
64
32
16
8
4
2
1
Equivalent dose (Gy)

Figure 3.6

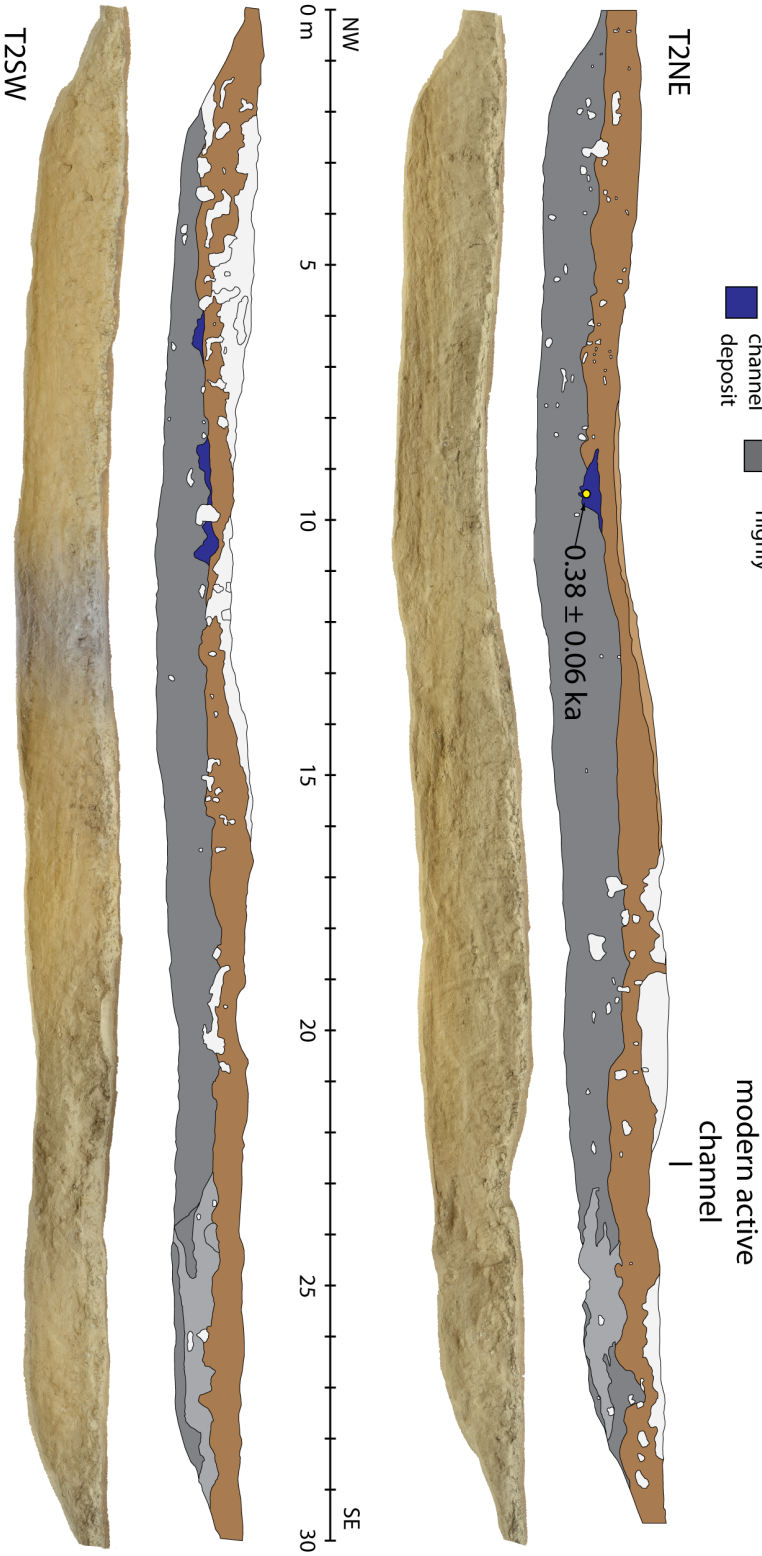
Explanation
burrow/ bioturbated zone
bioturbated young fans
pIR-IRSL sample
lightly indurated fan
channel deposit
highly
T2 Logs and Photomosaics
modern active channel
T2NE
0.38 ± 0.06 ka
T2SW
NW
SE
0 m
5
10
15
20
25
30

Figure 3.7

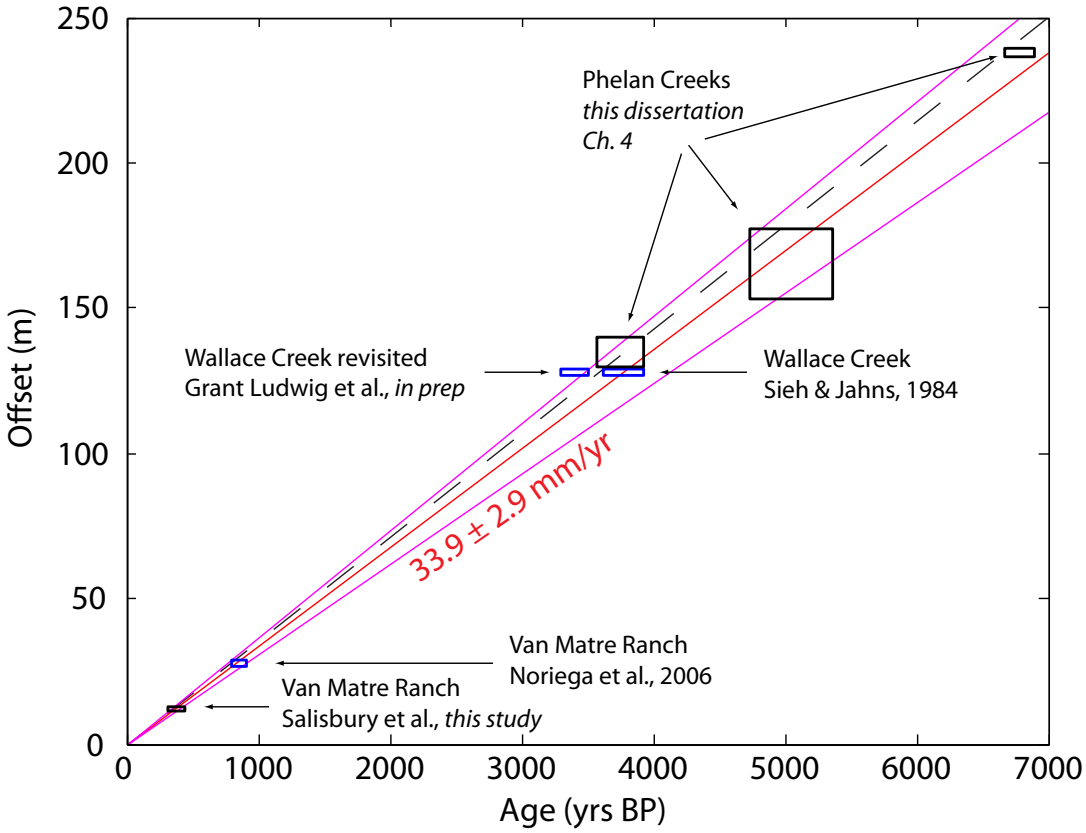
250
200
150
100
50
0
Offset (m)
0
1000
2000
3000
4000
5000
6000
7000
Age (yrs BP)
Phelan Creeks
this dissertation
Ch. 4
Wallace Creek revisited
Grant Ludwig et al., in prep
Wallace Creek
Sieh & Jahns, 1984
33.9 ± 2.9 mm/yr
Van Matre Ranch
Noriega et al., 2006
Van Matre Ranch
Salisbury et al., this study

Figure 3.8

T1 Trench Logs and Photomosaics
modern active channel
T1NE
7.45 ± 0.58 ka
6.62 ± 0.51 ka
7.72 ± 0.63 ka
8.12 ± 0.77 ka
6.33 ± 0.48 ka
7.13 ± 0.54 ka
T1SW
NW
SE
0 m
5
10
15
20
25
30
35

Figure 3.9

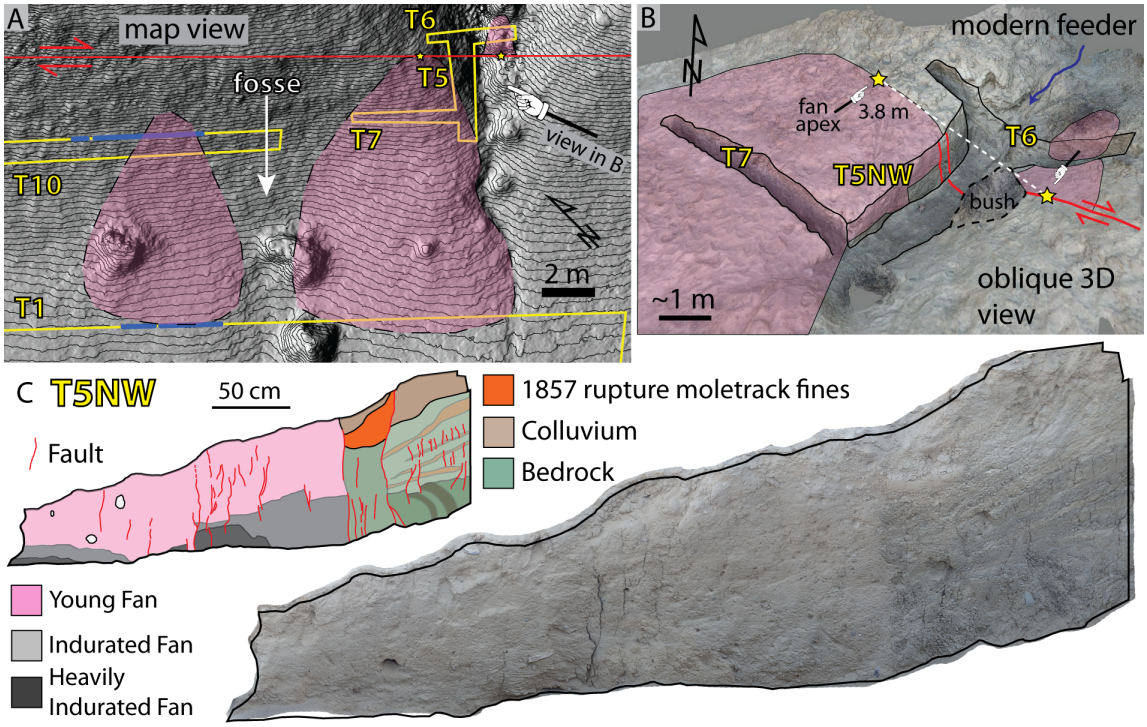
A
map view
T6
T5
fosse
T7
T10
view in B
2 m
T1
B
N
modern feeder
fan apex
3.8 m
T7
T5NW
T6
bush
~1 m
oblique 3D view
C T5NW
50 cm
Fault
1857 rupture moletrack fines
Colluvium
Bedrock
Young Fan
Indurated Fan
Heavily Indurated Fan

Figure 3.10

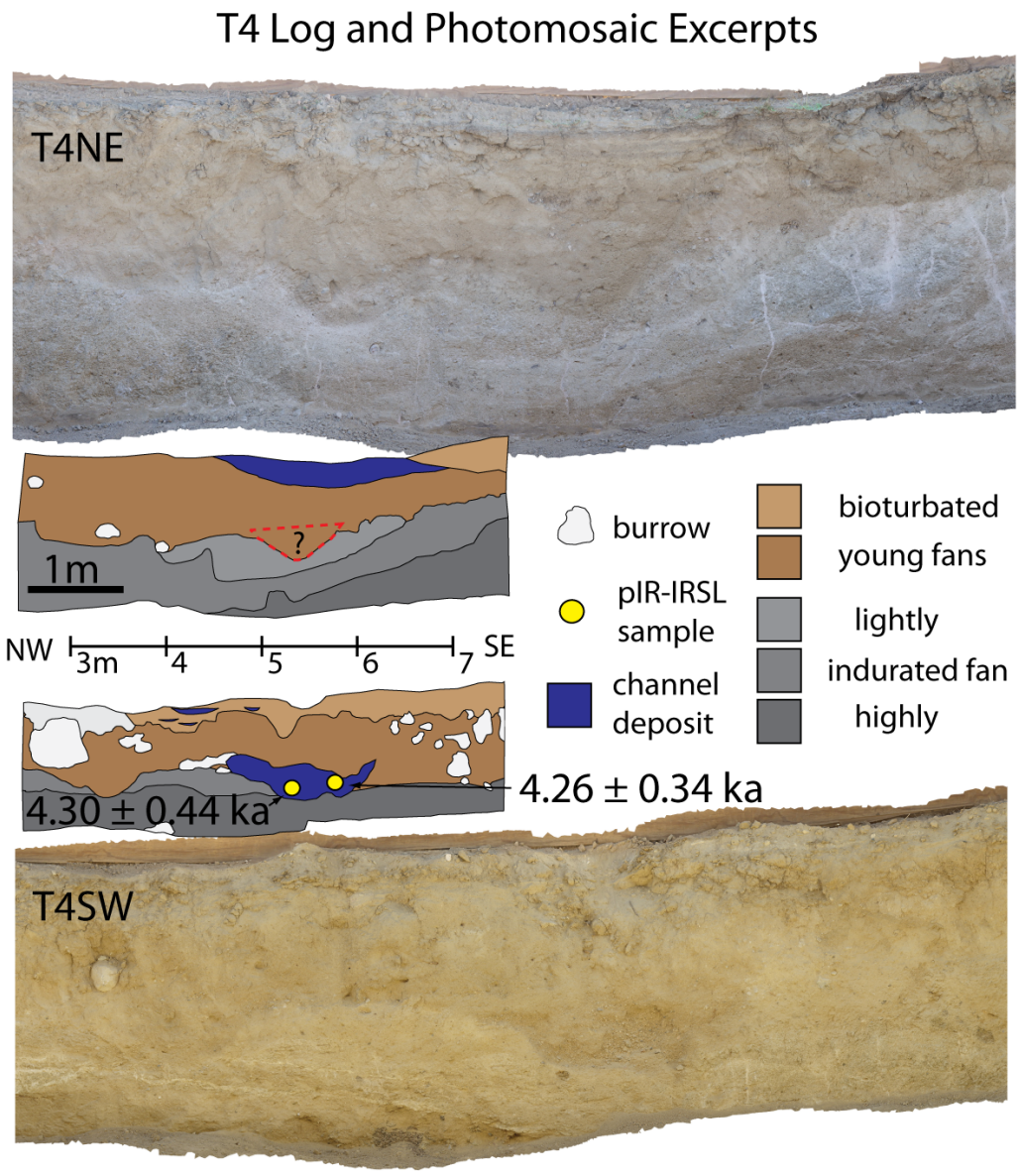
T4 Log and Photomosaic Excerpts
T4NE
1m
?
NW
3m
4
5
6
7
SE
burrow
pIR-IRSL sample
channel deposit
bioturbated
young fans
lightly
indurated fan
highly
4.30 ± 0.44 ka
4.26 ± 0.34 ka
T4SW

Figure 3.11

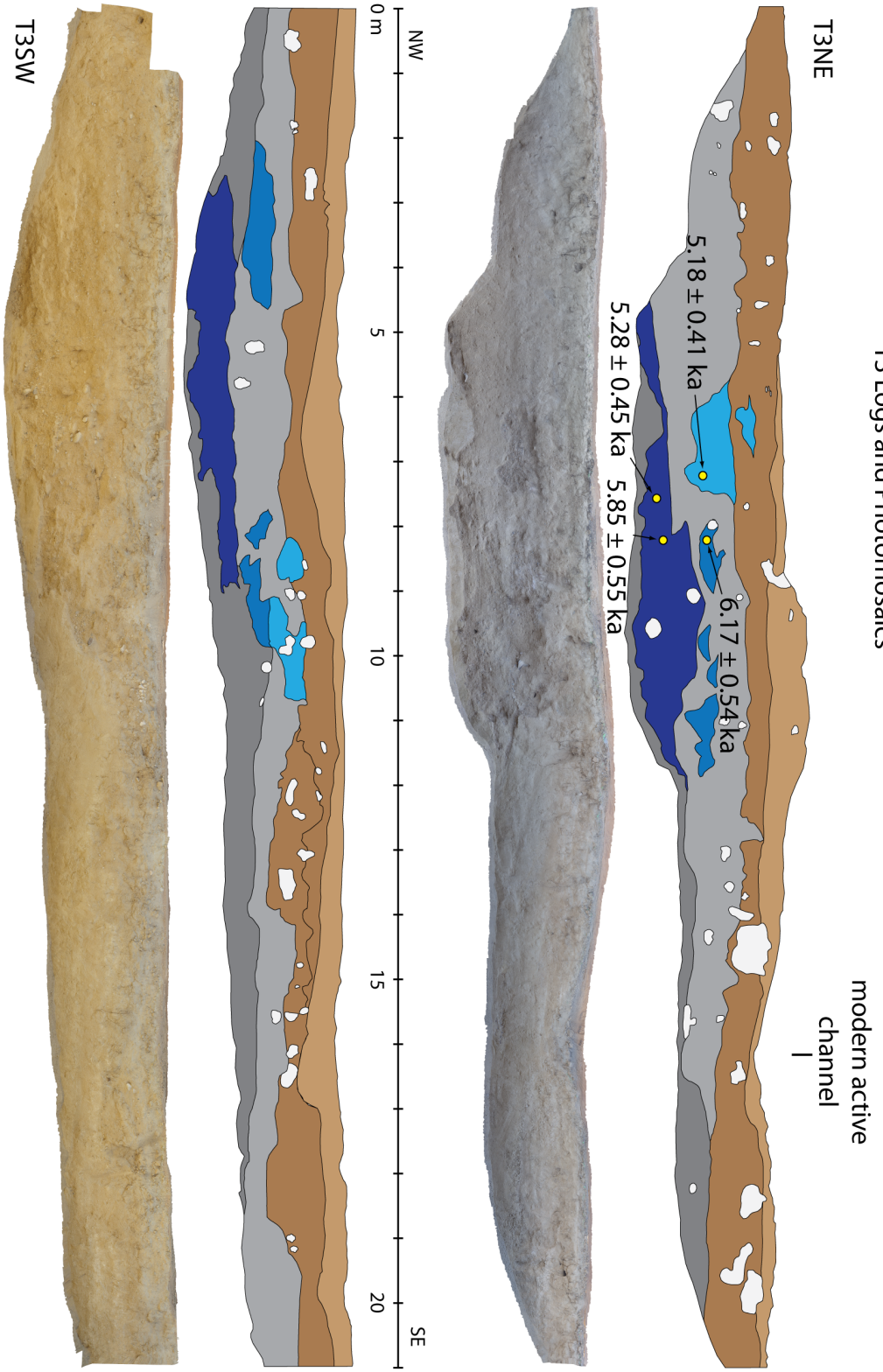
T3 Logs and Photomosaics
T3NE
T3SW
NW
SE
0 m
5
10
15
20
5.18 ± 0.41 ka
5.28 ± 0.45 ka
5.85 ± 0.55 ka
6.17 ± 0.54 ka
modern active channel

CHAPTER 4

REFINING THE SOUTH-CENTRAL SAN ANDREAS FAULT SLIP RATE AT THE MILLENNIAL TIMESCALE USING RECONSTRUCTED OFFSET PALEO-CHANNELS IN THE CARRIZO PLAIN, CALIFORNIA

ABSTRACT

Geologic slip rates of active faults are essential for seismic hazard analysis and their comparison with decadal geodetic measurements can be used to assess the constancy of strain accumulation and earthquake-modulated strain release. Inherent to the proper interpretation of geologic fault slip markers is a thorough understanding of the geomorphic processes responsible for the formation and preservation of such landforms. We investigated these processes at the Phelan Creeks site along the San Andreas Fault (SAF), 1.6 km southeast of Wallace Creek in the Carrizo Plain—a region with simple fault geometry, the highest millennial-scale slip rate in California (>3 cm/yr), a M_w 7.8 surface rupture in 1857, and abundant well-preserved geomorphic slip markers at several length scales. The Phelan Creeks area consists of three downstream channel complexes on the southwest side of the SAF that emanated from a pair of feeder channels ("Little" and "Big" Phelan Creeks) on the northeast side of the SAF. These channel complexes record offsets of ~16.5 m (average of the two modern channel offsets), ~125 m (partially infilled abandoned paleo-channel), and ~238 m (mostly infilled abandoned paleo-channel). We pieced together sedimentologic data from 24 excavations that record a detailed ~7,000-year history of channel processes during progressive offset and eventual abandonment of channel complexes along the semi-arid reach and provide a simplified tectono-stratigraphic model to describe the geomorphic response of stream channels to

continued strike-slip faulting. Additionally, we dated sediments from multiple reconstruction stages throughout the ~238 m of cumulative offset to fill a spatio-temporal gap in age-offset constraints at Wallace Creek and show that there is minimal slip-rate variability along the south-central SAF during the past 7,000 years (13,000 years if we include dates and offsets from Wallace Creek).

INTRODUCTION

The south-central San Andreas Fault (the portion between Parkfield, CA and the Big Bend) has a relatively simple geometry, ruptured historically in the M_w 7.8 Fort Tejon earthquake of 1857, and has the highest slip rate in California (>3 cm/yr over the millennial timescale) (Sieh and Jahns, 1984; Meade and Hager, 2005; Noriega et al., 2006, Schmalzle et al., 2006) (Figure 4.1A). This reach of the SAF has been known for its high-quality examples of well-preserved, right-laterally offset geomorphic landforms since the early 1900's (Lawson et al., 1908; Arnold and Johnson, 1910; Wood and Buwalda, 1931; Hill and Dibblee, 1953; Wallace, 1968; Sieh, 1978). Several significant landforms—at scales of only a few meters to several hundreds of meters of offset—have been investigated in detail (Wallace, 1968; Sieh and Jahns, 1984; Grant and Sieh, 1994; Liu et al., 2004; Liu-Zeng et al., 2006; Noriega et al, 2006; Zielke, et al., 2010, 2012), but despite their high degree of preservation, no sub-surface investigations of channel deposits have been published at Phelan Creeks until now. In this study we focused on a 250 m-long reach (~1.6 km southeast of Wallace Creek) known as Phelan Creeks, where two groups of preserved beheaded stream channels are offset ~238 and ~125 m from the feeder channels named Little and Big Phelan Creeks (Figures 4.1A and 4.1B).

The complex geomorphic history preserved at Phelan Creeks has great potential to provide insights into the tectonic history there as well. Geologic slip rates are an essential input for earthquake rupture forecasts (e.g., UCERF3; Field et al., 2014) and the fast-slipping Carrizo Plain segment of the SAF is a key component in the SAF system. Despite its simple geometry, high slip rate, and potential for great earthquakes, the slip rate in the Carrizo Plain is defined by just a few published studies. In the southern

Carrizo Plain, ~16 km southeast of Phelan Creeks at the Van Matre Ranch (VMR) site, sediments dated at ~856 yr BP in a ~28 m offset channel yield a slip rate of 29.3 – 35.6 mm/yr (Noriega et al., 2006). Only ~1.6 km to the northwest of Phelan Creeks at Wallace Creek there are two well-preserved offset landforms: a channel offset 128 m in ~3,780 yrs (33.9 ± 2.9 mm/yr) and an alluvial fan deposit offset ~475 m in ~13,250 ± 1,650 yrs (35.8 +5.4/-4.1 mm/yr) (Sieh and Jahns, 1984; Figure 4.1A). Simple comparisons of geologic slip rates with the decadal velocity gradients across the SAF (36 +2/-1.5 mm/yr, Schmalzle et al., 2006; 35.9 ± 0.5 mm/yr, Meade and Hager, 2005) suggest the apparent steadiness of earthquake-modulated strain accumulation and release. The older channel complex at Phelan Creeks, offset ~238 m, provides an important opportunity to fill a spatio-temporal gap in age-offset history between the ~128 m and ~475 m offsets at Wallace Creek, providing another much-needed data point to test the constancy of millennial-scale slip in the Carrizo Plain.

In this paper, we present a detailed account of the complex tectono-stratigraphic history of the beheaded channels at Phelan Creeks. Over several field campaigns, we excavated and logged 24 trenches in the upstream, along-fault, and downstream segments of the modern and beheaded channels. This body of work encompasses the major, multi-year undertaking that John D. Sims began in the early 1990's with the United States Geological Survey. Except for a few meeting abstracts, this early work of Sims et al. was compiled for project reports and remains largely unpublished. We conducted the final field campaign in 2010 with additional excavations, refined geochronology, and an overhauled approach to data synthesis and interpretation.

We draw correlations between specific sedimentary packages from not only within the individual beheaded channels, but also within the along-fault and paleo-feeder channel segments where possible to reconstruct eight distinct paleo-configurations of the Phelan Creeks channels during the ~238 m cumulative offset. Where possible, we dated these reconstructed stages with radiocarbon and post-infrared infrared-stimulated luminescence dating (pIR-IRSL). We propose a simplified model of tectonically influenced sedimentation in the upstream, along-fault, and downstream channel segments to explain complicated sedimentary relations. These results allow us to speculate about the constancy of millennial-scale slip rate for the fastest slipping segment of the SAF.

SITE DESCRIPTION

The local bedrock at the Phelan Creeks site is carbonate-rich, heavily indurated Pleistocene alluvial fan (Qf) derived from the Temblor Range to the northeast (range divide is ~ 5.8 km to the northeast). These old fan deposits are generally massive sandy silts and preserve laminated sands and stratified gravel lenses. Uppermost sediments (the top 0.5 – 3 m) are generally bioturbated by rodents, but modern-day A soil horizons form in the uppermost ~15 cm of deposits. We refer to completely bioturbated sediments as diamicton (d). We describe alluvial sedimentary packages in greater detail in subsequent sections.

Big Phelan Creek, the larger, southeastern of the two channels, is ~4 m deep at its intersection with the SAF and has a drainage area of ~2 km^2 (Figure 4.1B). Upstream and downstream channel elements of Big Phelan Creek are at nearly right angles to the SAF. Little Phelan Creek is significantly smaller (only ~1.25 m deep), intersects the fault ~55 m northwest of Big Phelan Creek, and has a drainage area of ~0.4 km^2 (Figure 4.1B). The

upstream channel element intersects the SAF at a nearly right angle, but the downstream channel element flows away at ~30˚ from normal. Between the two channels along the SAF, there is a relatively flat surface underlain by stream terrace and overbank (i.e., low energy "slack") deposits. The downstream segments of these channels converge ~350 m southwest of the SAF and flow into Soda Lake basin (~7 km to the southwest).

Tectonically offset channels of any size have three segments: an upstream, along-fault, and a downstream segment (Figure 4.1B). Channels that intersect strike-slip faults at nearly right angles are most sensitive to recording strike slip offsets, but there are a myriad of channel/fault configurations throughout the Carrizo Plain. The along-fault segment typically crosses the fault at a low (subparallel) angle. The outsides of the bends at the fault are zones of heightened erosion, which serve to lengthen the along-fault segment over time. However, oversteepened channel banks also tend to increase colluviation in the outsides of the bends. The upstream and downstream channel segments commonly exhibit some degree of warping on the outsides of the bends that is dependent on local fault width and complexity.

METHODS

High-Resolution Topography

We used low-altitude balloon aerial photographs (14 megapixel) to generate a high-resolution (10 cm) digital elevation model (DEM) of the Phelan Creeks site in Agisoft PhotoScan Pro during our last field campaign in 2013 (see review by Johnson, et al., 2014) (Figure 4.1B). We took photographs from ~30 m, ~100 m, and ~290 m elevations with at least 40% overlap. We georeferenced our new dataset using the B4 lidar data (Bevis, et al., 2005).

Excavations

Over the course of several field seasons (largely completed in the mid 1990s by J.D. Sims and his USGS colleagues), we employed a backhoe to excavate a total of 24 trenches that ranged from 2 – 4 m deep and 10 – 70 m long (Figure 4.1B). We focused mainly on the downstream (fault-parallel trenches) and along-fault (fault-perpendicular trenches) channel elements of the various topographic depressions, but we also dug trenches in the upstream channel elements of Little and Big Phelan creeks to document the location and nature of sediments in paleo-channels upstream of the SAF. We logged trench exposures at a range of scales (1:10 to 1:25) with a variety of logging approaches, including on blank grid paper (earlier trenches) as well as on high-resolution orthophotographs generated in Agisoft Photoscan Pro (2013 study; see Bemis, et al., 2015). We surveyed the trench locations, channel features (thalwegs and margins), faults, radiocarbon, and luminescence (pIR-IRSL) sample locations with a total station. We named paleo-channel deposits by the trenches in which they were most complete, best expressed, and most representative of related deposits.

Excavations on the southwest side of the SAF were focused on two main channel complexes—a ~238 m offset pair (paleo-channels M and K), and a ~125 m offset channel (paleo-channel H) (Figure 4.1B). Excavations on the northeast side of the SAF were focused on paleo-locations of Little and Big Phelan Creeks (paleo-channels O and LS, respectively) (Figure 4.1B). We also dug trenches to the southeast of Phelan Creeks to exclude the possibility that either of the Phelan Creeks flowed to the southeast along the SAF (Figure 4.1B).

Geochronology

We used detrital charcoal for radiocarbon analysis and K-feldspar single-grain post-infrared infrared-stimulated luminescence (p-IR IRSL) analyses for age control of channel deposits and underlying bedrock material. We found abundant charcoal unevenly distributed throughout our exposed deposits. Charcoal fragments ranged from a few cubic millimeters to a cubic centimeter and were most abundant in fine-grained, low energy alluvial deposits identified in the excavations. We successfully dated 19 of 410 total charcoal samples (Table 4.1). The bulk of our samples were either too small for a radiocarbon determination, were contaminated by modern radiocarbon, or were deemed inferior compared to other samples from within the same unit. Our earliest samples (16 of 368) were analyzed by Accelerator Mass Spectrometry Laboratory at the University of Arizona, Tucson. The remainder of our samples (3 of 42) were analyzed at the W. M. Keck Carbon Cycle Accelerator Mass Spectrometry Laboratory at the University of California, Irvine. We gave priority to large, angular, or intricately shaped samples as we inferred these characteristics to indicate that they have not been transported significant distance or persisted in the landscape for extended periods of time. Regardless, we treat our age estimates as maximum ages for the deposits. Where samples were taken from the same stratigraphic column, most of our results are in stratigraphic order, though we do see some stratigraphic reversals.

Our pIR-IRSL analyses were conducted at the Department of Earth, Planetary, and Space Sciences department at the University of California, Los Angeles. We used fading-corrected, single-grain K-feldspar crystals and a post-infrared infrared-stimulated luminescence (p-IR IRSL) protocol to measure the equivalent dose distributions of

samples. Additionally, we used a portable NaI gamma spectrometer to measure the *in situ* gamma dose-rate. We estimated the beta dose-rates by measuring the U and Th contents with inductively-coupled plasma mass spectrometry (ICP-MS) and the K content with inductively-coupled optical emission spectrometry (ICP-OES). We derived the alpha dose-rates using an assumed internal potassium content of 12.5 ± 0.12 wt. % (Huntley and Baril, 1997) and measured the water content by oven-drying a portion of sediment from each sample tube. Table 4.2 summarizes our pIR-IRSL results.

RESULTS

Excavations exposed complex sequences of gravel-rich cut-and-fill fluvial stratigraphy interfingered with poorly sorted colluvial deposits sourced from local channel margins. Fault zone trenches exposed evidence of the 1857 rupture all the way to the surface, typically characterized by 2 to 25 cm-thick gouge zones and zones of distributed shear up to 2 m wide. In many instances, the top few meters of our exposures were heavily bioturbated and contained few traces of stratigraphy. Where there is little or no bioturbation, modern-day A soil horizons form in the uppermost ~15 cm. Where channels were deposited directly on highly indurated, carbonate-rich Pleistocene alluvial fan units, we interpreted the contacts to represent timing of initial incision and subsequent fill.

We identified the trends of modern channel thalwegs (i.e., the lines connecting the deepest parts of the channel margin downstream) by first assessing the total amount of recent colluvial degradation of over-steepened channel banks. Small-scale colluvial deposits add meter-scale sinuosity to the channels that is not representative of the overall channel trend. We projected these piercing lines (i.e., the linear trends of the true channel thalwegs) into the fault trace and measured the horizontal, along-fault separation between the two identified piercing points. The thalwegs of the modern-day Little and Big Phelan Creeks are offset and 16 ± 1 m and 17.5 ± 2 m, respectively (Figure 4.1B). Excavations in the intermediate, alluvium-filled younger abandoned paleo-channel (in Trench B, see Figure 4.1B for location) revealed a single channel thalweg buried beneath modern topography in the downstream channel segment. This single thalweg is offset 102 ± 2 m from Little Phelan Creek and 152 ± 2 m from Big Phelan Creek. For simplicity, we

averaged these two measurements and refer to the intermediate abandoned paleo-channel as the ~125 m offset channel (Figure 4.1B). Trenches in the ~125 m offset channel exposed four distinct phases of alluviation (Hc-1 through Hc-4). The oldest pair of abandoned paleo-channels (K and M) are offset 238 ± 2 m from the equivalent modern-day channel thalwegs (Figure 4.1B). Trenches in the ~238 m offset pair (and along-fault segment to the southeast) exposed three distinct phases of alluviation that are capped by two phases of mixed alluvial and colluvial deposits (Mc-1 through Mc-5). Age estimates for the oldest channel materials indicate the excavations at Phelan Creeks exposed a rich history of ~7,000 years of faulting, geomorphic response, and sedimentation. For a symbolic representation of paleo-channel elements preserved in each of our excavations, refer to Figure 4.1C. For an explanation of symbols used in trench logs, refer to Figure 4.2.

Channel Elements Southwest of SAF

~238 m Offset Paleo-Channel Pair. We excavated a total of 11 trenches in the ~238 m offset channel pair (fault-perpendicular trenches L, M, I, B-north; fault-parallel trenches K, J, 2, 3, A, and 1) (Figure 4.1C & Figures 4.3 – 4.12). The two paleo-channels in the ~238 m offset pair were named after trenches with the best channel deposits, Trenches K and M. However, paleo-channel K deposits are small and poorly preserved, so in our stratigraphic summaries we refer to the paleo-channel deposits in trenches K, L, and 2 as equivalents of paleo-channel M. Trenches A and 1 exposed sediments of the combined paleo-channels K and M. The following section includes descriptions of trenches by channel element in the ~238 m offset pair.

Paleo-Channel K sediments, exposed in trenches L, K, and 2, are the oldest channel sediments in this study (Figures 4.1C, 4.3, 4.7, and 4.9). Trenches K and 2 were fault-parallel and each exposed a complex set of poorly stratified, cross-cutting lensoidal (as few as 7 and as many as a dozen) gravel packages representing channel deposits unconformably deposited on local bedrock (Figures 4.7 and 4.9). We found no signs of bedding, laminations, or pebble imbrication in these gravel lenses. Similarly, we found few interfingering colluvial aprons. We did not subdivide the deposits within paleo-channel K because we lacked sufficient stratigraphic indicators to do so. Trench L was fault-perpendicular and crossed the SAF just southeast of the remnant topographic depression of paleo-channel K (Figure 4.2). We did not find any channel gravel lenses in trench L suggesting that there are no along-fault deposits associated with paleo-channel K.

Paleo-Channel M sediments, exposed in trenches M, J, and 3 (Figures 4.3, 4.8, and 4.10), are named after trench M—a fault-perpendicular trench that crossed the SAF. The stratigraphic units Mc-1 through Mc-5 were exposed at the southwest end of the trench, ~8 m from the active trace of the SAF (Figure 4.4).

Mc-1, the basal unit, was unconformably deposited on local bedrock at elevation 674.4 m. The unit is a <1 m thick medium-grained gravel that fines upwards to a pebbly sand. Mc-2 is 50 – 60 cm thick and is composed of medium-grained matrix-supported gravels and fines upwards to sandy fine-grained pebbles. Mc-3 is 25 – 35 cm thick and is composed of sand matrix-supported gravels that fine upwards to sandy pebbles. Mc-4 is dark greenish gray sandy silt and Mc-5 is a similar dark greenish gray sandy silt with few pebbles. There are two sandy channels at the base of Mc-5 and the uppermost ~15 cm is

the modern soil A horizon. We sampled several sedimentary packages for radiocarbon and OSL ages in trench 3.

Trench J was fault-parallel and intersected trench M a few meters southwest of the SAF in the southeastern channel of the ~238 m offset paleo-channel pair (Figure 4.8). We exposed three gravel units across the width of the trench with imbrication characteristics suggesting deposition occurred nearly parallel to the length of the trench.

Trenches I and B-north exposed the along-fault segment of paleochannel M (Figures 4.5 and 4.6). Trench I clearly exposed five paleo-channel fill units, the lower three units fluvial and the uppermost two units mainly colluvial, similar to the five deposits exposed in trench M. The same correlative units were also exposed in trenches N and B, though they are partially faulted in trench B.

Combined Paleo-Channel KM. Trenches A and 1 (Figures 4.11 and 4.12) were below the confluence of paleo-channels K and M, ~58 m and ~77 m southwest of the SAF, respectively (Figure 4.1B). Trenches exposed a single paleo-channel incised into the older, indurated fan material ~3.5 m northwest of the modern-day topographic depression. Channel deposits are capped by 1.5 m of heavily bioturbated colluvium. Channel units are predominately coarse, sandy gravels with sandy silt lenses up to ~8 cm thick. In trench 1, we found several sandy silt lenses suitable for OSL sampling (Figure 4.12). Stratigraphy indicates up to three individual fill events, some of which are potentially correlative to the Mc channels.

~125 m Offset Paleo-Channel

We exposed paleo-channel H in trenches B, H, C, D, F-91, E, E-91, and O (Figure 4.1B, 4.6, and 4.13 – 4.19). All trench exposures of paleo-channel H were in along-fault deposits except trench B that exposed the downstream segment of the paleo-channel. We separated paleo-channel H fill into four sub-units, Hc-1 through Hc-4 (Figure 4.13).

Hc-1 was unconformably deposited on local bedrock and is ~1.25 m thick. This unit is composed of clast-supported coarse, sandy gravels with laminated silts and fine sands up to a few cm thick. The unit is capped by silty colluvium.

Hc-2 was unconformably deposited on Hc-1 and is composed of several sub-units with cut and fill structures whose contacts are defined by sandy silt laminations. The basal subunit, Hc-2L, is a coarse-grained gravel that fines upwards to sandy pebble deposits that are interfingered with laminated medium-grained sands. The upper subunit, Hc-2U, is matrix-supported, laminated, medium-grained gravel that fines upwards to a medium-grained sand with silty matrix. The entire subunit is capped by a massive medium-grained sand.

Hc-3 eroded a trough into Hc-2, and is composed of massive, matrix-supported medium-grained gravels. The subunit is capped by a sandy colluvial deposit.

Hc-4 is composed of a medium- to fine-grained sand matrix-supported pebble unit. The subunit is also capped by a sandy colluvial deposit.

Channel Elements Northeast of SAF

We investigated two paleo-channel segments northeast of the SAF near the modern-day Big and Little Phelan Creeks.

Paleo-Channel LS

We exposed paleo-channel LS in a refreshed cut into the northwest bank of Big Phelan Creek (Figure 4.20). We exposed a complex sequence of cross-cutting coarse gravel and laminated sands, as well as overbank deposits characterized by thin, laterally extensive sandy laminations, fine gravels, and some capping silts. We subdivided the deposits found here into five main stratigraphic packages named LSc-1 through LSc-5 (Figure 4.20). We made a strong correlation between Ls deposits and the deposits of Trench S, a fault-perpendicular trench between Little and Big Phelan Creeks (Figure 4.21).

LSc-1 is the basal unit of the LS sequence, was deposited directly on old alluvial fan material at elevation 675 m, is ~60 cm thick and is composed of several cross-cutting subunits of medium to coarse gravel with discontinuous laminated sands. The top of LSc-1 was eroded (precluding a width measurement for the top of the deposit) by LSc-2, and the erosional unconformity is at an elevation of 675.6 m. The southwestern edge of the channel deposit was eroded by the modern-day Big Phelan Creek channel.

LSc-2 is ~125 cm thick and is composed of medium- to fine-grained gravel and indistinctly laminated sand lenses. A dark gray, silty sand colluvial subunit containing abundant disseminated pedogenic carbonate material, angular ~1 mm charcoal fragments, and 1 to 3 mm diameter carbonate nodules caps the unit. The contact between LSc-2 and the overlying LSc-3 is gradational and is at elevation 676.9 m.

LSc-3 is ~130 cm thick and is composed of three sub-units, each with a fine-grained, partly-laminated gravels deposit that fines upwards to a well-laminated sand cap. Gravel imbrication indicates a southwest transport direction nearly perpendicular to the SAF. The uppermost member of LSc-3 is truncated by modern-day Big Phelan Creek.

LSc-4 is ~100 cm thick and is composed of a pebbly colluvial basal member that grades upwards into poorly bedded fluvial gravel and laminated sands. Imbrication of gravels indicate materials were transported to the southwest away from Big Phelan Creek.

LSc-5 is also ~100 cm thick and is composed of two indistinctly bedded sub-units: a lower medium-gray, sandy colluvial deposit and an upper fine-grained gravel with silt and sand. The modern-day soil caps LSc-5, the top of which is at elevation 680.0 m. The units of the LS section are traceable as far as 9 m upstream Big Phelan Creek before they are covered by substantial colluvial deposits, each with little upstream variability.

Paleo-Channel O

We exposed paleo-channel O in a fault-perpendicular trench a few meters northwest of the northwest bank of Little Phelan Creek (Figure 4.19). We subdivided paleo-channel O, deposited on eroded bedrock surface, into four unconformity-bound units named Oc-1 through Oc-5. These units record four distinct episodes of channel filling. The bottom of Oc-1 was not fully exposed but we estimated its elevation by projecting the slope of exposed channel margins downwards. We also exposed similar sequences of sediments in trenches R, Q, and F (Figures 4.22 – 4.24).

Oc-1 is 1.2 – 1.5 m thick and is composed of alternating fine- to medium-grained gravels with laminated sand and silt packages. The upper third of the unit has abundant cut and fill structures whereas the bottom two thirds are a mostly continuous sedimentary package. The unit flares upwards to a width of ~4 m.

Oc-2 is ~75 cm thick and is composed primarily of fine- to medium-grained gravels with poorly-laminated sand deposits. The lower half of the unit contains abundant cut and fill structures and the unit is capped by a bed of dark gray silty sand that contains faint silt laminations interfingered with pedogenic carbonate-rich colluvial deposits. The capping deposit on Oc-2 is ~5 m wide.

Oc-3 is only ~55 cm thick and is composed of two main sub-units. Each sub-unit is a fining upward sequence of medium-grained (and some coarse) sandy gravels that grade into dark gray sandy silts with no laminations. The upper part of the unit is ~5 m wide.

Oc-4 is 50 – 60 cm thick and is composed of pebbles that fine upward into poorly laminated sands with abundant detrital charcoal. The unit is capped by a 4 m-wide non-laminated silt layer with tabular sand deposits suggesting low-energy deposition in a broad, shallow channel. The present-day soil is forming in the topmost ~15 cm of Oc-4.

Additional Trenches

We excavated a fault-perpendicular trench G southeast of Little and Big Phelan Creeks to investigate the possibility that Big (and Little) Phelan Creeks may at one point have flowed southeast along the SAF (Figure 4.25). We exposed a complex, 10 m-wide zone of faulting that preserved evidence of the 1857 rupture up to the surface with only a thin sandy colluvial cover. Stratigraphic units within the fault zone are sub-horizontally

bedded and consist of laminated gravels, pebbles, sands, and silts deposited on older bioturbated colluvial units (i.e., re-worked bedrock material). The strata outside the fault zone are similar in composition but were deposited on local bedrock. All deposits lack distinct cut-and-fill structures or other sedimentary features that would suggest stream channel deposition. We conclude that there is no evidence of along-fault flow from Little and Big Phelan Creeks to the southeast.

We added an additional trench, T, ~150 m upstream from the SAF between the channels of Little and Big Phelan Creek (Figure 4.26). There is a 2.5 m-high ridge that separates the two channels, where the channels are ~40 m apart and there is a subtle saddle in the separating ridge. Here we investigated the possibility that the saddle represents the location of a prior connection between Little and Big Phelan Creeks. Trench T exposed local bedrock overlain by a thin veneer of sub-horizontal, parallel-bedded silty pebble to gravel terrace deposits. We found no evidence of prior channel connection at this location.

Unit Correlations

We based of our stratigraphic correlations on a number of criteria, the most important of which is the ability to directly trace units from one trench to another where possible (Figure 4.1B and 4.1C). Where this was not possible, we used detailed stratigraphic facies similarities to correlate units. These criteria included deposit compositions, the relative stratigraphic positions of packages, sequences of cross-cutting relationships, absolute elevations of upper and lower contacts, unit thicknesses, and radiocarbon and pIR-IRSL age estimates of materials within channel or colluvial

deposits. For a summary of stratigraphic units in all trenches and the correlations we draw between them see Figure 4.1C.

~238 m Offset Paleo-Channel Pair

For the ~238 m offset paleo-channel pair we traced paleo-channel M deposits where they were described (in Trench M) into intersecting trench J (Figure 4.1B). We identified a similar sequence of at least 3 fluvial units in Trenches 3, A, and in the west wall of Trench 1 (Figures 4.10 – 4.12), but the facies similarities were less clear in Trenches A and 1 as these trenches are below the confluence of paleo-channels K and M (Figures 4.1B and 4.1C, 4.4, and 4.7). We identified these same units along-fault to the southeast through Trenches I and the northernmost part of Trench B (Figures 4.1B and 4.5 – 4.6). Paleo-channel M sediments are faulted and disappear in the southeast wall of Trench B (Figure 4.6). Paleo-channel K sediments have ambiguous facies characteristics that precluded us from differentiating between individual subunits. Our fault-perpendicular Trench L (that intersected paleo-channel K) did not contain similar gravel-rich sediments so we have no evidence that there was along-fault flow of paleo-channel K (Figures 4.3 and 4.7). At Trench 2 (Figure 4.9) we saw similar ambiguous gravel deposits lacking any clearly discernable cut-and-fill structures but at Trenches A and 1 the sediments more closely resembled paleo-channel M deposits. We think that this is reasonable given that there are no along-fault channel sediments between paleo-channels K and M and the drainage are of Big Phelan Creeks is substantially larger than Little Phelan Creeks.

~125 m Offset Paleo-Channel

For the ~125 m offset paleo-channel we identified the four major stratigraphic packages (Hc-1 through Hc-4) described in Trench H in intersecting Trenches B and C (Figure 4.1B). We also identified the same packages in upstream trenches D, F-91, E, and E-91 (Figures 4.15 – 4.18).

Northeast of the SAF

We drew correlations between paleo-channel O deposits and trenches R and Q to the southeast (Figure 4.1B, 4.19, and 4.22 – 4.23). Based on the relationships of paleo-channel O units in Trench F, and the paleo-channel LS units in trench S, we correlated all the channel deposits on the northeast of the fault with those southeast of the fault (Figure 4.1C).

Unit Chronology

We calibrated our radiocarbon ages using OxCal v4.2.4 (Bronk Ramsey, 2013) and the r:5 IntCal3 atmospheric curve (Reimer et al., 2013). Age control (including pIR-IRSL ages) for stratigraphic packages is summarized in Figure 4.27. We provide a list calibrated radiocarbon ages in Table 4.1, pIR-IRSL ages in Table 4.2.

~238 m Offset Paleo-Channel Pair

The oldest unit that we dated is the Pleistocene bedrock into which the ~238 m offset channel pair and the ~125 m offset channel were cut. We have a single pIR-IRSL age estimate of 22,130 ± 144 yrs BP (OSL.12) in Trench 2 and a ^{14}C age estimate of 12,373 ± 357 yrs CAL BP (D-7) in Trench D (Figures 4.9 and 4.15). These radiocarbon and pIR-IRSL ages for the underlying fan materials are similar to the 13,250 ± 1,650 yr

BP and 19,340 ± 1000 yr BP ages for the local bedrock at Wallace Creek (Sieh and Jahns, 1984).

The oldest age estimate we have for a paleo-channel deposit is an indirect, bracketed age between the bedrock and a colluvial wedge that caps the oldest gravel deposits in Trench K, the northwest channel of the ~238 m offset pair (Figure 4.7). The colluvial deposit was dated at 6,748 ± 255 yrs BP. We correlated these gravel deposits in Trench K with unit Mc-1, the oldest gravel deposits in the neighboring channel (M) to the southeast (Figure 4.1B). Mc-1, therefore, was deposited between 12,373 ± 357 yrs CAL BP and 6,748 ± 255 yrs BP (Figure 4.27).

We dated unit Mc-2 with three pIR-IRSL ages (OSL.03 and OSL.04 from Trench 1, OSL.05 from Trench 3) and two radiocarbon samples (3-3 and 3-22 from Trench 3) (Figures Figures 4.10 and 4.12). The oldest age for Mc-2 is 5,050 ± 310 yrs BP (OSL.03) and the youngest is 4,400 ± 280 yrs CAL BP (Figure 4.27).

We have the most samples in Mc-3: five pIR-IRSL ages (OSL.01, 02, 06 – 08) in trenches 1 and 3, and two radiocarbon samples (3-2 and B-10) from trenches B and 3 (Figures 4.10, 4.12, and 4.6). The oldest age for Mc-3 is 5,050 ± 310 yrs BP (OSL 08) and 3,382 ± 462 yrs CAL BP (B-10) (Figure 4.27).

We do not have a good age estimate for Unit Mc-4. Instead, we bracketed the age of Mc-4 between the youngest age of Mc-3 (3,382 ± 462 yrs CAL BP) and the overlying unit, Mc-5. The age estimate of Mc-5 is from Sample I-12 in Unit Mc-4 is dated at 3,749 ± 178 yr CAL BP (Figure 4.27).

~125 m Offset Paleo-Channel

We have more abundant radiocarbon age estimates from detrital charcoal deposited in paleo-channel H. We have no pIR-IRSL ages from these younger units. The age of unit Hc-1 is narrowly constrained by samples D-17 and D-21 (from the same colluvial unit interfingered with deposits of Unit Hc-1) at 2,485 ± 137 yr CAL BP and 2,430 ± 116 yr CAL BP, respectively (Figures 4.15 and 4.27). Charcoal from channel LSc-1 (sample LSc-4, Figure 4.20), that we interpreted to be correlative to the lowermost unit in paleo-channel H, corroborate the age of this unit at 2,236 ± 501 yr CAL BP.

We have five dated charcoal samples from Hc-2 deposits in several trenches, D, Q, F, B, and S (samples D-18, Q-5, F-19, B-65, and LS-7) that range in age from 1,611 ± 549 yr CAL BP to 845 ± 339 yr CAL BP (Figures 4.6, 4.15, 4.21, 4.23, 4.24, and 24.7).

Two of the three radiocarbon dates from unit Hc-3 fall within a narrow range. Samples Q-2 and E-7 are 734 ± 66 yr CAL BP and 730 ± 70 yr CAL BP, respectively. D-38 is significantly older at 1520 ± 221 yr CAL BP. We attributed the anomalously older age to detrital age inheritance (Figures 4.15, 4.17, 4.23, and 4.27).

We have two radiocarbon samples from the youngest unit, Hc-4 (samples O-1 and B-49). Unit O-1 is dated at 655 ± 70 yr CAL BP and B-49 is significantly older at 1,313 ± 765 yr CAL BP. Given the stratigraphic constraints for the younger unit Hc-3, we attributed the older age of sample B-49 to detrital age inheritance and use 655 ± 70 yr CAL BP as the age of Hc-4.

DISCUSSION

Chronology

In general, the pIR-IRSL and radiocarbon age estimates are remarkably consistent where we have both from within the same unit (Mc-2 and Mc-3). This is impressive because most our radiocarbon samples were analyzed in the early 1990's. In the older units, Mc-2 and Mc-3, there is some age overlap between the stratigraphic sequences (Figure 4.27), however, the chronostratigraphic succession can still be assembled given the wide age uncertainties of the pIR-IRSL ages.

The radiocarbon age estimate for unit Mc-5 (I-12) is slightly older than expected. This sample was from the very bottom of unit Mc-5, directly above an active fault trace that terminates upwards within the unit. If unit Mc-5 were exposed at the surface and aggrading at the time of faulting, it is not unreasonable for the older sample to have been moved up section and incorporated into unit Mc-5. Alternatively, the sample may have been reworked from an older deposit elsewhere and re-deposited in unit Mc-5 with inherited age.

Units Hc-1 through Hc-4 also show a remarkable stratigraphic succession. In units Hc-3 and Hc-4, samples D-38 and B-49 do fall out of the sequence (with older ages), but given the consistency of other samples in Hc-3 (samples Q-2 and E-7 from different trenches) we attribute these older ages to age inheritance, which is common in sparsely vegetated, semi-arid landscapes.

Tectono-Stratigraphic Model for Laterally Offset Streams

We see similar packages of sedimentary deposits in both abandoned paleo-channels—coarse- to medium-grained gravels that fine upwards through a series of cut-and-fill sequences to pebbly sands, all of which are capped by wider, reworked pebble and sand colluvial materials (e.g., the succession of units Mc-1 through Mc-5; Hc-1 through Hc-4). Toward the upper parts of these stratigraphic sections, we see bioturbation playing a more significant role in mixing sediments and obliterating any bedding traces. We propose a process-response model that links tectonically-induced sedimentation episodes to ongoing strike-slip faulting. This model provides an evolutionary understanding of offset channels in semi-arid landscapes. We start with the simpler case of an idealized, single offset channel before applying the model to our paired set of channel feeders at Phelan Creeks.

An important consideration is the role of effectively diffusive surface processes occurring between the intermittent, geomorphically significant rainfall delivery. In the Carrizo Plain, there is extensive bioturbation of the uppermost few meters of soil by kangaroo rats, foxes, insects, and other burrowing animals (see also Arrowsmith, et al., 1998). Between floods, colluvial debris fill the freshly cut channels where banks have been oversteepened and we commonly see distinct, repeating patterns of interfingering colluvial and fluvial deposits. As channel activity subsides, we see the formation of more prominent, poorly sorted colluvial caps perforated by active burrows. We interpret these colluvial deposits to represent a significant decrease in fluvial activity. Where the colluvial deposits are devoid of sandy, lensoidal fluvial deposits, we interpret them to

represent significant periods of non-fluvial activity in the ephemeral channels (i.e., abandonment).

At the Phelan Creeks site, the strike of the of the SAF is normal to the slope of the Pleistocene alluvial fan surface into which the channels are incised (Figure 4.1B). Little and Big Phelan creeks, therefore, are prime for sensitivity to tectonic offset. We mark this as our initial idealized condition—a stream follows the regional slope of the landscape and crosses the strike-slip fault at a nearly perpendicular angle. The channel in eroded into bedrock material (after repeated fluvial events), and the system is in a state of equilibrium. During this early stage, deposits within and outside the channel are rare or absent (Figure 4.28A). For a stream channel that is initially in such a state of hydrologic equilibrium, the primary result of lateral offset, therefore, is to instantaneously create an along-fault channel segment that (in the simplest case) is perpendicular to the rest of the channel (Figure 4.28B). At a local scale (i.e., between two fixed reference points up- and downstream from the fault) this instantaneous addition of a channel segment lengthens the longitudinal channel profile, thereby decreasing the local channel slope.

The ratio of the offset magnitude to the channel cross-section width is an important consideration. If the offset is significantly smaller than the width of the channel, then channel processes may destroy evidence of the slip event. At the other end of the spectrum, if the offset is significantly larger than the width of the channel, then the upstream channel element may be dammed completely and the downstream channel element may be beheaded completely. Particularly around the upstream segment of Little Phelan Creeks feeder, we see evidence of upstream overbank deposits that likely indicate

some earthquakes had substantial slip—enough to fully or partially dam the upstream channel segment.

After a strike-slip earthquake offset, there are geomorphic responses that leave morpoholgical and sedimentological records. We divide these responses into three scenarios based on the relative magnitude of lateral offset versus local channel width: a complete damming event, a partial damming event, and no damming whatsoever. In the first scenario, a complete damming event, the lateral offset is sufficiently larger than the channel width and there is complete damming in the upstream segment (e.g., Wallace, 1968). If this occurs, the downstream channel element will be completely abandoned and there is no formation of an along-fault channel segment. After re-incision through the alluviated upstream segment, a new downstream channel segment will be incised as the newly incised upstream reach overtops the young shutter ridge.

In the second scenario, a partial damming event, the lateral offset only partially dams the upstream segment and may induce ponding behind the fresh shutter ridge (e.g., Wallace, 1968). These sediments are not necessarily preserved in the upstream reach of the channel, however, because renewed flow may erode the initial ponded sediments upstream of the fault. Following a partial damming, there will be flow in the newly-formed along-fault channel segment. We discovered significant evidence (e.g., low-energy, over-bank flood deposits northeast of the SAF) that suggests there have been several partial-damming events. For example, there are finely laminated over-bank sand deposits within the gravel-rich fluvial deposits of unit Ls-2, and unit Ls-3 is capped by a distinctly laminated fine-grained sand cap. The third scenario, the lateral offset is so small that there is no upstream ponding or alluviation. These types of scenarios may not

leave any significant morphological or sedimentological records. During the early stages of cumulative channel offset (when there is little accrued slip in the channel form), it is more likely that the third scenario will occur. The stream, offset less than its width, will be able to continue flowing and re-attain equilibrium hydrologic conditions (i.e., not aggrading or incising) without leaving any sedimentary evidence.

After flow obliterates any full or partial dam, the lengthened along-fault channel segment has a decreased slope that may induce sedimentation in the along-fault segment (Figure 4.28C). This is strongly influenced by the strength of storms that follow tectonic offset and the duration of the interseismic period. Furthermore, the new bends in the originally straight channel cause a sedimentary response. The outside bends of the channel become zones of heightened erosion, typically causing over-steepening of the channel banks. On the inside of the bends there may be moderate point-bar formation. Oversteepened channel banks will likely experience colluviation in all channel segments, and if there are fresh fluvial deposits, will form aprons that cover the alluvial materials (Figure 4.28D). We see interfingering alluvial and colluvial deposits in many of our trenches consistent with this process (e.g., Trench 1, Figure 4.12).

Additional faulting increases the along-fault channel segment until a critical length threshold is reached. This threshold is dependent on the size and frequency of storms that occur during the interseismic period. If the stream channel is unable to accommodate the modest decrease in slope between significant earthquake events (i.e., fault-induced sedimentation and colluvial deposition in the along-fault reach causes significant slope reduction) then the downstream segment will be abandoned as the existing upstream channel overtops the channel bank at the intersection with the fault

(Figure 4.28E). When this happens, the along-fault and downstream channel element become abandoned. We denote this critical along-fault channel length as the length to abandonment.

This simple model may explain how the sequence of stratigraphic units are formed in relation to continued strike-slip faulting along the SAF. We believe that the Phelan Creeks site has the capability to preserve these types of sediments that fit reasonably well into our model. However, our interpretation at Phelan Creeks must account for existing beheaded downstream channel elements that may be faulted in front of active feeders (Figure 4.28E). These existing topographic depressions may complicate the story, causing piracy of drainage basins, potentially even causing deflection of along-fault stream segments opposite the true sense of slip. This depends on the relative sizes of existing drainage basins and beheaded topographic depressions. We have checked for this possibility of deflected, southeast flow at trench G and we do not see evidence for significant channel flow to the southeast.

Stages of Offset at Phelan Creeks

We apply our tectono-stratigraphic model at Phelan Creeks using the excavated and dated channel deposits in the upstream, along-fault, and downstream channel elements throughout the entire suite of beheaded and offset stream channels. We divide the Holocene history of Phelan Creeks into three main cycles that denote the major evolving downstream elements, starting with the oldest channel configuration and progressing toward modern-day configuration. Cycle 1 (containing two stages) is the initiation of and eventual abandonment of paleo-channels K and M, Cycle 2 (containing four stages) is the initiation of and eventual abandonment of paleo-channel H, and Cycle

3 (containing three stages, including the modern configuration) is the initiation of and offset of the modern-day Little and Big Phelan Creeks. Figure 4.29 shows a simplified topographic contour map with trench locations of the present-day site configuration. Figures 4.30 – 4.37 show each of the 8 stages of offset, with the sequence starting at the oldest stage (Stage 1) with ~238 m of total back-slip from the modern-day configuration. The progression gets younger, and successive stages bring the model closer to present-day configuration. The following subdivisions are based on our ability to correlate full units or channel features (e.g., channel margins, distinct cut-and-fill sequences) not only from trench to trench, but also across the SAF to reconstruct a best estimate of channel geometries at each specific time. Our reconstructions become more ambiguous in the later stages of reconstruction (towards the modern day). This is counterintuitive, but the complexity of channel deposits and topographic forms increases towards the modern configuration making our interpretations more ambiguous. In contrast, we interpret the initial channel configuration (when the ~238 m channels were incised) with very little ambiguity.

Cycle 1

Stage I. For Stage 1 we interpret that paleo-channels K and M did in fact originate in their current configuration as the downstream elements of Little and Big Phelan Creeks. For these paleo-channels, there are no preserved (discernable) deposits to the northeast of the SAF. Instead of correlating distinguishable sedimentary deposits, we use the eroded bedrock "v's" exposed in trenches R and LS that we interpret as paleo-thawlegs. We match those with the channel thalwegs exposed in paleo-channels K and J (Figures 4.4 and 4.8). We think this interpretation is reasonable given the similarity in

channel widths across the SAF, the relative sizes of Little and Big Phelan Creeks, and the similarity of deposits preserved in paleo-channels K and M to that of the younger sediments we see at the surface and exposed in small pits within the upstream elements of the modern channels.

We estimate the total amount of back-slip required for this restoration at 238 ± 2 m by projecting the paleo-thalwegs through trenches 2 to K and 3 to J to the fault plane and re-aligning with Little and Big Phelan Creeks (Figure 4.1B). This is our highest-confidence, least ambiguous reconstruction. With this amount of backslip, bedrock embankments exposed in trenches K and M (in addition to paleo-thalwegs) align with bedrock paleo-embankments exposed in trenches Q and LS. We compare the relative elevations of bedrock thalwegs used for offset reconstruction and our surveying shows that for 238 m of total offset, there is only 2 m of total down-to-the-southwest vertical offset, a small portion of which is attributable to the natural channel slope.

There are few fluvial deposits in paleo-channel K at this earliest stage of offset because it was sourced from Little Phelan Creeks. However, we interpret these first gravel deposits in paleo-channel K to have been deposited at the same time as the first (lowest) gravel deposits in paleo-channel M. Collectively, these early deposits represent the initial incision of paleo-channels K and M and the first preserved evidence of deposit Mc-1. We date the colluvial apron above Mc-1 gravels in paleo-channel K with radiocarbon sample K-12 at 6,780 ± 110 yr CAL BP. This colluvial deposit is therefore younger than deposit Mc-1. We do not have an upper age limit for these early channel deposit other than that they must be younger than the Pleistocene alluvial fan dated at 12,373 ± 357 yr CAL BP.

We hypothesize that paleo-channel K was probably no wider than the modern-day Little Phelan Creek channel (~4 m wide). Slip estimates for large events in the Carrizo Plain are generally at least this large (Zielke et al., 2010), suggesting that Little Phelan Creek was partially or potentially even fully dammed after the initial offset and may have caused upstream ponding or deflection to the southeast along-fault into paleo-channel M. However, we do not find evidence of preserved overbank ponding in the upstream segment from that time, nor do we see strong evidence of along-fault flow to the southeast in trench L.

Stage 2. Our next identifiable reconstruction stage requires ~195 m ± 10 m of total back-slip from the modern-day configuration. At this point, the downstream element of the original paleo-channel M has captured Little Phelan Creek and the upper section of Mc-1 is deposited (Figure 4.31). The colluvial apron within Mc-1 in trench J confirms the depositional hiatus of Mc-1 between Stages 1 and 2 (recognized by colluvial wedges between Mc-1 and deposition of Mc-2). Also, we know that the remainder of Mc-1 is deposited in this configuration because we can correlate the upper units of Mc-1 with deposits in Trenches I and B-north, confirming that Big Phelan Creeks flowed northwest into paleo-channel M (Figure 4.31). We also hypothesize that deposition of Mc-2 took place before the end of this stage. The width and thickness of unit Mc-2 in trench J (~ 1 m thick, ~ 12 m wide) suggests that it was deposited before flow into paleo-channel M diminished (when Big Phelan Creek cut a new channel). Additionally, we see evidence of significant incision into unit Mc-1 by unit Mc-2 (Trench I northwest, Figure 4.5) partially re-exposing bedrock before deposition. Age constraints from unit Mc-2 suggest that it

was deposited between 5,330 ± 370 yr BP (OSL.03) and 4,400 ± 280 yr CAL BP (OSL.05).

By this point, paleo-channel K was abandoned, having only accumulated a few fluvial gravel deposits. We also see no major gravel deposits in trench L that would represent along-fault flow into trench K. Gravel deposits in paleo-channel K are sparse and the majority of channel fill material is slope-derived colluvium. (Figure 4.7). For a channel this size (Little Phelan Creek, catchment of 0.4 km^2), the offset to abandonment is ~40 m.

Cycle 2

Stage 3. We recognize the beginning of this stage after ~165 m ± 12 m of total back-slip from the modern-day configuration. This is our second-best reconstruction. Several major changes occur at Stage 3, the most notable of which is the initiation of the downstream channel element straight across the SAF from Big Phelan Creek in the depression that will eventually be known as paleo-channel H (Figure 4.32). This is the first unit that we correlate across the fault; the oldest units in paleo-channel H (designated Hc-1) we correlate with the oldest deposits in exposure LS in the northwest bank of Big Phelan Creeks. For now, we refer to these deposits southwest of the SAF as Hc-1/LS-1 as they are relatively minor in extent. In addition to these new deposits, we see evidence for this change in channel configuration in the along-fault and downstream segments of paleo-channel M as flow from Big Phelan Creek is pirated away from flowing along-fault into paleo-channel M (a marked reduction in flow capacity) and into paleo-channel H instead (initiation of a new channel).

Stage 3 marks the last predominately fluvial paleo-channel M deposits, unit Mc-3, in trenches B, I, M, J, 3, A, and 1. We have six pIR-IRSL age estimates and one radiocarbon age from Mc-3. The age of Mc-3 ranges from 5050 ± 310 yr BP (OSL.08) to 3382 ± 462 yr CAL BP (B-10). We prefer the oldest age of Mc-3 to represent this 165 m reconstruction because the bottom of the unit has the coarse-grained gravel deposits (suggesting high stream capacity) that we associate with the along-fault connectivity of Big Phelan Creek and paleo-channel M. The uppermost part of Mc-3 fines upwards into a colluvial deposit. After the complete deposition of Mc-3, there are no major fluvial deposits in the along-fault segment that connects Big Phelan Creek with paleo-channel M, and the first of two capping deposits of paleo-channel M (Mc-4) is also predominately colluvial. This colluvial deposition suggests a significant change in processes occurring in the along-fault channel segment. The thickness of Mc-4 at and near the SAF suggest that a large portion of colluvial material is scarp-derived with some channel bank-derived sediment. The fluvial deposits in Mc-4 are small, and are more likely sourced from Little Phelan Creeks. We have no direct age control for unit Mc-4.

Stage 4. This stage designation is marked by the complete disconnection of paleo-channel M from Big Phelan Creek. The only input for paleo-channel M is what flowed from Little Phelan Creek down the lengthening along-fault segment. Additionally, the along-fault segment of paleo-channel LS fed by Big Phelan Creek lengthens to ~30 m (Figure 4.33). This configuration requires ~135 m ± 5 m of total back-slip from the modern-day configuration. This is our third-best reconstruction.

The uppermost colluvial unit (Mc-5) found in trenches M and 3 is a thick colluvial cap. In trench M there is a single gravel channel cut into and buried by

colluvium (Figure 4.4). The deposition of these fluvial gravels in Trench M is the last fluvial deposit from Little Phelan Creek before complete abandonment of paleo-channel M. We know that this happens before paleo-channel LS/H captures Little Phelan Creek because deposition of the gravel channel in Mc-5 precludes that Little Phelan Creek had been captured and flowed to the southeast. Radiocarbon sample I-12 from within unit Mc-5 is dated at 3,749 ± 178 yr CAL BP. During or soon after cessation of unit Mc-5 deposition there is continued deposition of uppermost Unit Hc-1 that we correlate with unit LSc-1 on the northeast side of the SAF. We have two samples from trench D, D-21 and D-17 that are from within a colluvial apron that is interfingered with the basal gravel units of Hc-1. These samples are 2,485 ± 137 yr CAL BP and 2,430 ± 116 yr CAL BP, respectively. These ages are significantly younger than the age taken from the bottom of Mc-5. We think that this is reasonable given that the colluvial apron represents a period of non-fluvial deposition and that there was a hiatus during the deposition of Hc-1. Therefore, we use the date of unit Mc-5 (from Sample I-12) as we are confident that this was the last indicator of connectivity between Little Phelan Creek and paleo-channel M but before Little Phelan Creek had been captured by paleo-channel H.

Stage 5. This stage is marked by the capture of Little Phelan Creek by downstream element LS (while still being fed by Big Phelan Creek) and the deposition of the upper half of Hc-1 (the sedimentary package above the previously mentioned colluvuial apron in Hc-1 containing samples D-21 and D-17) (Figure 4.34). At this point we change the name of the downstream element from paleo-channel LS to paleo-channel H, as the downstream element is now sourced by both Little and Big Phelan Creeks. This stage also marks the complete abandonment of paleo-channel M and requires ~95 ± 40 m

of total back-slip from the modern-day configuration. The controls we use for reconstruction of this stage are the LSc-2 channel margins (correlates to lower Hc-2) eroded into the heavily indurated colluvial deposits in trenches D, E, O, and R on the southwest side of the fault. (Figures 4.17, 4.19, and 4.22). However, these correlations do not provide any unique across-fault piercing points.

We bracket Stage 5 between the deposition of the upper half of unit Hc-1 (after D-21 and D-17; 2,485 ± 137 yr CAL BP and 2,430 ± 116 yr CAL BP, respectively) and before the deposition of Hc-2 deposits. We have five radiocarbon ages for the Hc-2 deposit (samples LS-7, B-65, F-19, Q-5, and D-18). The oldest sample of Hc-2 is LS-7, dated at 1,611 ± 549 yr CAL BP.

Stage 6. Stage 6 is characterized by continued lengthening of the along-fault segment of paleo-channel H, fed by both Little and Big Phelan Creeks (Figure 4.35). This reconstruction requires ~55 m ± 30 m of total back-slip from the modern-day configuration. Again, we lack distinctive piercing points for the total cumulative offset. The along-fault portion of paleo-channel H is a single, broad, aggrading channel on and slightly west of the SAF and extends nearly ~115 m northwest from Big Phelan Creek. The complete deposition of Hc-2 and the initiation of Hc-3 mark this intermediate stage of development of paleo-channel H. The oldest radiocarbon date from Hc-2 is D-18 (845 ± 339 yr CAL BP) and the youngest (stratigraphic) age from Hc-3 is E-7 (730 ± 70 yr CAL BP).

Cycle 3

Stage 7. We reconstruct this stage with ~35 – 20 m of total back-slip based on the distribution of Hc-3 (Figure 4.36). This is the last stage during which major fluvial deposits sourced from Little Phelan Creeks are found in the along-fault segment of paleo-channel H. We see a distinct change in paleo-channel H deposits from purely fluvial gravels, sands, and silts (Hc-2) to smaller, more confined gravel channels that are interfingered with widespread colluvial aprons from channel banks and thicker scarp-derived colluvial wedges (Hc-3). As with paleo-channel M, we interpret this change from primarily fluvial to colluvially-dominated deposits to represent disconnection between the downstream channel element and Big Phelan Creek, the significanty larger of the two drainage basins. Two radiocarbon samples from Hc-3 (Q-2 and E-7) are dated at 734 ± 66 yr CAL BP and 730 ± 70 yr CAL BP, respectively. The younger fluvial deposit, Hc-4, is a small gravel channel only ~1 m wide and is found within a predominately colluvial unit. After deposition of Hc-4, we interpret paleo-channel H as being totally abandoned. There are two sample from Hc-4 (samples O-1 and B-49) at 589 ± 30 yr CAL BP and 1064 ± 72 yr CAL BP, respectively. We interpret the anomalously old age of B-49 as a result of detrital age inheritance. The abandonment of paleo-channel H therefore occurs at some point after deposition of O-1 (585 ± 70 yr CAL BP). We hypothesize that at the same time as or shortly after this point the modern Little and Big Phelan Creeks began incising.

Stage 8. This is our final reconstruction, requiring ~20 m of total back-slip from the modern-day configuration (Figure 4.37). We have very few constraints for this reconstruction, but the lack of overbank deposits caused by partial or full damming of the

Phelan Creeks suggests that by this time the modern-day channels have begun to incise. This stage post-dates 589 ± 30 yr CAL BP.

Stage Modern. The final stage in the evolution of the Phelan Creeks is the modern-day configuration, where Little Phelan creek is offset 15.8 ± 0.6 m and Big Phelan Creek is offset 17.4 ± 1.6 m (Figure 4.29).

Millennial Slip Rates

Though we identify 8 individual paleo channel configurations, only three stages (Stages 1, 3, and 4) have piercing points that provide unambiguous matching of features across the fault for slip rate calculation. Stage 1 is the initial configuration of Little and Big Phelan creeks, and requires 238 m ± 1.5 m of backslip. We have a radiocarbon date from within a colluvial apron deposit just up-section of the gravels (Mc-1) deposited during this initial stage at 6,780 ± 110 yr CAL BP. The bracketing age for Mc-1 gravels is the substantially older Pleistocene alluvial fan with a minimum age of 12,373 ± 357 yr CAL BP. We know that the colluvial apron above Mc-1 must have been deposited at 238 m of offset or less, suggesting that the slip rate based on the older Mc-1 gravels at ~238 m of offset must be less than 35.1 ± 0.6 mm/yr. Stage 3 is the configuration of the paleo-channels after 165 m ± 12 m of backslip. We are confident in this amount of backslip as we have evidence for the alignment of paleo-channel LS/H with Big Phelan Creek concurrent with the deposition of unit Hc-3. The oldest age of Mc-3 is 5050 ± 310 yr BP (OSL.08) and provides a slip rate of 32.7 + 2.1/-1.9 mm/yr. Stage 4 is the configuration after 135 m ± 5 m of backslip. The deposition of unit Mc-5 represents the last connectivity of paleo-channel M with Little Phelan Creek. The radiocarbon sample I-12

from within unit Mc-5 is dated at 3,749 ± 178 yr CAL BP, providing a slip rate of 36 +1.8/-1.6 mm/yr.

We summarize slip rates in Figure 4.38 and 4.39. These slip rate estimates are consistent with geologic and geodetic slip rates for the Carrizo Plain segment of the San Andreas Fault (3.4 – 3.6 cm/yr, Sieh and Jahns, 1984; 3.6 cm/yr, Meade and Hager, 2005; 3.6 cm/yr, Schmalzle et al, 2006; 3.1 cm/yr, Noriega et al., 2006). Understanding how centennial-scale earthquake recurrence accommodates strain through multiple, millennial-scale earthquake sequences is essential for seismic hazard characterization. Comparison of short- and long-term slip rates is a key to assessing the constancy of earthquake-modulated strain release and may ultimately help reconcile discrepancies between competing models of earthquake recurrence (e.g., characteristic slip vs variable slip, etc). This work shows that for the the Holocene, the slip rate of the SAF has been relatively constant (Figure 4.38 and 4.39).

We have shown that episodes of strike-slip faulting increase the along-fault channel length, thereby reducing local channel slope and potentially inducing sedimentation shortly after an earthquake. In an ideal case, the earthquake offset history could be represented by a sequence of stacked channel fills in the along-fault channel segment. Interpretation of these sediment sequences (coupled with high-resolution geochronology) could therefore shed light on the timing of earthquake offset episodes. We explore this possibility at Phelan Creeks—this was a major motivator for Sims' early work—but given our uncertainty regarding past climate episodes (e.g., decades of wet vs. dry conditions and days-long geomorphically significant storms events), slip and moment

release (e.g., Chapter 3), and external factors (e.g., fire, land use change, drainage capture) we cannot prove that any one deposit is earthquake-induced.

CONCLUSION

The Phelan Creeks site is a well-preserved assemblage of fault-offset and abandoned fluvial channels along the San Andreas Fault in the Carrizo Plain. The landforms preserved here are as spectacular as the well-known Wallace Creek to the northwest. Here we explore the rich, subsurface sedimentological history to document the last ~7,000 years of feature evolution, including a pair of channels abandoned and offset a total of ~238 m and a younger paleo-channel abandoned and offset a total of ~125 m. We formulate a tectono-stratigraphic model that incorporates not only the tectonic drivers of fault-offset ephemeral stream channels but also the sedimentary response of watersheds in a semi-arid landscape. We show that the slip rate of the San Andreas in the Carrizo Plain is relatively uniform through the middle and late Holocene at several timescales, largely in agreement with the published geologic rate of 33.9 ± 2.9 mm/yr at the nearby Wallace Creek (Sieh and Jahns, 1984). For offset reconstructions of 238 m, 165 m, and 135 m we calculate slip rates of <35.1 ± 0.6 mm/yr, ~32.7 +2.1/-1.9 mm/yr, and 36 +1.8/-1.6 mm/yr.

TABLES

Radiocarbon Age Results

Sample ID	14C Det. (Age BP)	Calibrated yrs CalBP	+/-	Confidence (%)
O-1	565 ± 51	585	70	95.4
E-7	799 ± 53	730	70	91.2
Q-2	816 ± 51	734	66	88.3
D-18	840 ± 200	845	339	94.8
Q-5	1,017 ± 50	901	106	89.4
B-49	1,142 ± 144	1,039	274	95.4
F-19	1,170 ± 65	1,075	115	84.8
B-65	1,545 ± 100	1,458	171	93.2
D-38	1,610 ± 120	1,520	221	92.7
LS-7	1,662 ± 256	1,611	549	94.4
K-20	1,765 ± 60	1,686	138	95.4
LS-4	2,184 ± 208	2,236	501	95.4
D-21	2,374 ± 56	2,430	116	75.7
D-17	2,415 ± 60	2,485	137	75.7
B-10	3,170 ± 190	3,382	462	94.7
3-2	3,300 ± 30	3,523	70	95.4
I-12	3,475 ± 74	3,749	178	94.7
3-3	4,230 ± 20	4,732	23	75.2
3-22	4,220 ± 150	4,779	366	89.5
M-12	5,606 ± 72	6,421	140	95.4
K-12	5,920 ± 100	6,748	255	95.4
D-7	10,550 ± 150	12,373	357	95.4

Table 4.1 – Radiocarbon sample age results. We calibrated our radiocarbon ages using OxCal v4.2.4 (Bronk Ramsey, 2013) and the r:5 IntCal3 atmospheric curve (Reimer et al., 2013). The first character in the sample ID indicates the trench in which the sample was found. Sample ID's beginning with a letter were analyzed by Accelerator Mass Spectrometry Laboratory at the University of Arizona, Tucson. Sample ID's beginning with a number were analyzed at the W. M. Keck Carbon Cycle Accelerator Mass Spectrometry Laboratory at the University of California, Irvine.

pIR-IRSL Age Results

Sample ID	Trench	D*e* (Gy)	Total dose rate (Gy/ka)	Age (ka)	+/- (ka)
OSL.01	T1_W	18.55	3.76	4.94	0.27
OSL.02	T1_W	15.26	3.77	4.05	0.26
OSL.03	T1_W	19.89	3.73	5.33	0.37
OSL.04	T1_W	17.69	3.82	4.63	0.28
OSL.05	T3_E	17.87	4.06	4.40	0.28
OSL.06	T3_W	17.08	4.21	4.06	0.26
OSL.07	T3_W	17.98	4.10	4.39	0.30
OSL.08	T3_W	18.79	3.72	5.05	0.31
OSL.12	T2_W	101.11	4.57	22.13	1.44

Table 4.2 – pIR-IRSL age results. Our analyses were conducted at the Department of Earth, Planetary, and Space Sciences department at the University of California, Los Angeles. We use fading-corrected, single-grain K-feldspar for our analyses.

ACKNOWLEDGEMENTS

We wish to thank Mr. A. J. Phelan for his generosity in allowing us to access his property to conduct this research. We could not have completed this work without his assistance and interest. Cristofer Garvin did a wonderful job of digitizing, editing, and correcting trench logs and field notes. His organizational skills and perseverance were an immense help. We thank Nancy Warner of Nature Conservancy for her interest in our work and for answering questions about the present and past flora of the region. We also thank our colleagues who visited the trench site and discussed problems with us. We would like to thank Allyn Foss, Tom Fumal, Daniel Halford, John Hamilton, Emily Kleber, Gayatri Marliyani, Daniel Meier, Carol Prentice, Tsurue Sato, and Kerry Sieh.

This research was supported by the United States Geological Survey and the Southern California Earthquake Center (Contribution No. 7154). SCEC is funded by NSF Cooperative Agreement EAR-1033462 & USGS Cooperative Agreement G12AC20038.

REFERENCES

Arnold, R., and Johnson, H. R., 1910, Preliminary report on the McKittrick-Sunset oil region, Kern and San Luis Obispo counties, California: U. S. Geological Survey Bulletin 406.

Arrowsmith, J. R., Rhodes, D. D., and Pollard, D. D.,1998, Morphologic dating of scarps formed by repeated slip events along the San Andreas Fault, Carrizo Plain, California: Journal of Geophysical Research: Solid Earth, v. 103, no. 5.

Bemis, S. P., Micklethwaite, S., Turner, D., James, M. R., Akciz, S. O., Thiele, S. T., and Bangash, H. A., 2014, Ground-based and UAV-based photogrammetry: A multi-scale, high-resolution mapping tool for structural geology and paleoseismology: Journal of Structural Geology, v. 69, p. 163 – 178, doi: 10.1016/j.jsg.2014.10.007.

Bevis, M., Hudnut, K., Sanchez, R., Toth, C., Grejner-Brzezinska, D., Kendrick, E., Caccamise, D., Raleigh, D., Zhou, H., Shan, S., Shindle, W., Yong, A., Harvey, J., Borsa, A., Ayoub, F., Shrestha, R., Carter, B., Sartori, M., Phillips, D., and Colma, F., 2005, The B4 project: Scanning the San Andreas and San Jacinto fault zones: EOS (Transactions American Geophysical Union), v. 86., no. 52, fall meeting supplement, H34B-01.

Billham, R., 2004, Urban earthquake fatalities: a safer world, or worse to come?: Seismological Research Letters, v. 75, p. 706 – 712.

Bronk Ramsey, C., and Lee, S., 2013, Recent and planned developments of the program OxCal: Radiocarbon, vol 55, no. 2-3, p. 720 – 730.

Field, E. H., Arrowsmith, J R., Biasi, G. P., Bird, P., Dawson, T. E., Felzer, K. R., Jackson, D. D., Johnson, K. M., Jordan, T. H., Madden, C., Michael, A. J., Milner, K. R., Page, M. T., Parsons, T., Powers, P. M., Shaw, B. E., Thatcher, W. R., Weldon, R. J., and Zeng, Y., 2014, Uniform California Earthquake Rupture Forecast, Version 3 (UCERF3)—The time-independent model: Bulletin of the Seismological Society of America, v. 104, no.3, p. 1122 – 1180, doi: 10.1785/0120130164.

Grant, L. B., and Sieh, K., 1994, Paleoseismic evidence of clustered earthquakes on the San Andreas fault in the Carrizo Plain, California: Journal of Geophysical Research, v. 99, no. B4, p. 6819 – 6841.

Grant Ludwig, L., Akciz, S. O., Arrowsmith, J R., and Salisbury, J. B., *in press*, Re-measurement of the San Andreas Fault slip rate at Wallace Creek, Carrizo Plain, CA.

Hill, M. L., and Dibblee, T. W., 1953, San Andreas, Garlock, and Big Pine faults, California study of the character, history, and tectonic significance of their displacements: Bulletin of the Geological Society of America, v. 64, p. 443 – 458.

Huntley, D.J., and Baril, M.R., 1997, The K content of the K-feldspars being measured in optical dating or in thermoluminescence dating: Ancient TL, v. 15, no. 1, p. 11 – 13.

Johnson, K., Nissen, E., Saripalli, S., Arrowsmith, J R., McGarey, P., Scharer, K., Williams, P., and Blisniuk, K., 2014, Rapid mapping of ultrafine fault zone topography with structure from motion: Geosphere, v. 10, no. 5, p 969 – 986, doi: 10.1130/GES01017.1.

Lawson, A. C., and others, 1908, Report of the earthquake investigation commission upon the California earthquake of April 18, 1906: Carnegie Institution of Washington, D. C.

Liu, J., Klinger, Y., Sieh, K., and Rubin, C., 2004, Six similar sequential ruptures of the San Andreas fault, Carrizo Plain, California: Geology, v. 32, no. 8, pp. 649 – 652, doi: 10.1130/G20478.1.

Liu-Zeng, J., Klinger, Y., Sieh, K., Rubin, C., and Seitz, G., 2006, Serial ruptures of the San Andreas fault, Carrizo Plain, California, revealed by three-dimensional excavations: Journal of Geophysical Research, v. 111, B02306, doi: 10.1029/2004JB003601.

Meade, B. J., and Hager, B. H., 2005, Block models of crustal motion in southern California constrained by GPS measurements: Journal of Geophysical Research, v. 110, B03403, doi: 10.1029/2004JB003209.

Noriega, G.R., Arrowsmith, J R., Grant, L. B., Young, J. J., 2006, Stream Channel Offset and Late Holocene Slip Rate of the San Andreas Fault at the Van Matre Ranch Site, Carrizo Plain, California: Bulletin of the Seismological Society of America, v. 96, no. 1, p.33 – 47, doi: 10.1785/0120050094.

Reimer, P. J., Bard, E., Bayliss, A., Beck, J. W., Blackwell, P. G., Bronk Ramsey, C., Grootes, P. M., Guilderson, T. P., Haflidason, H., Hajdas, I., Hattz, C., Heaton, T. J., Hoffmann, D. L., Hogg, A. G., Hughen, K. A., Kaiser, K. F., Kromer, B., Manning, S. W., Niu, M., Reimer, R. W., Richards, D. A., Scott, E. M., Southon, J. R., Staff, R. A., Turney, C. S. M., and van der Plicht, J., 2013, IntCal13 and Marine13 Radiocarbon Age Calibration Curves 0 – 50,000 Years cal BP: Radiocarbon, vol 55, no. 4.

Salisbury, J. B., Arrowsmith J R., Brown, N., Rockwell, T. K., Akciz, S. O., Grant Ludwig, L., *in press*, The age and origin of small offsets at Van Matre Ranch along the San Andreas Fault in the Carrizo Plain, California.

Schmalzle, G., Dixon, T., Malservisi, R., and Govers, R., 2006, Strain accumulation across the Carrizo segment of the San Andreas Fault, California: Impact of laterally varying crustal properties: Journal of Geophysical Research: Solid Earth, vol. 111, no. B5, https://doi.org/10.1029/2005JB003843.

Sieh, K.E., 1978, Slip along the San Andreas fault associated with the great 1857 earthquake: Bulletin of the Seismological Society of America, v. 68, no. 5, p.1421 – 1448.

Sieh, K. E., and Jahns, R. H., 1984, Holocene activity of the San Andreas fault at Wallace Creek, California: Geological Society of America Bulletin, v. 95, p. 883 – 896.

Wallace, R.E., 1968, Notes on stream channels offset by the San Andreas fault, southern Coast Ranges, California: in Proceedings of Conference on Geologic Problems of the San Andreas Fault System, Stanford University Publications in Geological Sciences, eds. Dickinson W. R., and Grantz, A., v. 11, pp.6 – 21.

Wood, H. O., and Buwalda, J. P.,1931, Horizontal displacement along the San Andreas fault in the Carrizo Plain, California: Geological Society of America Bulletin, v. 42, p. 298 – 299.

Zielke, O., Arrowsmith J R., Grant Ludwig, L., Akciz, S. O., 2010, Slip in the 1857 and Earlier Large Earthquakes Along the Carrizo Plain, San Andreas Fault: Science, v. 327, p.1119 – 1122, doi: 10.1126/science.1182781.

Zielke, O., Arrowsmith, J R., Grant Ludwig, L., Akciz, S. O., 2012, High-resolution topography-derived offsets along the 1857 Fort Tejon earthquake rupture trace, San Andreas Fault: Bulletin of the Seismological Society of America, v. 102, no. 3, p. 1135 – 1154, doi: 10.1785/0120110230.

FIGURE CAPTIONS

Figure 4.1 – (A) Location map of Carrizo Plain in south-central California and 1 m B4 lidar hillshade of the Carrizo Plain between Wallace Creek and Phelan Creeks. (B) 10 cm semi-transparent Structure from Motion-derived digital elevation model over hillshade of the Phelan Creeks area. Trenches are shown in yellow. Trench T is ~10 m upstream of the figure edge between Little and Big Phelan Creeks. (C) Symbolic representation of channel stratigraphy contained within all excavations at our site. Gray units in the ~238 m offset pair do not have correlatives near Little and Big Phelan Creeks. Age control points are shown as yellow stars in the trenches from which they came. Stars show the approximate stratigraphic positions of each sample.

Figure 4.2 – Explanation of symbols used in trench logs (Figures 4.3 – 4.25).

Figure 4.3 – Log for Trench L. See Figure 4.1 for location.

Figure 4.4 – Log for Trench M. See Figure 4.1 for location.

Figure 4.5 – Log for Trench I. See Figure 4.1 for location.

Figure 4.6 – Log for Trench B. See Figure 4.1 for location.

Figure 4.7 – Log for Trench K. See Figure 4.1 for location.

Figure 4.8 – Log for Trench J. See Figure 4.1 for location.

Figure 4.9 – Log for Trench 2. See Figure 4.1 for location.

Figure 4.10 – Log for Trench 3. See Figure 4.1 for location.

Figure 4.11 – Log for Trench A. See Figure 4.1 for location.

Figure 4.12 – Log for Trench 1. See Figure 4.1 for location.

Figure 4.13 – Log for Trench H. See Figure 4.1 for location.

Figure 4.14 – Log for Trench C. See Figure 4.1 for location.

Figure 4.15 – Log for Trench D. See Figure 4.1 for location.

Figure 4.16 – Log for Trench F-91. See Figure 4.1 for location.

Figure 4.17 – Log for Trench E. See Figure 4.1 for location.

Figure 4.18 – Log for Trench E-91. See Figure 4.1 for location.

Figure 4.19 – Log for Trench O. See Figure 4.1 for location.

Figure 4.20 – Log for Trench LS. See Figure 4.1 for location.

Figure 4.21 – Log for Trench S. See Figure 4.1 for location.

Figure 4.22 – Log for Trench R. See Figure 4.1 for location.

Figure 4.23 – Log for Trench Q. See Figure 4.1 for location.

Figure 4.24 – Log for Trench F. See Figure 4.1 for location.

Figure 4.25 – Log for Trench G. See Figure 4.1 for location.

Figure 4.26 – Log for Trench T. See Figure 4.1 for location.

Figure 4.27 – ^{14}C and pIR-IRSL age model for paleo-channel deposits at Phelan Creeks. The first letter of ^{14}C sample names indicates the trench from which the sample came. For pIR-IRSL samples, trenches are labeled after the sample name. See Figure 4.1C for a schematic representation of sample locations.

Figure 4.28 – Tectono-stratigraphic model of sedimentation induced by along-fault channel segment lengthening. The left column shows a map view of the stream, the middle column shows the channel longitudinal profile, and the right column shows a channel cross-sectional profile (that corresponds to the cross-section line in the map view column). Steps A – E show a time progression involving several earthquakes.

Figure 4.29 – Present-day channel configurations and trench locations. We use this map for back-slipping evaluations.

Figure 4.30 – Stage 1 in the evolution of Phelan Creeks paleo-channels K and M. Channels are reconstructed with 238 m of back-slip. The 1857 rupture trace has been simplified for simplicity of back-slipping. Control points represent correlative channel indicators on opposite trench walls.

Figure 4.31 – Stage 2, shown with 195 m of back-slip. Paleo-channel K is abandoned and paleo-channel M captures Little Phelan Creeks. By this point, unit Mc-1 has been deposited.

Figure 4.32 – Stage 3, shown with 165 m of back-slip. Unit Mc-2 is deposited (recognized in Trenches N and I) and also in the downstream element of M. Paleo-channel LS is initiated. Paleo-channel LS will later be named paleo-channel H when Big Phelan Creeks no longer flows along-fault into paleo-channel M and both Little and Big Phelan Creeks flow into the same downstream element.

Figure 4.33 – Stage 4, shown after 135 m of back-slip. Big Phelan Creek no longer flows into paleo-channel M, and the originally straight paleo-channel LS is offset with an along-fault segment.

Figure 4.34 – Stage 5, shown 95 m of back-slip. The along-fault portion of Big Phelan Creek captures Little Phelan Creek, both flowing out the same downstream channel element, now named paleo-channel H. Paleo-channel M is now completely abandoned, colluvial deposits begin to form in the abandoned along-fault segments (trenches N and I).

Figure 4.35 – Stage 6, shown after 55 m of back-slip. There is continued offset of paleo-channel H. Big Phelan Creek along-fault segment continues to lengthen.

Figure 4.36 – Stage 7, shown after 35 m of back-slip. The along-fault segment of paleo-channel H continues lengthens and Big Phelan Creek initiates its modern down-stream element. Little Phelan Creek may also begin to abandon paleo-channel H but it is unclear.

Figure 4.37 – Stage 8, shown with 20 m of back-slip. There is continued incision of Little and Big Phelan Creeks.

Figure 4.38 – Age vs. Offset plot for the Carrizo Plain for the last 7,000 years. Box dimensions represent age and offset uncertainties. The red line represents the slip rate calculated by Sieh and Jahns (1984) for the last 3,700 years from the small (130 m) offset at Wallace Creek. Magenta lines represent uncertainties. The dashed black line is the slip rate (36 mm/yr, ~475 m offset) calculated at the 13,250 yr timescale in the same study. The dashed black line also represents the geodetic rate of 36 mm/yr (Schmalzle et al., 2006).

Figure 4.39 – Age vs. Offset plot for the Carrizo Plain for the last 15,000 years. Box dimensions represent age and offset uncertainties. The red line represents the slip rate calculated by Sieh and Jahns (1984) for the last 3,700 years from the small (130 m) offset at Wallace Creek. Magenta lines represent uncertainties. The dashed black line is the slip rate (36 mm/yr, ~475 m offset) calculated at the 13,250 yr timescale in the same study. The dashed black line also represents the geodetic rate of 36 mm/yr (Schmalzle et al., 2006).

FIGURES

Figure 4.1

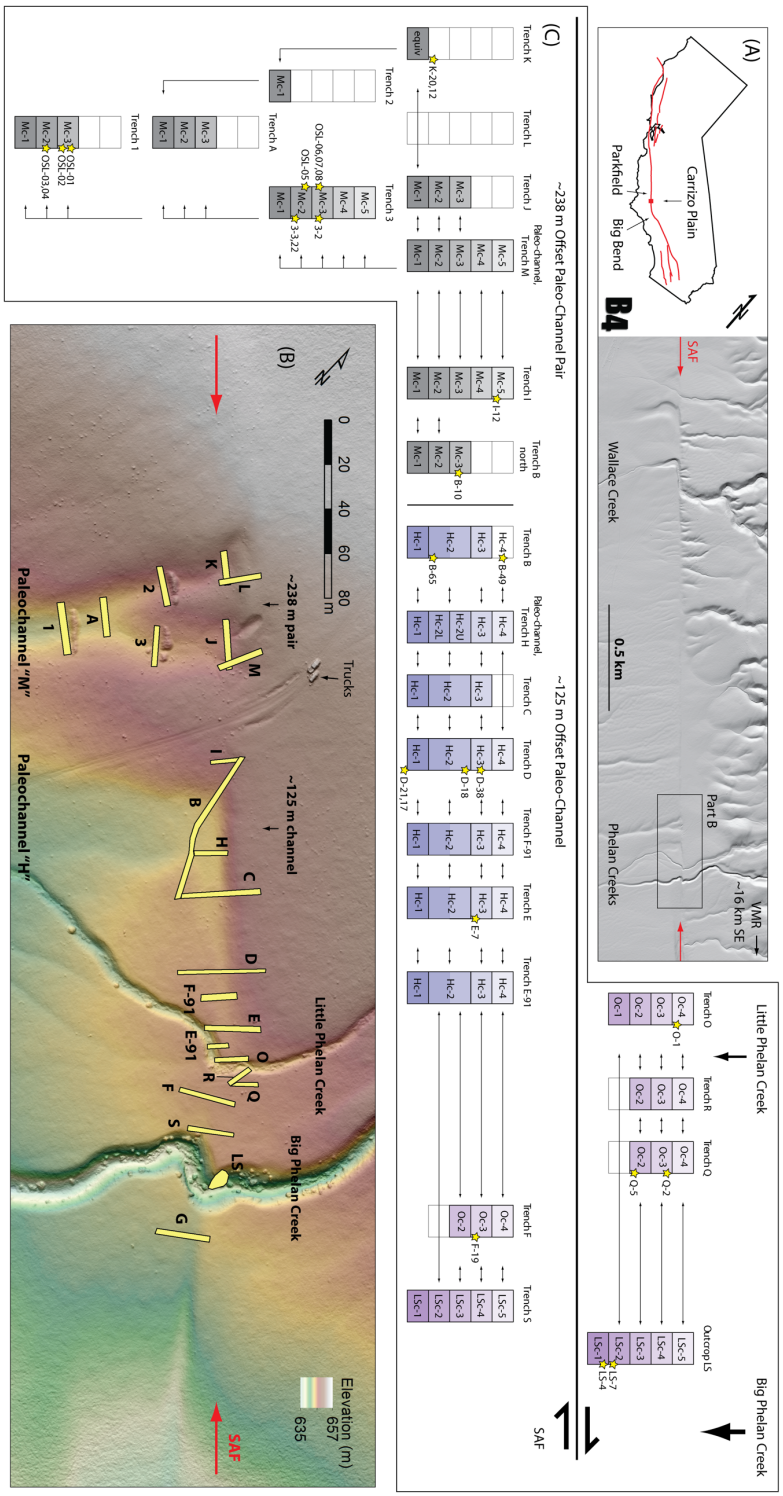

Figure 4.2

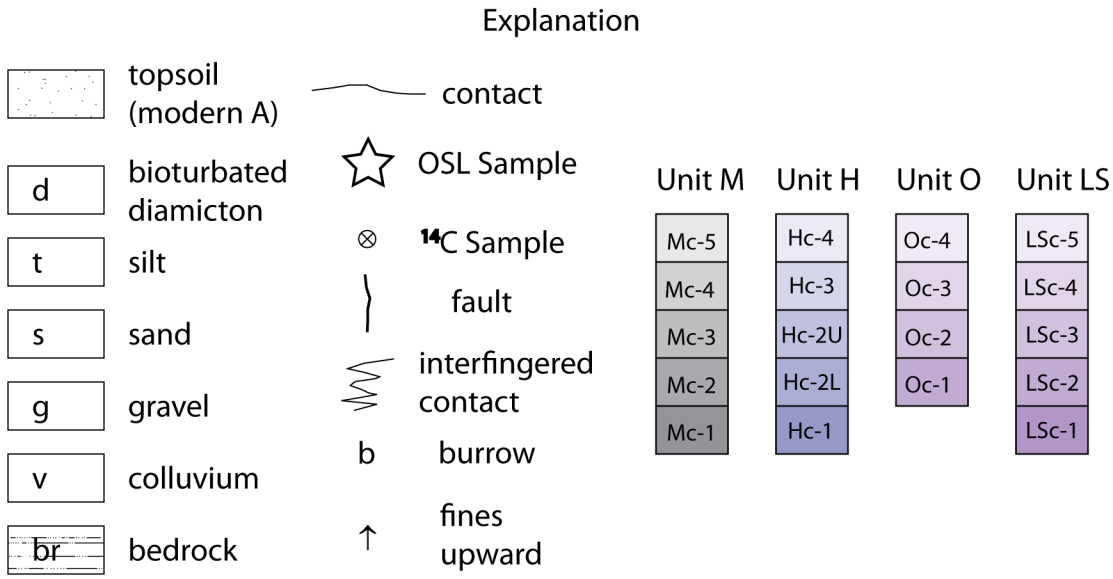
Explanation
topsoil (modern A)
d
bioturbated diamicton
t
silt
s
sand
g
gravel
v
colluvium
br
bedrock
contact
OSL Sample
14C Sample
fault
interfingered contact
b
burrow
fines upward
Unit M
Mc-5
Mc-4
Mc-3
Mc-2
Mc-1
Unit H
Hc-4
Hc-3
Hc-2U
Hc-2L
Hc-1
Unit O
Oc-4
Oc-3
Oc-2
Oc-1
Unit LS
LSc-5
LSc-4
LSc-3
LSc-2
LSc-1

Figure 4.3

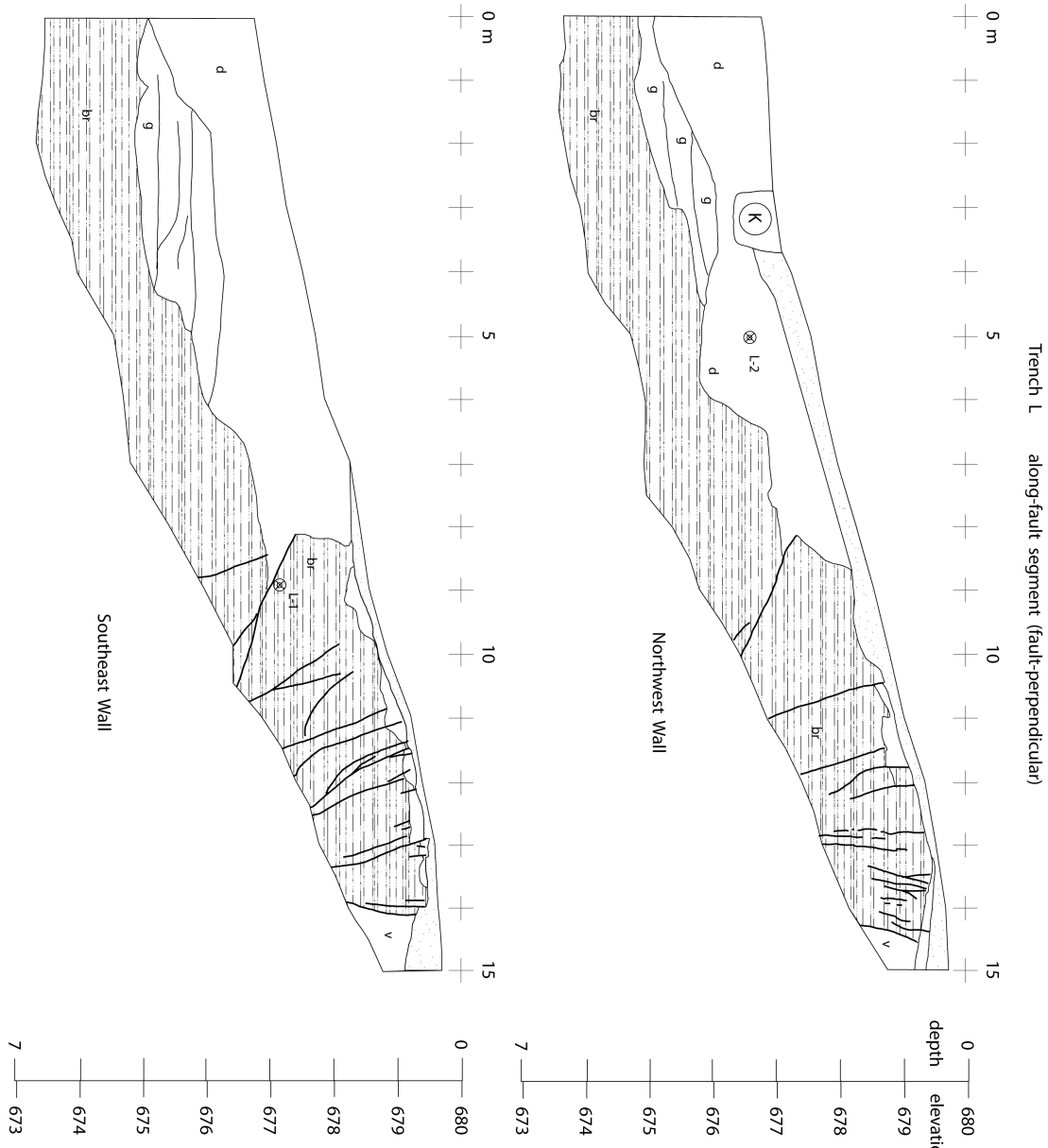
Trench L
along-fault segment (fault-perpendicular)
0 m
5
10
15
depth
0
elevation
680
679
678
677
676
675
674
673
7
Northwest Wall
Southeast Wall
K
L-2
L-1
d
g
br
v

Figure 4.4

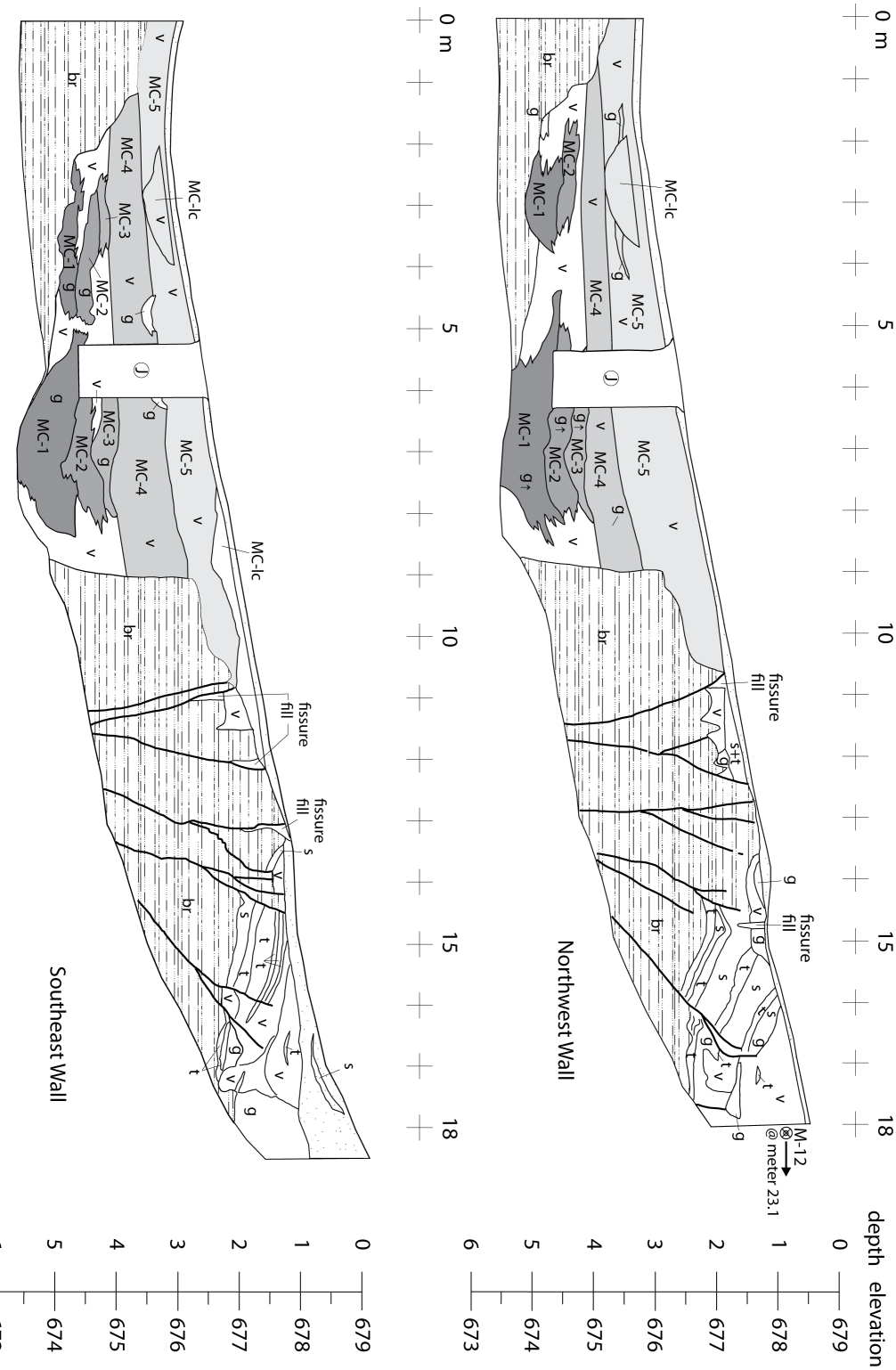
Trench M
along-fault segment (fault-perpendicular)
0 m
5
10
15
18
depth
elevation
679
678
677
676
675
674
673
0
1
2
3
4
5
6
Northwest Wall
Southeast Wall
MC-lc
MC-5
MC-4
MC-3
MC-2
MC-1
fissure fill
M-12
meter 23.1
v
g
br
s
t

Figure 4.5

Trench I along-fault segment (fault-perpendicular)
0 m
5
10
15
depth
elevation
680
679
678
677
676
675
674
6
Northwest Wall
Southeast Wall
Mc-1
Mc-2
Mc-3
Mc-4
Mc-5
I-1
I-2
I-3
I-4
I-5
I-6
I-7
I-12
I-14
I-15
I-?
B

Figure 4.6

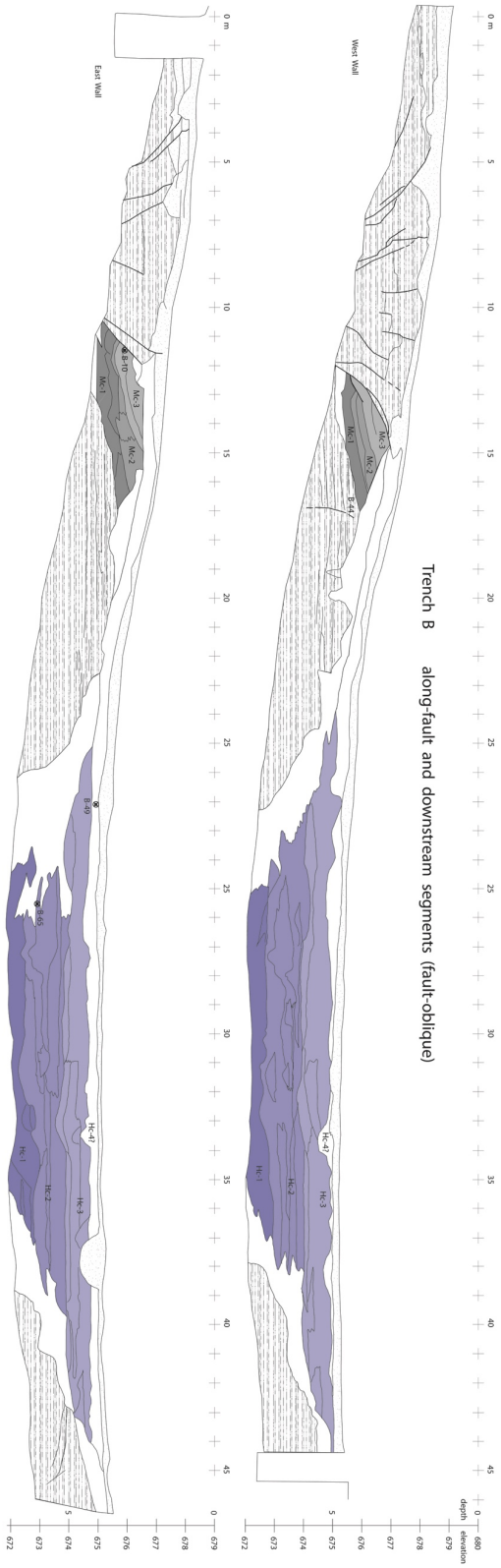
Trench B
along-fault and downstream segments (fault-oblique)
East Wall
West Wall
Mc-1
Mc-2
Mc-3
Mc-4
Hc-1
Hc-2
Hc-3
Hc-4?
B-05
B-09
B-10
depth
elevation

Figure 4.7

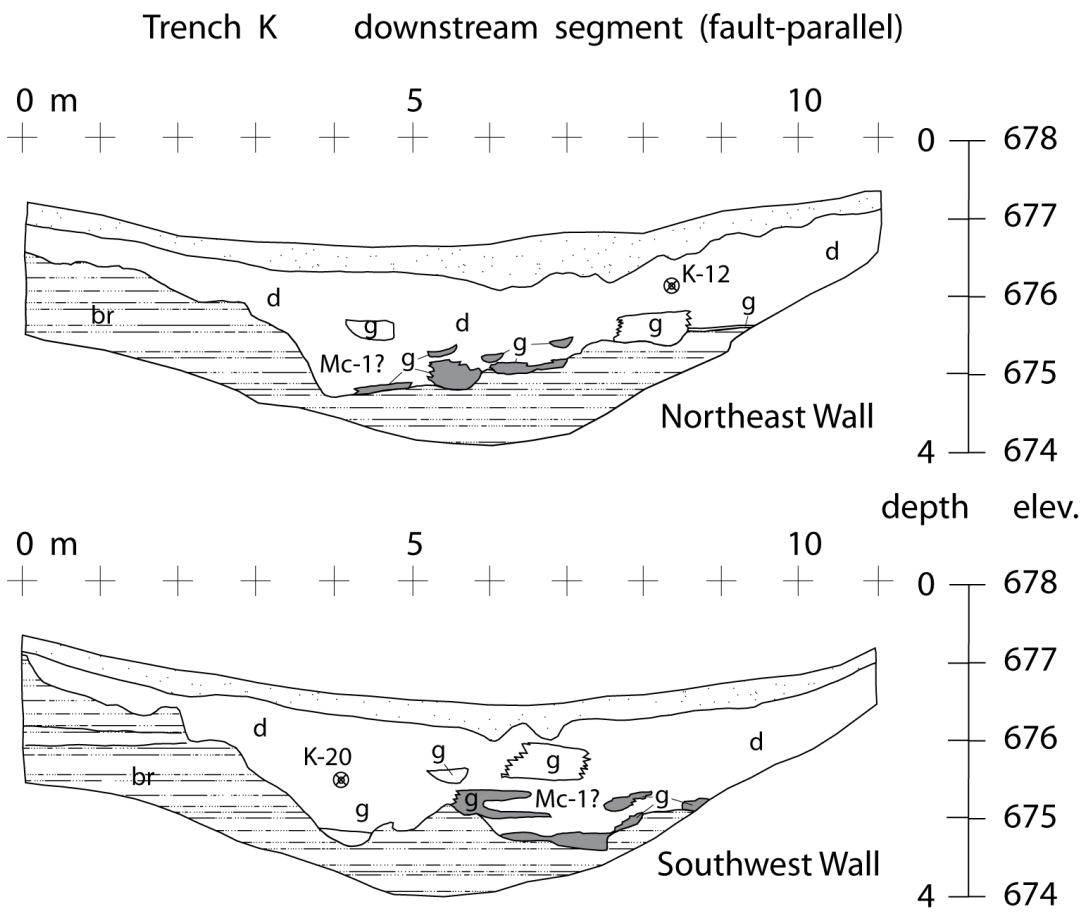
Trench K downstream segment (fault-parallel)
0 m
5
10
0
678
677
676
675
4
674
depth
elev.
d
K-12
br
g
Mc-1?
Northeast Wall
K-20
Southwest Wall

Figure 4.8

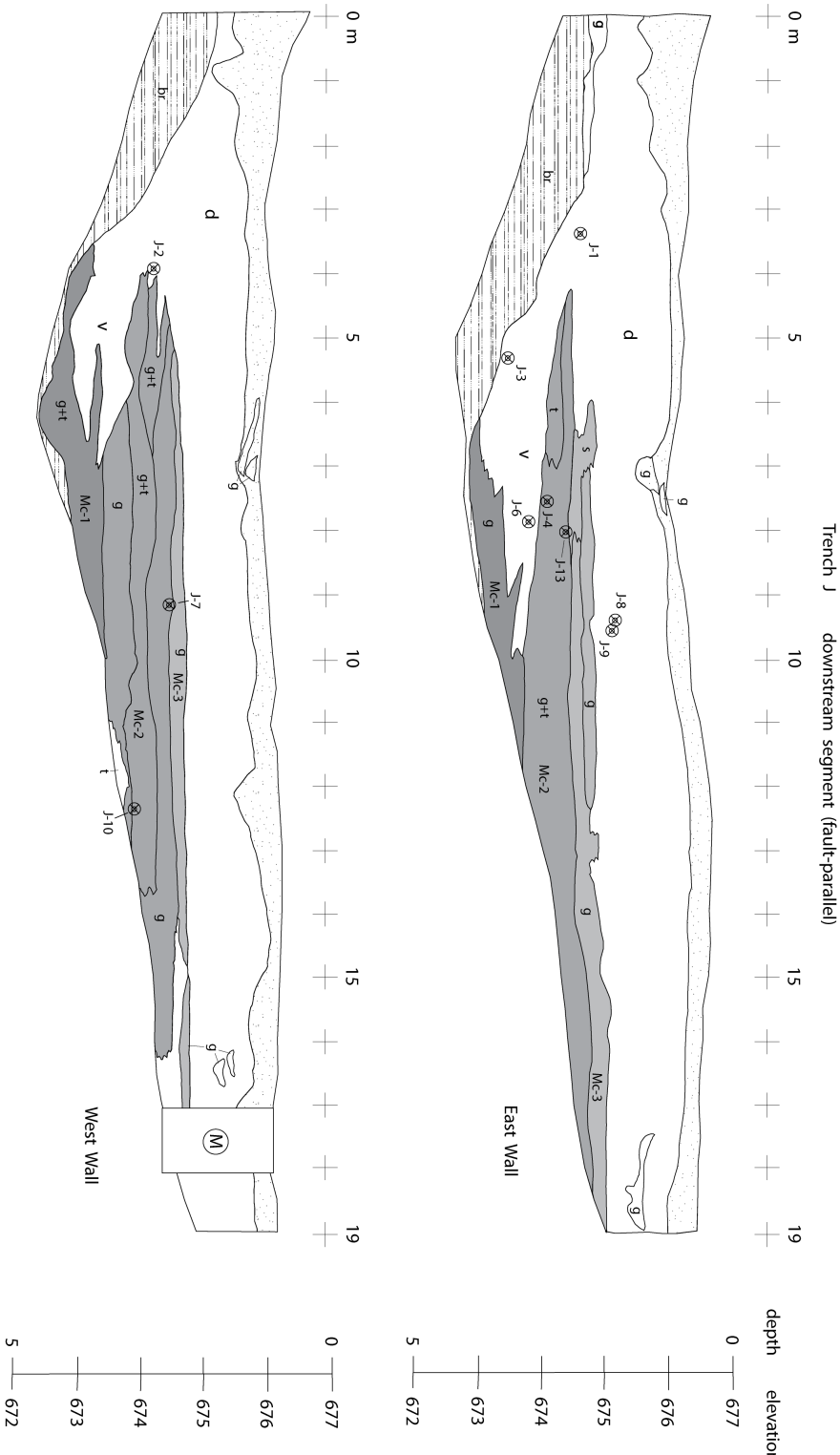
Trench J
downstream segment (fault-parallel)
0 m
5
10
15
19
East Wall
West Wall
depth
elevation
0
5
677
676
675
674
673
672
g
br
d
v
t
s
J-1
J-2
J-3
J-4
J-5
J-6
J-7
J-8
J-9
J-10
J-13
g+t
Mc-1
Mc-2
Mc-3
M

Figure 4.9


Trench 2 downstream segment (fault-parallel)
Northeast Wall
Southwest Wall
0 m
5
8
depth
0
4
v
d
g+s+t
br
2-9
2-8
2-4
2-2
2-6
2-7
2-3
OSL-10
OSL-11
OSL-12
g
10

Figure 4.10

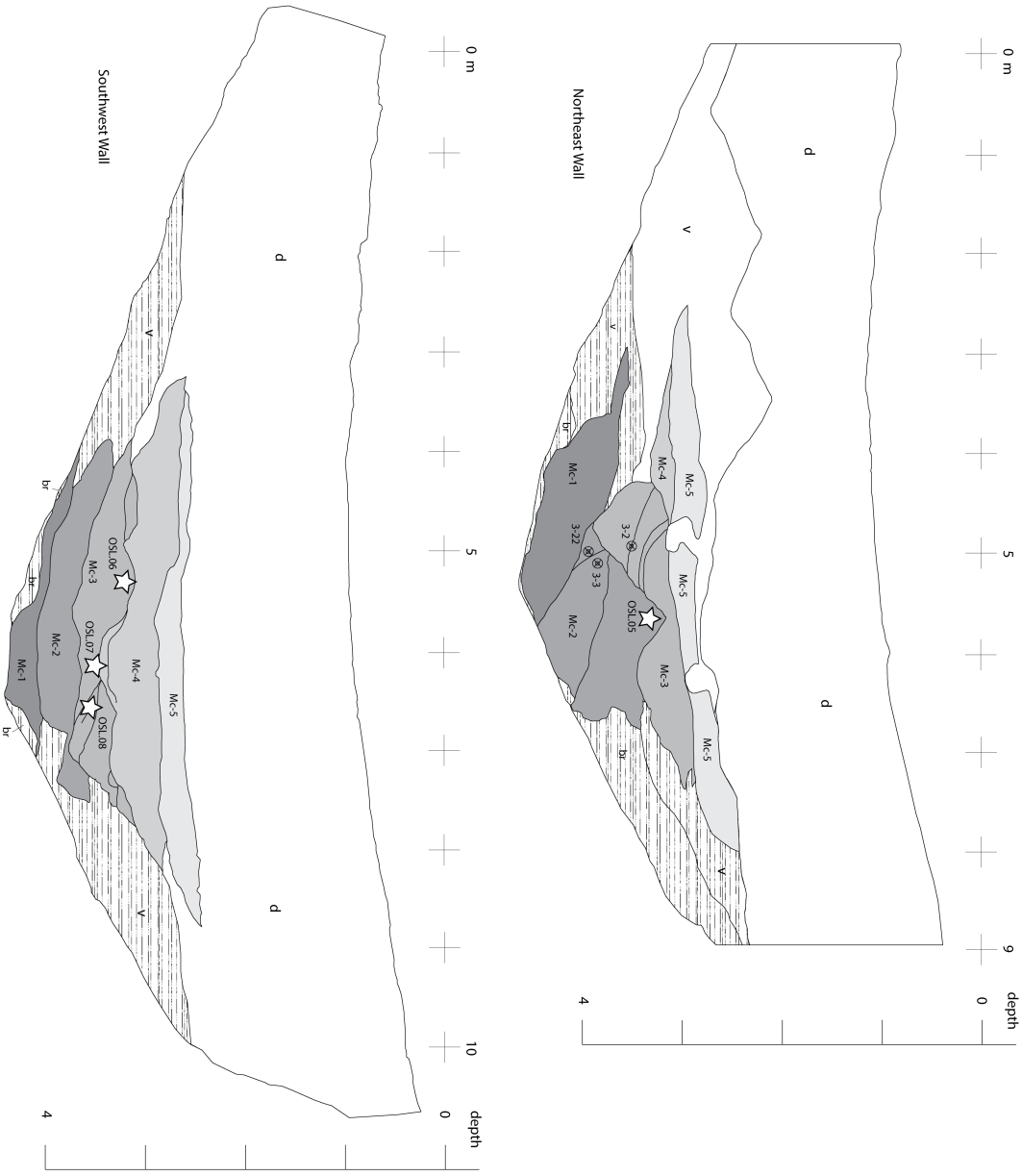
Trench 3 downstream segment (fault-parallel)
Northeast Wall
Southwest Wall
0 m
5
9
10
depth
0
4
d
v
br
Mc-1
Mc-2
Mc-3
Mc-4
Mc-5
3-22
3-2
3-3
OSL05
OSL06
OSL07
OSL08

Figure 4.11

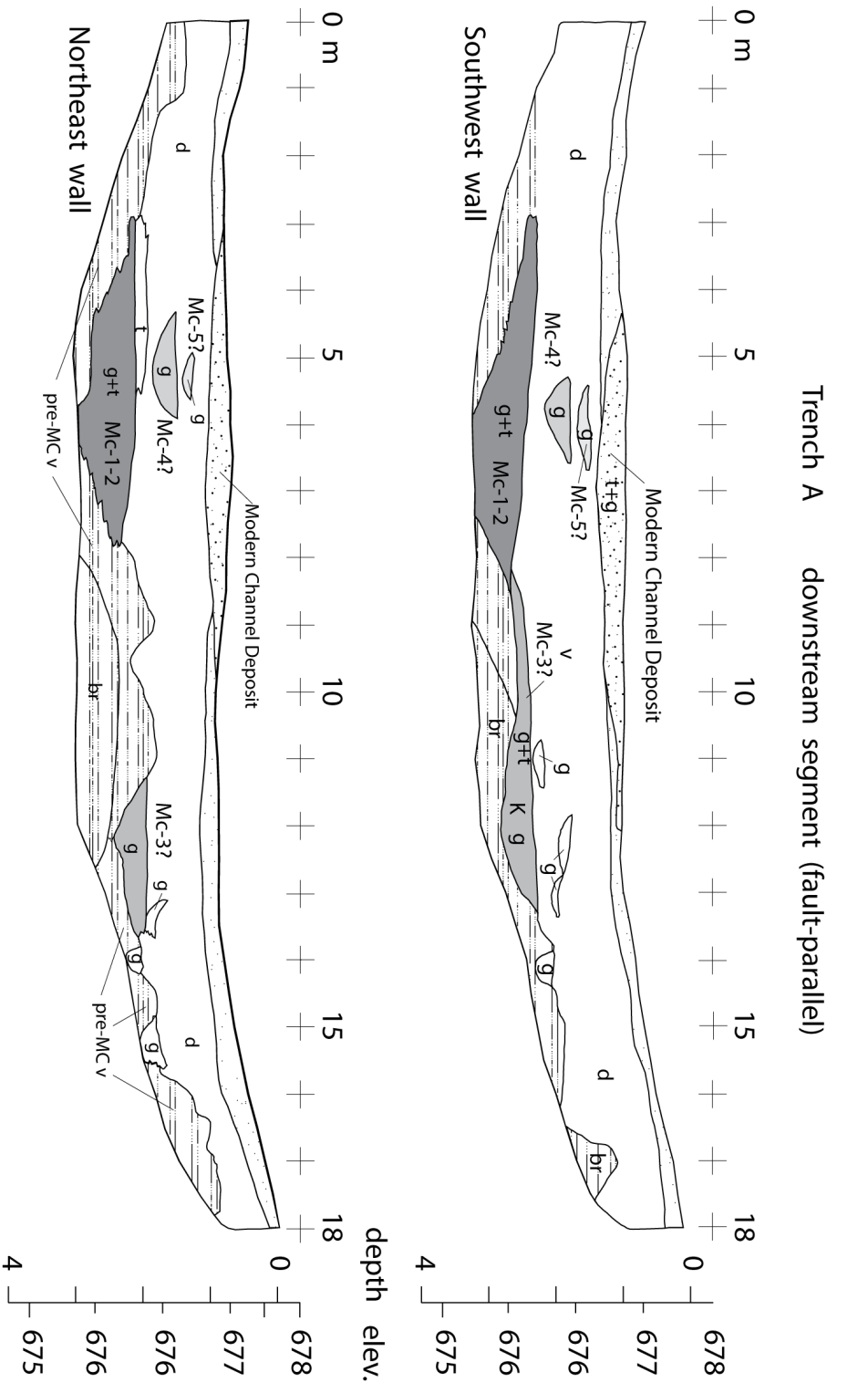
Trench A downstream segment (fault-parallel)
Southwest wall
Northeast wall
0 m
5
10
15
18
0
4
depth
elev.
678
677
676
675
Modern Channel Deposit
d
br
t+g
g
Mc-5?
Mc-4?
g+t Mc-1-2
v
Mc-3?
K
t
pre-MC v

Figure 4.12

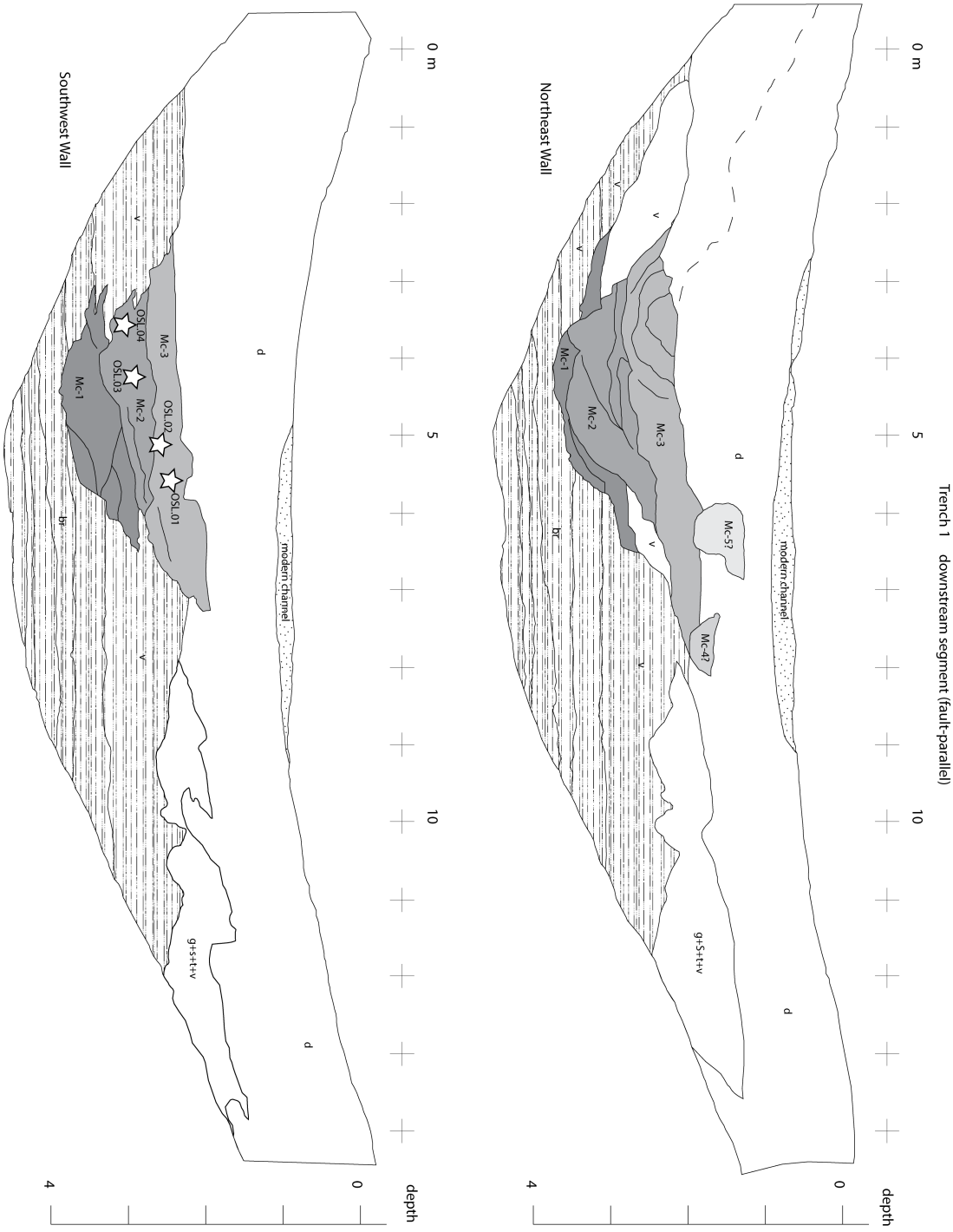
Trench 1 downstream segment (fault-parallel)
Northeast Wall
Southwest Wall
0 m
5
10
depth
0
4
Mc-1
Mc-2
Mc-3
Mc-4?
Mc-5?
OSL01
OSL02
OSL03
OSL04
modern channel
g+s+t+v
d
v
br

Figure 4.13

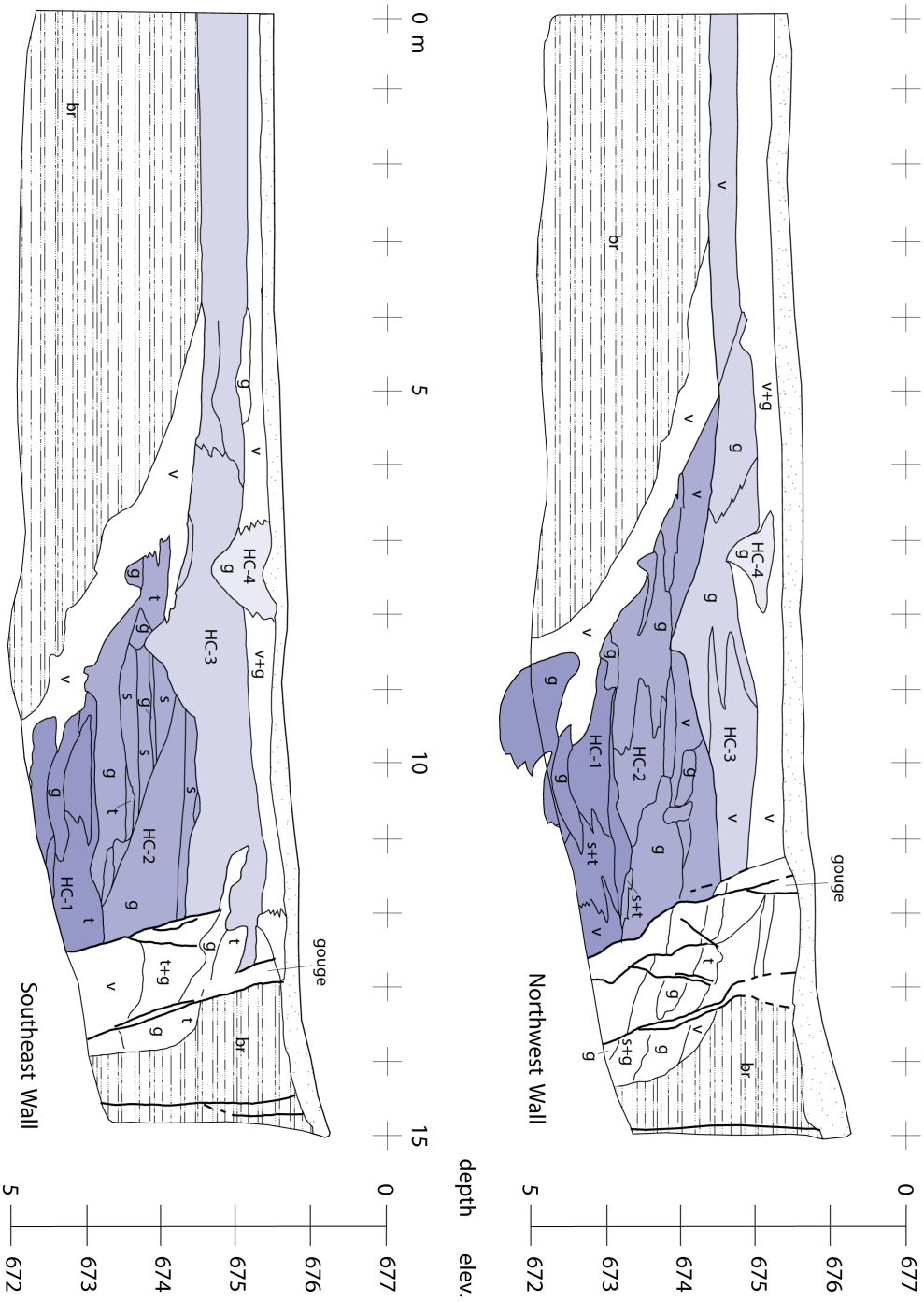
Trench H along-fault segment (fault-perpendicular)
Northwest Wall
Southeast Wall
HC-1
HC-2
HC-3
HC-4
gouge
br
depth
elev.
0 m
5
10
15
0
677
676
675
674
673
672

Figure 4.14

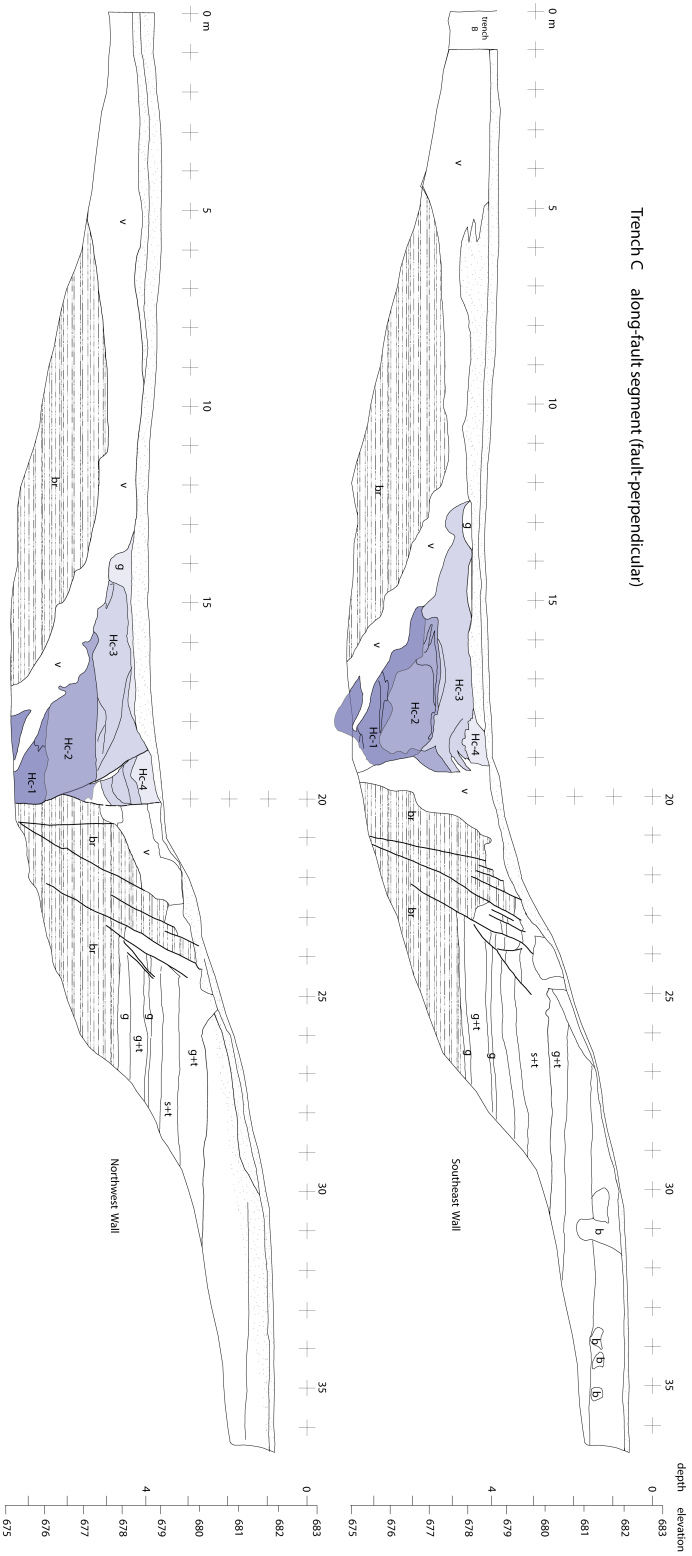
Trench C along-fault segment (fault-perpendicular)
Southeast Wall
Northwest Wall
trench B
Hc-1
Hc-2
Hc-3
Hc-4
v
br
g
g+t
s+t
b
depth
elevation

Figure 4.15

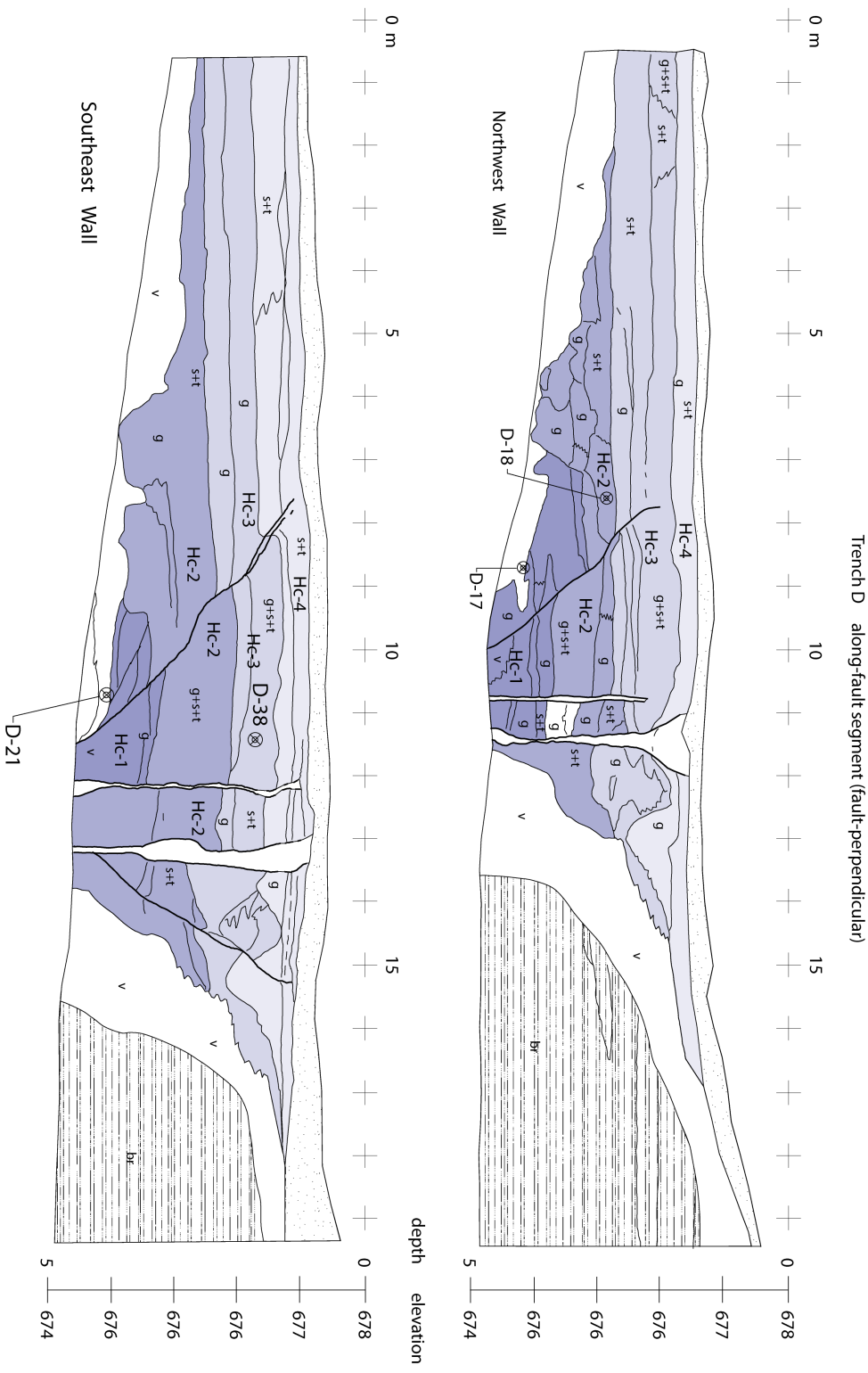
Trench D along-fault segment (fault-perpendicular)
Northwest Wall
Southeast Wall
Hc-1
Hc-2
Hc-3
Hc-4
D-17
D-18
D-21
D-38
s+t
g+s+t
g
v
br
0 m
5
10
15
depth
elevation
678
677
676
674

Figure 4.16

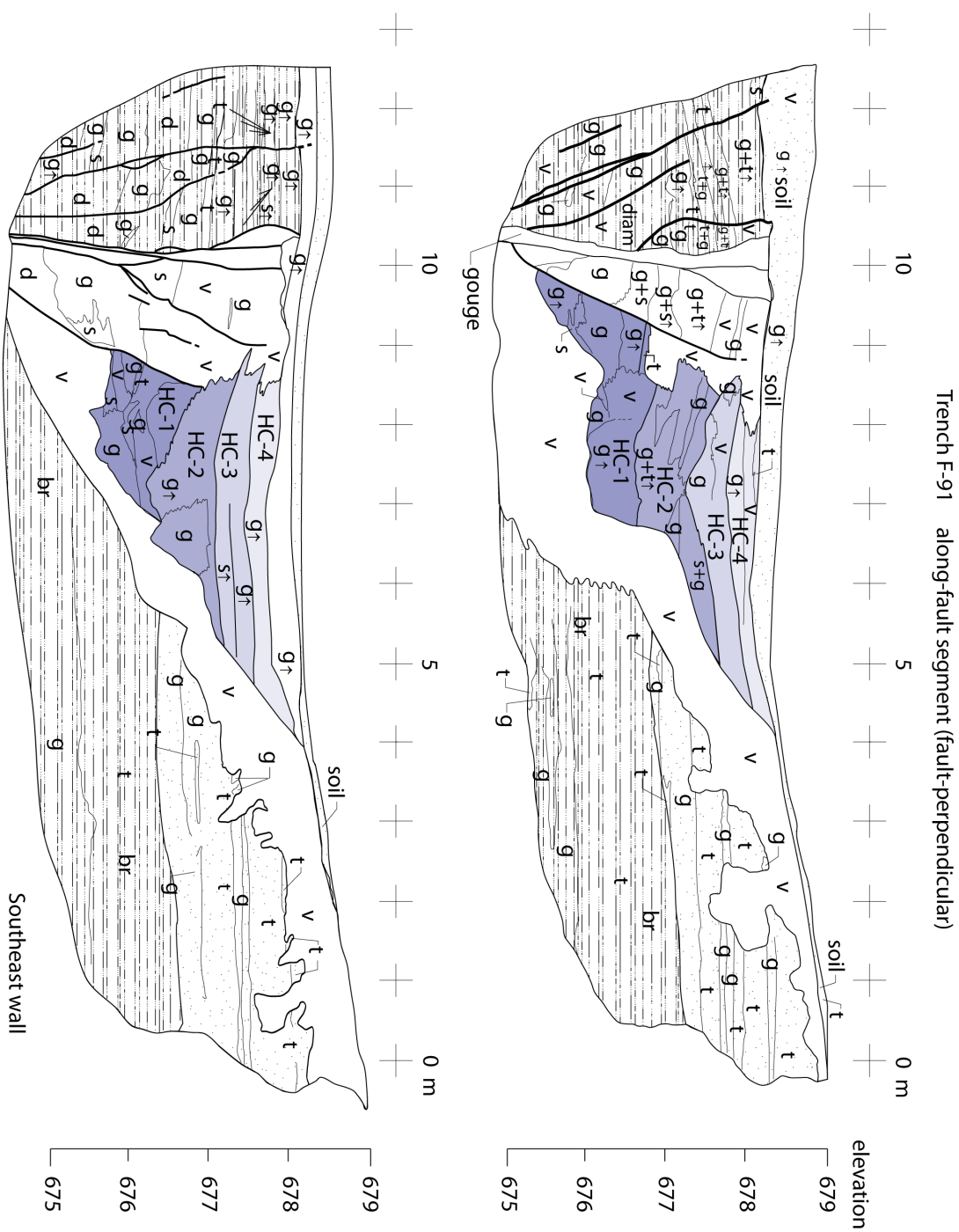
Trench F-91 along-fault segment (fault-perpendicular)
10
5
0 m
soil
gouge
diam
HC-1
HC-2
HC-3
HC-4
soil
Southeast wall
elevation
679
678
677
676
675

Figure 4.17

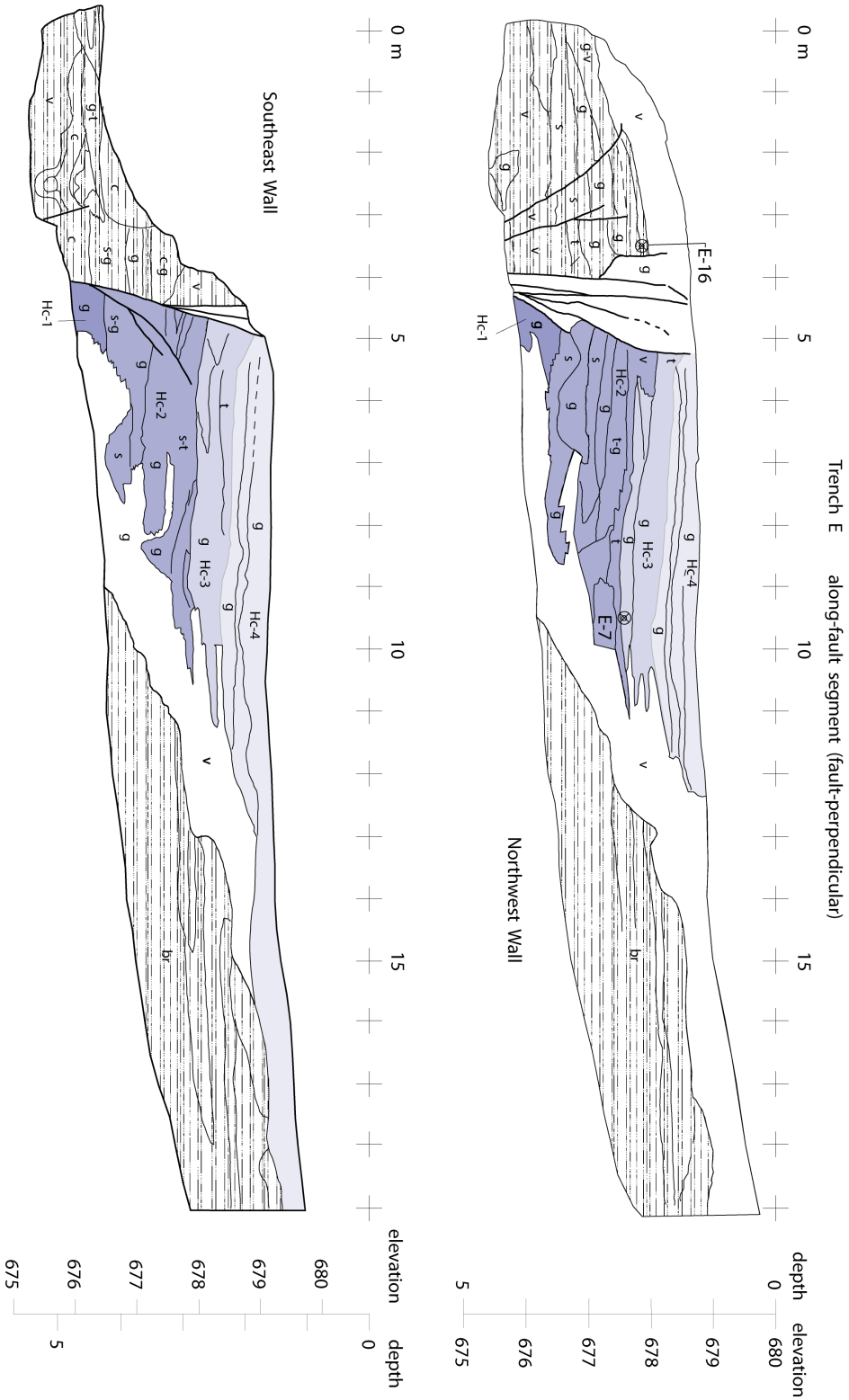
Trench E
along-fault segment (fault-perpendicular)
Northwest Wall
Southeast Wall
E-16
E-7
Hc-1
Hc-2
Hc-3
Hc-4
0 m
5
10
15
depth
elevation
0
5
675
676
677
678
679
680

Figure 4.18

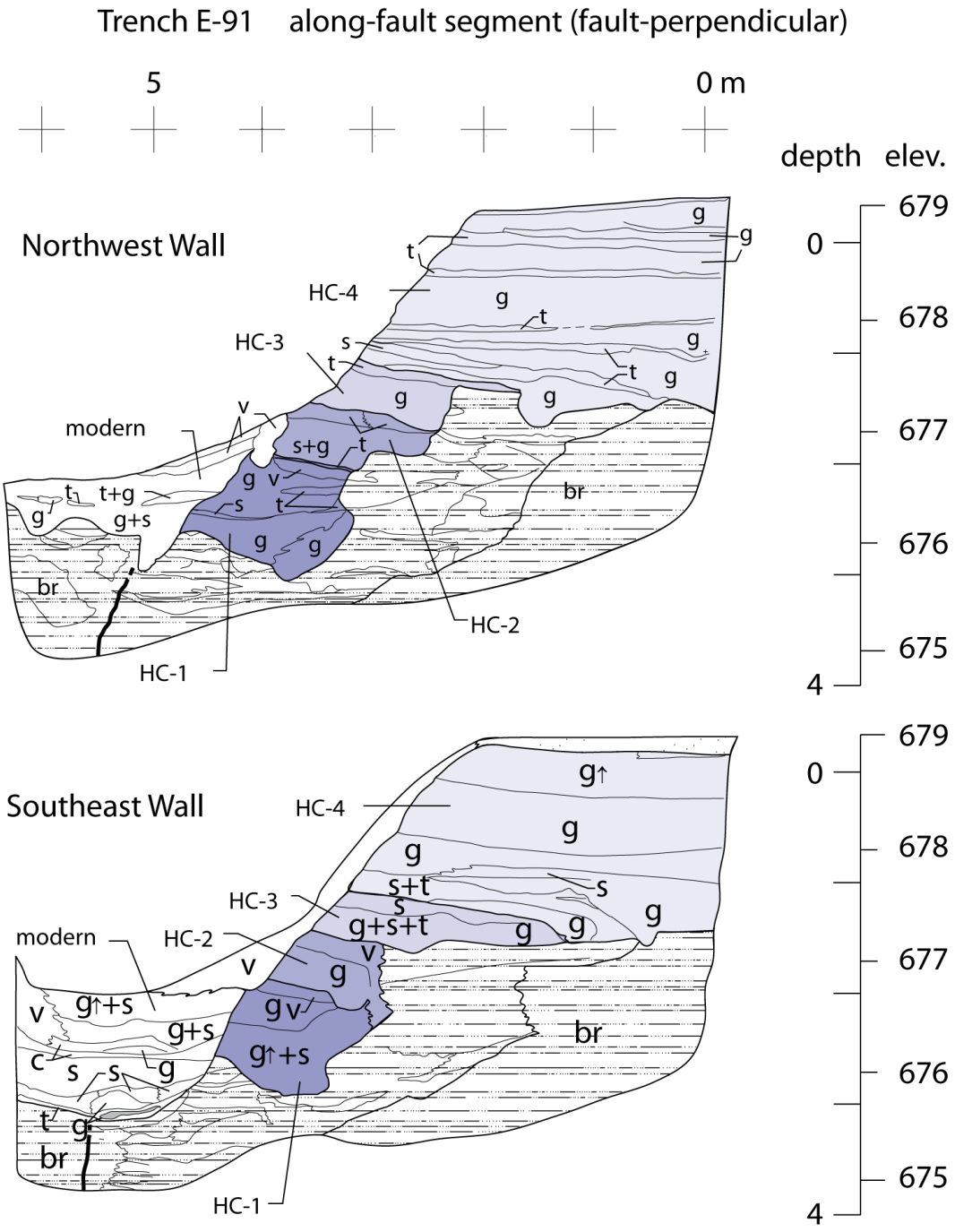
Trench E-91 along-fault segment (fault-perpendicular)
5
0 m
depth elev.
Northwest Wall
HC-4
HC-3
modern
HC-2
HC-1
br
0
679
678
677
676
675
4
Southeast Wall
HC-4
HC-3
modern
HC-2
HC-1
br
0
679
678
677
676
675
4

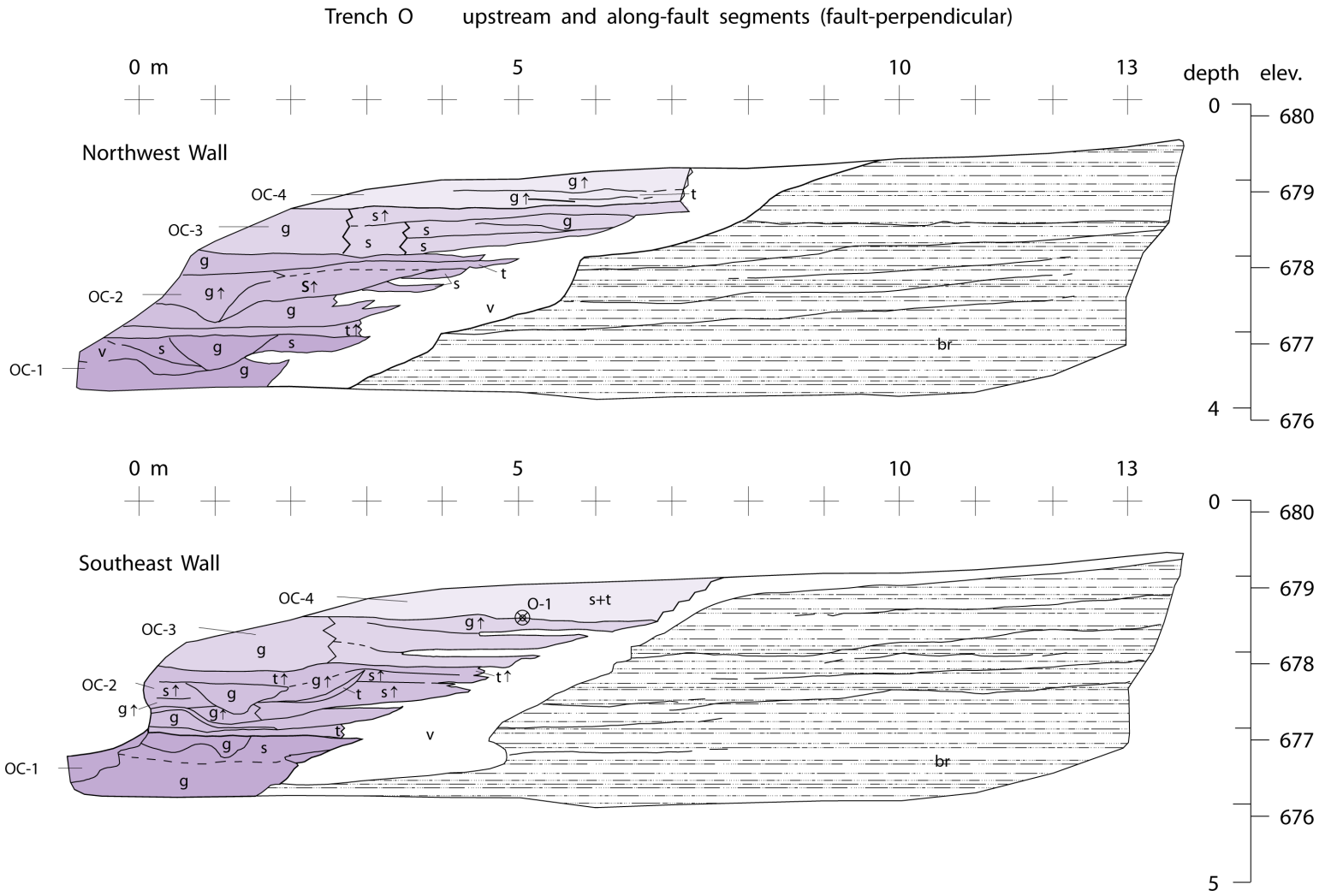
Trench O upstream and along-fault segments (fault-perpendicular)
0 m
5
10
13
depth
elev.
0
680
679
678
677
4
676
Northwest Wall
OC-4
OC-3
OC-2
OC-1
g
s
t
v
br
0 m
5
10
13
0
680
679
678
677
676
5
Southeast Wall
OC-4
OC-3
OC-2
OC-1
O-1
s+t
g
s
t
v
br

Figure 4.19

Figure 4.20

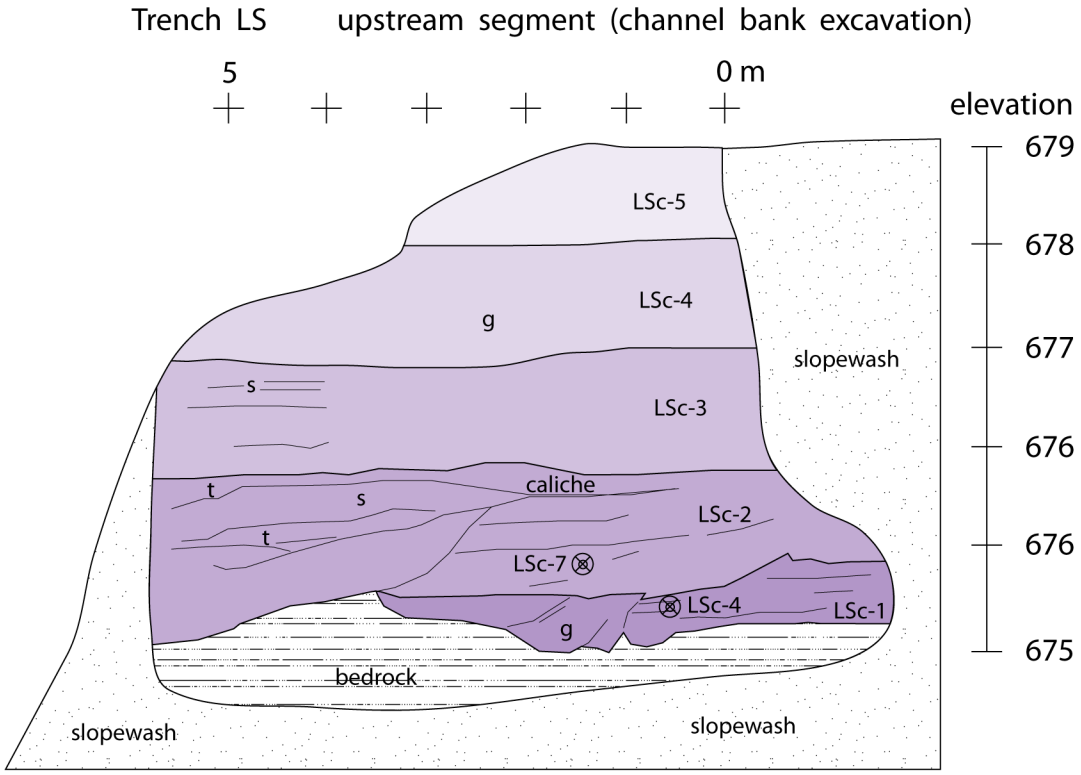
Trench LS
upstream segment (channel bank excavation)
5
0 m
elevation
679
678
677
676
676
675
LSc-5
LSc-4
g
slopewash
s
LSc-3
t
s
caliche
LSc-2
t
LSc-7
LSc-4
LSc-1
g
bedrock
slopewash
slopewash

Figure 4.21

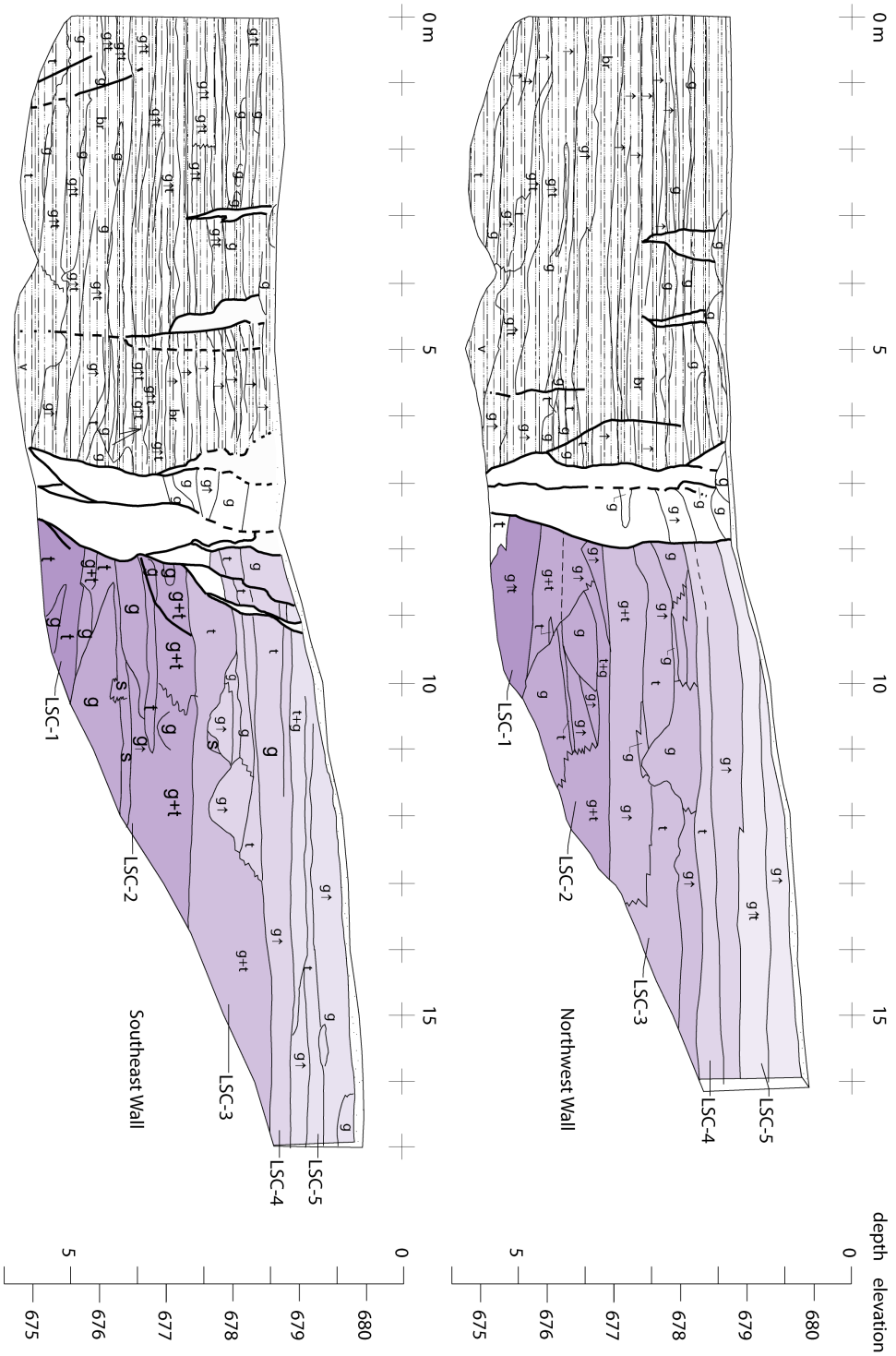
Trench S upstream and along-fault segment (fault-perpendicular)
0 m
5
10
15
depth
elevation
0
5
680
679
678
677
676
675
LSC-1
LSC-2
LSC-3
LSC-4
LSC-5
Northwest Wall
Southeast Wall

Figure 4.22

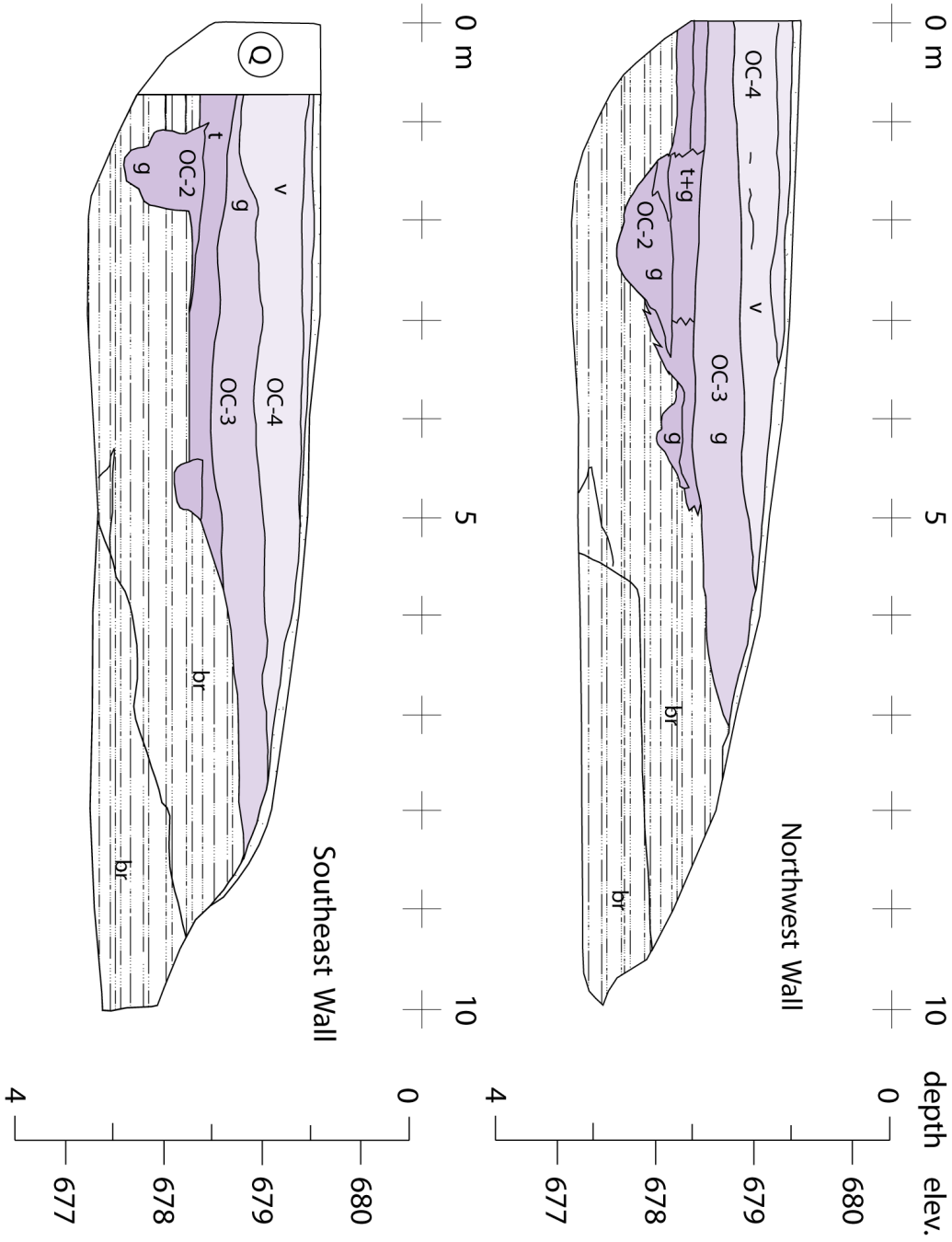
Trench R upstream segment (fault-oblique)
0 m
5
10
depth
elev.
0
680
679
678
677
4
Northwest Wall
OC-4
v
OC-3
g
t+g
OC-2
g
br
Southeast Wall
Q
v
OC-4
g
OC-3
t
OC-2
g
br

Figure 4.23

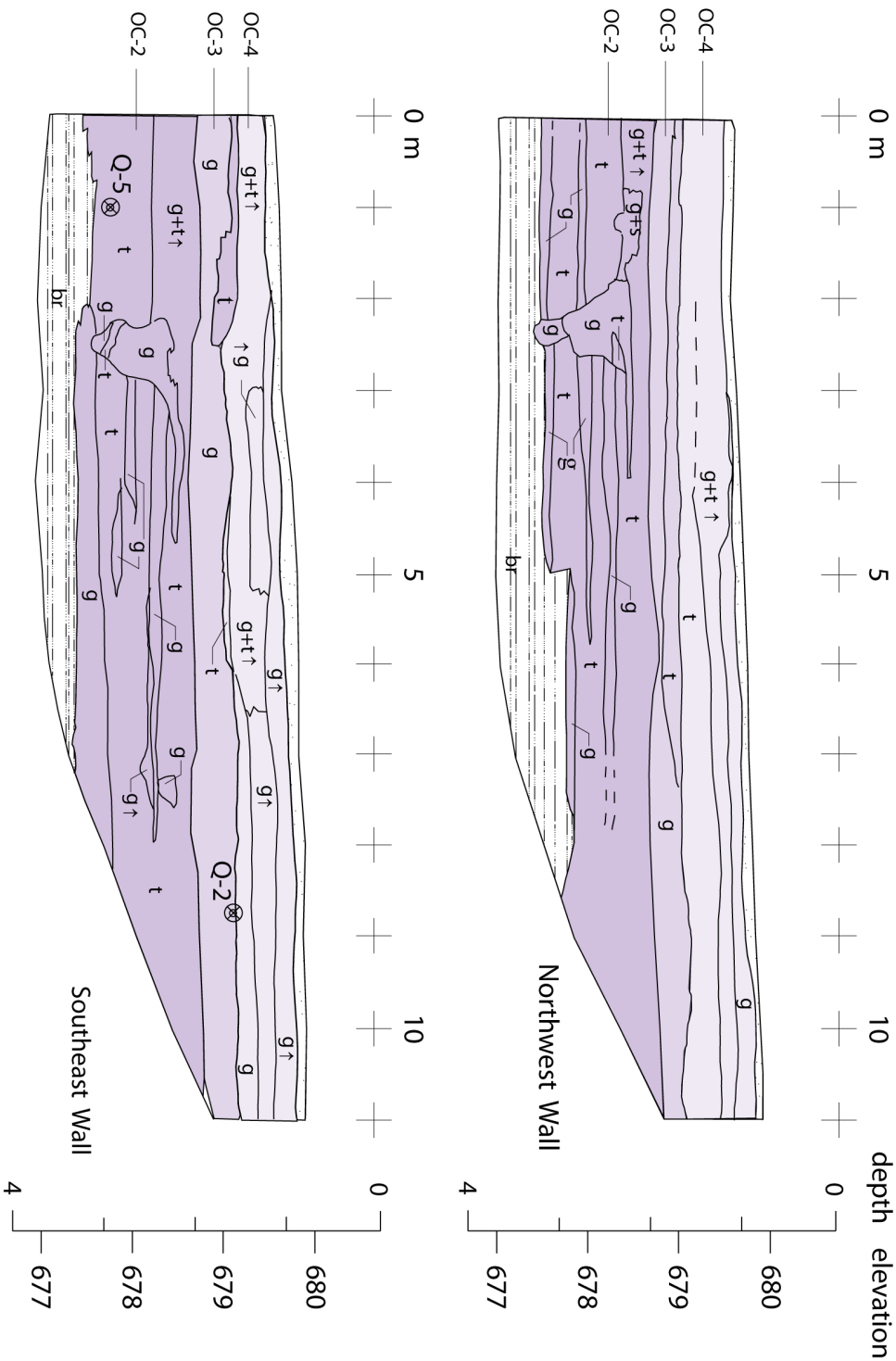
Trench Q upstream segment (fault-perpendicular)
0 m
5
10
depth
elevation
OC-4
OC-3
OC-2
Northwest Wall
Southeast Wall
Q-5
Q-2
br
0
4
680
679
678
677

Figure 4.24

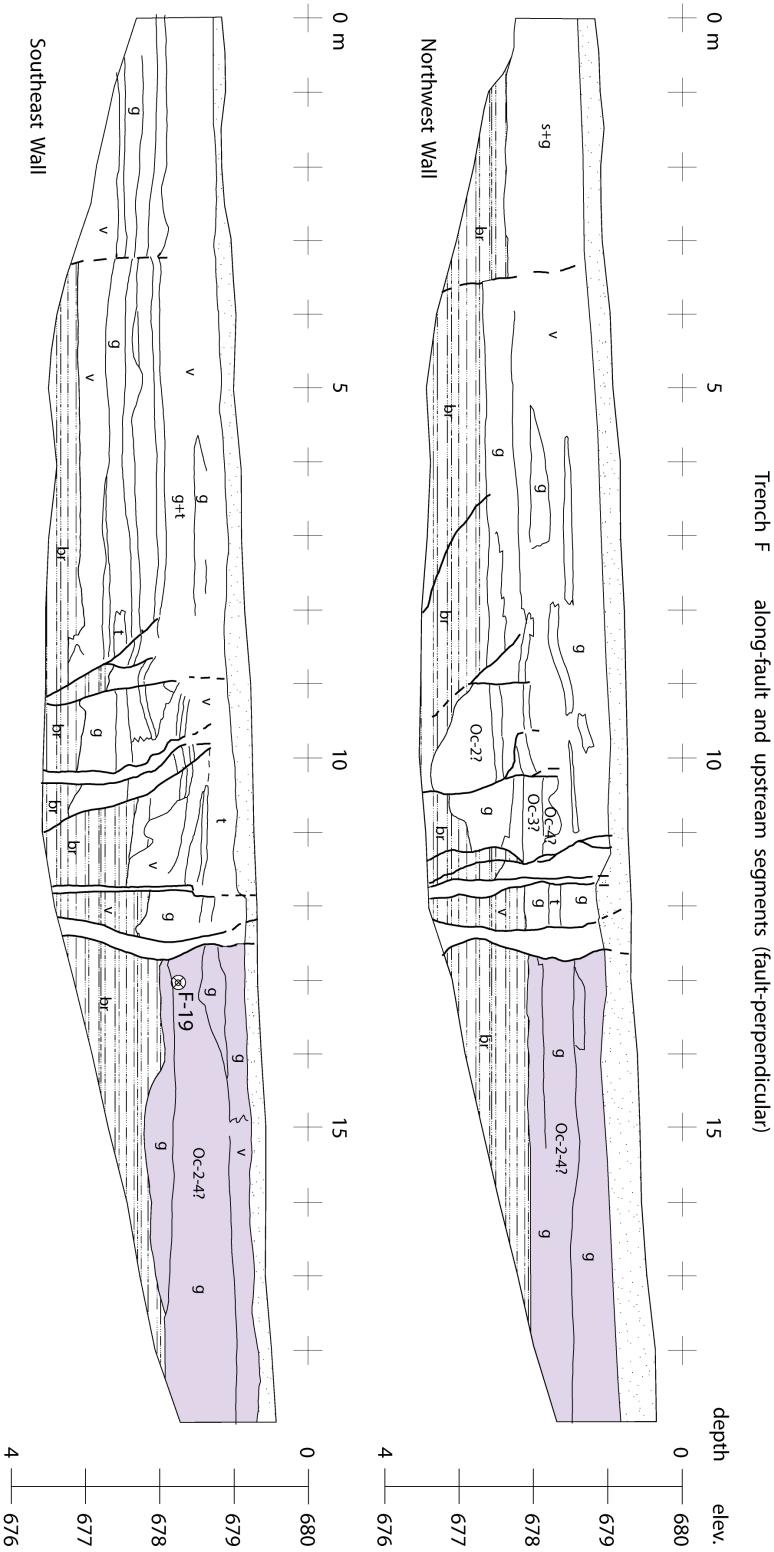
Trench F along-fault and upstream segments (fault-perpendicular)
Northwest Wall
Southeast Wall
0 m
5
10
15
depth
elev.
0
4
679
678
677
676
680
s+g
g
v
br
t
g+t
Oc-2?
Oc-3?
Oc-2-4?
F-19

Figure 4.25

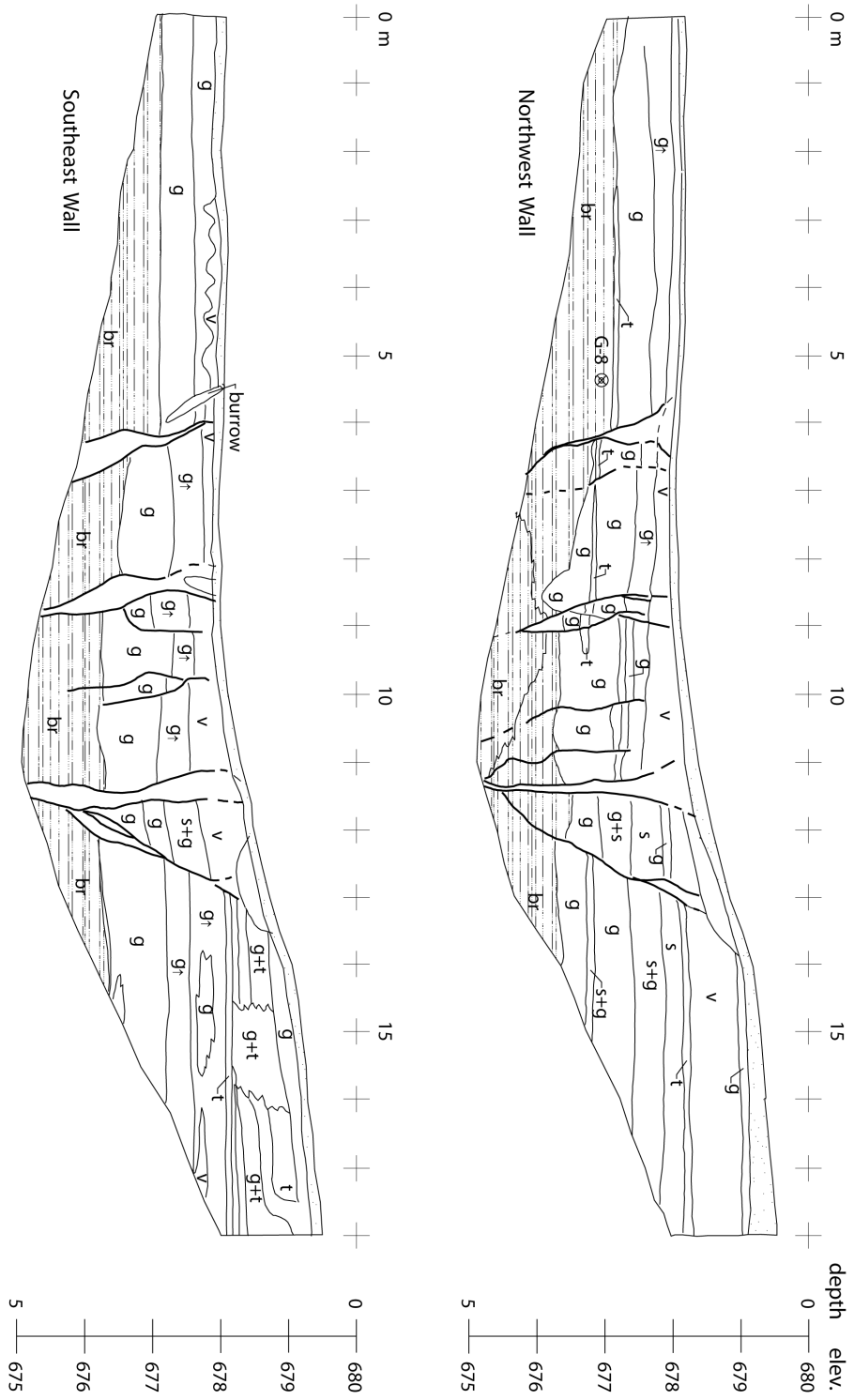
Trench G
along-fault segment (fault perpendicular)
Northwest Wall
Southeast Wall
G-8
burrow
0 m
5
10
15
depth
elev.
0
5
675
676
677
678
679
680

Figure 4.26

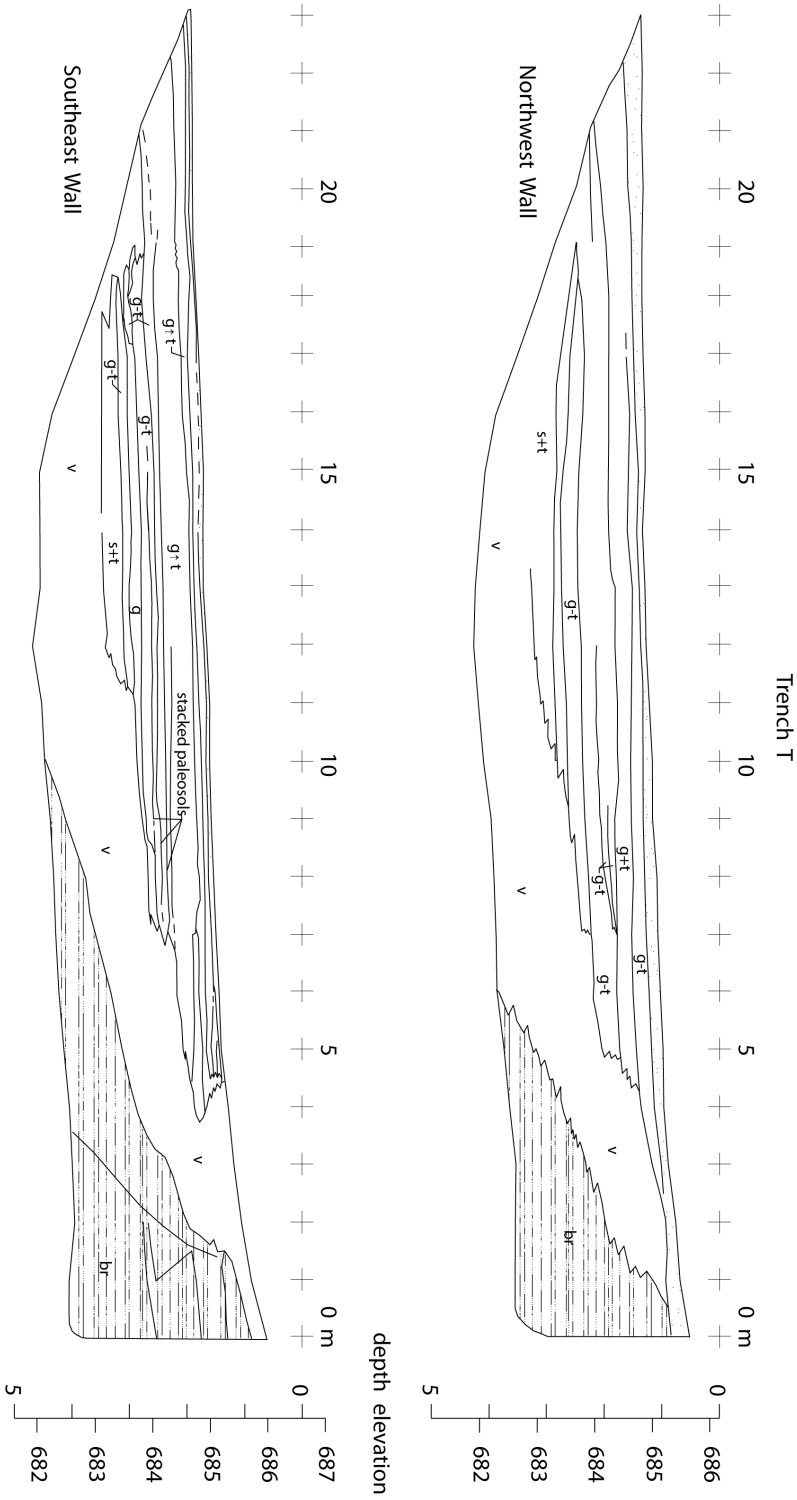
Trench T
Northwest Wall
Southeast Wall
depth elevation
0 m
5
10
15
20
0
686
685
684
683
682
687
s+t
g-t
g↑t
v
br
g
stacked paleosols

Figure 4.27

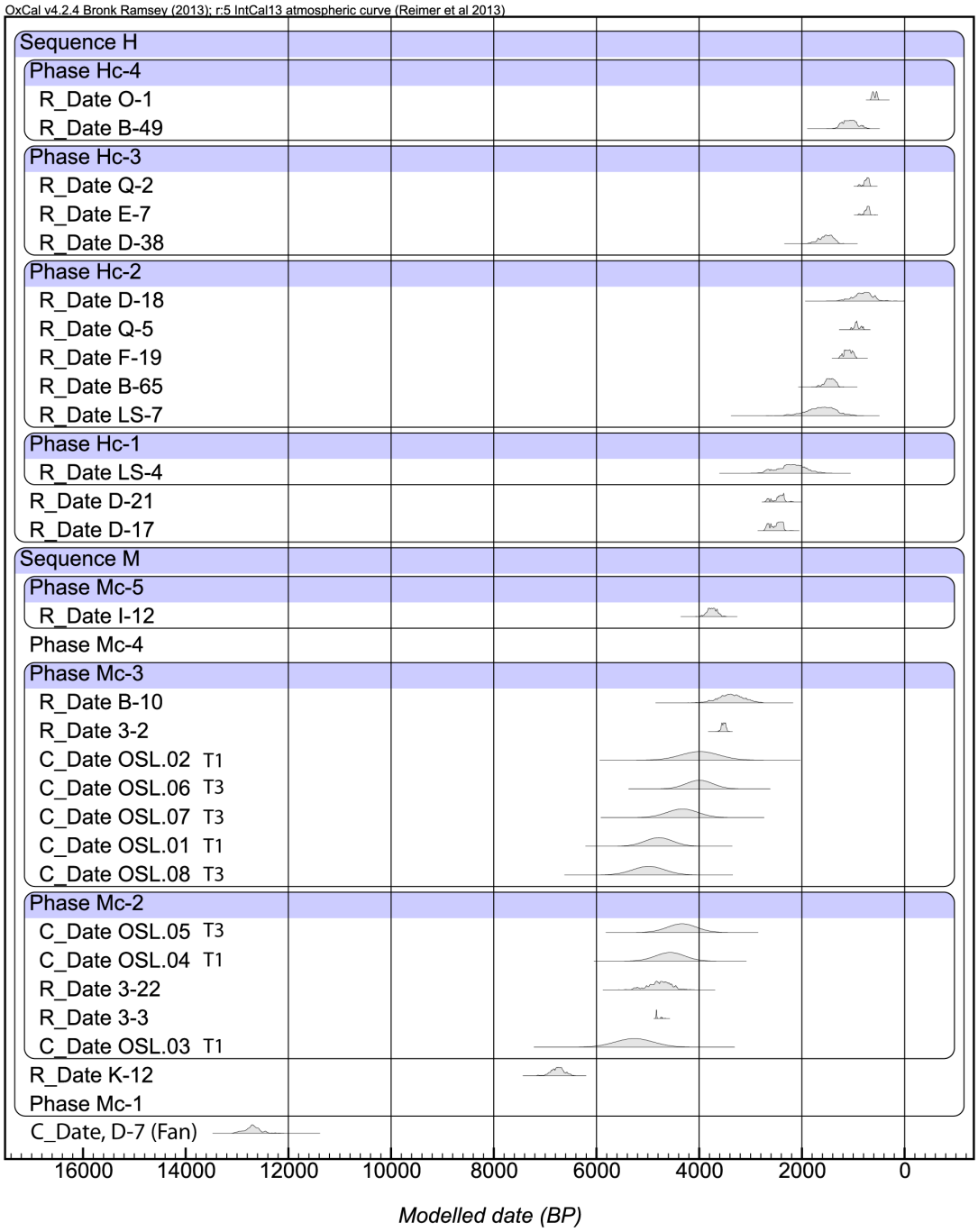
OxCal v4.2.4 Bronk Ramsey (2013); r:5 IntCal13 atmospheric curve (Reimer et al 2013)
Sequence H
Phase Hc-4
R_Date O-1
R_Date B-49
Phase Hc-3
R_Date Q-2
R_Date E-7
R_Date D-38
Phase Hc-2
R_Date D-18
R_Date Q-5
R_Date F-19
R_Date B-65
R_Date LS-7
Phase Hc-1
R_Date LS-4
R_Date D-21
R_Date D-17
Sequence M
Phase Mc-5
R_Date I-12
Phase Mc-4
Phase Mc-3
R_Date B-10
R_Date 3-2
C_Date OSL.02 T1
C_Date OSL.06 T3
C_Date OSL.07 T3
C_Date OSL.01 T1
C_Date OSL.08 T3
Phase Mc-2
C_Date OSL.05 T3
C_Date OSL.04 T1
R_Date 3-22
R_Date 3-3
C_Date OSL.03 T1
R_Date K-12
Phase Mc-1
C_Date, D-7 (Fan)
16000
14000
12000
10000
8000
6000
4000
2000
0
Modelled date (BP)

Figure 4.28

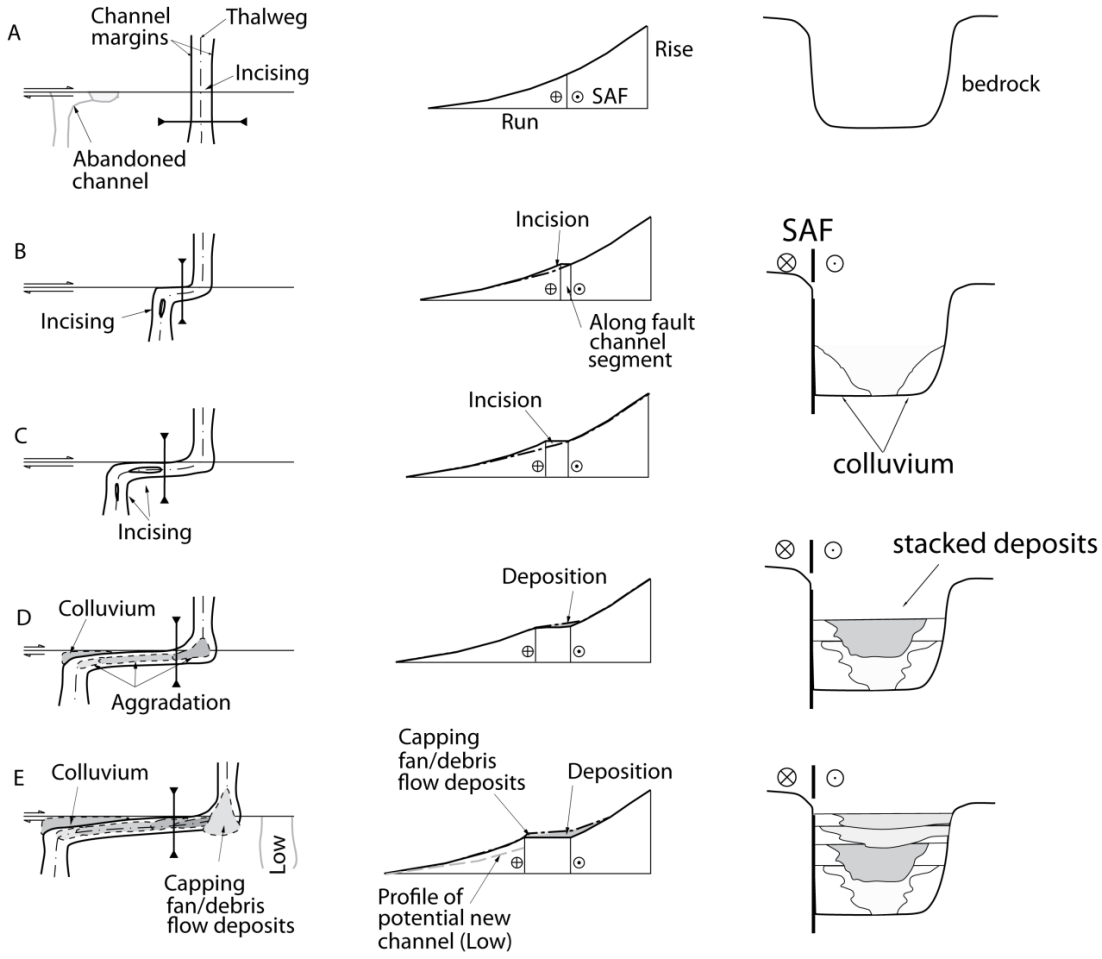
A
Channel margins
Thalweg
Incising
Abandoned channel
B
Incising
C
Incising
D
Colluvium
Aggradation
E
Colluvium
Low
Capping fan/debris flow deposits
Rise
SAF
Run
bedrock
Incision
Along fault channel segment
Incision
SAF
colluvium
stacked deposits
Deposition
Capping fan/debris flow deposits
Deposition
Profile of potential new channel (Low)

Figure 4.29

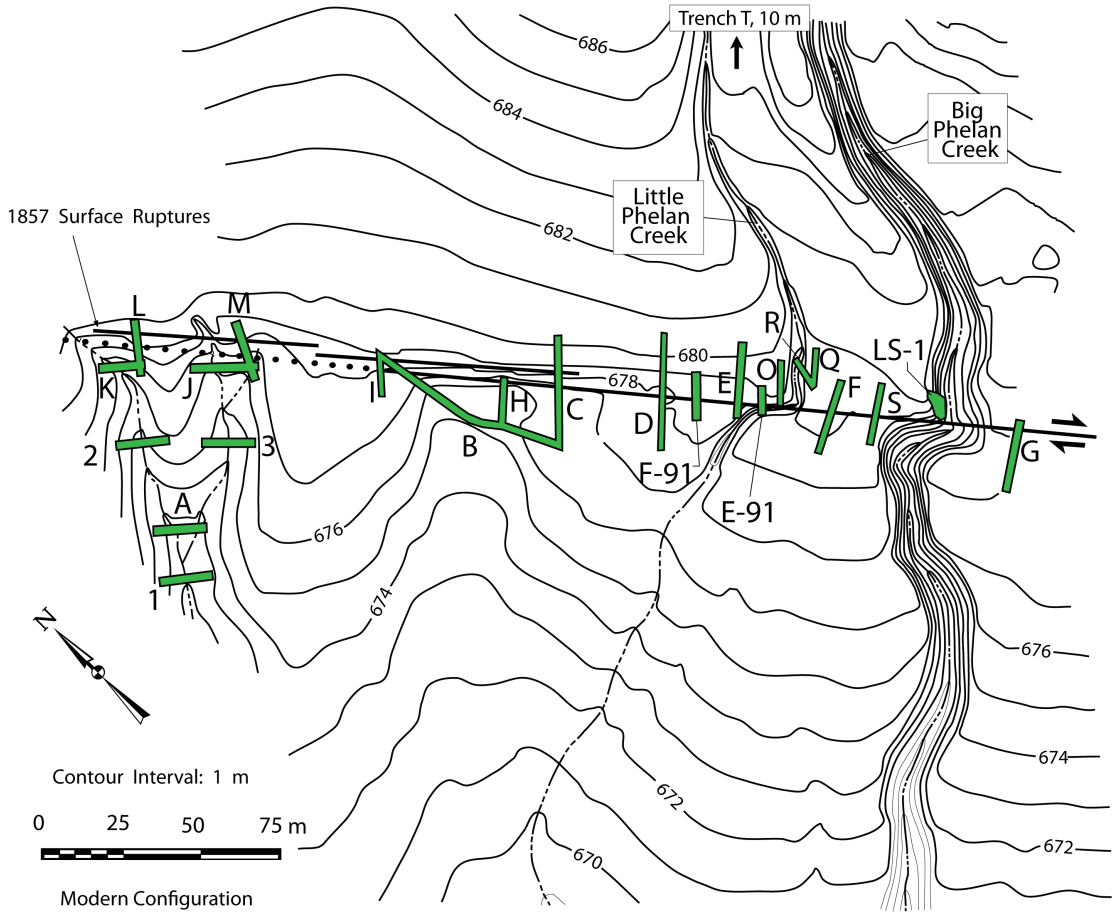
Trench T, 10 m
686
684
682
680
678
676
674
672
670
Big Phelan Creek
Little Phelan Creek
1857 Surface Ruptures
L
M
K
J
I
H
C
B
D
E
R
O
N
Q
F
S
LS-1
G
F-91
E-91
2
3
A
1
N
Contour Interval: 1 m
0 25 50 75 m
Modern Configuration

Figure 4.30

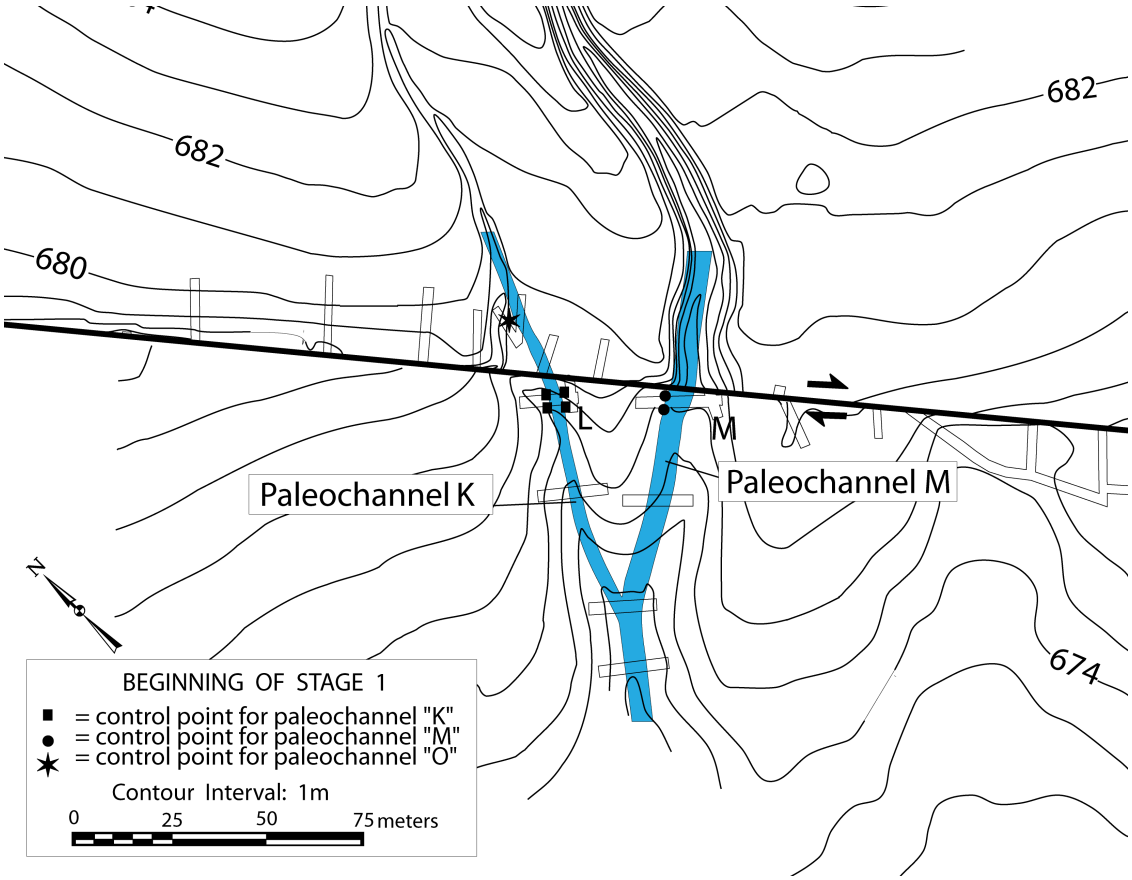
682
682
680
674
L
M
Paleochannel K
Paleochannel M
N
BEGINNING OF STAGE 1
= control point for paleochannel "K"
= control point for paleochannel "M"
= control point for paleochannel "O"
Contour Interval: 1m
0
25
50
75 meters

Figure 4.31

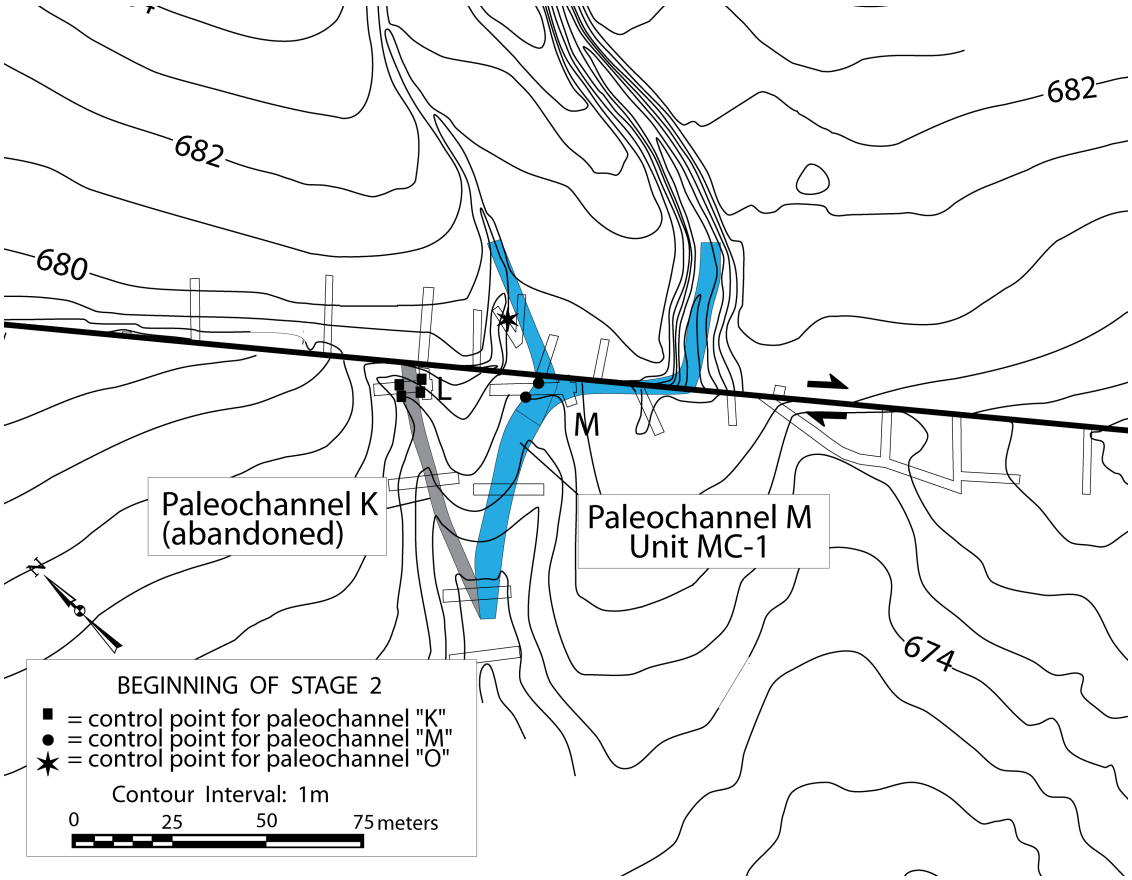
682
682
680
674
L
M
Paleochannel K
(abandoned)
Paleochannel M
Unit MC-1
N
BEGINNING OF STAGE 2
= control point for paleochannel "K"
= control point for paleochannel "M"
= control point for paleochannel "O"
Contour Interval: 1m
0
25
50
75 meters

Figure 4.32

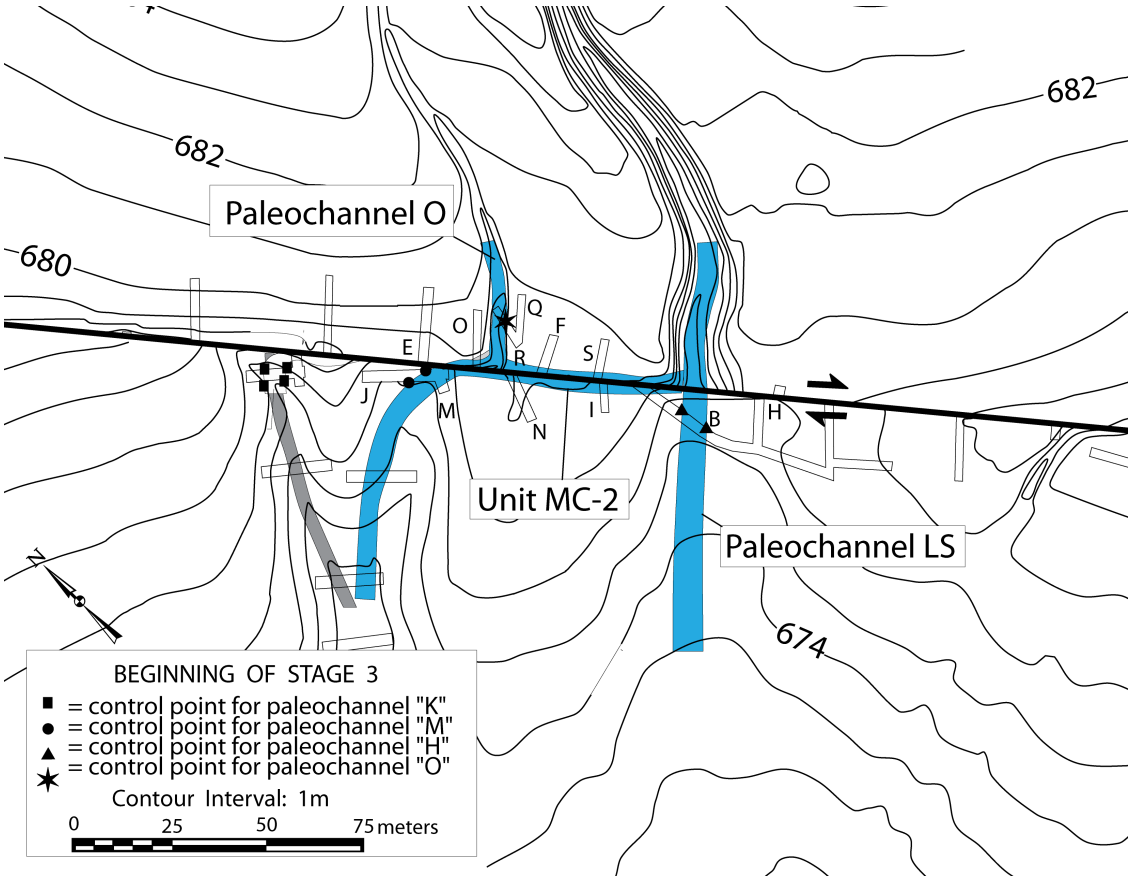
682
682
Paleochannel O
680
Q
O
F
E
R
S
J
M
N
I
B
H
Unit MC-2
Paleochannel LS
674
N
BEGINNING OF STAGE 3
= control point for paleochannel "K"
= control point for paleochannel "M"
= control point for paleochannel "H"
= control point for paleochannel "O"
Contour Interval: 1m
0
25
50
75 meters

Figure 4.33

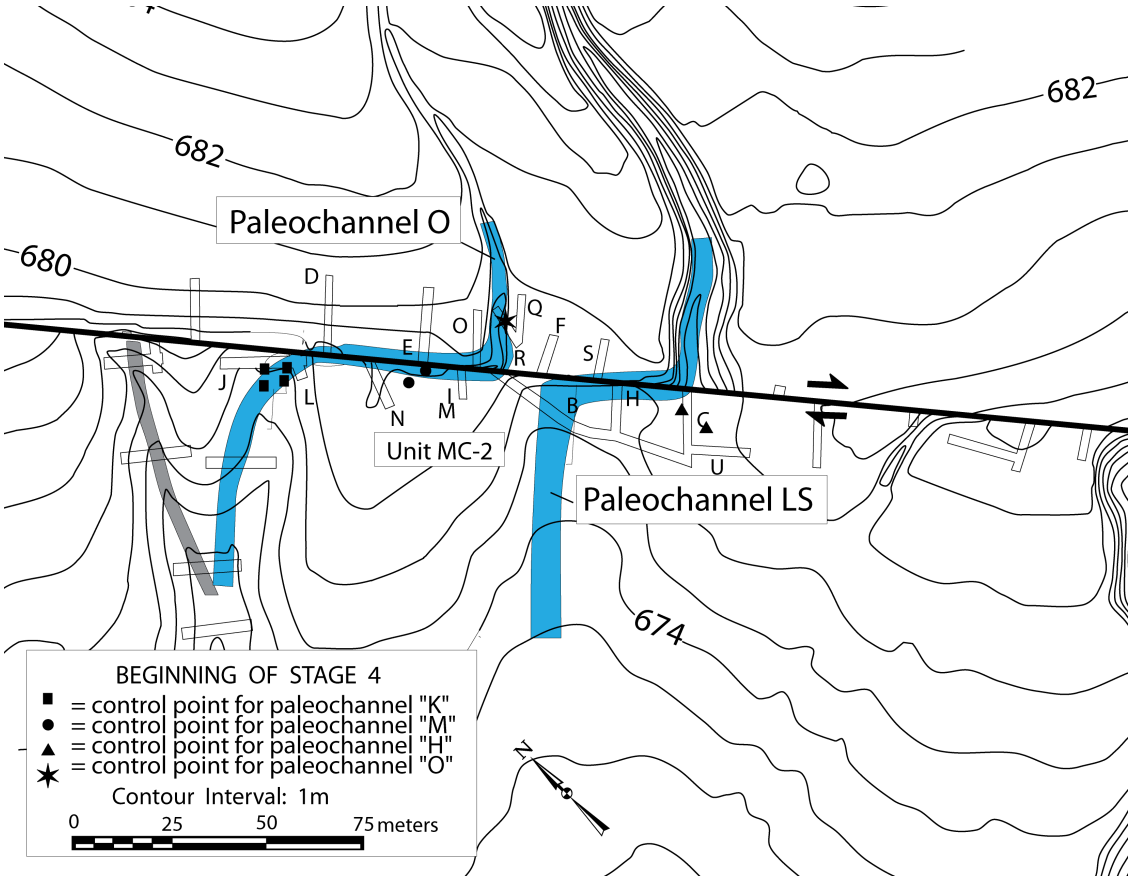
682
682
680
Paleochannel O
D
Q
F
O
E
R
S
J
L
N
M
I
B
H
C
U
Unit MC-2
Paleochannel LS
674
BEGINNING OF STAGE 4
= control point for paleochannel "K"
= control point for paleochannel "M"
= control point for paleochannel "H"
= control point for paleochannel "O"
Contour Interval: 1m
0
25
50
75 meters
N

Figure 4.34

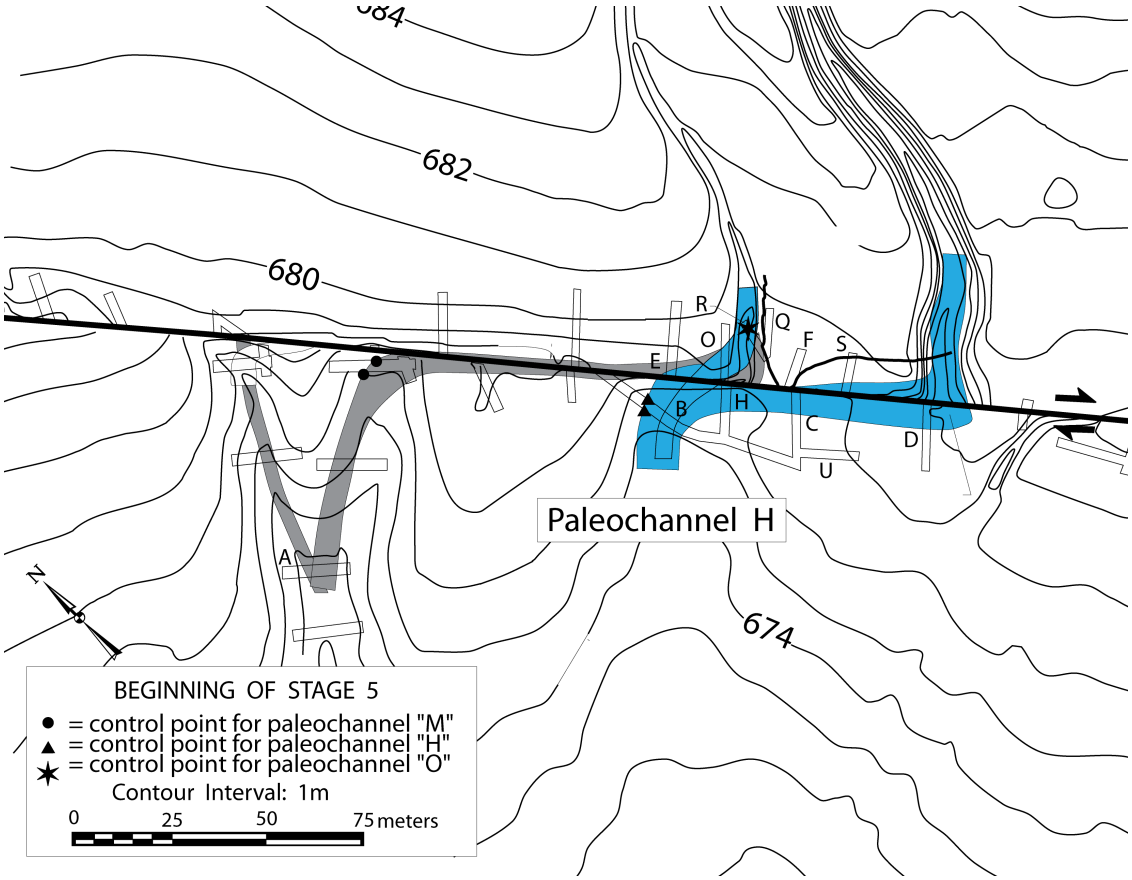
684
682
680
674
R
O
Q
F
S
E
H
B
C
D
U
A
Paleochannel H
N
BEGINNING OF STAGE 5
= control point for paleochannel "M"
= control point for paleochannel "H"
= control point for paleochannel "O"
Contour Interval: 1m
0
25
50
75 meters

Figure 4.35

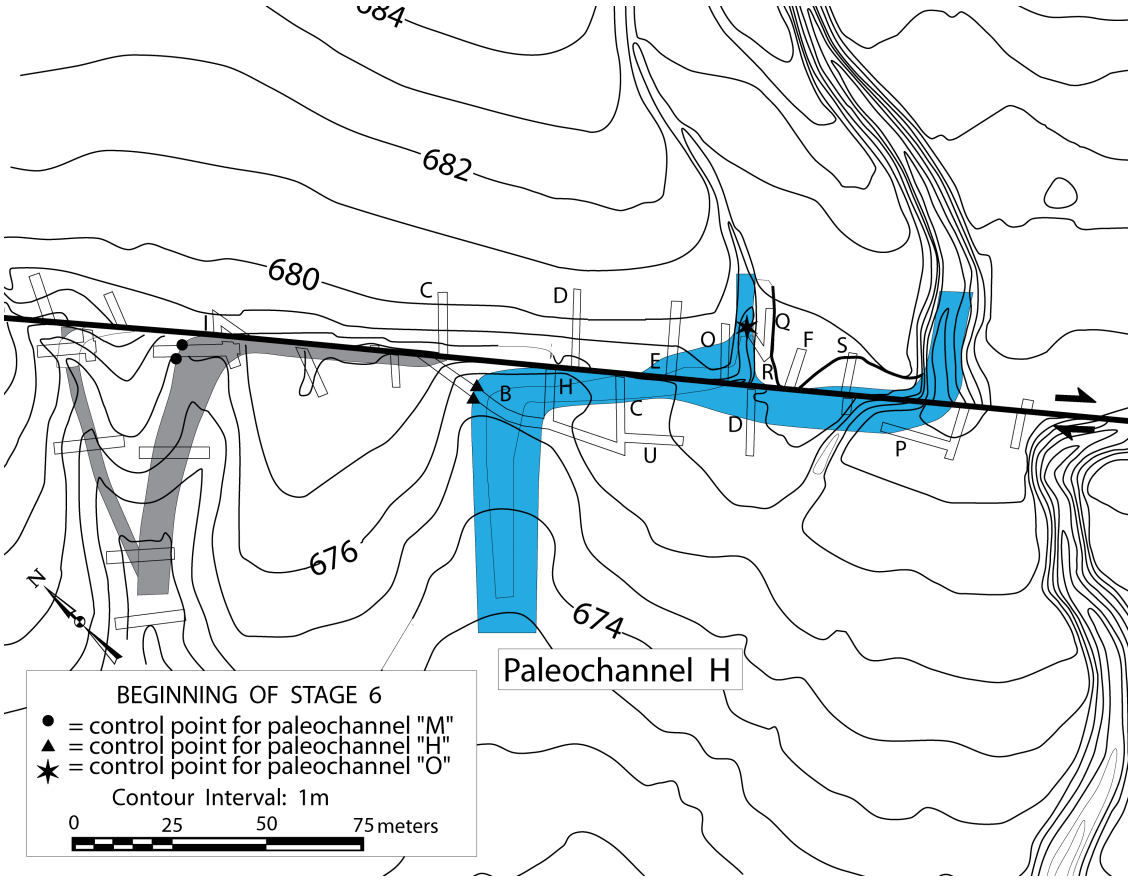
684
682
680
676
674
C
D
E
O
Q
F
S
R
B
H
C
D
U
P
Paleochannel H
BEGINNING OF STAGE 6
= control point for paleochannel "M"
= control point for paleochannel "H"
= control point for paleochannel "O"
Contour Interval: 1m
0
25
50
75 meters

Figure 4.36

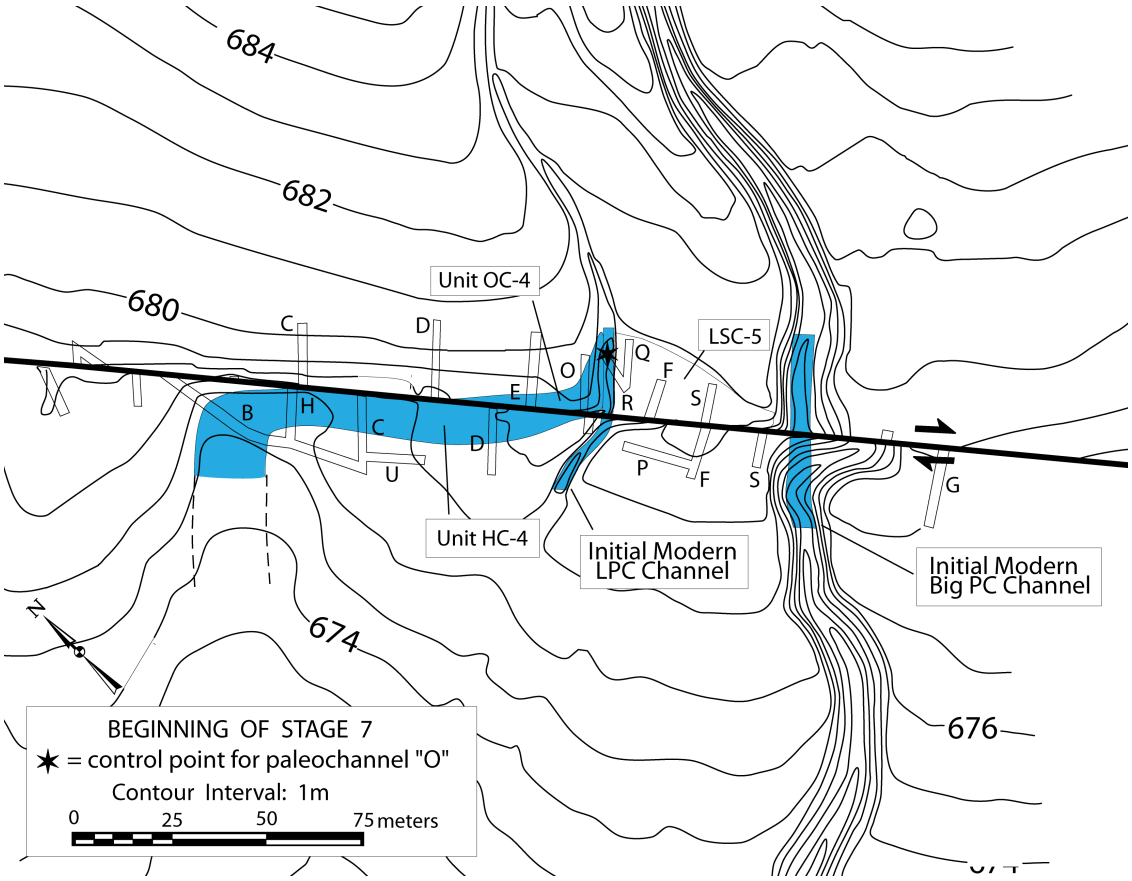
684
682
680
674
676
Unit OC-4
LSC-5
Unit HC-4
Initial Modern
LPC Channel
Initial Modern
Big PC Channel
C
D
O
Q
F
S
E
R
B
H
C
D
U
P
F
S
G
N
BEGINNING OF STAGE 7
= control point for paleochannel "O"
Contour Interval: 1m
0
25
50
75 meters

Figure 4.37

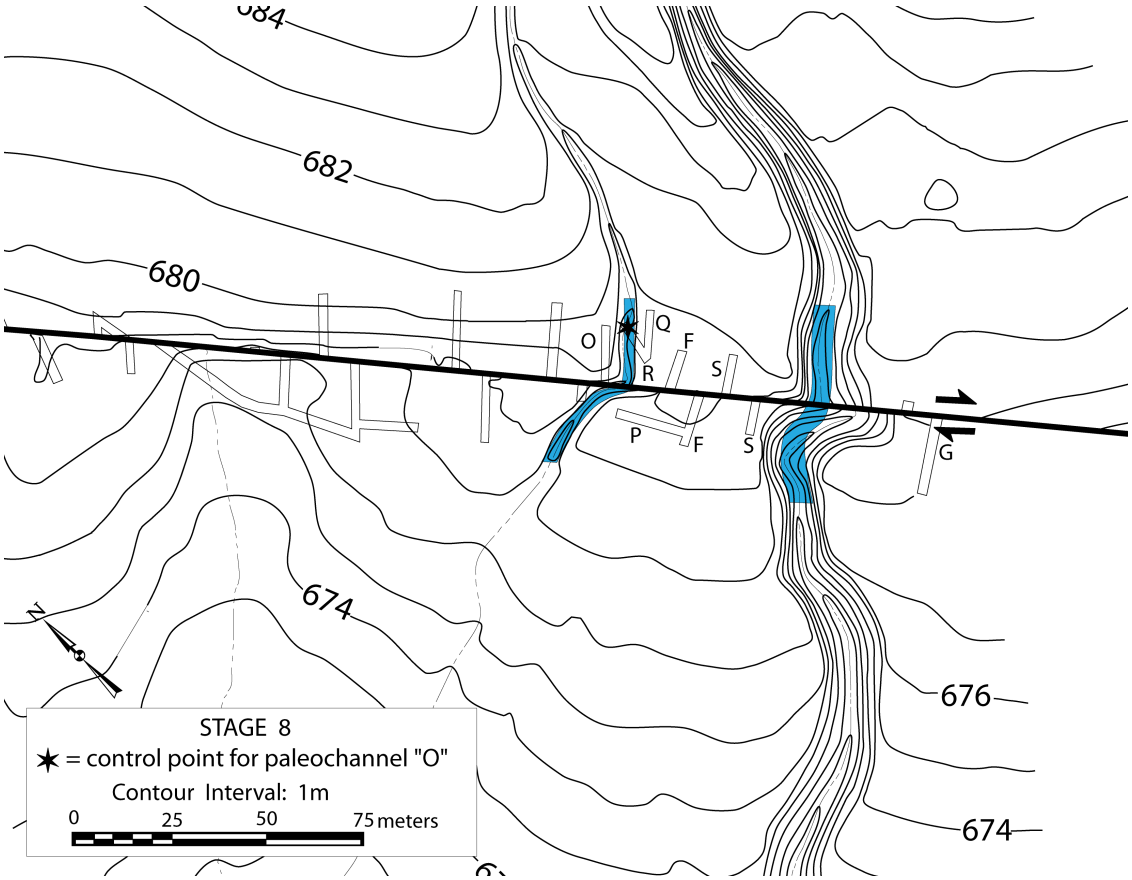
684
682
680
674
676
674
O
Q
F
S
R
P
F
S
G
STAGE 8
= control point for paleochannel "O"
Contour Interval: 1m
0
25
50
75 meters

Figure 4.38

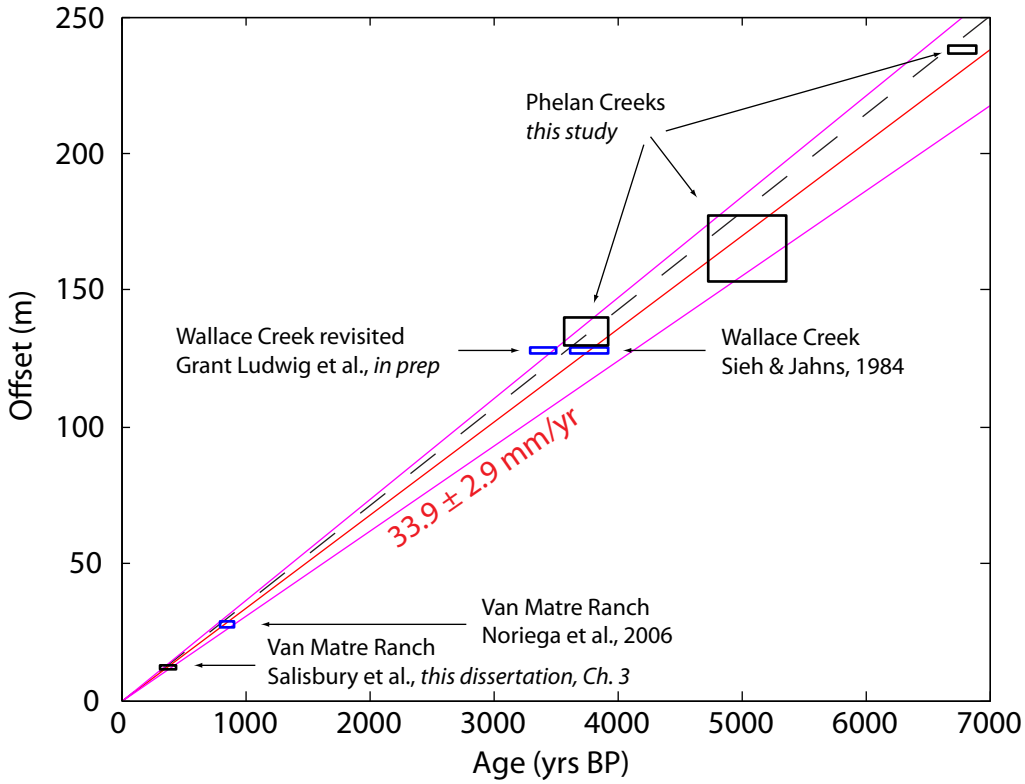
Offset (m)
Age (yrs BP)
0
50
100
150
200
250
0
1000
2000
3000
4000
5000
6000
7000
Phelan Creeks
this study
Wallace Creek revisited
Grant Ludwig et al., in prep
Wallace Creek
Sieh & Jahns, 1984
33.9 ± 2.9 mm/yr
Van Matre Ranch
Noriega et al., 2006
Van Matre Ranch
Salisbury et al., this dissertation, Ch. 3

Figure 4.39

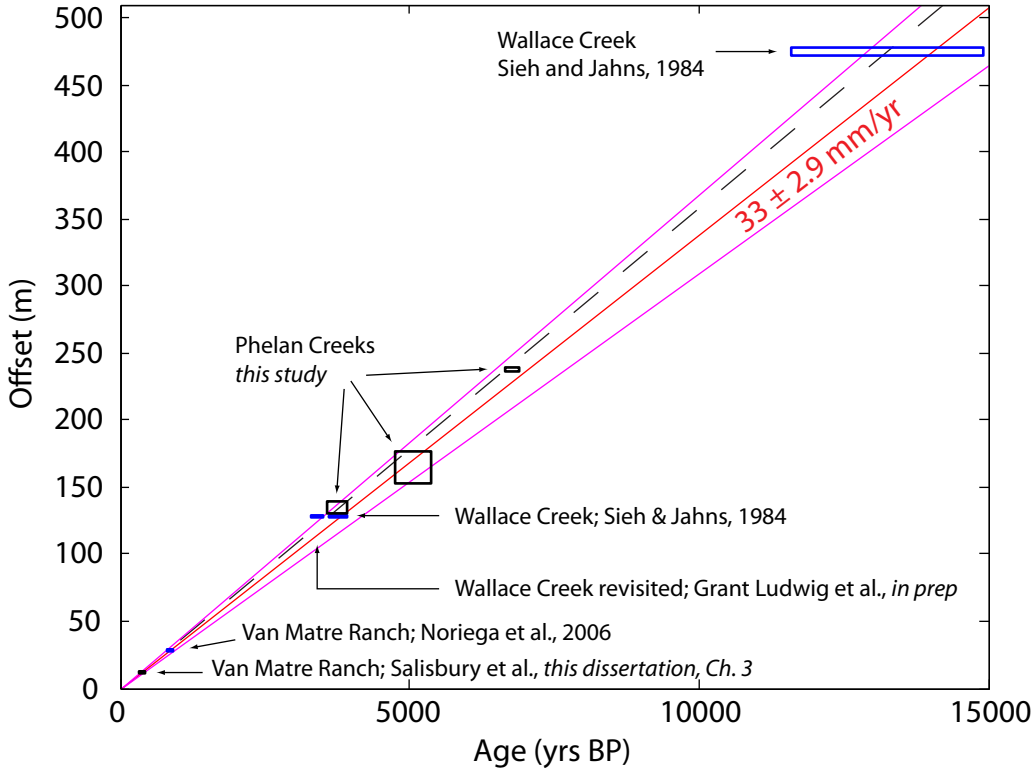
Wallace Creek
Sieh and Jahns, 1984
33 ± 2.9 mm/yr
Phelan Creeks
this study
Wallace Creek; Sieh & Jahns, 1984
Wallace Creek revisited; Grant Ludwig et al., in prep
Van Matre Ranch; Noriega et al., 2006
Van Matre Ranch; Salisbury et al., this dissertation, Ch. 3
Offset (m)
Age (yrs BP)
0
50
100
150
200
250
300
350
400
450
500
0
5000
10000
15000

CHAPTER 5

LATE HOLOCENE EARTHQUAKE BEHAVIOR OF THE WEST-CENTRAL ALTYN TAGH FAULT, XINJIANG, CHINA

ABSTRACT

The earthquake behavior of intra-continental strike-slip faults is poorly understood, particularly where actively deforming areas lie adjacent to stable regions. Strain concentration along large structures can produce great earthquakes, but what is the longest rupture (i.e., the biggest earthquake) possible along a geometrically simple strike-slip fault? At over 1,300 km in length, the Altyn Tagh Fault (ATF) in northwestern China is one of the largest intra-continental strike-slip faults in the world. Despite its potential for great earthquakes, the earthquake history of the ATF remains poorly known. We combine detailed structural and geomorphic mapping with paleoseismic excavations along the western third of the ATF (86-88˚E) to compare the earthquake rupture histories on opposite sides of the Sulamu Tagh (37.8˚N, 87.3˚E) double-bend restraining step that forms a ~6,000 m-elevation, ~40 km-long geometric complexity in the otherwise linear, ~200 km-long Cherchen He section of the ATF. We excavated and documented structural relationships of displaced stratigraphic horizons in five small (<50 m-long, <15 m-wide) shutter ridge-ponded basins along the most recent rupture trace. Three trench sites are west (TJ, 37.69˚N, 86.55˚E; T105, 37.71˚N, 86.61˚E; and T123, 37.72˚N, 86.68˚E) and two are to the east (DQT1 & DQT2, 37.98˚N, 87.82˚E) of Sulamu Tagh. We build a two-event earthquake catalog to the west of the Sulamu Tagh and tentatively date a single event (the most recent earthquake) east of the Sulamu Tagh. Additionally, we combine our new paleoseismic results with previously unpublished work from the same region as

a check on logging technique and event interpretation. With these combined results, we build a four-event earthquake catalog west of the Sulamu Tagh. Lastly, we speculate about the synchronicity of the most recent earthquake on opposite sides of the double-bend restraining step. Future work will allow for better correlation of earthquake histories and potentially reveal its likelihood as a barrier to ruptures.

INTRODUCTION

The Altyn Tagh Fault (ATF) in Xinjiang, China is the largest sinistral strike-slip fault within the Indo-Asian collision zone, and at ~1,300 km is one of the largest intracontinental strike-slip faults in the world (Figure 5.1). Striking ~65-70˚, this fault defines the northwest boundary of the Tibetan Plateau and it is assumed that together, the Altyn Tagh, Kunlun, and Karakoram faults have accommodated a significant portion of the eastward motion of the raised physiographic province (Molnar and Tapponnier, 1975; Tapponnier and Molnar, 1977; Cowgill et al., 2003) (Figure 5.1). The surface expression of the ATF is remarkably well-preserved and linear, with general fault geometry complicated by only a few restraining double-bends and steps of various sizes (10's to 100's of km). For this study, we focus on a ~200 km reach of the western ATF where the Sulamu Tagh (elevation ~6,000 m) restraining double-bend (length ~40 km) is the main geometric complexity (Figure 5.1).

Despite the tectonic significance of the ATF, the slip rate and the earthquake history of the west-central ATF remain unclear. Even for the late Holocene, slip rate estimates range from 9-30 mm/yr (Chen et al., 2000; Shen et al., 2001; Washburn et al, 2001 & 2003; Meriaux et al., 2004 & 2005; Royer et al., 2006; Gold et al, 2009; Cowgill et al, 2009). These large discrepancies are attributed to several different factors. For example, results depend on the type of measurement being made: measured offset of a dated geologic landform, inferred from a paleoseismic trench event history and small-scale displaced landforms, or inferred from geodetic strain rates.

Millennial-scale slip rates estimated from offset landforms in the Cherchen He and Sulamu Tagh regions are nearly 30 mm/yr (Peltzer 1989; Meriaux et al., 2004 &

2005). The few paleoseismic studies along the ATF suggest slower slip rates, albeit with significantly greater uncertainties. Washburn et al. (2001, 2003) suggest that the ATF accommodates a maximum of 20 mm/yr of slip northeast of the Qing Shui Quan reach (Figure 5.1). Similarly, paleoseismic data at the western end of the ATF from Muretta (2009) suggest slip rates that range from 4-26 mm/yr along Cherchen He, but their preferred interpretations suggest slip rates of 3-15 mm yr. Similarly, geodetic measurements made continuously over the last few decades imply slip rates that agree with the few paleoseismic datasets along the fault. Displacements of dense, northwest trending, GPS transects orthogonal to the central ATF estimate 9.0 +4.4/-3.2 mm/yr of left-lateral displacement (He et al., 2013). These studies agree with earlier linear GPS transect results (9 ± 5 mm/yr; Wallace et al., 2004; Bendick et al., 2000) and regional GPS network estimates (up to ~10 mm/yr; Zhang et al., 2007).

This project provides an important opportunity to build earthquake chronologies on opposite sides of a crustal-scale geometric complexity and to evaluate its likelihood as a barrier to through-going rupture. We investigate three trenches (TJ, 37.69˚N, 86.55˚E; T105, 37.71˚N, 86.61˚E; and T123, 37.72˚N, 86.68˚E) west of Sulamu Tagh in the Cherchen He reach and two trenches (DQT1 & DQT2, 37.98˚N, 87.82˚E) east of the Sulamu Tagh in the Qing Shui Quan reach (Figure 5.1). Trenches west of the Sulamu Tagh were initially excavated in 2007 by Muretta (2009; unpublished MS thesis). The westernmost Cherchen He trench (TJ; Figure 5.1, orange star) was unlogged and undated. The other two western trenches (T105 and T123; Figure 5.1, yellow stars) were previously logged by Muretta (2009) and one of which (T105) was sampled for age constraints. We re-excavated, re-logged, and re-sampled all three of these trenches for

earthquake chronologies. Our new work in the Cherchen He reach establishes the timing for the two most recent ruptures of the western ATF.

In addition to building an earthquake chronology west of the Sulamu Tagh, we extended these efforts by traveling eastward to the Qing Shui Quan area and excavating two new paleoseismic trenches where strike-slip and thrust faulting are distributed among two separate fault strands (~10 m apart) (Figure 5.1, green star, and Figure 5.2). We present results from new excavations east of the Sulamu Tagh where we have tentative evidence for the most recent surface-rupturing earthquake. We discuss the potential for the most recent earthquakes on opposite sides of the Sulamu Tagh to be the same event.

Lastly, to extend our earthquake chronology, we compare our paleoseismic logging, event interpretations, and earthquake timing to the existing, unpublished work by Muretta (2009) in the Cherchen He reach. Where possible, based on stratigraphic correlation between old and new excavations, we combine datable materials from the two studies to form a single earthquake catalog for the last four events. This re-visitation of existing trenches and combination of geochronologic controls between studies is necessary to build a more robust multi-event earthquake chronology. There is a marked lack of radiocarbon material in the arid region and adequate dating of individual layers throughout a faulted sequence of sediments is crucial to estimating earthquake ages.

METHODS

During the summer field season of 2012, we revisited three fault-perpendicular trenches (TJ, T105, and T123) in the Cherchen He reach west of the Sulamu Tagh that were originally excavated by Muretta in 2007 (Figure 5.1). At these sites, trench face degradation and aeolian deposition had partially re-filled trenches. We exposed pristine stratigraphic sections by cutting back the existing, degraded faces ~1 m from their original cuts. We also excavated two new trenches (DQT1 and DQT2) east of the Sulamu Tagh (Figures 5.1 and 5.2). Trench locations were initially identified based on a combination of detailed structural, geologic, and geomorphic mapping. In addition to locating sites on the most recently active fault traces, it is important that deposition of sedimentary facies occurs frequently enough to identify individual deformation events, but not at such a high rate that earthquake deformation is completely buried and unreachable by hand excavations. East of the Sulamu Tagh, we used the same criteria to locate new trench sites. We mapped active fault traces, fault-related geomorphic features, and other lineaments using mylar overlays on Digital Globe satellite imagery (e.g., Figure 5.2). We dug several shallow test-pits to assess sedimentation rates and package thicknesses before excavating new trenches.

We dug our trenches by hand to depths of ~1.5 m. In some important fault zones, we added narrow slot trenches down to depths of ~2 m. After excavation, we constructed 1 m-wide by 0.5 m-tall nail and string grids on all excavated faces as a reference for trench logging and digital photographs. We used 1 mm blank grid paper to log trench exposures at scales ranging from 1:25 to 1:20. After the fieldwork, we used photographs to construct high-resolution photomosaics of the trenches for reference. We took a total

of 58 radiocarbon samples from all of our trenches and 46 survived pre-treatment and were large enough to be measured (Table 5.1). Five of our samples contained positive parts per million fractions of the Modern Standard and are therefore unusable (modern), leaving us with 41 radiocarbon dates (Table 5.1). These age constraints are crucial to properly dating earthquake events.

In the simplest scenario, (i.e. dating the most recent surface-rupturing earthquake at a site), ages from two sedimentary layers are required. The first age must come from a sedimentary package that was faulted in the most recent earthquake. The second age must come from a younger, un-faulted package of sediments deposited after the most recent earthquake. The span of time between the two sedimentary packages, therefore, defines a window during which the earthquake must have occurred. The interface between two units, known as an event horizon, represents the window during which the most recent earthquake must have occurred. We use OxCal v4.2.4 (Bronk Ramsey, 2013) to calibrate our individual radiocarbon results with the r:5 IntCal3 atmospheric curve (Reimer et al., 2013) and to calculate 95.4% confidence ranges for timing of individual event horizons.

We extensively sampled stratigraphic units in all four of our trenches for radiocarbon (^{14}C) age control of past earthquakes but the well-preserved event horizons are particularly difficult to date due to a marked lack of preserved organic materials. The most abundant available organic materials are buried pieces of friable rabbit dung. We see modern-day evidence of intermittent ponding in our selected sag structures, and small-scale ripple action aligns the dung at the edges of past shallow ponds. Even the modern examples of dried rabbit dung are highly friable and we think it is unreasonable for them to persist at the ground surface for more than a few years (unlike pieces of

charcoal, for instance, that may persist in the landscape for some time). In general, we assume that there is very little inherited age to the majority our buried ^{14}C samples (this was also noted by Washburn, et al., 2003). All ages shown in trench logs are represented as ^{14}C ages BP. We calibrate ^{14}C ages using OxCal and use it for determining earthquake age models in trenches 105 and DQT2 (Bronk Ramsey, 2013; Reimer et al., 2013) (Figures 5.9 and 5.10). Additionally, we show the locations of OSL samples (green hexagons) that we hope to analyze at a later date.

RESULTS

In general, our excavations expose distinct, alternating layers of coarse-grained, locally-sourced alluvial fan deposits and finely laminated, sandy silt loess (aeolian) deposits. In most cases, younger packages of material are deposited on top of or are faulted against older metamorphic bedrock or highly indurated alluvial fan material. Our sites preserve evidence of significant deformation and in the best scenarios provide evidence for three to four surface-rupturing earthquakes in the top few meters of sediment. The next several paragraphs will discuss the results of individual trenches from southwest to northeast. We present simplified, interpreted trench logs and associated photomosaics for reference. In some cases, we lack photograph coverage to completely reconstruct entire trenches, but we have sufficient records for areas with the most significant deformation.

TJ

Trench J, the westernmost trench in the Cherchen He reach, is ~13 m long and 1.5 m deep (Figure 5.1 and 5.3). This trench was originally excavated by Muretta in 2007 but was not logged or sampled until this study in 2012. Trench J contains evidence of

significant deformation in the most recent event, with several fault splays cutting through alluvial sag-pond sands butted against bedrock to the south. Ruptures reach the surface over a ~5 m-wide zone. The faults that we can trace to the surface correlate well with degraded geomorphic evidence of surface ruptures, including small (<~50 cm tall) fault scarps and mole tracks (that capture aeolian sediments) that intersect our trench (e.g., Figure 5.4). We see cracking across the entire width of the trench. The north end of the trench is buried beneath a largely un-faulted, poorly stratified, ~1 m-thick silty sand aeolian deposit that contains disparate ^{14}C ages (Figure 5.3). Sample 4, at 1060 ± 20 ^{14}C BP is a maximum age and likely represents a rare case of detrital age inheritance. We prefer sample 5, at 140 ± 20 ^{14}C BP as the age of this young deposit in TJ. It is clear, particularly near samples 4 and 5 (Figure 5.3) that this unit caps the most recent episode of major deformation. Sample 3, from the heavily faulted fluvial sands below the aeolian deposit (on the east face) pre-dates the most recent surface rupturing event. We therefore bracket the age of the most recent event here between 530 ± 25 ^{14}C BP and 140 ± 20 ^{14}C BP. We calculated the 95.4% probability range of the earthquake event at 329 ± 219 yr Cal BP. Because most fault strands rupture to the surface, we are unable to interpret any earthquakes older than the most recent event at this site.

T105

Trench 105, the central trench in the Cherchen He reach, is ~8 m wide and nearly 2 m deep at its deepest point (Figures 5.1 and 5.5). This trench was originally excavated, logged, and sampled by Muretta in 2007. We cut both faces of the trench back ~1 m to expose a fresh representation of the local stratigraphy. Figure 5.5 shows the west face of our interpreted trench logs. By cutting back the existing (2007) eastern exposure ~1 m,

we moved into slightly different sedimentary environment outside of the meter-scale shutter-ridge ponded basin and lack stratigraphic packages and resolution to build an earthquake chronology. Therefore, we only present the log of the west face.

This excavation exposes alternating finely-laminated silt deposits and coarse-grained, sand-supported pebble and gravel units derived from local drainages to the north. The fluvial units commonly fine upwards from pebbles to fine sands. These alternating packages are deposited against highly faulted metamorphic bedrock at the south end of our trench. We identify evidence for three, and possibly four earthquake events in the west wall of T105 (Figure 5.5). The most recent event horizon (shown in red) is un-deformed and we have two ^{14}C samples (13 and 22) from above and one sample (15) from below this event. The penultimate event at this site (shown in green) shows evidence for disruption in the most recent event but also caps several fault splays from the penultimate event. We have one sample (15) from above and five samples (18, 24, 17, 20, and 21) from below this event horizon (See Tables 5.1 and 5.2). Evidence for the third (blue) earthquake is less clear (Figure 5.5). However, the fourth event at this site is well-represented by a clear angular unconformity between laminated silts (dipping to the south) below the event and a horizontally-bedded coarse sand that fines upwards above the event horizon. We have no age control for the third and fourth events.

Our radiocarbon samples alone are sufficient to establish age ranges for the last two events with 95.4% confidence. Expressed as median age estimates (calibrated years BP) with associated uncertainties (for 95.4% confidence intervals), the most recent and penultimate events occurred at 295 ± 136 yr CalBP and 606 ± 219 yr CalBP, respectively (Table 5.2).

T123

Trench 123 is the easternmost of three trenches in the Cherchen He reach and is located higher above the valley floor than TJ and T105 (Figures 5.1, 5.6, and 5.7). T123 is ~8 m long and is beyond ~2 m deep at its deepest point. Like the other trenches in this hillside bench setting in Cherchen He, there are alternating packages of fluvially-derived sandy pebbles and gravels and finer-grained, sandy aeolian silt packages. These units are deposited against a poorly sorted mix of highly indurated silt, sand, and pebbles that represent old alluvial fan materials. The main fault zone is localized and only <3 m-wide, but we have cracking over a ~7 m-wide zone in both trench exposures.

The sediments exposed in trench 123 preserve clear evidence of the most recent surface-rupturing event and potentially one other event (Figure 5.6). Faults from the most recent event are capped by ~25 cm of young ponded alluvial sands mixed with finer-grained, aeolian-derived silt deposits. We do not have an age estimates for the youngest capping unit. The second event, tentatively identified in only the west trench face as an upward-terminating fault splay in the lowest meter of the trench, is also of unknown age.

DQT1 and DQT2

We excavated two trenches east of the Sulamu Tagh in an area known as Duoge Quan, named from the several bedrock springs sourced <700 m north of the trench site. The surface expression of the ATF here is more complicated than in the Cherchen He, with strike- and dip-slip partitioned between two main fault strands <50 m apart (Figure 5.2). At this site, the northernmost strand is strike-slip and the southern strand is mainly dip-slip. Together, these two strands produce a <50 m wide pop-up structure rising several meters above the surrounding sloping alluvial fan. We excavated two trenches,

DQT1 on the predominately strike-slip strand, and DQT2 on the western end of the pop-up structure on the predominately dip-slip (reverse) strand (Figure 5.2).

DQT1 is ~ 10 m wide and <2 m deep (Figure 5.8). In DQT1 we exposed a distinctly alternating sequence of locally-sourced, fluvial coarse-grained pebbles, gravels, and sub-angular cobbles with finer-grained, aeolian sands and silts. We identified a distinct marker bed, consisting of finely-laminated sands and silts, across the entire trench in both the east and west faces (Figure 5.8, light blue). Evidence of the most recent earthquake is identifiable to within a few centimeters of the surface, but in most instances, the upward terminations of various fault strands are ambiguous. We found few radiocarbon samples in DQT1, unfortunately, and are not able to constrain the age of the most recent event.

DQT2 is just over 5 m wide and because it is dug into a reverse fault, is slightly deeper than 2 m (Figure 5.19). We excavated DQT2 at the western end of the pop-up structure at the Duoge Quan site, where the structure is only a few meters above the surrounding alluvial fan surface. We exposed several reverse fault splays that bring older, coarse gravel and sub-angular cobble alluvial fan materials up over younger, finer-grained gravel-rich deposits. The uppermost unit in the trench is a poorly laminated silt (loess) deposit. This young loess deposit has been thinned in the north half of the trench and is distinctly thickened at and below the reverse fault strands. From the top of the older, gravel-rich alluvial fan surface we find seven, several thousand year-old radiocarbon samples that include rabbit dung and buried plant materials (Figure 5.19). In the overlying fine-grained loess deposit, we found a single piece of rabbit dung (sample

6) dated at 195 ± 15 ^{14}C BP (Figure 5.19). We discuss the calibration of sample 6 in the following section.

DISCUSSION

We see preserved evidence of significant ground deformation in all trenches. However, even where we have significant stratigraphic resolution to identify event horizons, we lack sufficient datable materials. In two of our trenches (T105, T123) we compare our trench logs to existing, unpublished data and at one trench (T105), where stratigraphic sections are similar, we combine datable materials from both studies for better age constraints of past earthquakes. We approached the re-logging task blindly—we did not use the original trench logs as a reference. Furthermore, Arrowsmith was the only investigator to participate in both studies, logging a single trench in 2007 (T105) and a different trench in 2012 (T123). In general, where we exposed similar sedimentary sequences, our new trench-logging results are consistent with those made in 2007 but they are not identical. We will begin with a review of T123 (with no age control) and then finish with a discussion of logging and age control for T105.

Trench 123 (Figure 5.6 and 5.11) is within the steepest side-hill ponded environment, and sedimentary packages, though finely laminated, are quite thick. Our log comparisons show that we consistently identify major sedimentary packages and their respective boundaries. However, log interpretations from 2007 tentatively identify three distinct event horizons whereas we only identify two earthquake event horizons. Furthermore, our older event horizon is tentative, as we only see evidence for it in the west face of T123.

Trench 105 (Figures 5.1 and 5.5), our most promising trench, contains four potential earthquake event horizons but we are only able to build a two-event earthquake catalog because we lack adequate age control for the older, more-deformed units. This is in part because we only have proper stratigraphy in the west wall of T105. In the east, we cut into a stratigraphic section with poorly defined units, slightly outside the well-bedded stratigraphy of the small-scale ponded basin. In this exposure, although we saw evidence of recent earthquake behavior, we lacked the depositional resolution needed to identify earthquake event horizons.

In the western face of T105, we exposed a well-bedded section like that seen by Muretta in 2007. We correlate many of the individual laminated silt beds used to distinguish offset across fault strands and to define the earthquake event horizons. In our trench, however, we do not see strong evidence for the third event back, whereas Muretta interpreted the evidence to be as strong as all the others. We use radiocarbon samples from both studies to produce a single age model for the last four events at T105.

Where we identify equivalent event horizon-bound sedimentary packages, we share the radiocarbon dates from both studies. Table 5.2 shows a summary of earthquake age estimates at T105. It is important to note for the fourth event back (the oldest event, OE) we provide only a minimum age constraint. We do not have an old age for bracketing, and the most we can say is that the oldest event occurred before the stated age Cal BP.

We show four age models for earthquakes at T105, expressed as median ages (and associated uncertainties) from within the 95.4% confidence interval of the overall event age range. The first two columns show age results from the individual studies alone. For

the most recent and penultimate events (MRE and PE, respectively), the independent age estimates of rupture overlap within the associated uncertainty ranges. In the third model, MurettaJBS, we add new T105 age constraints for the MRE only. In the fourth model, MurettaJBS2, we add new T105 age constraints for all possible event horizons (samples bracketing the two most recent event horizons). The complete, calibrated age model MurettaJBS2 is shown in Figure 5.12 and we prefer this model because it includes all age constraints from both studies 2007 and 2012 field campaigns. We consistently show that the most recent event at T105 is probably only several hundred years old (286 ± 119 yr CalBP), and the penultimate event occurred around 739 ± 141 yr CalBP. Age estimates for the most recent event at TJ (329 ± 219 yr Cal BP) are consistent with T105 estimates for a young (several hundred year-old) rupture.

At DQT2, we only find a single radiocarbon sample from the young, loess-rich colluvial wedge on the reverse strand of a small pop-up structure (Figures 5.2 and 5.9). The radiocarbon age for this sample (DQT2-6, Figure 5.13) is 195 ± 15 yrs BP. The calibrated age is ambiguous, as the radiocarbon curve at this time is highly variable (Figure 5.13). There are four age ranges that are potentially likely for the sample: a 21.1 % probability that the sample is 290-267 yr CalBP; a 6.5 % probability that the sample is 213-195 yr CalBP; a 40.9 % probability that the sample is 189-146 yr CalBP; and a 26.9 % probability that the sample is modern. If we interpret that the friable rabbit dung was incorporated in a colluvial wedge shortly after the earthquake rupture, then we can use this sample to constrain the age of the most recent event east of the Sulamu Tagh. Though we cannot say for sure, if we choose the oldest possible age for this sample at

290-267 yr CalBP (21.2 % probability) then the age of this rupture is strikingly similar to the most recent event west of the Sulamu Tagh that was dated at T105 and TJ.

CONCLUSION

We re-visited three trenches west of and excavate two trenches east of the Sulamu Tagh double-bend restraining step in the western third of the Altyn Tagh Fault, a ~1,300 km-long left-lateral fault. In all of our trenches we saw evidence for significant ground deformation. We combine radiocarbon age control at T105 from an existing, unpublished study in 2009 (Muretta) with our age control acquired in 2012 to establish a four-event earthquake chronology west of the Sulamu Tagh in the Cherchen He reach. We have tentative evidence from the Duoge Quan reach east of the Sulamu Tagh that suggests the most recent event there is potentially of similar age. However, we cannot say with greater than 21.1 % certainty that the most recent event ruptured through the Sulamu Tagh, primarily due to poor radiocarbon calibration and the inherent age uncertainties associated with radiocarbon dating. At T105, we show that there have been three events in the Cherchen He reach after ~1054 yr CalBP. We have evidence for another surface rupture before ~1054 but no maximum age estimate for that earthquake. Age uncertainties of our radiocarbon samples suggest that recurrence intervals for this section of the fault are likely on the order of ~400 years, but that in extreme cases, they may be as short as ~100 years or as many as ~700 years. Continued work on both sides of the Sulamu Tagh with alternative dating techniques (such as optically stimulated luminescence) could strengthen earthquake chronologies and help answer the questions of whether the crustal-scale geometric complexity acts a barrier to through-going surface ruptures on the major fault.

TABLES

Radiocarbon Determinations

^{14}C results

UCIAMS #	Sample name	d^{13}C (‰)	±	fraction Modern	±	D^{14}C (‰)	±	^{14}C age (BP)	±
130937	T1052012-1			0.7255	0.0021	-274.5	2.1	2575	25
130938	T1052012-4			0.7362	0.0017	-263.8	1.7	2460	20
130939	T1052012-5 .088mgC			0.8611	0.0041	-138.9	4.1	1200	40
130940	T1052012-7			0.9813	0.0026	-18.7	2.6	150	25
130941	T1052012-8			0.9678	0.0022	-32.2	2.2	265	20
130942	T1052012-9 .027mgC			0.9714	0.0148	-28.6	14.8	230	130
130943	T1052012-10 .094mgC			1.0133	0.0046	13.3	4.6	-100	40
130944	T1052012-11 .015mgC			0.9789	0.0293	-21.1	29.3	170	250
130945	T1052012-12			0.9798	0.0022	-20.2	2.2	165	20
130946	T1052012-13			0.9871	0.0023	-12.9	2.3	105	20
130947	T1052012-14			1.0790	0.0031	79.0	3.1	-605	25
130948	T1052012-15			0.9603	0.0021	-39.7	2.1	325	20
130949	T1052012-16			1.0775	0.0024	77.5	2.4	-595	20
130950	T1052012-17			0.8927	0.0020	-107.3	2.0	910	20
130951	T1052012-18			0.8862	0.0029	-113.8	2.9	970	30
130952	T1052012-20			0.8896	0.0023	-110.4	2.3	940	25
130953	T1052012-21			0.8500	0.0031	-150.0	3.1	1305	30
130954	T1052012-22			0.9820	0.0023	-18.0	2.3	145	20
130955	T1052012-23			0.7321	0.0017	-267.9	1.7	2505	20
130956	T1052012-24			0.8751	0.0030	-124.9	3.0	1070	30
130957	T1232012-1			0.8934	0.0021	-106.6	2.1	905	20
130958	T1232012-2			0.8865	0.0020	-113.5	2.0	970	20
130959	T1232012-3			0.9384	0.0022	-61.6	2.2	510	20
130960	T1232012-4			0.9332	0.0024	-66.8	2.4	555	25
130961	T1232012-5 .17mgC			0.8907	0.0021	-109.3	2.1	930	20
130962	T1232012-9			0.9640	0.0022	-36.0	2.2	295	20
130963	T1232012-10			0.9767	0.0022	-23.3	2.2	190	20
130964	ATF-J-2012-2			1.1036	0.0033	103.6	3.3	-785	25
130965	ATF-J-2012-3			0.9361	0.0024	-63.9	2.4	530	25
130966	ATF-J-2012-4			0.8764	0.0021	-123.6	2.1	1060	20
130967	ATF-J-2012-5			0.9825	0.0023	-17.5	2.3	140	20
130968	ATF-J-2012-9			0.9351	0.0022	-64.9	2.2	540	20
130969	ATF-J-2012-10			1.0169	0.0026	16.9	2.6	-130	25
130970	DQT1-4 .065mgC			0.5113	0.0043	-488.7	4.3	5390	70
130971	DQT1-5			0.9290	0.0022	-71.0	2.2	590	20
130972	DQT1-9			0.9287	0.0021	-71.3	2.1	595	20
130973	DQT1-11			0.2613	0.0011	-738.7	1.1	10780	35
130974	ATF-12-DQT2-1			0.7302	0.0017	-269.8	1.7	2525	20
130975	ATF-12-DQT2-2			0.7685	0.0018	-231.5	1.8	2115	20
130976	ATF-12-DQT2-3 .20mgC			0.7677	0.0020	-232.3	2.0	2125	25
130977	ATF-12-DQT2-4			0.7502	0.0017	-249.8	1.7	2310	20
130905	ATF-12-DQT2-5a, b, c			0.7626	0.0016	-237.4	1.6	2175	20
130906	ATF-12-DQT2-6			0.9763	0.0017	-23.7	1.7	195	15
130907	ATF-12-DQT2-7			0.9845	0.0018	-15.5	1.8	125	15
130908	ATF-12-DQT2-8a, b			0.7926	0.0014	-207.4	1.4	1865	15
130909	ATF-12-DQT2-9a, b			0.7550	0.0013	-245.0	1.3	2260	15

Table 5.1 – Accelerator Mass Spectrometer results for ^{14}C samples, conducted at the Keck Carbon Cycle AMS Facility in the Earth System Science Department, UC Irvine. We calibrated our radiocarbon ages using OxCal v4.2.4 (Bronk Ramsey, 2013) and the r:5 IntCal3 atmospheric curve (Reimer et al., 2013).

Table 5.2

Event ages expressed as CalBP

	Model			
Event #	**Muretta**	**JBS**	**MurettaJBS**	**MurettaJBS2**
1 - MRE	242 ± 159	295 ± 136	286 ± 119	286 ± 119
2 -PE	770 ± 205	606 ± 219	859 ± 124	739 ± 141
3 - PPE	909 ± 197		1018 ± 93	1012 ± 91
4 - OE	1049 ± 97		1061 ± 87	1054 ± 91

Table 5.2 – Comparison of earthquake chronologies. Event ages expressed as median CalBP age from within 95.4% confidence interval. Model Muretta is purely 2009 data from her thesis, Model JBS is only results of this study, Model MurettaJBS is the existing model plus new age constraints for the MRE, and Model MurettaJBS2 (preferred, shown in Figure 5.4) is the original model plus new age constraints for the MRE and PE. The maximum age for the Oldest Event (OE) is unconstrained, and the numbers in the table merely represent the date before which the event must have occurred.

REFERENCES

Bendick, R., Bilham, R., Freymueller, J., Larson, K., and Yin, G., 2000, Geodetic evidence for a low slip rate in the Altyn Tagh fault system: Nature, v. 404, p. 69-72, doi: 10.1038/35003555.

Bronk Ramsey, C., and Lee, S., 2013, Recent and planned developments of the program OxCal: Radiocarbon, vol 55, no. 2-3, p. 720-730.

Chen, Z., Burchfiel, B. C., Liu, Y., King, R. W., Royden, L. H., Tang, W., Wang, E., Zhao, J., and Zhang, X., 2000, Global positioning system measurements from eastern Tibet and their implications for India/Eurasia intercontinental deformation: Journal of Geophysical Research, v. 105, no. B7, p. 16,215-16,227, doi: 10.1029/2000JB900092.

Cowgill, E., Yin, A., and Harrison, T. M., 2003, Reconstruction of the Altyn Tagh fault based on U-Pb geochronology: Role of back thrusts, mantle sutures, and heterogeneous crustal strength in forming the Tibetan Plauteau: Journal of Geophysical Research, v. 108, no. B7, p. 2346, doi: 10.1029/2002JB002080.

Cowgill, E., Gold, R. D., Xuanhua, C., Xioa-Feng, W., Arrowsmith, J R., and Southon, J., 2009, Low Quaternary slip rate reconciles geodetic and geologic rates along the Altyn Tagh fault, northwestern Tibet: Geological Society of America, v. 37, no. 7, p. 647-650, doi: 10.1130/G25623A.1.

Gold, R.D., Cowgill, E., Arrowsmith, J R., Gosse, J., Chen, X., and Wang, X-F., 2009, Riser diachroneity, lateral erosion, and uncertainty in rates of strike-slip faulting: A case study from Tuzidun along the Altyn Tagh Fault NW China: Journal of Geophysical Research, v. 114, no. B04401, doi: 10.1029/2008JB005913.

He, J., Vernant, P., Chery, J., Wang, W., Lu. S., Ku, W., Xia, W., and Bilham, R, 2013, Nailing down the slip rate of the Altyn Tagh Fault: Geophysical Research Letters, v. 40, p. 5382 – 5386, doi: 10.1002/2013GL057497.

Mériaux, A.-S., Ryerson, F. J., Tapponnier, P., Van der Woerd, J., Finkel, R. C., Xu, X., Xu, Z., and Caffee, M. W., 2004, Rapid slip along the central Altyn Tagh fault: Morphochronologic evidence from Cherchen He and Sulamu Tagh: Journal of Geophysical Research, v. 109, no. B06401, doi: 10/1029/2003jb002558.

Mériaux, A.-S., Tapponnier, P., Ryerson, F. J., Xiwei, X., King, G., Van der Woerd, J., Finkel, R. C., Haibing, L., Caffee, M. W., Zhiqin, X., and Wenbin, C., 2005, The Aksay segment of the northern Altyn Tagh fault: Tectonic geomorphology, landscape evolution, and Holocene slip rate, Journal of Geophysical Research, v. 110, no. B04404, doi: 10.1029/2004JB003210.

Molnar, P., and Tapponnier, P., 1975, Cenozoic tectonics of Asia – Effects of a continental collision: Science, v. 189, no. 4201, p. 419-426, doi: 10.1126/science.189.4201.419.

Muretta, M., 2009, Holocene earthquake geology of the central Altyn Tagh fault, Xinjiang, China: Implications for recurrence interval, strain release, and fault behavior: M.S. Thesis, *unpublished*, Arizona State University.

Reimer, P. J., Bard, E., Bayliss, A., Beck, J. W., Blackwell, P. G., Bronk Ramsey, C., Grootes, P. M., Guilderson, T. P., Haflidason, H., Hajdas, I., Hattz, C., Heaton, T. J., Hoffmann, D. L., Hogg, A. G., Hughen, K. A., Kaiser, K. F., Kromer, B., Manning, S. W., Niu, M., Reimer, R. W., Richards, D. A., Scott, E. M., Southon, J. R., Staff, R. A., Turney, C. S. M., and van der Plicht, J., 2013, IntCal13 and Marine13 Radiocarbon Age Calibration Curves 0-50,000 Years cal BP: Radiocarbon, vol 55, no. 4.

Royer, J. Y., Gordon, R. G., and Horner-Johnson, B. C., 2006, Motion of Nubia relative to Antarctica since 11 Ma: Implications for Nubia-Somalia, Pacific–North America, and India-Eurasia motion: Geology, v. 34, p. 501-504.

Ryan, W. B. F., Carbotte, S. M., Coplan, J. O., O'Hara, S., Melkonian, A., Arko, R., Weissel, R. A., Ferrini, V., Goodwillie, A., Nitsche, F., Bonczkowski, J., and Zemsky, R., 2009, Global Multi-Resolution Topography synthesis: Geochemistry, Geophysics, Geosystems, v. 10, no. 3, doi: 10.1029/2008GC002332.

Shen, Z.-K., Wang, M., Li, Y., Jackson, D. D., Yin, A., Dong, D., Fang, P., 2001, Crustal deformation along the Altyn Tagh fault system, western China, from GPS: Journal of Geophysical Research, v. 106, p. 30,607–30,621, doi: 10.1029/2001JB000349.

Tapponnier, P and Molnar, P., 1977, Active faulting and tectonics in China: Journal of Geophysical Research, v. 82., p. 2905-2930, doi: 10.1029/JB082i020p02905.

Taylor, M. H., and Yin, A, 2009, Active structures of the Himalayan-Tibetan orogeny and their relationships to earthquake distribution, contemporary strain field, and Cenozoic volcanism: *Geosphere*, v. 5, no. 3, p. 199-214, doi: 10.1130/GES00217.1.

Wallace, K., Yin, G., and Bilham, R., 2004, Inescapable slow slip on the Altyn Tagh Fault: Geophysical Research Letters, v. 31, no. L09613, doi: 10.1029/2004GL019724.

Washburn, Z., Arrowsmith, J R., Forman, S. L., Cowgill, E., Xiaofeng, W., Yueqiao, Z., and Zhengle, C., 2001, Late Holocene earthquake history of the central Altyn Tagh fault, China: Geology, v. 29, no. 11, p. 1051–1054.

Washburn, Z., Arrowsmith, J R., Dupont-Nivet, G., Xiaofeng, W., Yueqiao, Z., and Zhengle, C., 2003, Paleoseismology of the Xorxol segment of the Central Altyn Tagh Fault, Xinjiang, China: Annals of Geophysics, v. 46, no. 5, p. 1015–1034.

Zhang, P-Z., Molnar, P., and Xu, X., 2007, Late Quaternary and present-day rates of slip along the altyn Tagh Fault, northern margin of the Tibetan plateau: Tectonics, v. 26, no. TC5010, doi: 10.1029/2006TC002014.

FIGURE CAPTIONS

Figure 5.1 – Inset map shows the Indo-Eurasian collision zone with major structures highlighted in black. Abbreviations: KAF – Karakorum Fault, ATF – Altyn Tagh Fault, KUF – Kunlun Fault, TB – Tarim Basin General location map showing the western ATF in relation to the Tibetan Plateau and Tarim Basin (to the northwest). The stars represent trench locations: yellow stars are trenches originally excavated and logged by Muretta (2009) and re-excavated/sampled by our 2012 field campaign, the orange star is a trench excavated by Muretta but not logged or sampled until our 2012 field campaign, and the green star represents our completely new double trench site (one focused on strike-slip strand and one focused on thrusting strand, ~10m apart) in Qing Shui Quan reach. Inset map made with GeoMapApp (*http://www.geomapapp.org*) with Global Multi-Resolution Topography (GMRT) Synthesis (Ryan et al., 2009), and background digital elevation model made from Shuttle Radar Topography Mission (SRTM) data. Fault catalog from Taylor and Yin, 2009.

Figure 5.2 – Annotated Digital Globe satellite image showing the Qing Shui Quan reach and trench site east of the Sulamu Tagh. Spring-fed streams flow from the north across the complex fault zone, shown here with a primarily strike-slip strand and a secondary reverse strand. DQT1 is across the most active trace of the strike-slip fault strand and DQT2 is across a ~3 m reverse fault scarp. Red dots indicate remotely-identified, potential trench sites. These sites were not excavated.

Figure 5.3 – Trench J logs and associated photomosaics. The areas above the dashed black lines represent young surficial aeolian/fluvial deposits interpreted to have been sourced from the slope to the north and deposited after the most recent event. Radiocarbon sample locations are shown as yellow stars and ages are represented as ^{14}C ages BP. We interpret the old age of sample 4 to represent a rare case of detrital age inheritance. Nearly all fault strands ruptured (or cracked) to the surface in the most recent event.

Figure 5.4 – Annotated field photograph of the Altyn Tagh fault in the Cherchen He reach, looking west. Foreground of photograph shows a meter-scale mole track with ponded fine-grained sediments. The location of Trench J is shown several hundred meters in the distance, though the actual trench is not visible.

Figure 5.5 – Simplified trench log and photomosaic of the western face of Trench 105. Radiocarbon sample locations are shown as yellow stars and ages are represented as ^{14}C ages BP. This is a refreshed exposure (cut 1 m back) of T105 west from Muretta, 2009. Colored lines represent interpreted event horizons, red - most recent earthquake; green - penultimate event; blue – third event; purple – fourth event.

Figure 5.6 – Simplified trench logs and photomosaics of Trench 123. Radiocarbon sample locations are shown as yellow stars and ages are represented as ^{14}C ages BP. This is a refreshed exposure (cut 1 m back) of T123 west from Muretta, 2009. We lack radiocarbon samples from young materials capping the most recent event rupture. Significant cracking in the northern third of the trench (seen best in the west face; unit containing samples 1 and 2) likely represents evidence of at least one significant, older event.

Figure 5.7 – A) Annotated field photograph of the eastern Cherchen He reach, looking west from Trench 123. B) Field photo of T123 (looking east at the eastern end of Cherchen He reach.

Figure 5.8 – Simplified trench logs and photomosaics of Trench DQT1. Radiocarbon sample locations are shown as yellow stars and ages are represented as ^{14}C ages BP. A distinct marker bed consisting of finely laminated sands and silts is shown in light blue. We exposed evidence for several earthquakes but lack adequate radiocarbon material to date event horizons. The youngest event here is capped by a thin, finely-laminated aeolian silt.

Figure 5.9 – Simplified trench logs and photomosaics of Trench DQT2. Radiocarbon sample locations are shown as yellow stars and ages are represented as ^{14}C ages BP. Both exposures are capped by a sandy silt (primarily loess) cap. At the north end of the trench, coarse-grained gravels and cobbles have been brought up over finer-grained fan material, and the loess cap is thinned above the up-thrown block. Down-slope of the mapped fault traces, the loess cap thickens preserving a sequence of small.

5.10 – Simplified trench log of the southern end of both faces of Trench 105 from Muretta, 2009. Earthquake event horizons are colored by age: red—most recent event; green—penultimate event; blue—third event; purple—fourth event.

Figure 5.11 – Simplified trench log of the southern end of both faces of Trench 123 from Muretta, 2009. Earthquake event horizons are colored by age: greed—most recent event; blue—penultimate event (tentative); purple—third event (weak evidence).

Figure 5.12 – Radiocarbon age model for the last four events at T105, showing samples from this study (numbered) and existing samples from Muretta, 2009 (lettered). Event ages are expressed in CalBP ages with associated percent certainty. Median ages are shown for referenence. We use an arbitrary (but reasonable) cap of AD 1850, as there have been no major historic earthquakes from this region since then. We do not have an age constraint from below the oldest (4^{th}) event, OE.

Figure 5.13 – Radiocarbon calibration curve for sample DQT2-6. We calibrated our radiocarbon ages using OxCal v4.2.4 (Bronk Ramsey, 2013) and the r:5 IntCal3 atmospheric curve (Reimer et al., 2013).

FIGURES

Figure 5.1

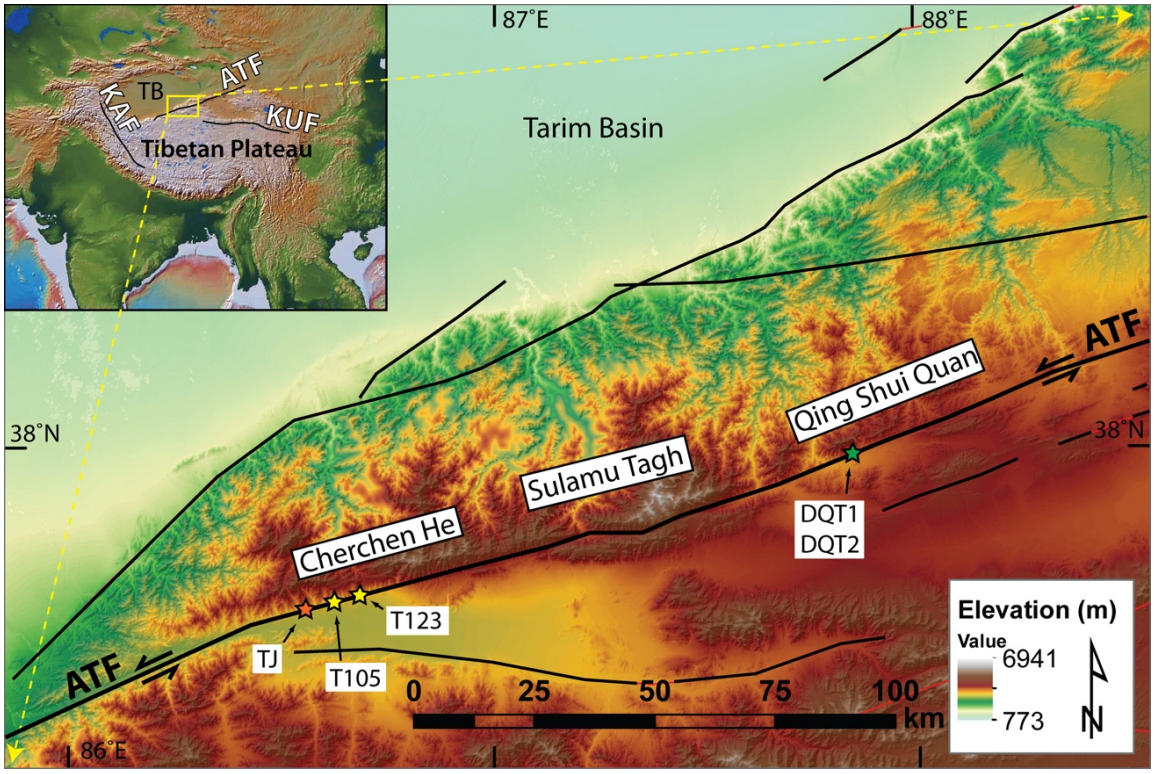

Figure 5.2

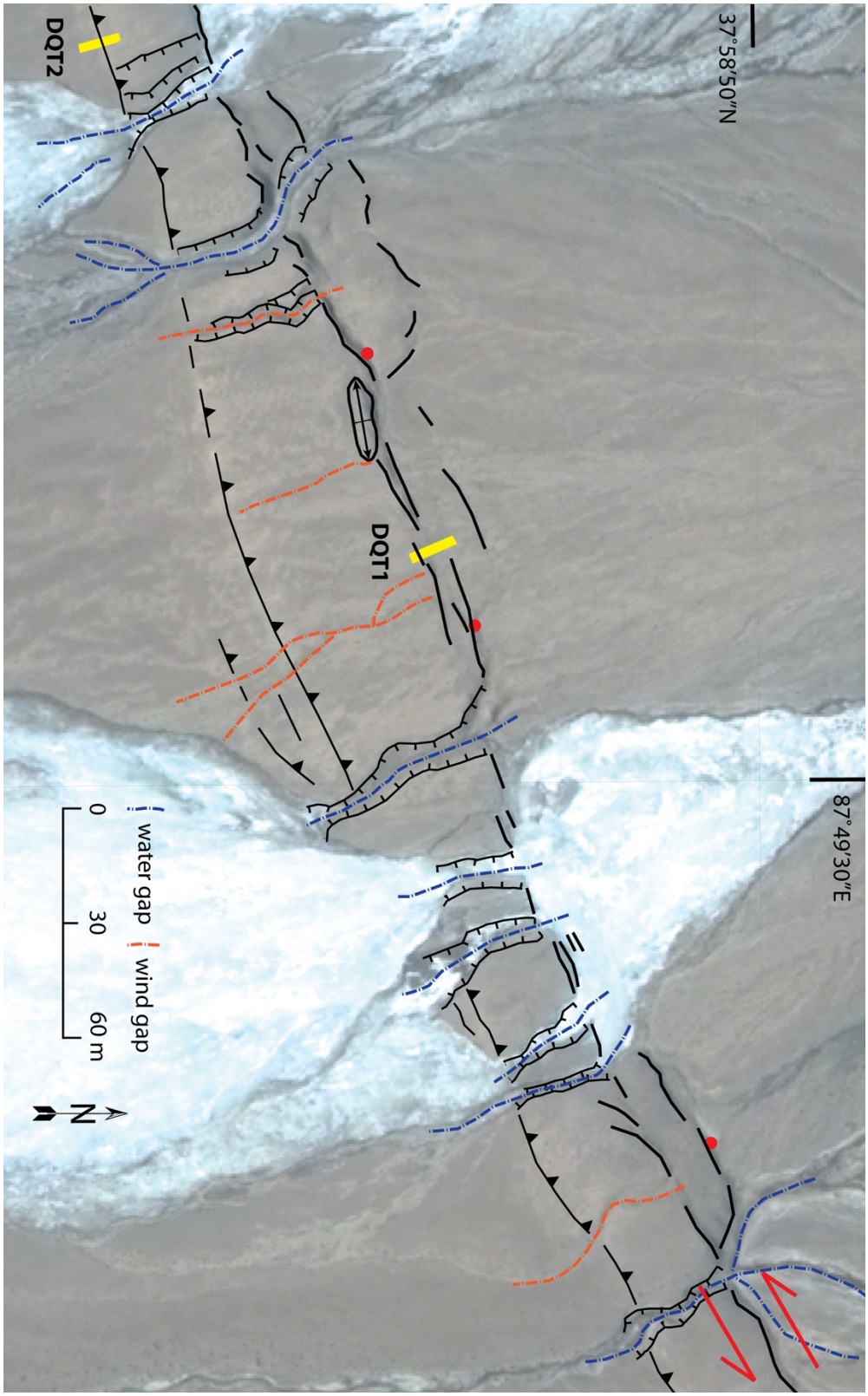

Figure 5.3

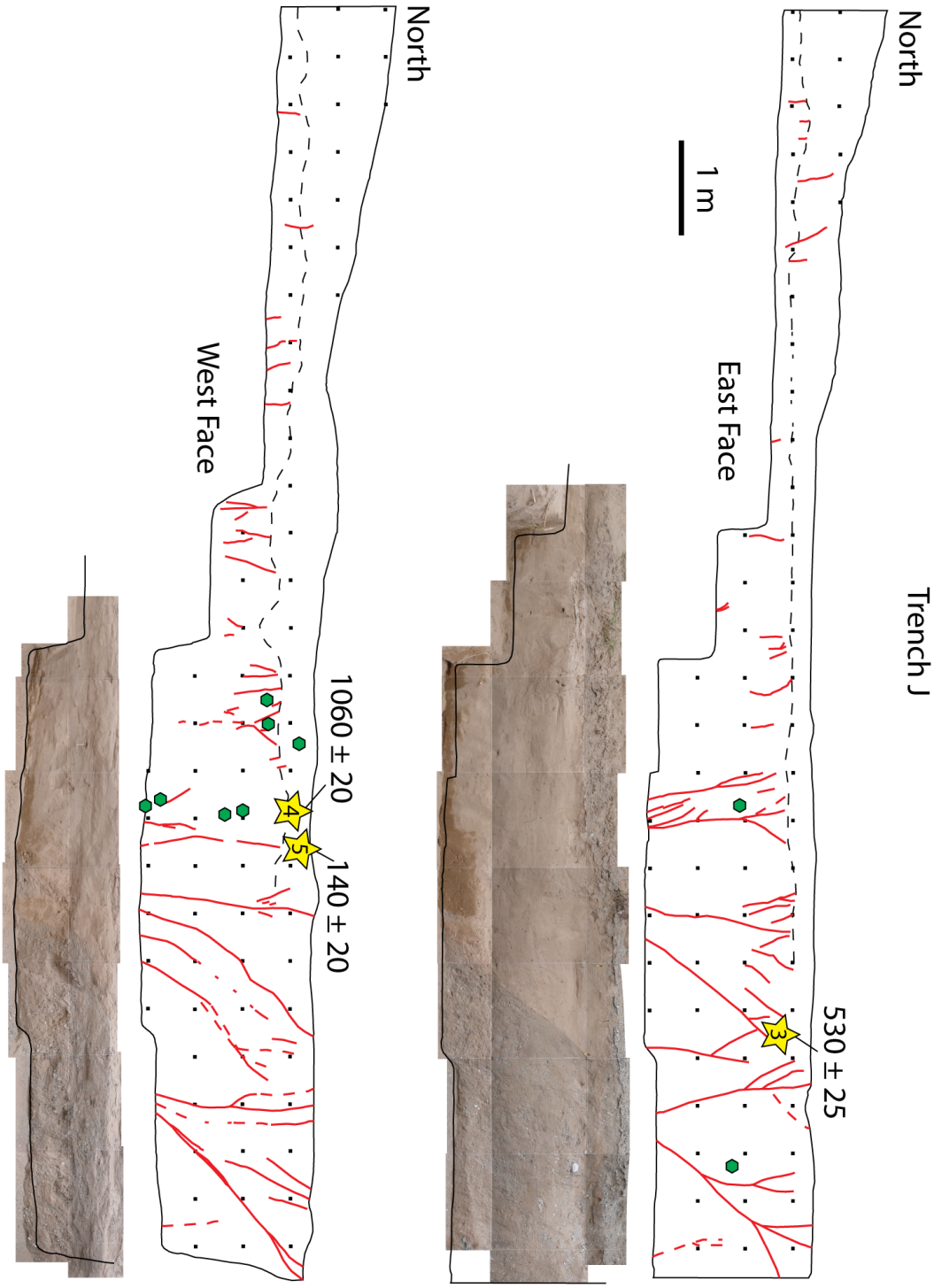
Trench J
North
East Face
1 m
530 ± 25
3
North
West Face
1060 ± 20
140 ± 20
4
5

Figure 5.4

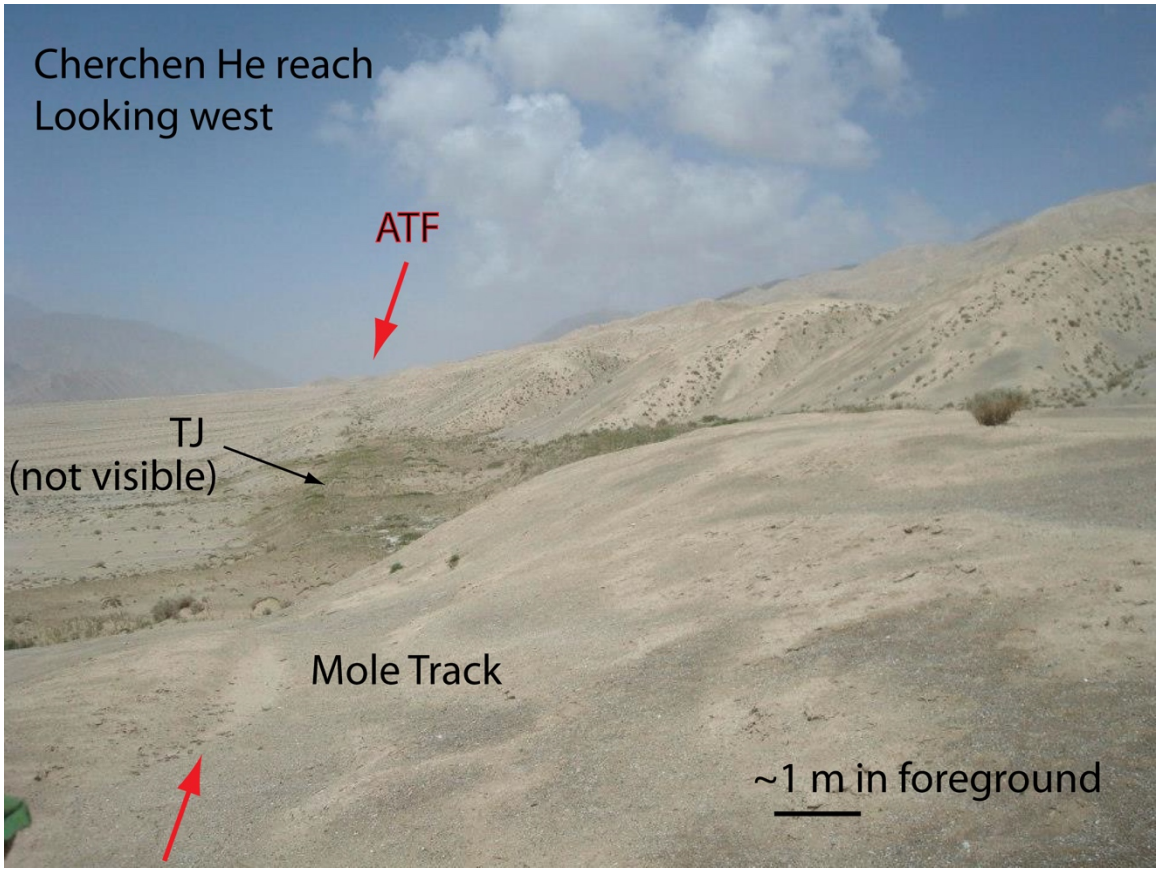
Cherchen He reach
Looking west
ATF
TJ
(not visible)
Mole Track
~1 m in foreground

Figure 5.5

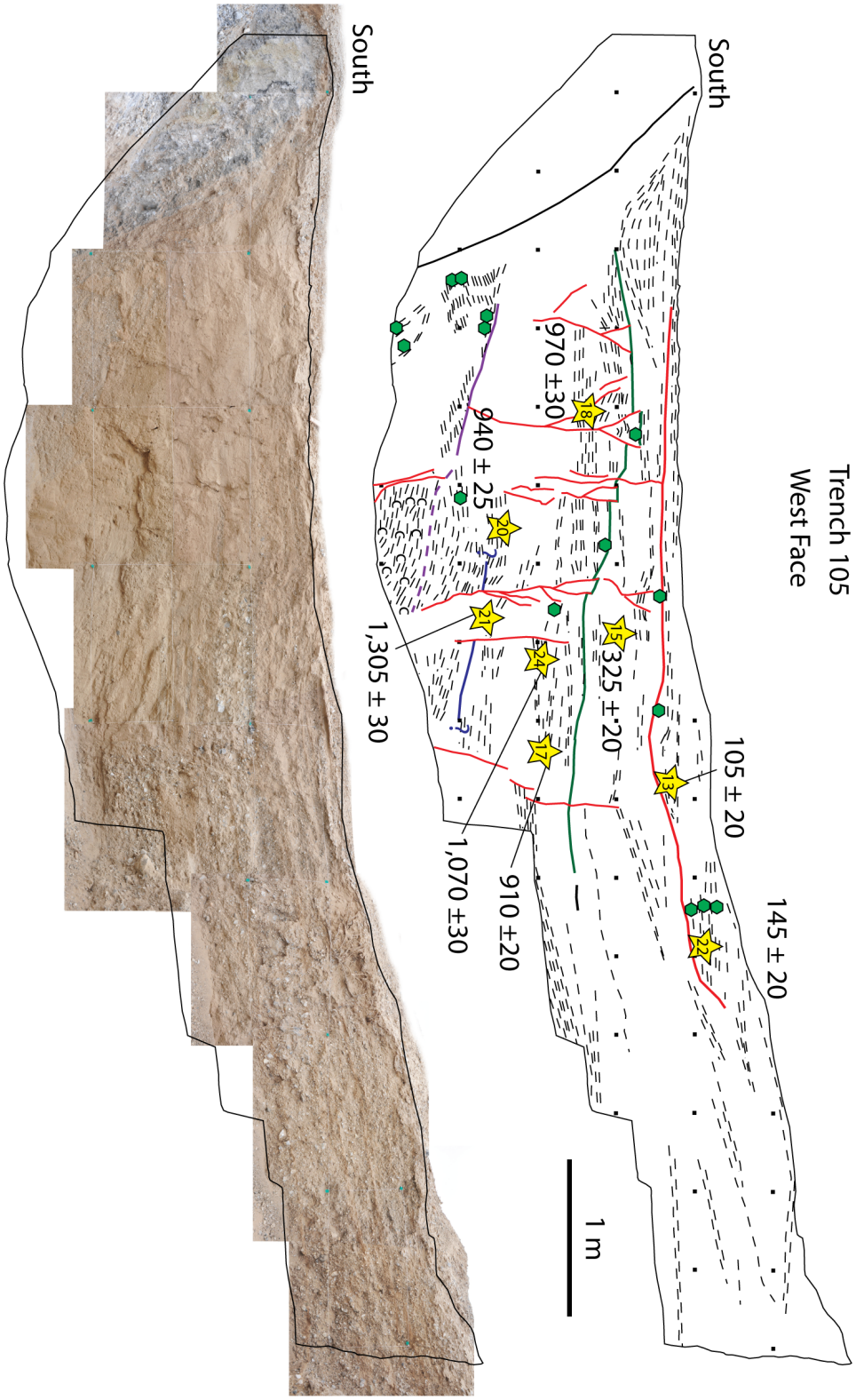
Trench 105
West Face
South
South
970 ±30
940 ± 25
1,305 ± 30
325 ±20
105 ± 20
145 ± 20
1,070 ±30
910 ±20
1 m

Figure 5.6

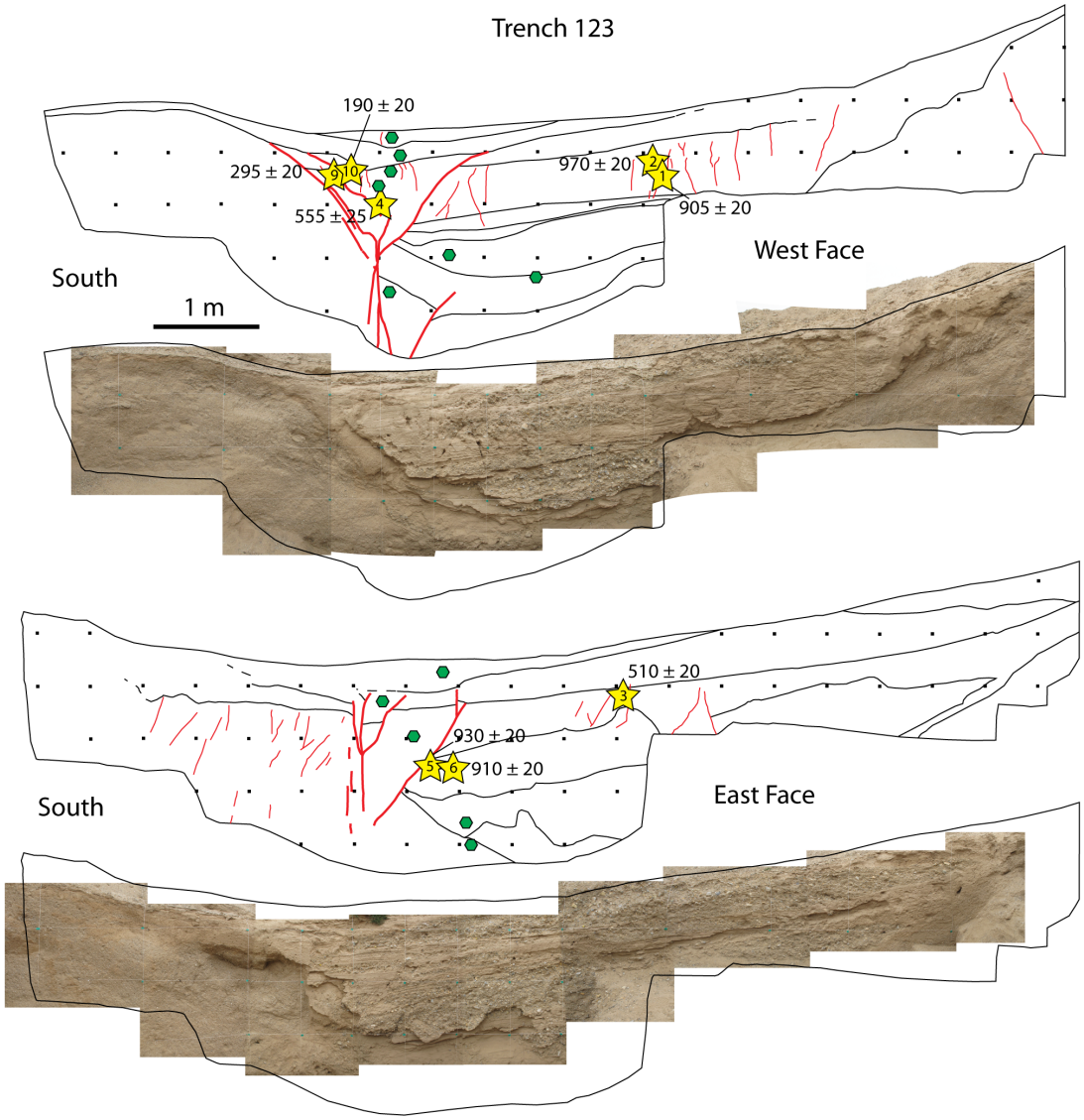
Trench 123
190 ± 20
295 ± 20
555 ± 25
970 ± 20
905 ± 20
West Face
South
1 m
510 ± 20
930 ± 20
910 ± 20
East Face
South

Figure 5.7


A)
Eastern Cherchen He
Looking West from T123
people for scale
within side hill bench
ATF
B)
Looking East
T123
ATF

Figure 5.8

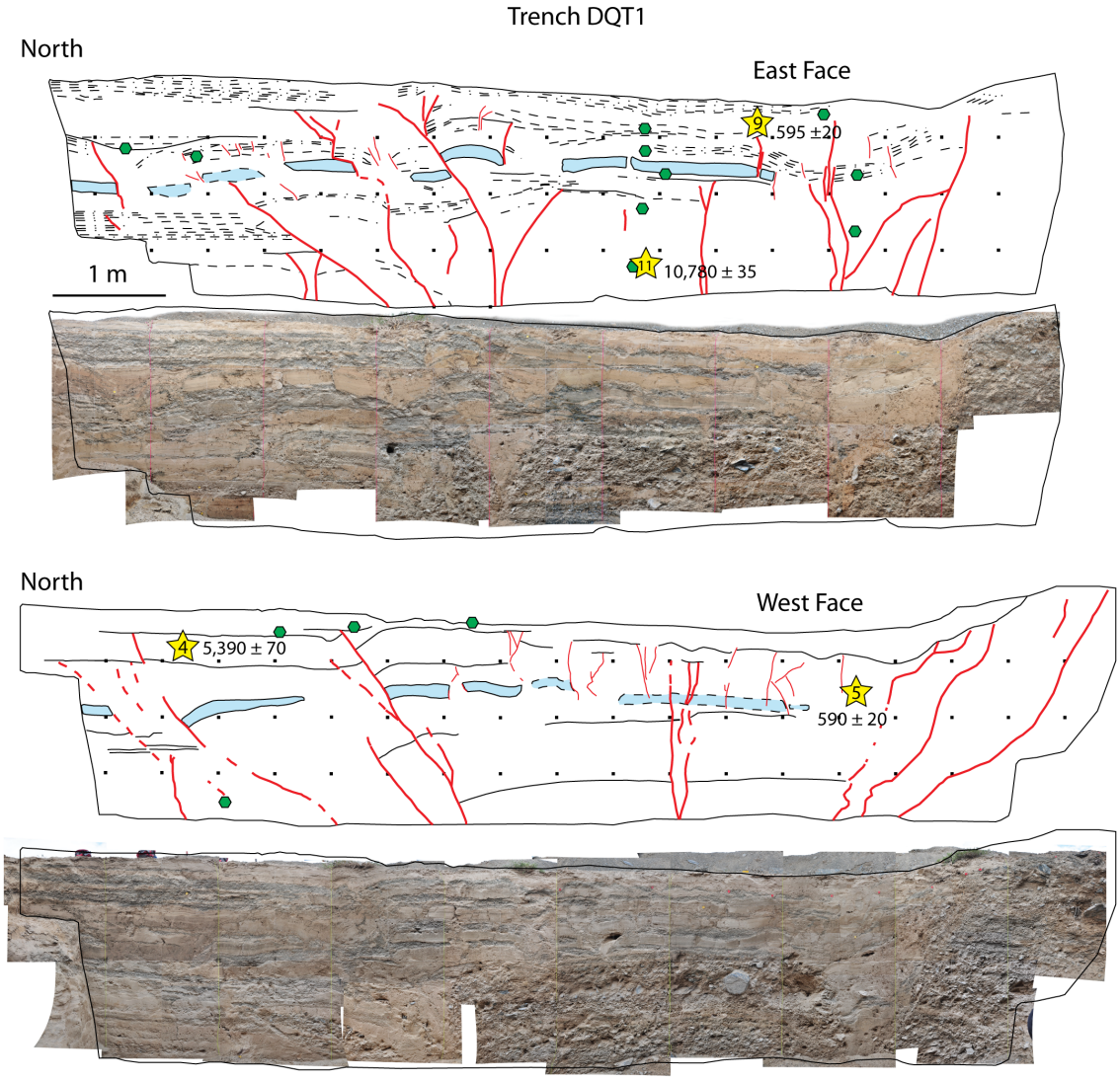
Trench DQT1
North
East Face
9
595 ±20
11
10,780 ± 35
1 m
North
West Face
4
5,390 ± 70
5
590 ± 20

Figure 5.9

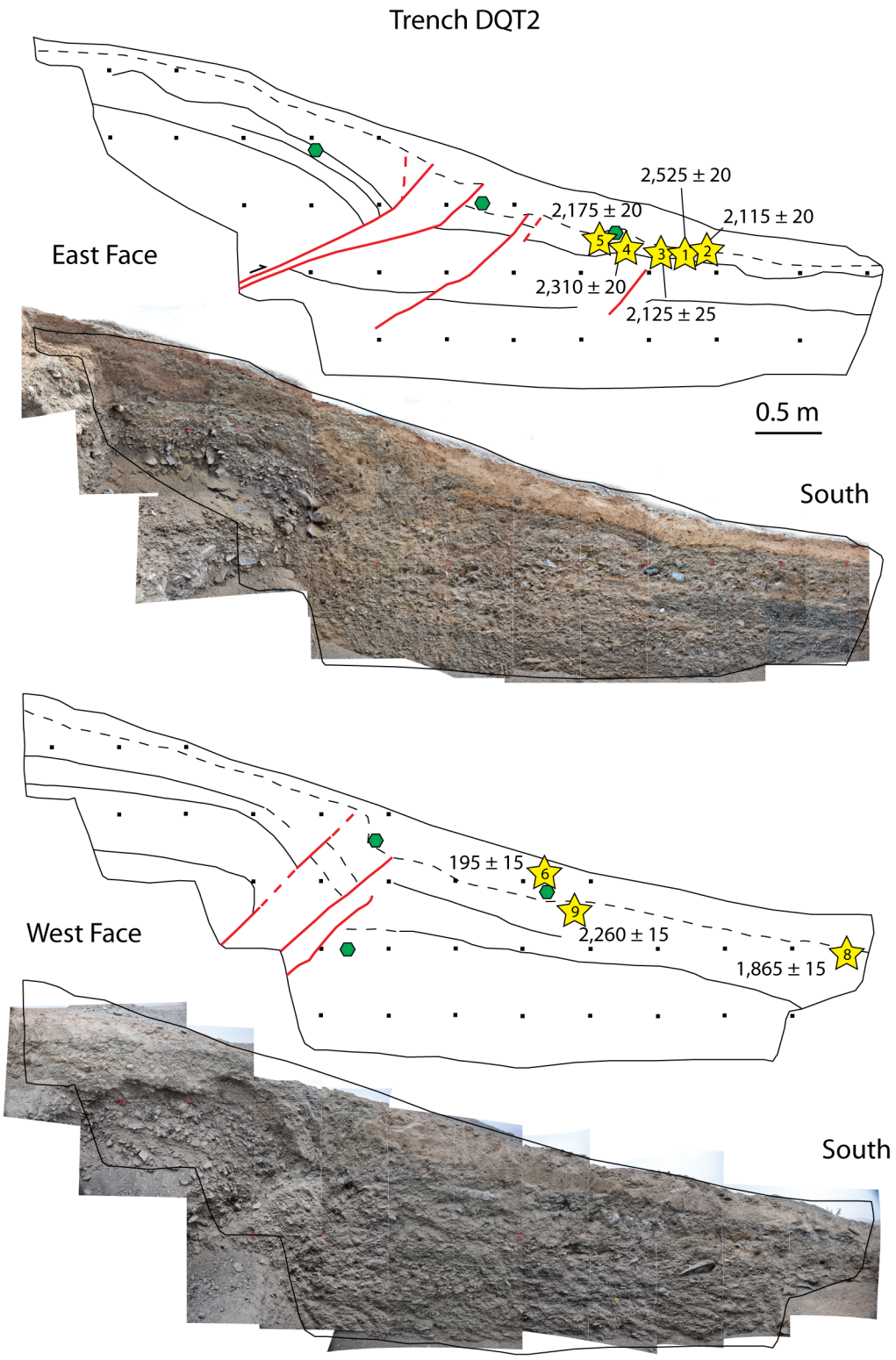
Trench DQT2
East Face
2,525 ± 20
2,175 ± 20
2,115 ± 20
2,310 ± 20
2,125 ± 25
0.5 m
South
West Face
195 ± 15
2,260 ± 15
1,865 ± 15
South

Figure 5.10

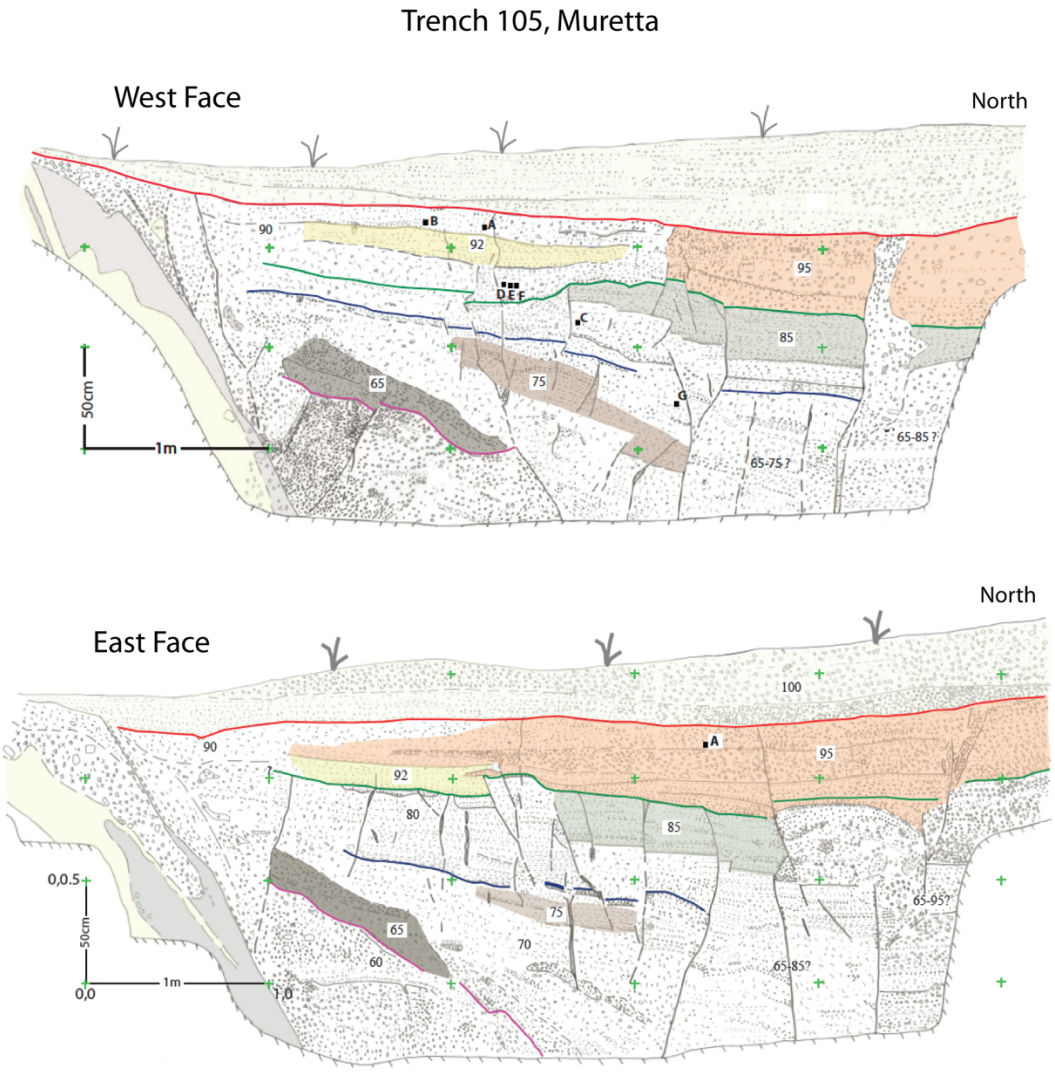
Trench 105, Muretta
West Face
North
90
B
A
92
D E F
C
95
85
65
75
G
65-85 ?
65-75 ?
50cm
1m
East Face
North
100
90
A
92
95
80
85
0,0.5
50cm
65
75
65-95?
70
60
65-85?
1m
0,0
1,0

Figure 5.11

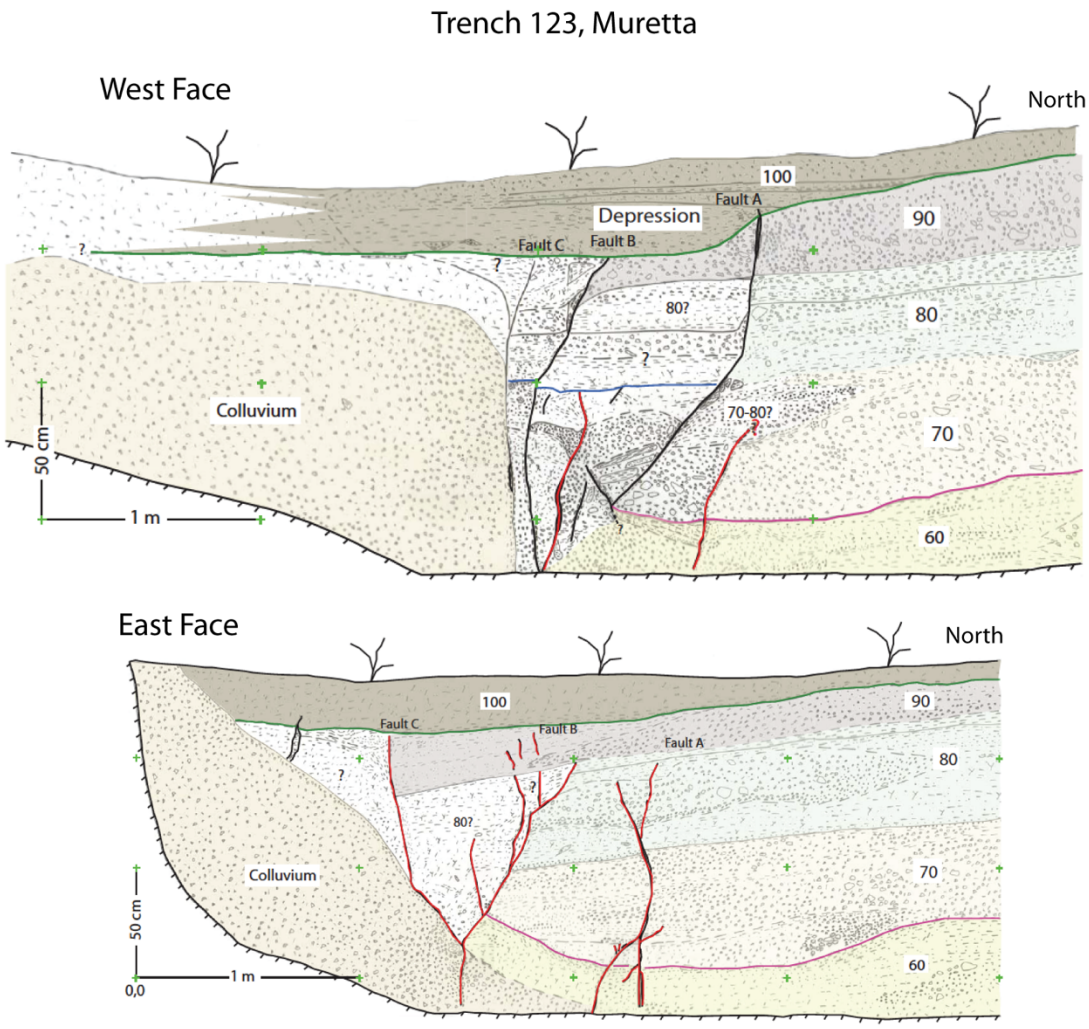
Trench 123, Muretta
West Face
North
100
Fault A
Depression
90
Fault C
Fault B
?
?
80?
80
?
Colluvium
70-80?
70
50 cm
1 m
60
East Face
North
100
90
Fault C
Fault B
Fault A
?
?
80?
80
Colluvium
70
50 cm
1 m
0,0
60

Figure 5.12

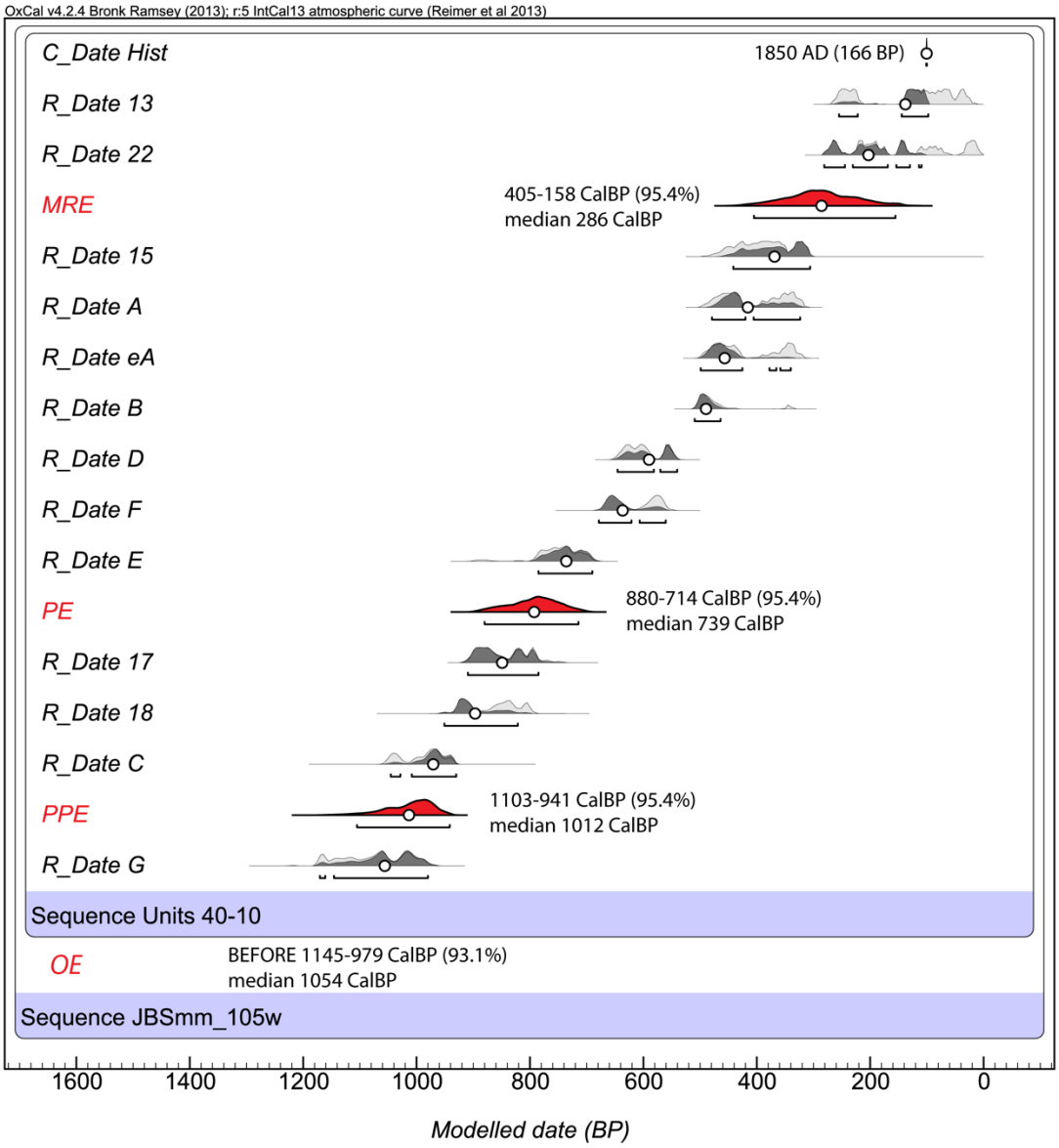
OxCal v4.2.4 Bronk Ramsey (2013); r:5 IntCal13 atmospheric curve (Reimer et al 2013)
C_Date Hist
1850 AD (166 BP)
R_Date 13
R_Date 22
MRE
405-158 CalBP (95.4%)
median 286 CalBP
R_Date 15
R_Date A
R_Date eA
R_Date B
R_Date D
R_Date F
R_Date E
PE
880-714 CalBP (95.4%)
median 739 CalBP
R_Date 17
R_Date 18
R_Date C
PPE
1103-941 CalBP (95.4%)
median 1012 CalBP
R_Date G
Sequence Units 40-10
OE
BEFORE 1145-979 CalBP (93.1%)
median 1054 CalBP
Sequence JBSmm_105w
1600
1400
1200
1000
800
600
400
200
0
Modelled date (BP)

Figure 5.13

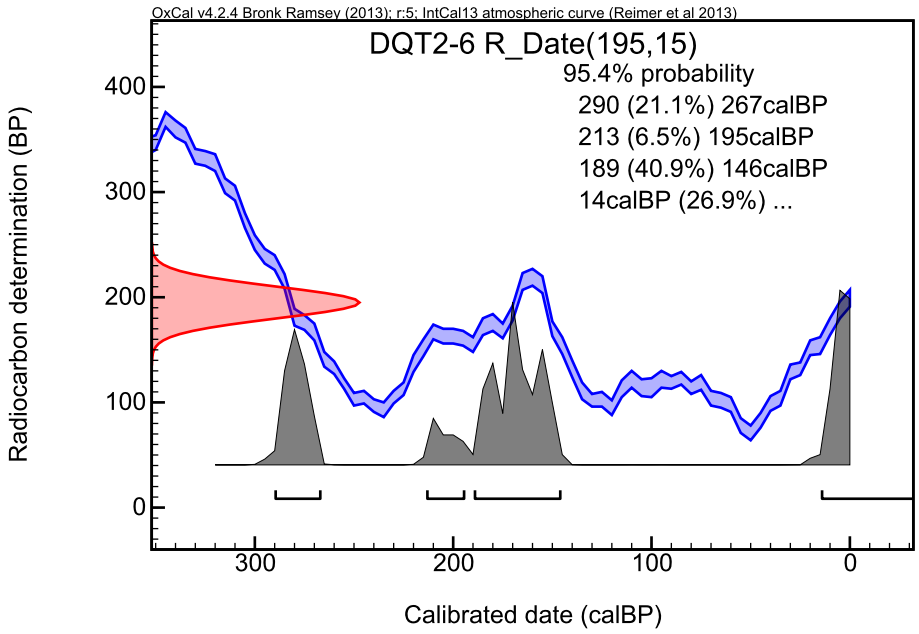
OxCal v4.2.4 Bronk Ramsey (2013); r:5; IntCal13 atmospheric curve (Reimer et al 2013)
DQT2-6 R_Date(195,15)
95.4% probability
290 (21.1%) 267calBP
213 (6.5%) 195calBP
189 (40.9%) 146calBP
14calBP (26.9%) ...
Radiocarbon determination (BP)
400
300
200
100
0
300
200
100
0
Calibrated date (calBP)

CHAPTER 6

CONCLUSIONS

OVERVIEW

This dissertation was driven by the desire to better understand faulting in the upper crust to better inform earthquake hazard forecasts. As the population of earthquake-prone people increases, so does the need for mitigating the potentially devastating impacts of large earthquakes (Allen, 2007). Slip accumulation patterns inferred from fault-offset geomorphic landforms provide important information regarding past rupture histories and constitute a significant portion of geologic constraints used in earthquake rupture forecasts (e.g., Field et al., 2014). This work is an investigation of such fault-offset landforms.

I used a combination of high-resolution surficial topographic forms and sub-surface fault zone geomorphology to investigate the tectonically-influenced evolution of geomorphic features preserving evidence for a few to hundreds of meters of cumulative slip along strike-slip faults. Understanding the frequency of small-scale landform formation versus landform displacement is essential to correct interpretation of small and large offsets alike.

The bulk of landform investigation happens in the field. However, recent methodological advances in acquiring cost-effective high-resolution topography have catalyzed a trend towards lidar- and other remotely-based studies to analyze fault-offset landforms (e.g., Hudnut et al., 2002; Haugerud et al., 2003; WGCEP, 1988; Grant-Ludwig et al., 2010; Zielke et al. 2010, 2012; Salisbury et al., 2012). While fieldwork is essential to many aspects of active fault studies (e.g., paleoseismic excavations for event

recurrence), in certain instances fieldwork and excavations can be impractical because of temporal, financial, and land access limitations. For these reasons, remote-sensing based studies of slip in active fault zones (e.g., detailed analysis of historic and prehistoric ruptures; fault slip accumulation) are also an important approach to understanding earthquake hazard. I explored some of the key challenges faced when measuring fault-offset geomorphic features not only in high-resolution topography but also in the field (e.g., Scharer et al., 2014; Salisbury et al., 2015) (Chapters 2 and 3). After identifying the problems shared by investigators of all experience levels, I focused on certain problems in the field (Chapters 3 and 4).

The bulk of fieldwork for this dissertation was conducted along the San Andreas fault in the Carrizo Plain where the significance of tectonic landforms has long been recognized (Lawson et al., 1908; Arnold and Johnson, 1910; Wood and Buwalda, 1931; Hill and Dibblee, 1953; Wallace, 1968; Sieh, 1978). I showed that even in an area where basic fault parameters are already known there is much to be gained from high-resolution geomorphic and geochronologic studies.

At the Van Matre Reach reach of the Carrizo Plain I demonstrated (with sub-surface excavation and high-resolution geochronology) that existing interpretations of single- and double-earthquake offset features need to be reconsidered. Several geomorphic offset measurements made there are of landforms that are not actually offset from the originally inferred sources, or if the reconstruction is correct, that the total offset is not from only a single earthquake. This implies that slip at a point in successive earthquakes is more variable than what was proposed by the earliest models of earthquake recurrence and that at least for the Carrizo Plain, it is inaccurate to assume a

perfect correspondence between the earthquakes preserved in subsurface sediments and with the earthquakes preserved in the geomorphic record (as suggested by Akciz, et al., 2010 and Zielke, et al, 2010, 2012, 2015). This type of inter-event slip variability must be considered for earthquake recurrence models to become more realistic.

At the same site, I calculated a new centennial-scale slip rate for the region and refined the estimate of slip in the most recent event. While the new short-term slip rate (31.6 +5.9/-4.3 mm/yr; Chapter 3) is consistent with existing studies in the Carrizo Plain (3.4 – 3.6 cm/yr, Sieh and Jahns, 1984; 3.6 cm/yr, Schmalzle et al., 2006 and Meade and Hager, 2005; 3.1 cm/yr, Noriega et al., 2006; Figure 6.1), my estimate of slip in the most recent event (3.8 m; Chapter 3) is significantly smaller than that of existing studies (>5 m; Sieh and Jahns, 1984; Liu-Zeng et al., 2006; Zielke et al., 2010 and 2012). I stress that there is a great need for similar studies involving sub-surface excavations and high-precision geochronology as the community continues to build worldwide databases of surface slip measurements for fault offset accumulation and earthquake hazard evaluation.

To further the understanding of fault-offset geomorphic features, I updated and explicated a tectono-stratigraphic, process-response model that incorporates not only the tectonic drivers of fault offset ephemeral channels but also the sedimentary response of watersheds in semi-arid landscapes as well. I used this model to interpret several stages of offset channel reconstruction at Phelan Creeks to show that the (millennial-scale) slip rate of the San Andreas fault in the Carrizo Plain is relatively uniform through the middle and late Holocene (e.g., Chapter 4; Figure 6.1).

In addition to the San Andreas fault, I focused on a reach of the west-central Altyn Tagh Fault, China, for a paleoseismic study. I built earthquake event catalogs on both sides of a crustal-scale geometric complexity to evaluate its potential as a barrier to rupture. I had a unique opportunity to compare trench log interpretations and earthquake event chronologies at the same site as a check on the consistency and repeatability of paleoseismic interpretations. I combined geochronologic constraints from an older, unpublished study (Muretta, 2009) with our new results to strengthen the earthquake catalog in an area where very little is known about earthquake recurrence.

DIRECTIONS FOR FUTURE RESEARCH

In this dissertation I showed several ways that remote analyses and sub-surface investigations, combined with new analytical techniques (e.g., structure-from-motion topography, pIR-IRSL age analyses) can advance our understanding of active fault behavior even in previously well-studied areas. Moving forward, it will be important to continue pursuing the pIR-IRSL dating technique, both to make it applicable in more geologic settings and for use as a supplement to more traditional methods of dating geologic materials and geomorphic processes. Also, continued use of SfM will allow for the high-resolution topographic analysis of faulted landforms in rapid response situations after modern earthquakes, and in areas where existing data are of insufficient quality.

With unlimited money and time, I would recommend that we increase the density of these directed studies along fault systems to refine field-based estimates of slip-per-event, slip rate, and earthquake recurrence. For example, many new faults have been explored in high-resolution topography (e.g., ~1 m per pixel light detection and ranging data) alone and preliminary interpretations about slip-per-event have been drawn. These

interpretations have already become a part of earthquake forecast model inputs. However, as a check on these interpretations, particularly where model-produced fault parameters are inconsistent with field observations, the hazard community needs more in-depth studies like this around which to base other, lesser-constrained datasets (e.g., surface slip catalogs).

Unfortunately, these types of studies involving sub-surface excavations and sufficient age control (including ^{14}C and pIR-IRSL) are time-consuming and expensive. While I focus on a relatively well-studied fault reach, what I hope is that this dissertation has embodied a methodological framework with which to approach fault systems that have not yet been well-explored. In this dissertation we use data from several different fault reaches, projects, and investigators to make significant interpretations about fault behavior. A take-away point of this study is how important proper methods documentation, sample metadata, and results presentation are to effective collaboration within and outside a single research group.

The goal is for future investigators of active faults to consider multiple spatio-temporal resolutions of active deformation when planning studies and choosing field sites. It is important to answer site-specific questions, but it is also important that data at a point be a viable contribution to the larger effort of understanding active fault behavior. The comedic response to the question of what to do next is to simply dig more holes. The real answer to this question is to continue the strategic planning and execution of remote and field studies with exciting new methodologies in a collaborative approach to enhancing earthquake rupture forecasts.

REFERENCES

The Working Group on California Earthquake Probabilities (WGCEP), 1988, Probabilities of large earthquakes occurring in California along the San Andreas fault: USGS Open File Report 88 – 398.

Akciz, S. O., Grant-Ludwig, L., Arrowsmith, J R., and Zielke, O., 2010, Century-long average time intervals between ruptures on the San Andreas Fault in the Carrizo Plain: Geology, v. 38, no. 9, p. 787 – 790, doi: 10.1130/G30995.1.

Allen, R. M., 2007, Earthquake hazard mitigation: new directions and opportunities: in Schubert, Gerald (Ed.), Treatise on Geophysics, Earthquake Seismology, vol. 4, Elsevier.

Arnold, R., and Johnson, H. R., 1910, Preliminary report on the McKittrick-Sunset oil region, Kern and San Luis Obispo counties, California: U. S. Geological Survey Bulletin 406.

Field, E. H., Arrowsmith, J R., Biasi, G. P., Bird, P., Dawson, T. E., Felzer, K. R., Jackson, D. D., Johnson, K. M., Jordan, T. H., Madden, C., Michael, A. J., Milner, K. R., Page, M. T., Parsons, T., Powers, P. M., Shaw, B. E., Thatcher, W. R., Weldon, R. J., and Zeng, Y., 2014, Uniform California Earthquake Rupture Forecast, Version 3 (UCERF3)—The time-independent model: Bulletin of the Seismological Society of America, v. 104, no.3, p. 1122 – 1180, doi: 10.1785/0120130164.

Grant-Ludwig, L., Akciz, S. O., Noriega, G. R., Zielke, O., and Arrowsmith, J R., 2010, Climate-modulated channel incision and rupture history of the San Andreas Fault in the Carrizo Plain: Science, v. 327, no. 5969, p. 1117 – 1119, doi: 10.1126/science.1182837.

Haugerud, R. A., Harding, D. J., Johnson, S. Y., Harless, J. L., Weaver, C. S., and Sherrod, B. L., 2003, High-Resolution lidar Topography of the Puget Lowland, Washington – A Bonanza for Earth Science, GSA Today, v. 13, no. 6, p. 4 – 10, doi: 10.1130/1052-5173(2003)13<0004:HLTOTP>2.0.CO;2.

Hill, M. L., and Dibblee, T. W., 1953, San Andreas, Garlock, and Big Pine faults, California study of the character, history, and tectonic significance of their displacements: Bulletin of the Geological Society of America, v. 64, p. 443 – 458.

Hudnut, K.W., Borsa, A., Glennie, C., and Minster, J. B., 2002, High-resolution topography along surface rupture of the 16 October 1999 Hector Mine, California, earthquake (M_w 7.1) from airborne laser swath mapping: Bulletin of the Seismological Society of America, v. 92, p. 1570 – 1576, doi: 10.1785/0120000934.

Lawson, A. C., and others, 1908, Report of the earthquake investigation commission upon the California earthquake of April 18, 1906: Carnegie Institution of Washington, D. C.

Liu-Zeng, J., Klinger, Y., Sieh, K., Rubin, C., and Seitz, G., 2006, Serial ruptures of the San Andreas fault, Carrizo Plain, California, revealed by three-dimensional excavations: Journal of Geophysical Research, v. 111, B02306, doi: 10.1029/2004JB003601.

Meade, B. J., and Hager, B. H., 2005, Block models of crustal motion in southern California constrained by GPS measurements: Journal of Geophysical Research, v. 110, B03403, doi: 10.1029/2004JB003209.

Muretta, M., 2009, Holocene earthquake geology of the central Altyn Tagh fault, Xinjiang, China: Implications for recurrence interval, strain release, and fault behavior: M.S. Thesis, *unpublished*, Arizona State University.

Noriega, G.R., Arrowsmith, J R., Grant, L. B., Young, J. J., 2006, Stream Channel Offset and Late Holocene Slip Rate of the San Andreas Fault at the Van Matre Ranch Site, Carrizo Plain, California: Bulletin of the Seismological Society of America, v. 96, no. 1, p.33 – 47, doi: 10.1785/0120050094.

Salisbury, J. B., Rockwell, T. K., Middleton, T., and Hudnut, K., 2012, Lidar and field observations of slip distribution for the most recent surface ruptures along the central San Jacinto fault: Bulletin of the Seismological Society of America, v. 102, no. 2, p. 598 – 619, doi: 10.1785/0120110068.

Salisbury, J. B., Haddad, D. E., Rockwell, T. K., Arrowsmith J R., Madugo, C., Zielke, O., and Scharer, K., 2015, Validation of meter-scale surface faulting offset measurements from high-resolution topographic data: Geosphere, v. 11, no. 6, doi: 10.1130/GES01197.1.

Scharer, K., Salisbury, J. B., Arrowsmith, J R., and Rockwell, T. K., 2014, Southern San Andreas Fault Evaluation field activity: Approaches to measuring small geomorphic offsets – challenges and recommendations for active fault studies: Seismological Research Letters, v. 85, no. 1, doi: 10.1785/0220130108.

Schmalzle, G., Dixon, T., Malservisi, R., and Govers, R., 2006, Strain accumulation across the Carrizo segment of the San Andreas Fault, California: Impact of laterally varying crustal properties: Journal of Geophysical Research: Solid Earth, vol. 111, no. B5, https://doi.org/10.1029/2005JB003843.

Sieh, K. E., 1978, Slip along the San Andreas fault associated with the great 1857 earthquake: Bulletin of the Seismological Society of America, v. 68, no. 5, p. 1421 – 1448.

Sieh, K. E., and Jahns, R. H., 1984, Holocene activity of the San Andreas fault at Wallace Creek, California: Geological Society of America Bulletin, v. 95, p. 883 – 896.

Wallace, R. E., 1968, Notes on stream channels offset by the San Andreas fault, southern coast ranges, California, *in* Dickson, W. R., and Grantz, A., eds., Proceedings of Conference on Geologic Problems of the San Andreas Fault system, Stanford University Publication, Geological Sciences, v. 11, p. 6 – 21.

Wood, H. O., and Buwalda, J. P.,1931, Horizontal displacement along the San Andreas fault in the Carrizo Plain, California: Geological Society of America Bulletin, v. 42, p. 298 – 299.

Zielke, O., Arrowsmith, J R., Grant-Ludwig, L., and Akciz, S. O., 2010, Slip in the 1857 and earlier large earthquakes along the Carrizo Plain, San Andreas Fault: Science, v. 327, p. 1119 – 1122.

Zielke, O., Arrowsmith, J R., Grant-Ludwig, and L., Akciz, S. O., 2012, High resolution topography-derived offsets along the 1857 Fort Tejon earthquake rupture trace, San Andreas Fault: Bulletin of the Seismological Society of America, v. 102, no. 3, p. 1135 – 1154, doi: 10.1785/0120110230.

Zielke, O., Klinger, Y., Arrowsmith, J R., 2015, Fault Slip and Earthquake Recurrence Along Strike-Slip Faults – Contributions of High-Resolution Geomorphic Data: Tectonophysics, v. 638, p. 43 – 62, doi: 10.1016/j.tecto.2014.11.004.

FIGURE CAPTIONS

Figure 6.1 – Age vs. Offset plot for the Carrizo Plain for the last 15,000 years. Box dimensions represent age and offset uncertainties. Black boxes represent age vs. offset plots provided by this dissertation. The red line represents the slip rate calculated by Sieh and Jahns (1984) for the last 3,700 years from the small (130 m) offset at Wallace Creek. Magenta lines represent uncertainties. The dashed black line is the slip rate (36 mm/yr, ~475 m offset) calculated at the 13,250 yr timescale in the same study. The dashed black line also represents the geodetic rate of 36 mm/yr (Schmalzle et al., 2006).

FIGURES

Figure 6.1

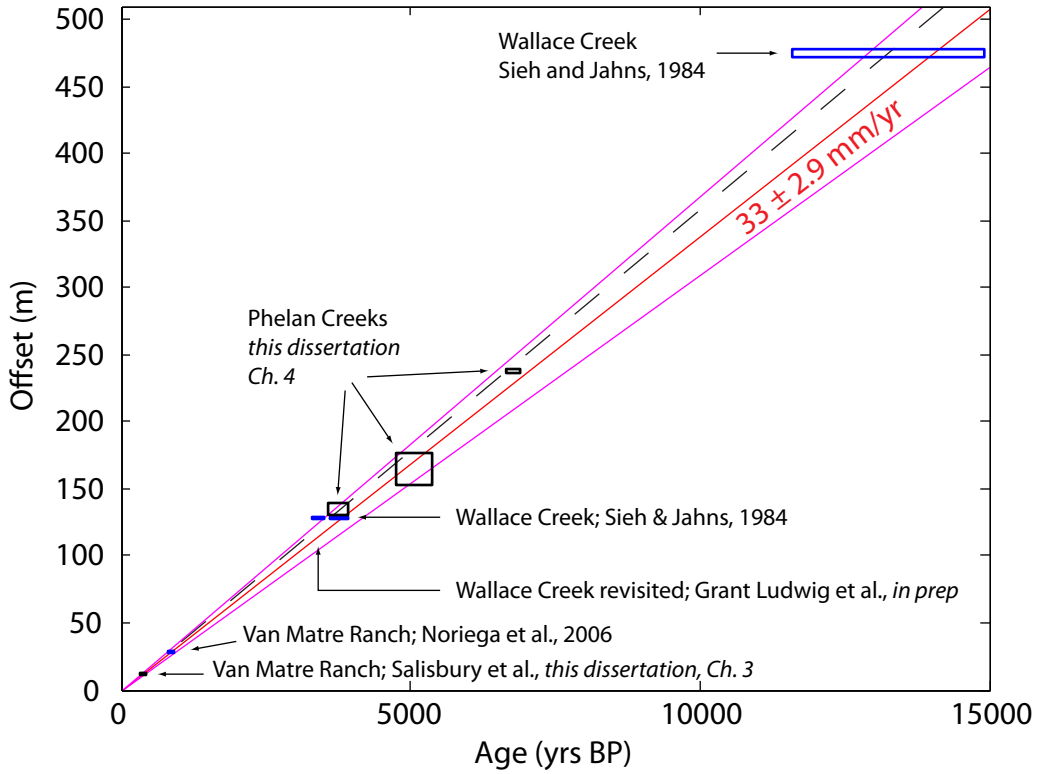

REFERENCES

The Working Group on California Earthquake Probabilities (WGCEP), 1988, Probabilities of large earthquakes occurring in California along the San Andreas fault: USGS Open File Report 88 – 398.

Adamiec, G., and Aitken, M., 1998, Dose-rate conversion factors: update: Ancient TL, v. 16, p. 37 – 50.

Akciz, S. O., Grant-Ludwig, L., Arrowsmith, J R., and Zielke, O., 2010, Century-long average time intervals between ruptures on the San Andreas Fault in the Carrizo Plain: Geology, v. 38, no. 9, p. 787 – 790, doi: 10.1130/G30995.1.

Allen, R. M., 2007, Earthquake hazard mitigation: new directions and opportunities: in Schubert, Gerald (Ed.), Treatise on Geophysics, Earthquake Seismology, vol. 4, Elsevier.

Arnold, R., and Johnson, H. R., 1910, Preliminary report on the McKittrick-Sunset oil region, Kern and San Luis Obispo counties, California: U. S. Geological Survey Bulletin 406.

Arnold, L.J., and Roberts, R.G., 2009, Stochastic modelling of multi-grain equivalent dose (D_e) distributions: Implications for OSL dating of sediment mixtures: Quaternary Geochronology, v. 4, p. 204 – 230, doi: 10.1016/j.quageo.2008.12.001.

Arrowsmith, J. R., Rhodes, D. D., and Pollard, D. D.,1998, Morphologic dating of scarps formed by repeated slip events along the San Andreas Fault, Carrizo Plain, California: Journal of Geophysical Research: Solid Earth, v. 103, no. 5.

Arrowsmith, J. R., and Zielke, O., 2009, Tectonic geomorphology of the San Andreas Fault zone from high resolution topography: An example from the Cholame segment: Geomorphology, v. 113, p. 70 – 81, doi: 10.1016/j.geomorph.2009.01.002.

Audemard, F. A., Ollarves, R., Bechthold, M., Diaz, G., Beck, C., Carrillo, E., Pantosti, D., and Diederix, H., 2008, Trench investigation on the main strand of the Bocono fault in its central section, at Mesa del Caballo, Merida Andes, Venezuela: Tectonophysics, v. 459, p. 38 – 53.

Awata, Y., Fu, B., and Zhang, Z., 2010, Geometry and slip distribution of the 1931 Fuyun Surface Rupture, northwest China. Forecasting large earthquakes from active faults in time and space: Abstracts of the HOKUDAN International Symposium on Active Faulting, Hokudan Earthquake Memorial Park, Awaji City, Japan.

Bemis, S. P., Micklethwaite, S., Turner, D., James, M. R., Akciz, S. O., Thiele, S. T., and Bangash, H. A., 2014, Ground-based and UAV-based photogrammetry: A multi-scale, high-resolution mapping tool for structural geology and paleoseismology: Journal of Structural Geology, v. 69, p. 163 – 178, doi: 10.1016/j.jsg.2014.10.007.

Bendick, R., Bilham, R., Freymueller, J., Larson, K., and Yin, G., 2000, Geodetic evidence for a low slip rate in the Altyn Tagh fault system: Nature, v. 404, p. 69 – 72, doi: 10.1038/35003555.

Bevis, M., Hudnut, K., Sanchez, R., Toth, C., Grejner-Brzezinska, D., Kendrick, E., Caccamise, D., Raleigh, D., Zhou, H., Shan, S., Shindle, W., Yong, A., Harvey, J., Borsa, A., Ayoub, F., Shrestha, R., Carter, B., Sartori, M., Phillips, D., and Coloma, F., 2005, The B4 Project: Scanning the San Andreas and San Jacinto Fault Zones: Eos Transactions American Geophysical Union, v. 86, no. 52, Fall meeting supplement, H34B-01.

Bond, C. E., Gibbs, A. D., Shipton, Z. K., and Jones, S., 2007, What do you think this is? "Conceptual uncertainty" in geoscience interpretation: GSA Today, v. 17, no. 11, p. 4 – 10, doi: 10.1130/GSAT01711A.1.

Bond, C. E., Philo, C., and Shipton, Z. K., 2011, When There isn't a Right Answer: Interpretation and reasoning, key skills for twenty-first century geoscience: International Journal of Science Education, v. 33, no. 5, p. 629 – 652.

Borsa, A., and Minster, J. B., 2012, Rapid Determination of Near-Fault Earthquake Deformation Using Differential lidar: Bulletin of the Seismological Society of America, v. 102, p. 1335 – 1347.

Bronk Ramsey, C., and Lee, S., 2013, Recent and planned developments of the program OxCal: Radiocarbon, vol 55, no. 2-3, p. 720 – 730.

Brooks, B.A., Hudnut, K.W., Akciz, S.O., Delano, J., Glennie, C.L., Prentice, C., and DeLong, S., 2013, On Offset Stream Measurements and Recent Coseismic Surface Rupture in the Carrizo Section of the San Andreas Fault: AGU Fall Meeting, Abstract T21D-01.

Brown, N.D., Rhodes, E.J., Antinao, J.L., McDonald, E.V., 2015, Single-grain post-IR IRSL signals of K-feldspars from alluvial fan deposits in Baja California Sur, Mexico: Quaternary International, v. 362, p. 132 – 138, doi: 10.1016/j.quaint.2014.10.024.

Burbank, D. W. and Anderson, R. S., 2001, Tectonic Geomorphology, 1st ed., Blackwell Science Inc., Malden, MA.

Buylaert, J.P., Murray, A.S., Thomsen, K.J., Jain, M., 2009, Testing the potential of an elevated temperature IRSL signal from K-feldspar: Radiation Measurements, v. 44, p. 560 – 565, doi: 10.1016/j.radmeas.2009.02.007.

Chen, Z., Burchfiel, B. C., Liu, Y., King, R. W., Royden, L. H., Tang, W., Wang, E., Zhao, J., and Zhang, X., 2000, Global positioning system measurements from eastern Tibet and their implications for India/Eurasia intercontinental deformation: Journal of Geophysical Research, v. 105, no. B7, p. 16,215 – 16,227, doi: 10.1029/2000JB900092.

Chen, T., Akciz, S. O., Hudnut, K. W., Zhang, D. Z., and Stock, J. M., 2015, Fault-Slip Distribution of the 1999 M_W 7.1 Hector Mine Earthquake, California, Estimated from Postearthquake Airborne LiDAR Data: Bulletin of the Seismological Society of America, v. 105, no. 2a, doi: 10.1785/0120130108.

Cowgill, E., Yin, A., and Harrison, T. M., 2003, Reconstruction of the Altyn Tagh fault based on U-Pb geochronology: Role of back thrusts, mantle sutures, and heterogeneous crustal strength in forming the Tibetan Plauteau: Journal of Geophysical Research, v. 108, no. B7, p. 2346, doi: 10.1029/2002JB002080.

Cowgill, E., Gold, R. D., Xuanhua, C., Xioa-Feng, W., Arrowsmith, J R., and Southon, J., 2009, Low Quaternary slip rate reconciles geodetic and geologic rates along the Altyn Tagh fault, northwestern Tibet: Geological Society of America, v. 37, no. 7, p. 647 – 650, doi: 10.1130/G25623A.1.

Cowgill, E., 2007, Impact of riser reconstruction on estimation of secular variation in rates of strike-slip faulting: Revisiting the Cherchen River site along the Altyn Tagh fault, NW China: Earth and Planetary Science Letters, v. 254, p. 239 – 255.

Dawson, T.E., 2013. Appendix A: Updates to the California reference fault parameter database: UCERF3 fault models 3.1 and 3.2: US Geological Survey Open-File Report.

Evans, J. S., and Hudak, A. T., 2007, A multiscale curvature algorithm for classifying discrete return lidar in forested environments: IEEE Transactions on Geoscience and Remote Sensing, v. 45, no. 4, p. 1029 – 1038, doi: 10.1109/TGRS.2006.890412.

Field, E. H., Arrowsmith, J R., Biasi, G. P., Bird, P., Dawson, T. E., Felzer, K. R., Jackson, D. D., Johnson, K. M., Jordan, T. H., Madden, C., Michael, A. J., Milner, K. R., Page, M. T., Parsons, T., Powers, P. M., Shaw, B. E., Thatcher, W. R., Weldon, R. J., and Zeng, Y., 2014, Uniform California Earthquake Rupture Forecast, Version 3 (UCERF3)—The time-independent model: Bulletin of the Seismological Society of America, v. 104, no.3, p. 1122 – 1180, doi: 10.1785/0120130164.

Galbraith, R.F., Roberts, R.G., Laslett, G.M., Yoshida, H., and Olley, J.M., 1999, Optical dating of single and multiple grains of quartz from Jinmium Rock Shelter, Northern Australia: Part I, Experimental design and statistical models: Archaeometry, v. 41, no. 2, p. 339 – 364, doi: 10.1111/j.1475-4754.1999.tb00987.x.

Gold, R.D., Cowgill, E., Arrowsmith, J R., Gosse, J., Chen, X., and Wang, X-F., 2009, Riser diachroneity, lateral erosion, and uncertainty in rates of strike-slip faulting: A case study from Tuzidun along the Altyn Tagh Fault NW China: Journal of Geophysical Research, v. 114, no. B04401, doi: 10.1029/2008JB005913.

Gold, P. O., Cowgill, E., Kreylos, O., and Gold, R. D., 2012, A terrestrial lidar-based workflow for determining three-dimensional slip vectors and associated uncertainties: Geosphere, v. 8, no. 2, p. 431 – 442, doi: 10.1130/GES00714.1.

Grant-Ludwig, L., Akciz, S. O., Noriega, G. R., Zielke, O., and Arrowsmith, J R., 2010, Climate-modulated channel incision and rupture history of the San Andreas Fault in the Carrizo Plain: Science, v. 327, no. 5969, p. 1117 – 1119, doi: 10.1126/science.1182837.

Grant Ludwig, L., Akciz, S. O., Arrowsmith, J R., and Salisbury, J. B., *in press*, Re-measurement of the San Andreas Fault slip rate at Wallace Creek, Carrizo Plain, CA.

Grant, L. B., and Sieh, K., 1994, Paleoseismic evidence of clustered earthquakes on the San Andreas fault in the Carrizo Plain, California: Journal of Geophysical Research, v. 99, no. B4, p. 6819 – 6841.

Haddad, D. E., Akciz, S. O., Arrowsmith, J R., Rhodes, D. D., Oldow, J. S., Zielke, O., Toke, N. A., Haddad, A. G., Mauer, J., and Shilpakar, P., 2012, Applications of airborne and terrestrial laser scanning to paleoseismology: Geosphere, v. 8, p. 771 – 785, doi: 10.1130/GES00701.1.

Haeussler, P. J., Schwartz, D. P., Dawson, T. E., Stenner, H. D., Lienkaemper, J. J., Sherrod, B., Cinti, F. R., Montone, P., Craw, P. A., Crone, A. J., and Personius, S. F., 2004, Surface rupture and slip distribution of the Denali and Totschunda faults in the 3 November 2002 M7.9 Earthquake, Alaska: Bulletin of the Seismological Society of America, v. 94, no. 6B, p. S23 – S52.

Hanks, T. C., 2000, The age of scarp-like landforms from diffusion equation analysis: Quaternary Geochronology: Methods and Applications, editors Noller, J. S., Sowers, J. M., Lettis W. R., AGU Reference Shelf, Washington, DC, vol. 4, p. 313 – 338.

Haugerud, R. A., Harding, D. J., Johnson, S. Y., Harless, J. L., Weaver, C. S., and Sherrod, B. L., 2003, High-Resolution lidar Topography of the Puget Lowland, Washington – A Bonanza for Earth Science, GSA Today, v. 13, no. 6, p. 4 – 10, doi: 10.1130/1052-5173(2003)13<0004:HLTOTP>2.0.CO;2.

He, J., Vernant, P., Chery, J., Wang, W., Lu. S., Ku, W., Xia, W., and Bilham, R, 2013, Nailing down the slip rate of the Altyn Tagh Fault: Geophysical Research Letters, v. 40, p. 5382 – 5386, doi: 10.1002/2013GL057497.

Hill, M. L., and Dibblee, T. W., 1953, San Andreas, Garlock, and Big Pine faults, California study of the character, history, and tectonic significance of their displacements: Bulletin of the Geological Society of America, v. 64, p. 443 – 458.

Hudnut, K.W., Borsa, A., Glennie, C., and Minster, J. B., 2002, High-resolution topography along surface rupture of the 16 October 1999 Hector Mine, California, earthquake (M_w 7.1) from airborne laser swath mapping: Bulletin of the Seismological Society of America, v. 92, p. 1570 – 1576, doi: 10.1785/0120000934.

Huntley, D.J., and Baril, M.R., 1997, The K content of the K-feldspars being measured in optical dating or in thermoluminescence dating: Ancient TL, v. 15, no. 1, p. 11 – 13.

Huntley, D.J., and Lamothe, M., 2001, Ubiquity of anomalous fading in K-feldspars and the measurement and correction for it in optical dating: Canadian Journal of Earth Science, v. 38, p. 1093 – 1106.

Johnson, K., Nissen, E., Saripalli, S., Arrowsmith, J R., McGarey, P., Scharer, K., Williams, P., and Blisniuk, K., 2014, Rapid mapping of ultrafine fault zone topography with structure from motion: Geosphere, v. 10, no. 5, p 969 – 986, doi: 10.1130/GES01017.1.

Jordan, T. H., Chen, Y., Gasparini, P., Madariaga, R., Main, I., Marzocchi, W., Papadopoulos, G., Sobolev, G., Yamoaka, K., and Zschau, J., 2011, Operational earthquake forecasting: state of knowledge and guidelines for utilization: Annals of Geophysics, v. 54, no. 4, p. 316 – 391.

Klinger, Y., Etchebes, M., Tapponnier, P., and Narteau, C., 2011, Characteristic slip for five great earthquakes along the Fuyun fault in China: Nature Geoscience, v. 4, p. 389 – 392, doi: 10.1038/NGEO1158.

Kondo, H., Awata, Y., Emre, Ö., Doğan, A., Özalp, S., Tokay, F., Yildirim, C., Yoshioka, T., and Okumura, K., 2005, Slip distribution, fault geometry, and fault segmentation of the 1944 Bolu-Gerede earthquake rupture, North Anatolian fault, Turkey: Bulletin of the Seismological Society of America, v. 95, p. 1234 – 1249.

Kondo, H., Özaksoy, V., and Yildirim, C., 2010, Slip history of the 1944 Bolu-Gerede earthquake rupture along the North Anatolian fault system – Implications for recurrence behavior of multi-segment earthquakes: Journal of Geophysical Research, v. 115, no. B4, doi: 10.1029/2009JB006413.

Kreutzer, S., Schmidt, C., Fuchs, M., Dietze, M., Fischer, M., Fuchs, M., 2012, Introducing an R package for luminescence dating analysis: Ancient TL, v. 30, no. 1, p. 1 – 8.

Lawson, A. C., and others, 1908, Report of the earthquake investigation commission upon the California earthquake of April 18, 1906: Carnegie Institution of Washington, D. C.

Lawson, M. J., Roder, B. J., Stang, D. M., Rhodes, E., 2012, OSL and IRSL characteristics of quarts and fledspar from Southern California, USA: Radiation Measurements, v. 27, no. 9, p. 830 – 836, doi: 10.1016/j.radmeas.2012.03.025.

Leprince, S., Hudnut, K.W., Akciz, S. O., Hinojosa Corona, A., and Fletcher, J.M., 2011, Surface rupture and slip variation induced by the 2010 El Mayor – Cucapah earthquake, Baja California, quantified using COSI-Corr analysis on pre- and post-earthquake lidar acquisitions: Southern California Earthquake Center Annual Meeting abstract.

Lienkaemper, J. J., 2001, 1857 Slip on the San Andreas Fault Southeast of Cholame, California: Bulletin of the Seismological Society of America, v. 91, no. 6, p. 1659 – 1672.

Lienkaemper, J. J., and Sturm, T. A., 1989, Reconstruction of a channel offset in 1857(?) by the San Andreas fault near Cholame, California: Bulletin of the Seismological Society of America, v. 79, no. 3, p. 901 – 909.

Lindvall, S. C., Rockwell, T. K., and Hudnut, K. W., 1989, Evidence for Prehistoric Earthquakes on the Superstition Hills Fault from Offset Geomorphic Features: Bulletin of the Seismological Society of America, v. 79, no 2, p. 342 – 361.

Liu, J., Klinger, Y., Sieh, K., and Rubin, C., 2004, Six similar sequential ruptures of the San Andreas fault, Carrizo Plain, California: Geology, v. 32, no. 8, pp. 649 – 652, doi: 10.1130/G20478.1.

Liu-Zeng, J., Klinger, Y., Sieh, K., Rubin, C., and Seitz, G., 2006, Serial ruptures of the San Andreas fault, Carrizo Plain, California, revealed by three-dimensional excavations: Journal of Geophysical Research, v. 111, B02306, doi: 10.1029/2004JB003601.

Madden, C., Haddad, D. E., Salisbury, J. B., Zielke, O., Arrowsmith, J R., Weldon II, R. J., and Colunga, J., 2013, Compilation of Slip-in-the-Last-Event Data and Analysis of Last Event, Repeated Slip, and Average Displacement for Recent and Prehistoric Ruptures, Appendix R *in* Field, E. H., Biasi, G. P., Bird, P., Dawson, T. E., Felzer, K. R., Jackson, D. D., Johnson, K. M., Jordan, T. H., Madden, C., Michael, A. J., Milner, K. R., Page, M. T., Parsons, T., Powers, P. M., Shaw, B. E., Thatcher, W. R., Weldon II, R. J., and Zeng, Y., 2013, Uniform California earthquake rupture forecast, version 3 (UCERF3), The time-independent model: U.S. Geological Survey Open-File Report 20131165, 97 p., California Geological Survey Special Report 228, and Southern California Earthquake Center Publication 1792, http://pubs.usgs.gov/of/2013/1165.

McCalpin, J., 1996, Paleoseismology, 1st ed., Academic Press, San Diego, CA.

McGill, S. F., and Sieh, K. E., 1991, Surficial offsets on the central and eastern Garlock fault associated with prehistoric earthquakes: Journal of Geophysical Research, v. 96, no. B13, p. 21597 – 21621.

Meade, B. J., and Hager, B. H., 2005, Block models of crustal motion in southern California constrained by GPS measurements: Journal of Geophysical Research, v. 110, B03403, doi: 10.1029/2004JB003209.

Mériaux, A.-S., Ryerson, F. J., Tapponnier, P., Van der Woerd, J., Finkel, R. C., Xu, X., Xu, Z., and Caffee, M. W., 2004, Rapid slip along the central Altyn Tagh fault: Morphochronologic evidence from Cherchen He and Sulamu Tagh: Journal of Geophysical Research, v. 109, no. B06401, doi: 10/1029/2003jb002558.

Mériaux, A.-S., Tapponnier, P., Ryerson, F. J., Xiwei, X., King, G., Van der Woerd, J., Finkel, R. C., Haibing, L., Caffee, M. W., Zhiqin, X., and Wenbin, C., 2005, The Aksay segment of the northern Altyn Tagh fault: Tectonic geomorphology, landscape evolution, and Holocene slip rate, Journal of Geophysical Research, v. 110, no. B04404, doi: 10.1029/2004JB003210.

Molnar, P., and Tapponnier, P., 1975, Cenozoic tectonics of Asia – Effects of a continental collision: Science, v. 189, no. 4201, p. 419 – 426, doi: 10.1126/science.189.4201.419.

Muretta, M., 2009, Holocene earthquake geology of the central Altyn Tagh fault, Xinjiang, China: Implications for recurrence interval, strain release, and fault behavior: M.S. Thesis, *unpublished*, Arizona State University.

Nissen, E., Krishnan, A. K., Arrowsmith, J R., and Saripalli, S., 2012, Three-dimensional surface displacements and rotations from differencing pre- and post-earthquake lidar point clouds: Geophysical Research Letters, v. 39, no. L16301, doi: 10.1029/2012GL052460.

Nissen, E., Maruyama, T., Arrowsmith, J R., Elliot, J. R., Krishnan, A. K., Oskin, M. E., and Saripalli, S., 2014, Coseismic fault zone deformation revealed with differential LiDAR: examples from Japanese Mw 7 intraplate earthquakes: Earth and Planetary Science Letters, v. 405, p. 244 – 256, doi: 10.1016/j.epsl.2014.08.031.

Noriega, G.R., Arrowsmith, J R., Grant, L. B., Young, J. J., 2006, Stream Channel Offset and Late Holocene Slip Rate of the San Andreas Fault at the Van Matre Ranch Site, Carrizo Plain, California: Bulletin of the Seismological Society of America, v. 96, no. 1, p.33 – 47, doi: 10.1785/0120050094.

Oreskes, N., Schrader-Frechette, K., and Belitz, K., 1994, Verification, validation, and confirmation of numerical models in the Earth sciences: Science, v. 263, no. 5147, p. 641 – 646.

Oskin, M., Le, K., and Strane, M. D., 2007, Quantifying fault-zone activity in arid environments with high-resolution topography: Geophysical Research Letters, v. 34, no. L23S05, p. 1 – 5, doi: 10.1029/2007GL031295.

Oskin, M., Arrowsmith, J R., Hinojosa Corona, A. H., Elliott, A. J., Fletcher, J. M., Fielding, E., Gold, P. O., Garcia, J. J. G., Hudnut, K. W., Liu-Zeng, J., and Teran, O. J., 2012, Complex surface rupture of the El Mayor-Cucapah earthquake imaged with airborne lidar: Science, v. 335, p. 702 – 705.

Ouchi, S., 2004, Flume experiments on the horizontal stream offset by strike-slip faults: Earth Surface Processes and Landforms, v. 29*,* p. 161 – 173, doi: 10.1002/esp.1017.

Prentice, C. S., Crosby, C. J., Whitehill, C. S., Arrowsmith, J R., Furlong, K. P., and Phillips D. A., 2009, GeoEarthScope LiDAR illuminates northern California's active faults: EOS Transactions of the American Geophysical Union, v. 90, no. 7.

Reimer, P. J., Bard, E., Bayliss, A., Beck, J. W., Blackwell, P. G., Bronk Ramsey, C., Grootes, P. M., Guilderson, T. P., Haflidason, H., Hajdas, I., Hattz, C., Heaton, T. J., Hoffmann, D. L., Hogg, A. G., Hughen, K. A., Kaiser, K. F., Kromer, B., Manning, S. W., Niu, M., Reimer, R. W., Richards, D. A., Scott, E. M., Southon, J. R., Staff, R. A., Turney, C. S. M., and van der Plicht, J., 2013, IntCal13 and Marine13 Radiocarbon Age Calibration Curves 0 – 50,000 Years cal BP: Radiocarbon, vol 55, no. 4.

Rhodes, E.J., 2015, Dating sediments using potassium feldspar single-grain IRSL: Initial methodological considerations: Quaternary International, v. 362, p. 14 – 22.

Rockwell, T. K., and Pinault, C. T., 1986, Holocene slip events on the southern Elsinore fault, Coyote Mountains, southern California, *in* Ehlig, P., ed., Neotectonics and Faulting in Southern California, Geological Society of America Guidebook and Volume, Cordilleran Section, Boulder, Colorado, p. 193 – 196.

Rockwell, T. K., 1990, Holocene activity of the Elsinore fault in the Coyote Mountains, Southern California, *in* Friends of the Pleistocene Winter Fieldtrip: Western Salton Trough Soils and Neotectonics Guidebook, San Diego State University, San Diego, California, p. 30 – 42.

Rockwell, T. K., Lindvall, S., Dawson, T., Langridge, R., Lettis, W., and Klinger, Y., 2002, Lateral offsets on surveyed cultural features resulting from the 1999 İzmit and Düzce Earthquakes, Turkey: Bulletin of the Seismological Society of America, v. 92, no 1, p. 79 – 94.

Rockwell, T. K., and Klinger, Y., 2013, Surface Rupture and Slip Distribution of the 1940 Imperial Valley Earthquake, Imperial Fault, Southern California: Implications for Rupture Segmentation and Dynamics: Bulletin of the Seismological Society of America, v. 103, no. 2A, p. 629 – 640, doi: 10.1785/0120120192.

Rockwell, T.K., Dawson, T. E., Young Ben-Horin, J., Seitz, G., 2014, A 21 event, 4,000-year history of surface ruptures in the Anza Seismic Gap, San Jacinto Fault, and implications for long-term earthquake production on a major plate boundary fault: Pure and Applied Geophysics, v. 172, no. 5, p. 1143 – 1165, doi: 10.1007/s00024-014-0955-z.

Royer, J. Y., Gordon, R. G., and Horner-Johnson, B. C., 2006, Motion of Nubia relative to Antarctica since 11 Ma: Implications for Nubia-Somalia, Pacific–North America, and India-Eurasia motion: Geology, v. 34, p. 501 – 504.

Ryan, W. B. F., Carbotte, S. M., Coplan, J. O., O'Hara, S., Melkonian, A., Arko, R., Weissel, R. A., Ferrini, V., Goodwillie, A., Nitsche, F., Bonczkowski, J., and Zemsky, R., 2009, Global Multi-Resolution Topography synthesis: Geochemistry, Geophysics, Geosystems, v. 10, no. 3, doi: 10.1029/2008GC002332.

Salisbury, J. B., Rockwell, T. K., Middleton, T., and Hudnut, K., 2012, Lidar and field observations of slip distribution for the most recent surface ruptures along the central San Jacinto fault: Bulletin of the Seismological Society of America, v. 102, no. 2, p. 598 – 619, doi: 10.1785/0120110068.

Salisbury, J. B., Haddad, D. E., Rockwell, T. K., Arrowsmith J R., Madugo, C., Zielke, O., and Scharer, K., 2015, Validation of meter-scale surface faulting offset measurements from high-resolution topographic data: Geosphere, v. 11, no. 6, doi: 10.1130/GES01197.1.

Salisbury, J. B., Arrowsmith J R., Brown, N., Rockwell, T. K., Akciz, S. O., Grant Ludwig, L., *in press*, The age and origin of small offsets at Van Matre Ranch along the San Andreas Fault in the Carrizo Plain, California.

Scharer, K., Salisbury, J. B., Arrowsmith, J R., and Rockwell, T. K., 2014, Southern San Andreas Fault Evaluation field activity: Approaches to measuring small geomorphic offsets – challenges and recommendations for active fault studies: Seismological Research Letters, v. 85, no. 1, doi: 10.1785/0220130108.

Scharer, K., Weldon, R., Streig, A., and Fumal, T., 2014, Paleoearthquakes at Frazier Mountain, California delimit extent and frequency of past San Andreas Fault ruptures along 1857 trace: Geophysical Research Letters, v. 41, no. 13, p. 4527 – 4534, doi: 10.1002/2014GL060318.

Schmalzle, G., Dixon, T., Malservisi, R., and Govers, R., 2006, Strain accumulation across the Carrizo segment of the San Andreas Fault, California: Impact of laterally varying crustal properties: Journal of Geophysical Research: Solid Earth, vol. 111, no. B5, https://doi.org/10.1029/2005JB003843.

Scholz, C. H., 2002, The mechanics of earthquakes and faulting, 2nd ed., Cambridge University Press, Cambridge, U.K.

Schwartz, D. P., and Coppersmith, K. J., 1984, Fault behavior and characteristic earthquakes: examples from the Wasatch and San Andreas fault zones: Journal of Geophysical Research, v. 89, no. B7, p. 5681 – 5698.

Shen, Z.-K., Wang, M., Li, Y., Jackson, D. D., Yin, A., Dong, D., Fang, P., 2001, Crustal deformation along the Altyn Tagh fault system, western China, from GPS: Journal of Geophysical Research, v. 106, p. 30,607 – 30,621, doi: 10.1029/2001JB000349.

Shimazaki, K., and Nakata, T., 1980, Time-predictable recurrence model for large earthquakes: Geophysical Research Letters, v. 7, no. 4, p. 279 – 282.

Sieh, K. E., 1978, Slip along the San Andreas fault associated with the great 1857 earthquake: Bulletin of the Seismological Society of America, v. 68, no. 5, p. 1421 – 1448.

Sieh, K. E., and Jahns, R. H., 1984, Holocene activity of the San Andreas fault at Wallace Creek, California: Geological Society of America Bulletin, v. 95, p. 883 – 896.

Tapponnier, P and Molnar, P., 1977, Active faulting and tectonics in China: Journal of Geophysical Research, v. 82., p. 2905 – 2930, doi: 10.1029/JB082i020p02905.

Taylor, M. H., and Yin, A, 2009, Active structures of the Himalayan-Tibetan orogeny and their relationships to earthquake distribution, contemporary strain field, and Cenozoic volcanism: *Geosphere*, v. 5, no. 3, p. 199 – 214, doi: 10.1130/GES00217.1.

Trifonov, V. G., Makarov, V. I., and Skobelev, S. F., 1992, The Talas-Fergana active right-lateral fault: Annales Tectonicae, v. 6, p. 224 – 237.

Wallace, R. E., 1968, Notes on stream channels offset by the San Andreas fault, southern coast ranges, California, *in* Dickson, W. R., and Grantz, A., eds., Proceedings of Conference on Geologic Problems of the San Andreas Fault system, Stanford University Publication, Geological Sciences, v. 11, p. 6 – 21.

Wallace, R. E., ed., 1990, The San Andreas fault system, California: United States Geological Survey Professional Paper 1515.

Wallace, K., Yin, G., and Bilham, R., 2004, Inescapable slow slip on the Altyn Tagh Fault: Geophysical Research Letters, v. 31, no. L09613, doi: 10.1029/2004GL019724.

Washburn, Z., Arrowsmith, J R., Forman, S. L., Cowgill, E., Wang, X. F., Zhang, Y. Q., and Chen, Z. L., 2001, Late Holocene earthquake history of the central Altyn Tagh fault, China: Geology, v. 29, p. 1051 – 1054.

Washburn, Z., Arrowsmith, J R., Dupont-Nivet, G., Xiaofeng, W., Yueqiao, Z., and Zhengle, C., 2003, Paleoseismology of the Xorxol segment of the Central Altyn Tagh Fault, Xinjiang, China: Annals of Geophysics, v. 46, no. 5, p. 1015 – 1034.

Weldon, R., Scharer, K., Fumal, T., Biasi, G., 2004, Wrightwood and the earthquake cycle: What a long recurrence record tells us about how faults work: GSA Today, v. 14, no. 9, p. 4 – 10, doi: 10.1130/1052-5173(2004)014<4:WATECW>2.0CO;2.

Wells, D. L., and Coppersmith, K. J., 1994, New empirical relationships among magnitude, rupture length, rupture width, rupture area and surface displacement: Bulletin of the Seismological Society of America, v. 84, no. 4, p. 974 – 1002.

Whipple, K. X, and Tucker, G. E., 1999, Dynamics of the stream-power river incision model: Implications for height limits of mountain ranges, landscape response timescales, and research needs: Journal of Geophysical Research, v. 104, no. B8, p. 17,661 – 17,674.

Wood, H. O., and Buwalda, J. P.,1931, Horizontal displacement along the San Andreas fault in the Carrizo Plain, California: Geological Society of America Bulletin, v. 42, p. 298 – 299.

Yeats, R. S., Sieh, K. E., and Allen, C. R., 1997, The Geology of Earthquakes, Oxford University Press, Oxford, New York, 568.

Zhang, P-Z., Molnar, P., and Xu, X., 2007, Late Quaternary and present-day rates of slip along the altyn Tagh Fault, northern margin of the Tibetan plateau: Tectonics, v. 26, no. TC5010, doi: 10.1029/2006TC002014.

Zielke, O., Arrowsmith, J R., Grant-Ludwig, L., and Akciz, S. O., 2010, Slip in the 1857 and earlier large earthquakes along the Carrizo Plain, San Andreas Fault: Science, v. 327, p. 1119 – 1122.

Zielke, O., and Arrowsmith, J R., 2012, LaDiCaoz and LiDARimager—MATLAB GUIs for lidar data handling and lateral displacement measurement: Geosphere - Special issue on high resolution topography, v. 8, no.1, p. 206 – 221, doi:10.1130/GES00686.1.

Zielke, O., Arrowsmith, J R., Grant-Ludwig, and L., Akciz, S. O., 2012, High resolution topography-derived offsets along the 1857 Fort Tejon earthquake rupture trace, San Andreas Fault: Bulletin of the Seismological Society of America, v. 102, no. 3, p. 1135 – 1154, doi: 10.1785/0120110230.

Zielke, O., Klinger, Y., Arrowsmith, J R., 2015, Fault Slip and Earthquake Recurrence Along Strike-Slip Faults – Contributions of High-Resolution Geomorphic Data: Tectonophysics, v. 638, p. 43 – 62, doi: 10.1016/j.tecto.2014.11.004.

APPENDIX A

IRB EXEMPTION

For work in Chapter 2, we received an exempt status from the Institutional Review Board* for our research involving the use of educational tests with human subjects: Federal law 45 CFR 46.101(b) exempt category 7.2.

*Arizona State University's Office of Research Integrity and Assurance

APPENDIX B

CLASSROOM SURVEY

Offset Validation, Classroom Exercise

Introduction:

Your participation in this exercise is ***completely voluntary*** and you may skip questions if you wish. Even if you are participating in this exercise as part of a classroom exercise you may withdraw at any time with no penalty. You must be 18 years of age or older to continue. Your responses will help quantify observational differences and ultimately help discern the reliability and objectivity of remotely determinedoffset measurements. This study is supported by the U.S. Geological Survey, the Southern California Earthquake Center, and the Working group on California Earthquake Probabilities.

The following pages contain examples of tectonically offset geomorphic features. All examples show right-lateral offset on northwest-trending faults. Each image consists of a combination of three Light Detection and Ranging-derived (LiDAR-derived) products: an opaque "hillshade," a transparent digital elevation model (DEM), and a contour map.

Please rate your prior experience level *(circle)*: 1 / 2 / 3 / 4

1) I have no prior experience whatsoever.
2) I am familiar with the basic geologic principles and/or high-resolution topographic data.
3) I have measured offset geomorphic features in the field or with high-resolution topography/imagery.
4) I have extensive experience measuring offset features in the field or with high-resolution topography/imagery.

Please circle all that apply:

Have previously measured offset features in/on:

a) the field b) aerial photography c) satellite photography d) topographic maps e) high-resolution DEM's

Have previously measured offset features using:

a) tape measure/ruler b) total station c) Google Earth d) ArcGIS e) LaDiCaoz f) other _____

Have a) taken b) taught

a) Field Geology b) Geomorphology c) Earthquake Geology d) Quat. Geo. e) Tectonic Geomorph. f) GIS

Instructions:

1) Sketch/trace the fault and geomorphic feature(s) (e.g. channel thalweg, channel margins, bar crest) that you will use to estimate tectonic offset. Some images contain multiple offsets and/or features.
2) Tear off the scale bar in the bottom right corner of each page for your measurement on that page.
3) Estimate measurement uncertainty (e.g. +/- 1.5 m) so that your offset measurement can be expressed as a range in meters. For example, a 12 m +/- 1.5 m measurement is a 10.5 - 13.5 m offset.
4) Rate the overall quality of the offset feature using the provided rubric*. List x-axis first, then the y-axis. (e.g. for a channel at 25° to a well-defined, narrow fault trace: "low-high") **Image courtesy of David Haddad*

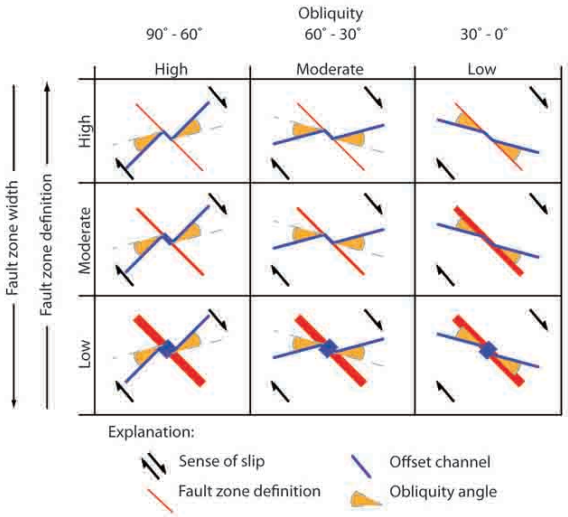

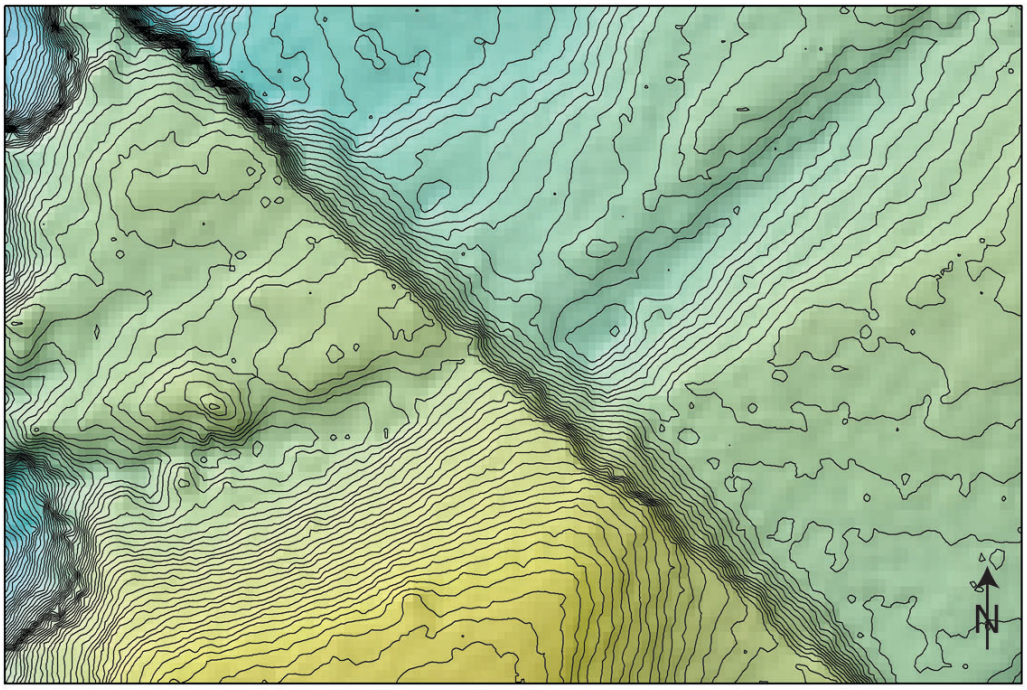

1:175, 10 cm contour interval

Please answer the following:

1) What is the magnitude of the offset(s) (in meters)? _____

2) What is the uncertainty of the offset(s) (+/- in meters)? _____

3) What is the quality of the offset(s)? _____

4) Additional comments? (optional) _____

1

0 5 10 Meters

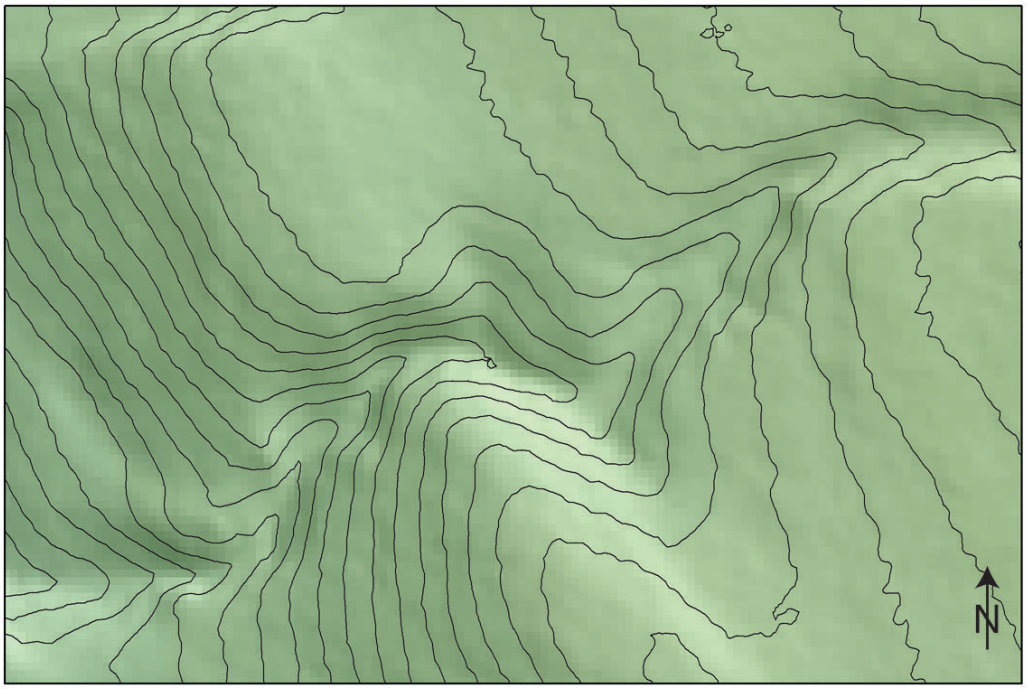

1:400, 50 cm contour interval

Please answer the following:

1) What is the magnitude of the offset(s) (in meters)? _____

2) What is the uncertainty of the offset(s) (+/- in meters)? _____

3) What is the quality of the offset(s)? _____

4) Additional comments? (optional) _____

2

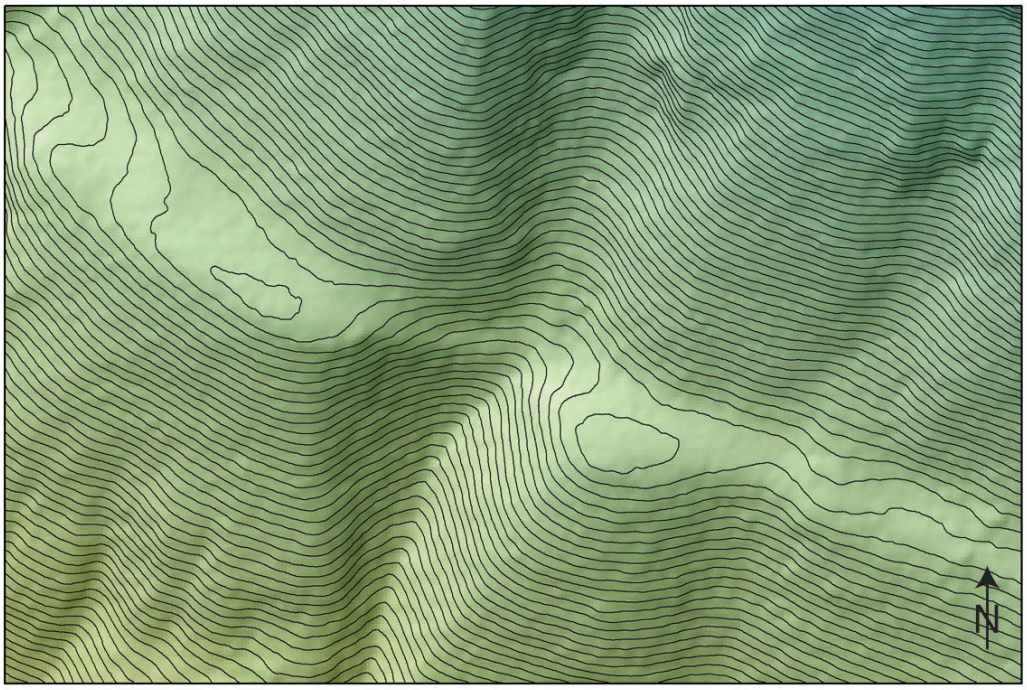

1:800, 100 cm contour interval

Please answer the following:

1) What is the magnitude of the offset(s) (in meters)? _____

2) What is the uncertainty of the offset(s) (+/- in meters)? _____

3) What is the quality of the offset(s)? _____

4) Additional comments? (optional) _____

3

0 10 20 30 40 Meters

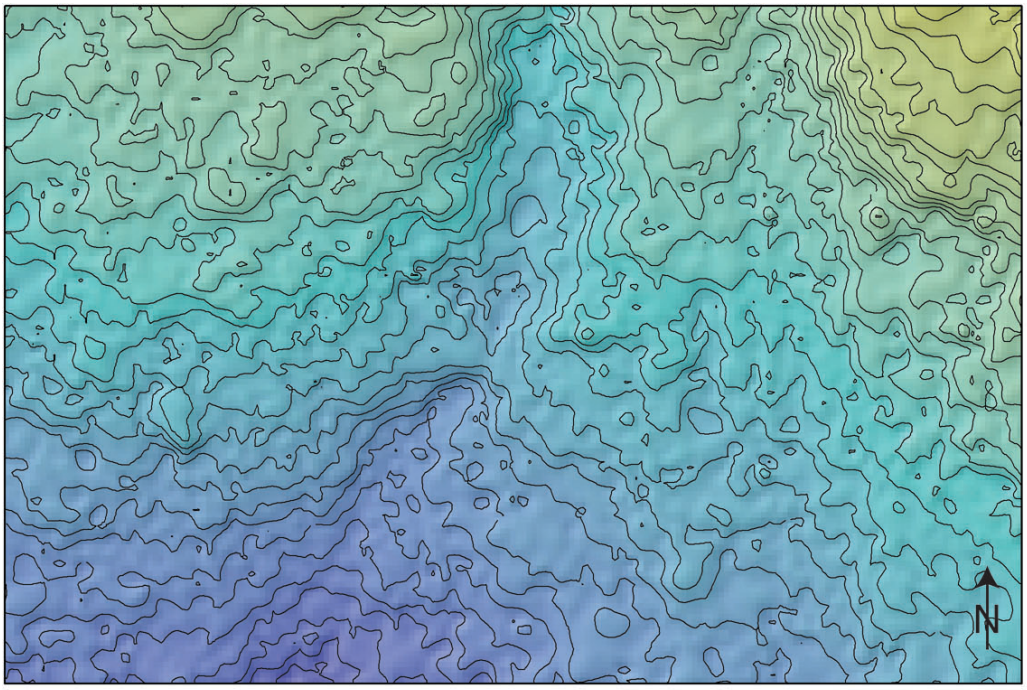

1:250, 10 cm contour interval

Please answer the following:

1) What is the magnitude of the offset(s) (in meters)? _____

2) What is the uncertainty of the offset(s) (+/- in meters)? _____

3) What is the quality of the offset(s)? _____

4) Additional comments? (optional) _____

4

0 5 10 15 20 Meters

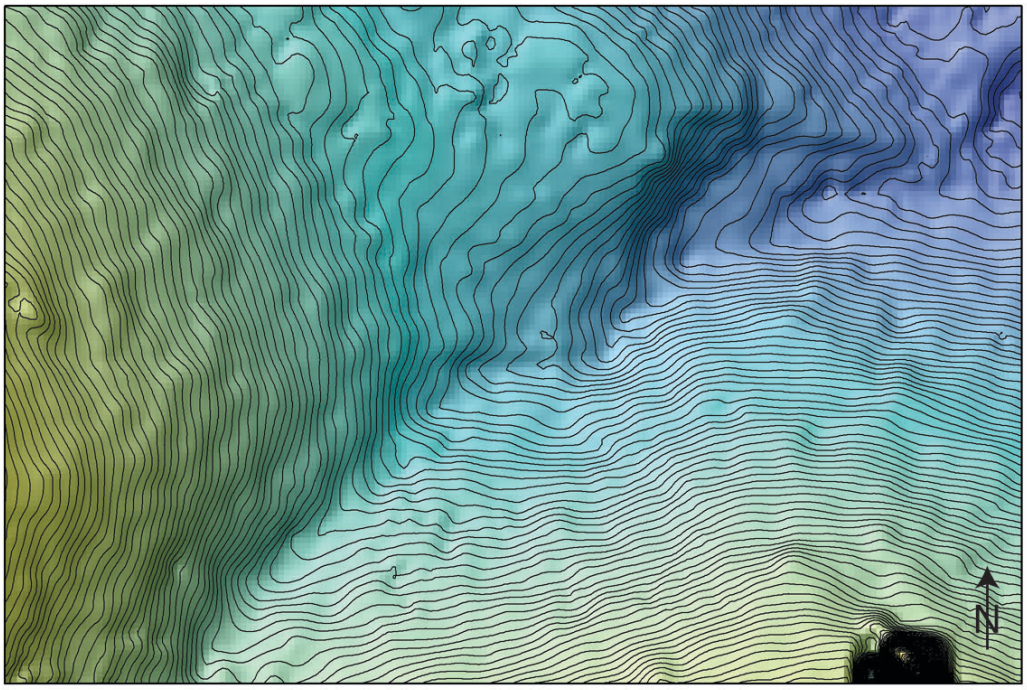

1:250, 25 cm contour interval

Please answer the following:

1) What is the magnitude of the offset(s) (in meters)? _____

2) What is the uncertainty of the offset(s) (+/- in meters)? _____

3) What is the quality of the offset(s)? _____

4) Additional comments? (optional) _____

5

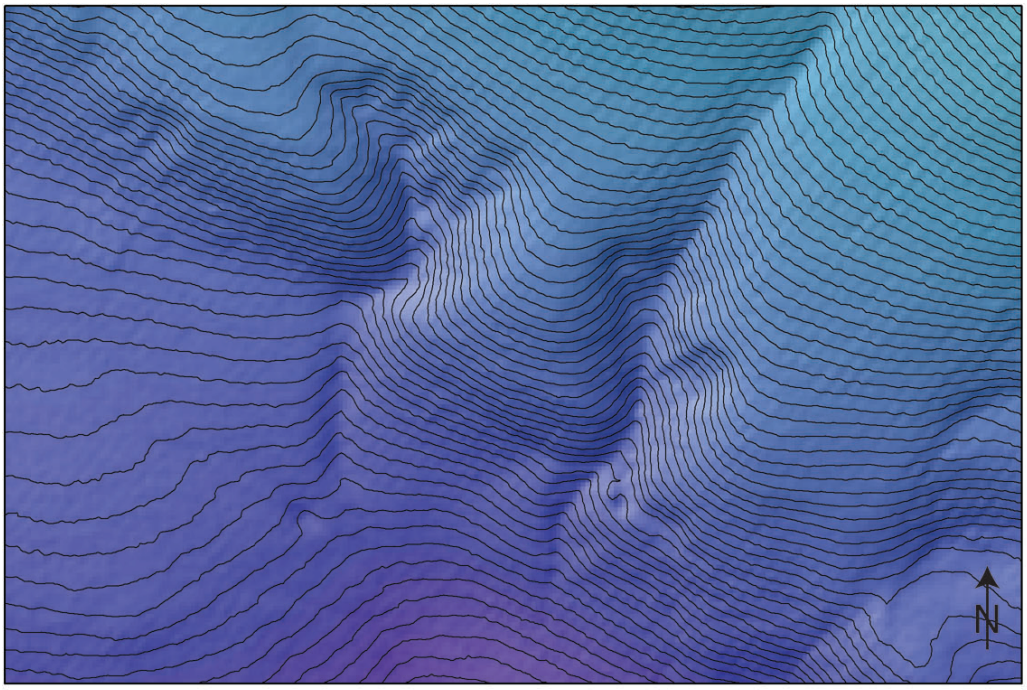

1:650, 50 cm contour interval

Please answer the following:

1) What is the magnitude of the offset(s) (in meters)? _____

2) What is the uncertainty of the offset(s) (+/- in meters)? _____

3) What is the quality of the offset(s)? _____

4) Additional comments? (optional) _____

6

0 10 20 30 40 Meters

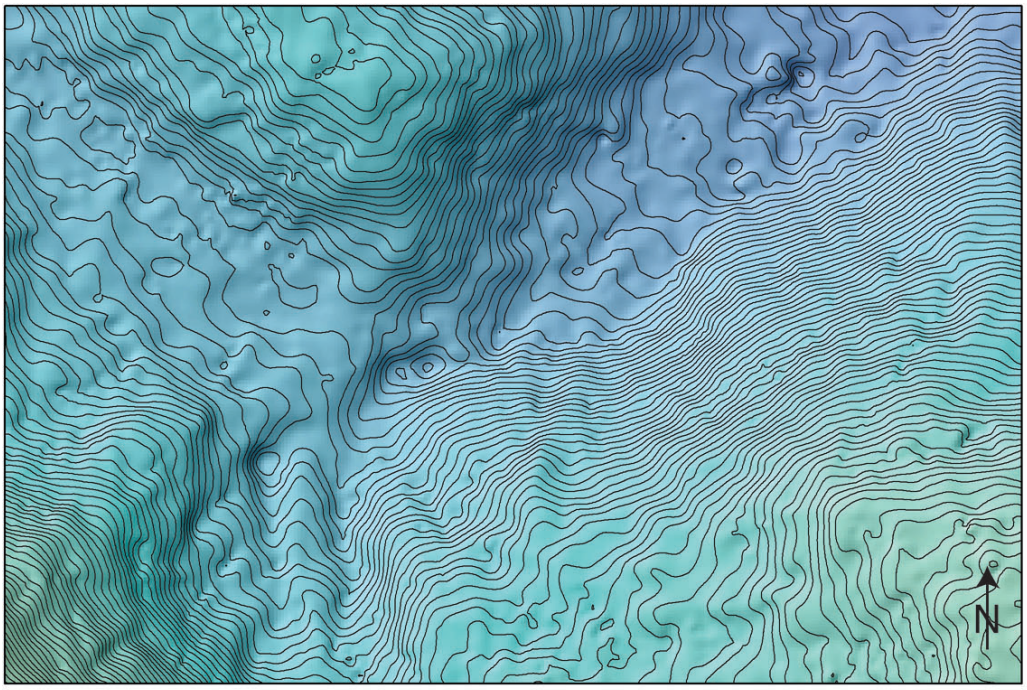

1:400, 25 cm contour interval

Please answer the following:

1) What is the magnitude of the offset(s) (in meters)? _____

2) What is the uncertainty of the offset(s) (+/- in meters)? _____

3) What is the quality of the offset(s)? _____

4) Additional comments? (optional) _____

7

0 5 10 15 20 Meters

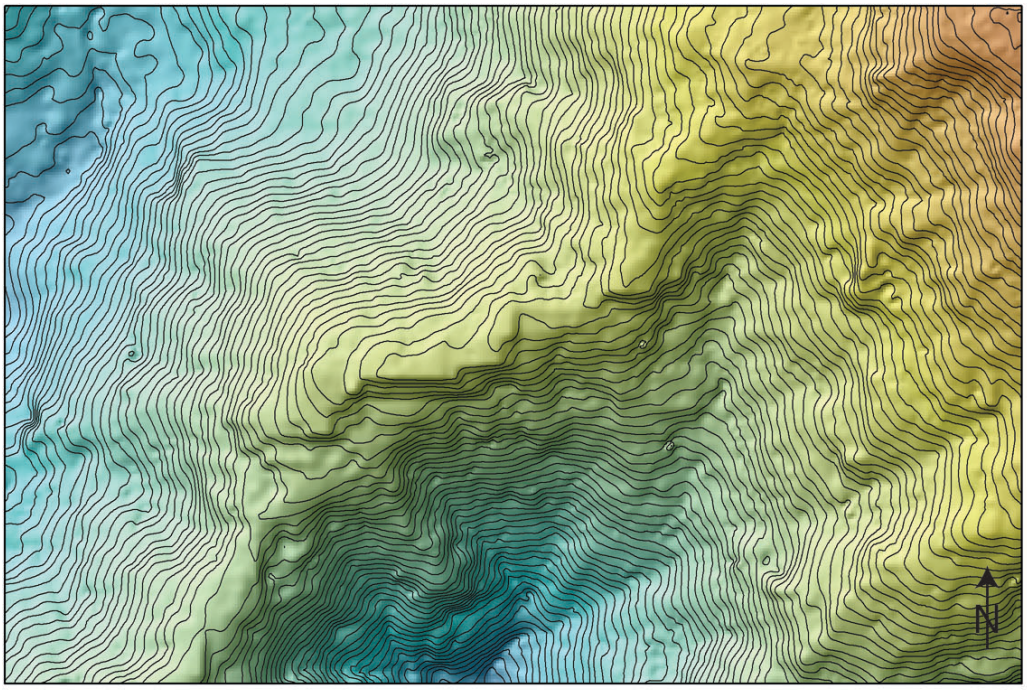

1:500, 50 cm contour interval

Please answer the following:

1) What is the magnitude of the offset(s) (in meters)? _____

2) What is the uncertainty of the offset(s) (+/- in meters)? _____

3) What is the quality of the offset(s)? _____

4) Additional comments? (optional) _____

8

0 10 20 30 40 Meters

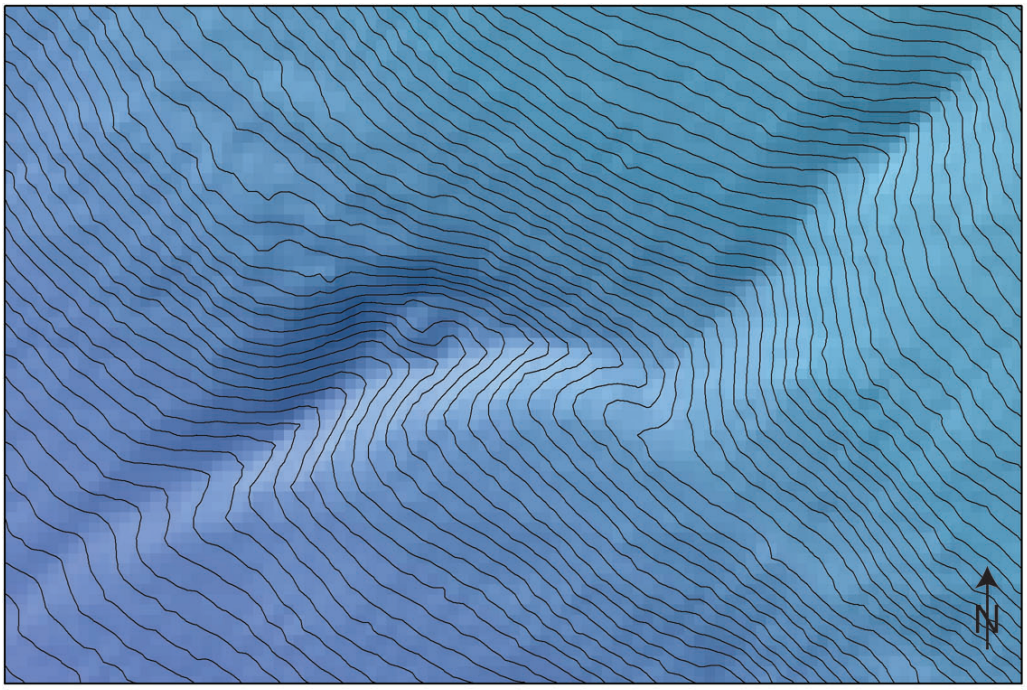

1:300, 25 cm contour interval

Please answer the following:

1) What is the magnitude of the offset(s) (in meters)? _____

2) What is the uncertainty of the offset(s) (+/- in meters)? _____

3) What is the quality of the offset(s)? _____

4) Additional comments? (optional) _____

9

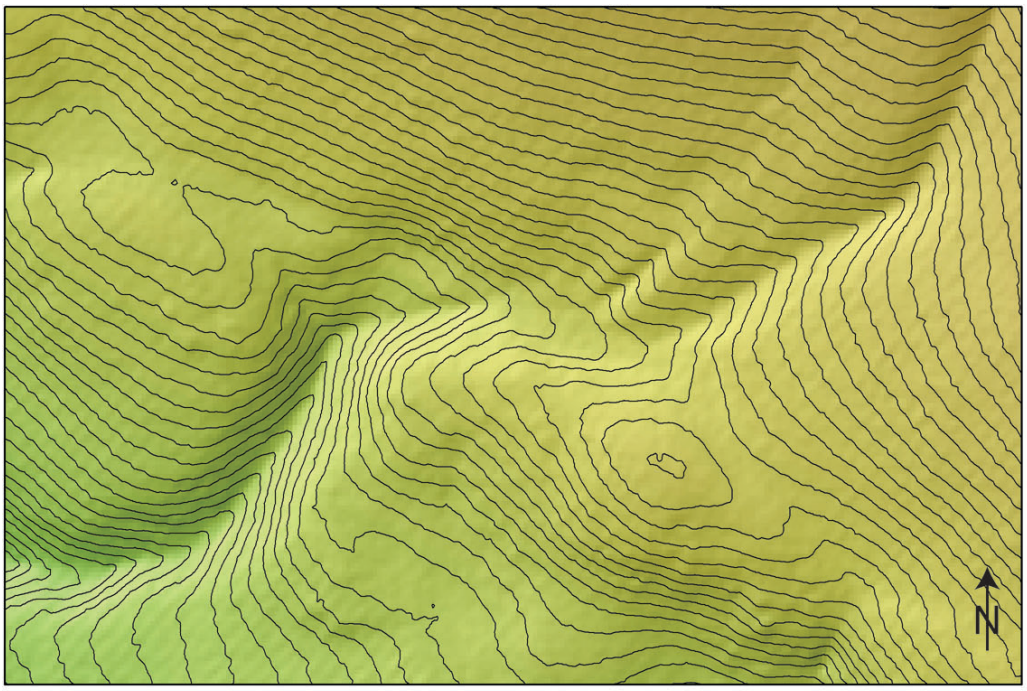

1:600, 50 cm contour interval

Please answer the following:

1) What is the magnitude of the offset(s) (in meters)? _____

2) What is the uncertainty of the offset(s) (+/- in meters)? _____

3) What is the quality of the offset(s)? _____

4) Additional comments? (optional) _____

10